ORNL-4741
UC-34 – Physics

A STUDY OF THE EFFECT OF SOURCE ASYMMETRY ON TIME-DEPENDENT NEUTRON AND SECONDARY GAMMA-RAY TRANSPORT IN AIR

D. J. McGregor
E. A. Straker

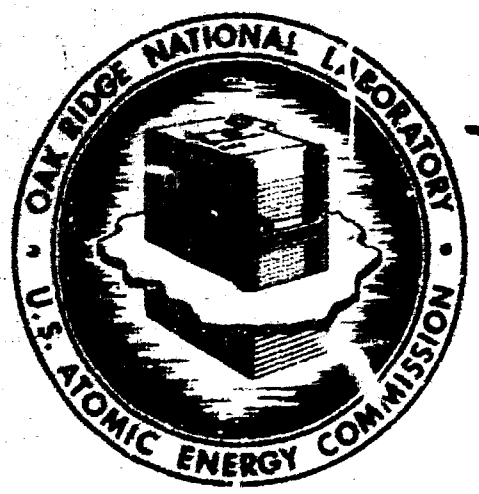

OAK RIDGE NATIONAL LABORATORY
operated by
UNION CARBIDE CORPORATION
for the
U.S. ATOMIC ENERGY COMMISSION

BLANK PAGE

Printed in the United States of America. Available from
National Technical Information Service
U.S. Department of Commerce
5285 Port Royal Road, Springfield, Virginia 22161
Price: Printed Copy $3.00; Microfiche $0.95

BLANK PAGE

ORNL-4741

Contract No. W-7405-eng-26

Neutron Physics Division

A STUDY OF THE EFFECT OF SOURCE ASYMMETRY ON TIME-DEPENDENT NEUTRON AND SECONDARY GAMMA-RAY TRANSPORT IN AIR

B. J. McGregor* and E. A. Straker†

NOTE:

This Work Funded by
DEFENSE NUCLEAR AGENCY
Under Subtask PE08001

*On assignment from the Australian Atomic Energy Commission.

†Present address: Science Applications, Inc., Huntsville, Alabama.

FEBRUARY 1972

OAK RIDGE NATIONAL LABORATORY
Oak Ridge, Tennessee 37830
operated by
Union Carbide Corporation
for the
U.S. ATOMIC ENERGY COMMISSION

Table of Contents

Abstract

The effects of several asymmetric sources on time-dependent and steady-state transport calculations for both 12.2- to 15-MeV and fission-neutron sources in air have been determined. The response functions considered were air kerma, nonionizing silicon kerma, and tissue dose for neutrons, and air kerma, silicon kerma, and tissue dose for gamma rays. Monte Carlo calculations were made to determine the time-dependent responses. Adjoint discrete ordinates results were obtained to compare with the time-integrated Monte Carlo data. The use of the one-dimensional adjoint solution to investigate source asymmetry effects is discussed in detail.

I. Introduction

Time-dependent neutron air kerma, neutron nonionizing silicon kerma, gamma-ray air kerma, gamma-ray silicon kerma, and neutron and gamma-ray Henderson tissue dose have been calculated as a function of r,z and time for a point source in infinite air of density 1.11 mg/cc. A 12.2- to 15-MeV band and a fission spectrum neutron source-energy distribution were utilized. In order to study the effect of source angular distribution, three extreme angular distributions were considered. These source distributions were the symmetric (or isotropic), the "pancake," and the "beam" sources. In the "pancake" case the source neutrons were chosen with μ, the cosine of the angle of emission and the z axis (vertical) being uniformly distributed between -0.1 and 0.1. For the "beam" case the source neutrons were chosen with μ, the cosine of the angle between the source direction and the z axis (vertical) being uniformly distributed between 1.0 and 0.95.

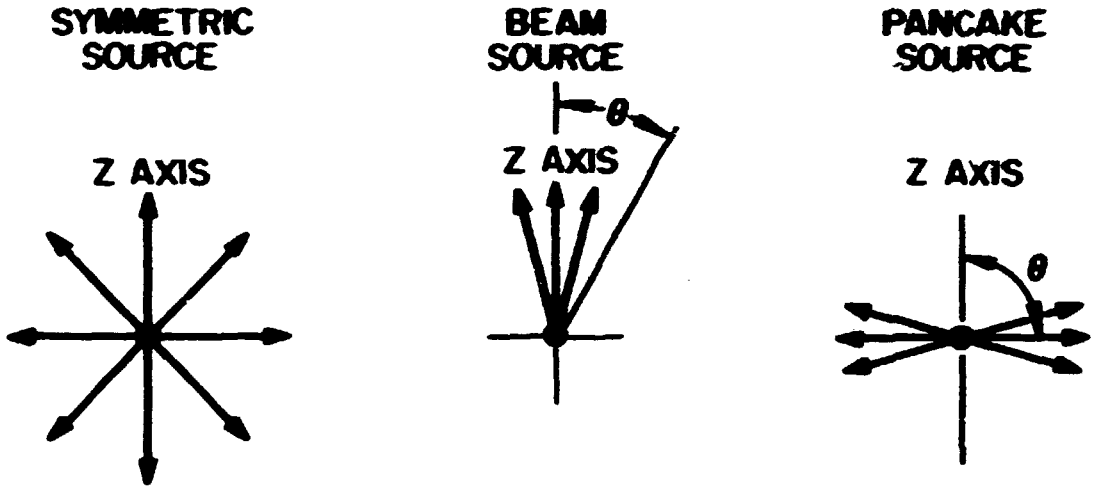

Source Angular Distributions.

The time dependence of the various responses as well as the time-integrated total values were calculated with the MORSE code, a general-purpose neutron and gamma-ray Monte Carlo transport code.[1] The time-integrated results are compared with adjoint results obtained using the ANISN[2] discrete ordinates code.

The cross sections (22 neutron, 18 gamma ray groups, with a P_3 expansion of the angular distributions) and response functions that were used were the same as those used by Straker and Gritzner[3] except that the gamma-ray air kerma in gamma group 8 used was changed to 7.13(-8). The response functions are tabulated in Table 1.

II. ANISN Adjoint Case

Since a dose detector response is isotropic, an adjoint ANISN calculation was performed using an isotropic source at the detector point which has an energy dependence according to the dose response function. The adjoint calculation produces a value function for each neutron or gamma-ray energy group as a function of distance from the source. At each point in space the value function is given for each polar angle increment with respect to the detector source axis. In the ANISN formulation, the radius vector corresponds to the direction between the detector and the source.

Once the adjoint solution was obtained for a given response function, any asymmetric source can be calculated by convoluting the angular fluxes with the appropriate source.

To calculate the response R for a detector at a radius r and angle θ to the z axis, it is only necessary to integrate the product of the number of neutrons in the source in each group and at each direction by the angular- and energy-dependent value function at a distance r and for an angle equal to that between the two directions.

$$R(r,\theta) = \sum_g \int S(\Omega')\phi_g(r,\Omega'\cdot\Omega_o)d\Omega' \ ,$$

where R is the response at distance r and angle θ to the z axis. $S(\Omega')$ is the fraction of the source in the solid angle $d\Omega'$ about Ω', Ω_o is direction between the origin and the detector position (r,θ), $\Omega' \cdot \Omega_o$ is the cosine of the angle between Ω' and Ω_o, and $\phi_g(r,\mu)$ is the value function at radius r and cosine μ in group g.

Symmetric Source

For the symmetric response, $S(\Omega') = 1.0$, and thus $R(r,\theta)$ is the scalar value function at distance r.

"Pancake" Source $|\omega| < 0.1$

For the "pancake" source the integration involves integrating $S(\Omega')$ from $\omega = -0.1$ to 0.1 and around the pancake from $\phi = 0$ to 2π with $d\Omega' = d\omega d\phi$. The cosine of the angle between the detector and the source at the direction given by ω and φ is

$$\mu = \sqrt{1 - \omega^2}\cos\phi \sin\theta + \omega\cos\theta$$

and

$$R(r,\theta) = \frac{1}{(0.4)\pi} \sum_g \int_0^2 \int_{-0.1}^{0.1} [\phi_g\{r,\mu(\omega,\phi)\}]d\phi d\omega$$

where $S(\Omega') = 1/(0.4)\pi$.

For the "Beam" Source $\omega > 0.95$

For the "beam" source the integration is from $\omega = 0.95$ to 1 and around the circle from $\phi = 0$ to 2π. Again

$$\mu = \sqrt{1 - \omega^2}\cos\phi \sin\theta + \omega\cos\theta$$

giving

$$R(r,\theta) = \frac{1}{(0.1)\pi} \sum_g \int_0^2 \int_{0.95}^{1} [\phi_g\{r,\mu(\omega,\phi)\}]d\phi d\omega$$

where $S(\Omega') = 1/(0.1)\pi$.

Six adjoint ANISN calculations were performed, one for each response function. An S-32 Gaussian quadrature was used with 115 space points. The value of the response in each group was used as the source in each group.

III. Theory: MORSE Forward Case

MORSE calculations were performed for three source-angular distributions and two source-energy distributions. A collision density estimator was used to obtain an estimate of the flux. The region of interest extended to 1100 meters and an estimate from every collision within that radius was made to the appropriate volumetric detector bin. Eight radial detector regions (Table 2) were used for each angular bin with seven angular bins for the symmetric and pancake sources ($|z|$ was used) and ten angular bins for the beam source. The response functions given in Table 1 were used to determine the time-dependent and time-integrated response. Path-length stretching was used to improve the statistics at large distances from the source and also at angles normal to the source direction in the asymmetric cases. Source-energy importance sampling of the fission source was necessary to obtain a sufficient sampling of gamma rays. Most of the gamma rays are due to neutrons born at high energies (above 5 MeV). The importance function decreased from 10 in group 1 to 1 in group 8 and lower. One gamma ray was produced per collision in groups 1-4. Gamma rays were produced by neutrons in groups 5-22 such that the gamma-ray weight was about one tenth of the weight of the neutron. Splitting and Russian roulette parameters were designed to enhance the important reactions (mostly gamma-ray production). Low-weight neutrons were allowed to continue colliding until they were below the threshold for gamma-ray production. Russian roulette was then used to eliminate most of them. No path-length stretching was applied for neutron energies below 0.5 MeV (or for gamma rays). Table 4 gives details. For the 12.2- to 15-MeV source only the first 13 time bins were used. MORSE calculations used a time cutoff of 1 second; however, time spectra were not obtained beyond 10^{-3} sec because of poor statistics.

IV. Results

Figures 1-36 give the steady-state isodose curves for the six response functions and six source conditions. The solid lines are the results of integrating the ANISN adjoint results while the dotted lines are the results from MORSE. The isovalues were obtained by logarithmic interpolation among the values at the midpoints of the radii recorded in Table 3. Results are meaningless within 50 meters from the source. For the neutron responses, the isodose curves for the 12.2- to 15-MeV source and for the fission source have the same values, while for the gamma-ray responses the isodose curves for the 12.2- to 15-MeV source have values a factor of 10 higher than those for the fission source. The three isovalues are printed on the curves. The accuracy of the position of the isocurves is estimated to $\pm$10 meters.

To reduce the volume of time-spectra results, only the kerma results are presented, and the gamma-silicon kerma time spectra are not given since they are essentially identical to the air kerma results when normalized. Thus the time spectra are presented for three responses - neutron air kerma, neutron silicon kerma, and gamma-ray air kerma. Dose rates are given in rads/(source neutron•sec) and kerma rates in (ergs/g)/(source neutron•sec).

The same time spectra are presented in two ways -- scaled and unscaled. The unscaled results are the usual form and show plots of spectra versus time on a log-log scale. Spectra for the symmetric source case have shapes which vary with radius due to the different time of arrival. To remove this effect and show the effects of source asymmetry on the shape of the time distributions, the scaled distributions are presented. Results are shown for three radii (300, 600, and 800 meters). Each spectrum is divided by the earliest time of arrival recorded in the calculation (actually the bottom of the first time bin with a nonzero entry). The time variable for each spectrum is the usual time divided by the earliest time of arrival of that radius. The scaled graphs have limited value for gamma-ray spectra due to statistical variations in the earliest time of arrival for gamma rays. The scaled spectra for a symmetric source fall on one curve. If at any angle the scaled spectra can be represented by a single curve, then there are no effects on the

shape of the spectra due to the asymmetric source. The time spectra at any intermediate radius can then be obtained by multiplying the single curve values by the earliest time of arrival at that radius and normalizing to the value obtained from the isoresponse curves.

Figures 37-39 give the scaled time spectra for the three response functions for the 12.2- to 15-MeV symmetric source case. The normalizations given on the figures are the total response at each radius per source neutron divided by the time of arrival. The product of these normalized values by the scaled response at any time is the calculated response rate at that time.

Figures 40-48 show the unscaled time spectra for the three responses and three ranges for the 12.2- to 15-MeV symmetric source case. The estimated errors (1 standard deviation) are included with the results. These spectra are normalized to 1 and the normalization constant given on each figure is the total response per source neutron at the given radius. The product of this value by the response rate at any time is the calculated response rate at that time.

Figures 49-56 give the scaled time spectra and Figs. 57-62 the unscaled time spectra for the 12.2- to 15-MeV beam source case ($\omega \geq 0.95$). The scaled neutron air kerma is shown at four angles (ω = 0.975, 0.60, 0, -0.85), while the neutron silicon kerma and gamma-ray air kerma are shown at two angles (ω = 0.975, 0). Unscaled results are given at two radii (300 and 800 meters) and with two angles (ω = 0.975, 0) on each figure.

Figures 63-70 give the scaled time spectra and Figs. 71-76 the unscaled time spectra for the 12.2- to 15-MeV pancake source ($|\omega| \leq 0.1$) at the same positions and similar angles as for the beam source.

Results similar to the 12.2- to 15-MeV source are presented for the fission source cases except that the time scale is extended to 10^{-3} sec. The symmetric, beam,and pancake results are in Figs. 77-88, 89-102, and 103-116,respectively. A summary list of figures is given in Table 2.

V. Discussion

One important result of this investigation comes from the excellent agreement between the MORSE results and the convoluted ANISN adjoint results for the isokerma and isodose curves. The use of the properties of the adjoint essentially results in turning a number of two-dimensional problems for each angular distribution into one one-dimensional calculation. Once the adjoint solution is obtained, any required angular-dependent source can be easily obtained by integrating over the source. The effect of angular distributions of gamma-ray sources could also be determined by the same method without performing additional ANISN calculations. In addition to the results shown here, MORSE isocurves were compared with two-dimensional discrete ordinates results. Several of the cases (12.2- to 15-MeV symmetric and pancake) were run with DOT (J. Pace, private communication) and agreed well with the MORSE results.

The isodose curves illustrate that the effects of the source anisotropy are as expected. Greater anisotropy is evident for the 12.2- to 15-MeV source than for the fission source. For example, for the pancake source, neutron air kerma results for the 12.2- to 15-MeV source (Fig. 3) still show marked effects from source asymmetry at 500 meters while the corresponding fission source case (Fig. 6) is much closer to the symmetrical case even at smaller radii. Again, for the beam source the ratio of the air kerma at +500 to that at -500 meters for the 12.2- to 15-MeV source (Fig. 2) is about 54 compared to 15 for the fission source (Fig. 5). An interesting feature of the beam source results is that the curves tend to be nearly circular from the horizontal around to the negative z axis even when the peaking is still strong in the +z direction. The symmetric results show that in general the neutron air kerma is approximately three times higher for the 12.2- to 15-MeV source (Fig. 1) than for the fission source at the same radius (Fig. 4).

The gamma-ray kerma results show markedly less effects due to source anisotropy. This is to be expected since the anisotropic source is neutron-only and secondary gamma-ray generation was assumed to be isotropic. For the beam source case the anisotropy factors at 500 meters are 13 for the 12.2- to 15-MeV source and 3.5 for the fission source. The curves are

much farther apart in the gamma-ray case, illustrating the larger mean free path of gamma rays as compared to the neutron mean free path. The symmetric results show that the gamma-ray air kerma is approximately ten times higher for the 12.2- to 15-MeV source than for the fission source. For the 12.2- to 15-MeV source the neutron and gamma-ray air kerma are equal at 500 meters, whereas the gamma-ray dose does not equal the neutron dose until about 1800 meters.

The isodose curves show similar effects of anisotropy as do the isokerma curves at the same radii.

The time spectra for the 12.2- to 15-MeV symmetric source have several interesting features. The nonionizing silicon kerma have a shape similar to the air kerma but with a higher peak rate and a faster decrease with time. The gamma-ray air kerma is approximately constant until about ten times the earliest time of arrival and then decreases steeply. Since there is no anisotropy for the symmetric source case, the scaled data at the three radii can be approximated with good accuracy by one curve (Fig. 37).

The scaled neutron air kerma for the 12.2- to 15-MeV beam source (Figs. 49-52) show the spectra at the four angles. The four spectra show a smooth variation with angle from the peaked distribution in the source direction around to the horizontal direction with a lesser variation around to the backward angle. The three radii cannot be approximated very accurately with one curve for the source angle direction (Fig. 49) but can be approximated by one curve for the other angles. The gamma-ray air kerma distributions (Figs. 55-56) have nearly the same shape in the source distribution as they have at right angles to this direction.

The time distributions for the fission source in general have much broader peaks with a less pronounced first collision peak. The time of arrival of the peak intensity occurs much later than that for the 12.2- to 15-MeV case and is also subject to larger statistical error due to undersampling of high-energy neutrons. The gamma-ray results show pronounced statistical variations. This undersampling occurs due to the lower

total gamma-ray kerma or dose and also the smaller proportion of gamma rays at times less than 10^{-3} sec. Most gamma rays in the fission-source problem arise from thermal-neutron captures at later times. A somewhat unexpected result was the variation of the time distribution of the gamma-ray air kerma with angle for the fission source. This variation is somewhat clouded by statistical considerations but it is apparent that there is significant variation with angle. For example, in the direction of the beam the gamma-ray air kerma at a radius of 300 meters (Fig. 101) shows a distinct peak (approximately 9×10^{4}) between 0.6 and 1×10^{-5} sec. However, a different (peak 3.5×10^{4} between 0.2 and 0.4×10^{-5} sec) distribution is evident for the horizontal direction. This peaking in the source direction occurs more in the fission-source case than in the 12.2- to 15-MeV case. It seems to be due to source neutrons born about group 4-5 (5-8 MeV). The peak of the product of the gamma-ray production cross section with the fission spectrum is in this energy range. In the source direction the gamma-ray peak is due to gamma rays born near the detector position, while for the horizontal direction the main gamma-ray source is due to collisions near the neutron source which give a peak at an earlier time.

A longer computer run yielding improved statistics confirmed the general nature of these spectra. At times less than 2 μsec (corresponding to neutron collisions very near the source) the absolute rates were approximately equal in the source and horizontal directions.

Table 1. Response Functions

Group No.	Neutron Air Kerma†	Neutron Si Kerma† Nonionizing	Henderson Neutron Dose*	Gamma Air Kerma†	Gamma Si Kerma†	Henderson Gamma Dose*
1	2.66(-7)	7.5(-9)	5.46(-9)	2.24(-7)	2.80(-7)	2.42(-9)
2	1.93(-7)	6.6(-9)	5.13(-9)	1.90(-7)	2.28(-7)	2.07(-9)
3	1.41(-7)	6.4(-9)	4.84(-9)	1.60(-7)	1.83(-7)	1.76(-9)
4	1.11(-7)	6.6(-9)	4.61(-9)	1.34(-7)	1.48(-7)	1.59(-9)
5	1.05(-7)	5.5(-9)	4.44(-9)	1.12(-7)	1.20(-7)	1.27(-9)
6	1.20(-7)	5.1(-9)	4.13(-9)	9.52(-8)	9.85(-8)	1.08(-9)
7	1.06(-7)	4.8(-9)	4.01(-9)	8.30(-8)	8.40(-8)	8.75(-10)
8	5.38(-8)	4.8(-9)	3.39(-9)	7.13(-8)	7.12(-8)	7.35(-10)
9	3.09(-8)	4.7(-9)	3.15(-9)	6.15(-8)	6.10(-8)	6.44(-10)
10	3.37(-8)	4.2(-9)	3.09(-9)	5.05(-8)	5.05(-8)	5.30(-10)
11	2.95(-8)	3.4(-9)	2.64(-9)	4.10(-8)	4.10(-8)	4.45(-10)
12	1.61(-8)	3.1(-9)	1.97(-9)	3.26(-8)	2.70(-8)	3.50(-10)
13	9.84(-9)	2.0(-9)	1.12(-9)	2.38(-8)	2.37(-8)	2.56(-10)
14	2.67(-9)	0	2.29(-10)	1.63(-8)	1.65(-8)	1.77(-10)
15	3.61(-10)	0	0	1.11(-8)	1.17(-8)	1.22(-10)
16	5.62(-10)	0	0	5.92(-9)	7.25(-9)	6.60(-11)
17	1.28(-9)	0	0	2.72(-9)	9.75(-9)	3.90(-11)
18	2.26(-9)	0	0	4.40(-9)	4.13(-8)	8.37(-11)
19	3.70(-9)	0	0			
20	6.71(-9)	0	0			
21	1.13(-8)	0	0			
22	2.43(-8)	0	0			

†Units are (ergs/gm)/(n or γ/cm^2).

*Units are rad/(n or γ/cm^2).

Table 2. MORSE Spatial and Time Bins

Radius (m)	Angular Bins Symm. + |W| < .1 Cases	Angular Bins W > .95 Case	Time Bins (sec)
0-50	0-0.1	-1.0 - -0.7	To-2(-6)
50-150	0.1-0.2	-0.7 - -0.4	2(-6)-4(-6)
150-250	0.2-0.3	-0.4 - -0.1	4(-6)-6(-6)
250-350	0.3-0.45	-0.1 - 0.1	6(-6)-8(-6)
350-500	0.45-0.6	0.1 - 0.3	8(-6)-1(-5)
500-700	0.6-0.8	0.3 - 0.5	1(-5)-1.2(-5)
700-900	0.8-1.0	0.5 - 0.7	1.2(-5)-1.5(-5)
900-1100		0.7 - 0.85	1.5(-5)-2(-5)
		0.85-0.95	2(-5)-3(-5)
		0.95-1.0	3(-5)-4(-5)
			4(-5)-5(-5)
			5(-5)-7(-5)
			7(-5)-1(-4)
			1(-4)-2(-4)
			2(-4)-5(-4)
			5(-4)-1(-3)

Table 3. List of Figures

1	Isoplot Neutron Air Kerma	12.2-15 MeV	symmetric
2	"	"	$\omega > .95$
3	"	"	$\|\omega\| < .1$
4	"	Fission	symmetric
5	"	"	$\omega > .95$
6	"	"	$\|\omega\| < .1$
7-12	Neutron Si Kerma	2 Energy Sources	3 ang. dist.
13-18	Gamma-Ray Air Kerma	"	"
19-24	Gamma-Ray Si Kerma	"	"
25-30	Neutron Dose	"	"
31-36	Gamma-Ray Dose	"	"
37	Scaled Time Spectra 12.2-15 MeV symmetric	Neutron Air Kerma	
38	"	Neutron Si Kerma	
39	"	Gamma Air Kerma	
40	Unscaled Time Spectra 12.2-15 MeV Symmetric	Neutron Air Kerma	300 M
41	"	"	600 M
42	"	"	800 M
43	"	Neutron Si Kerma	300 M
44	"	"	600 M
45	"	"	800 M
46	"	Gamma Air Kerma	300 M
47	"	"	600 M
48	"	"	800 M
49-62	Time Spectra 12.2-15 MeV	Beam	
63-76	"	Pancake	
77-88	Time Spectra Fission	Symmetric	
89-102	"	Beam	
103-116	"	Pancake	

Table 4. Weight Standards for MORSE Calculation

NGP1	NDG	NGP2	WTHIH1	WTLOW1	WTAVE1	PATH
1	1	5	10	0.002	0.1	0.5
6	1	12	10	0.01	0.1	0.5
13	1	22	10	0.01	0.1	0
23	1	37	10	0.002	0.1	0
38	1	40	10	1.0	3.0	0

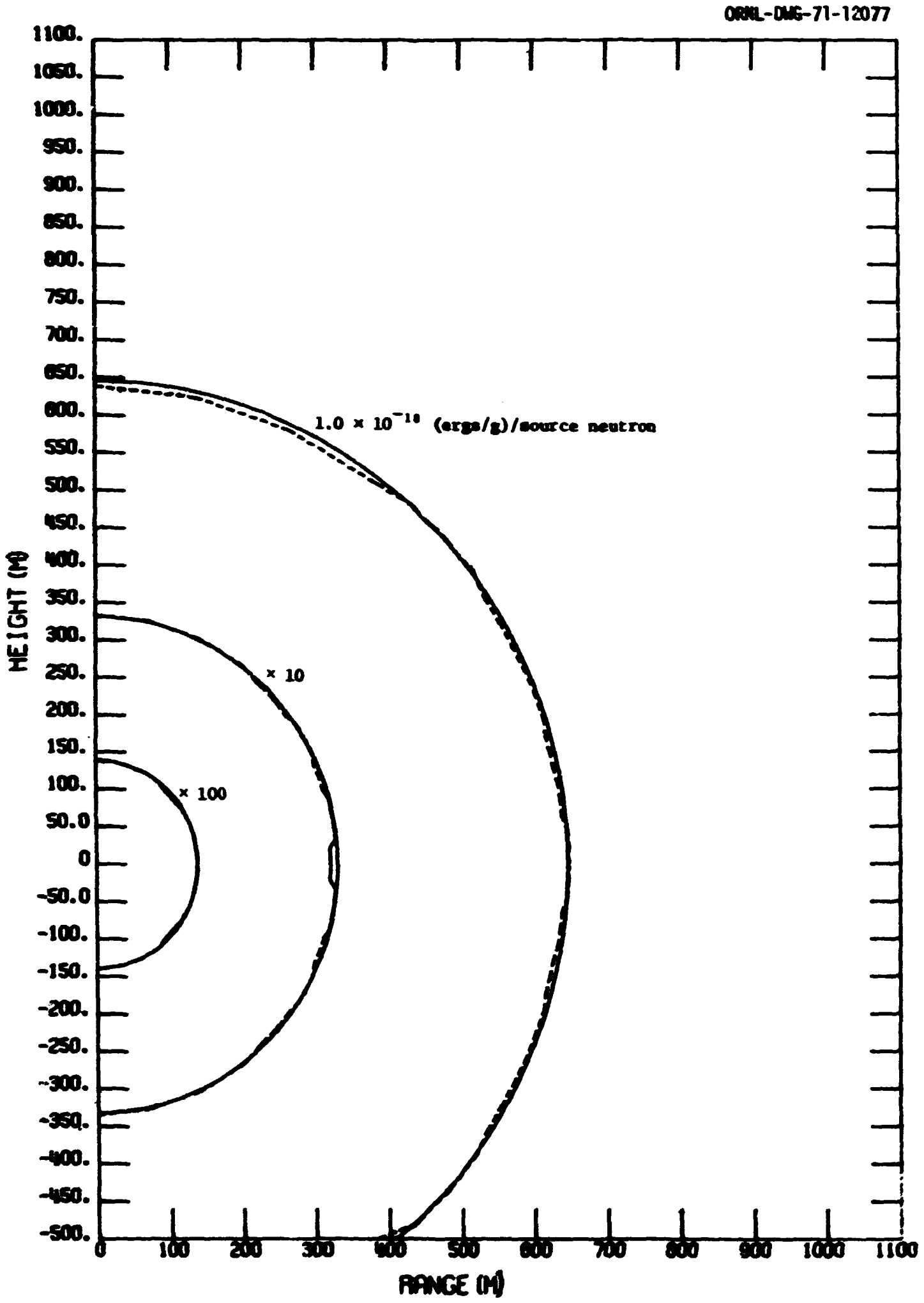

Fig. 1. Neutron Air Isokerma Curves for a 12.2-15-MeV Symmetric Source.

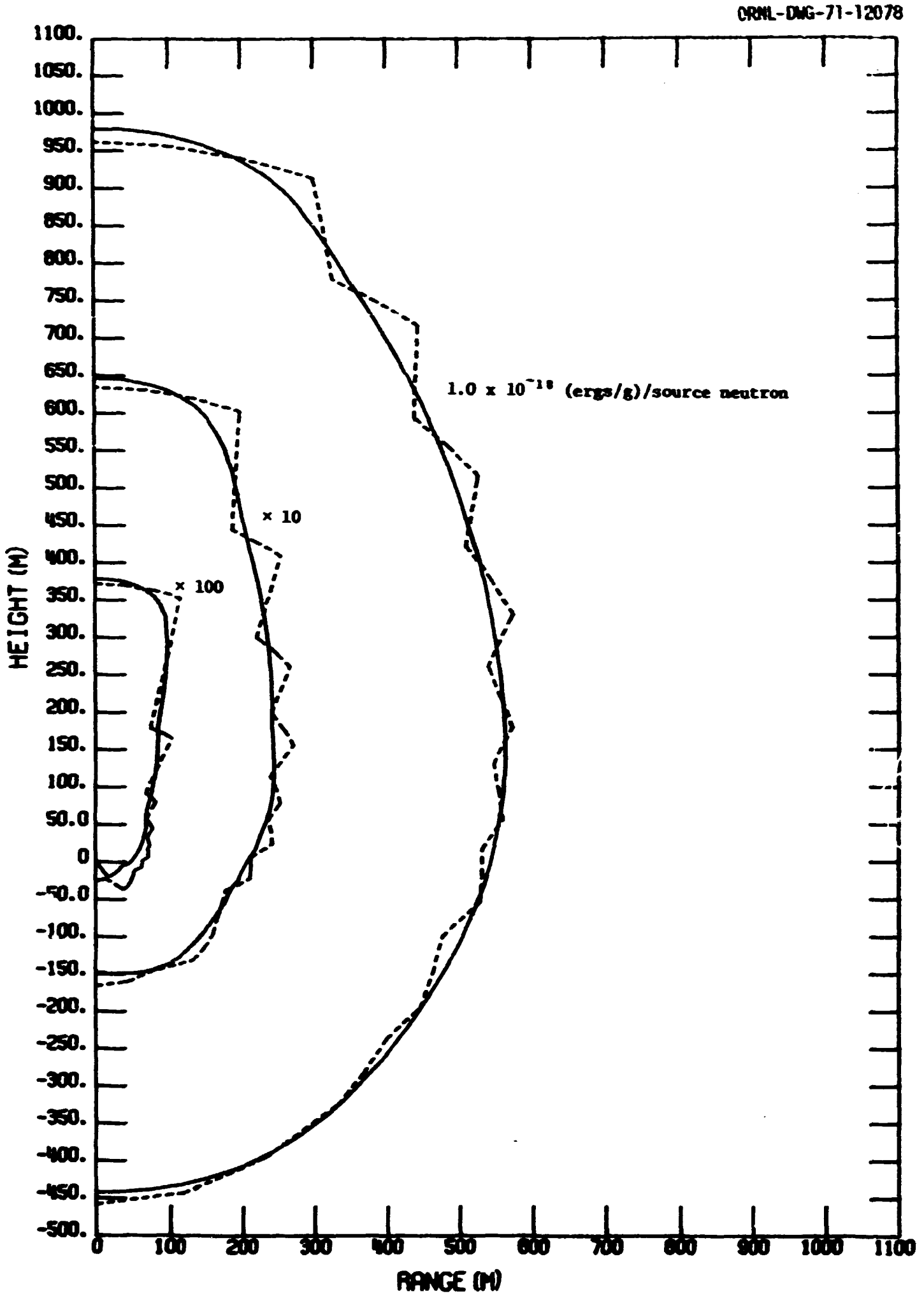

Fig. 2. Neutron Air Isokerma Curves for a 12.2-15-MeV Beam Source.

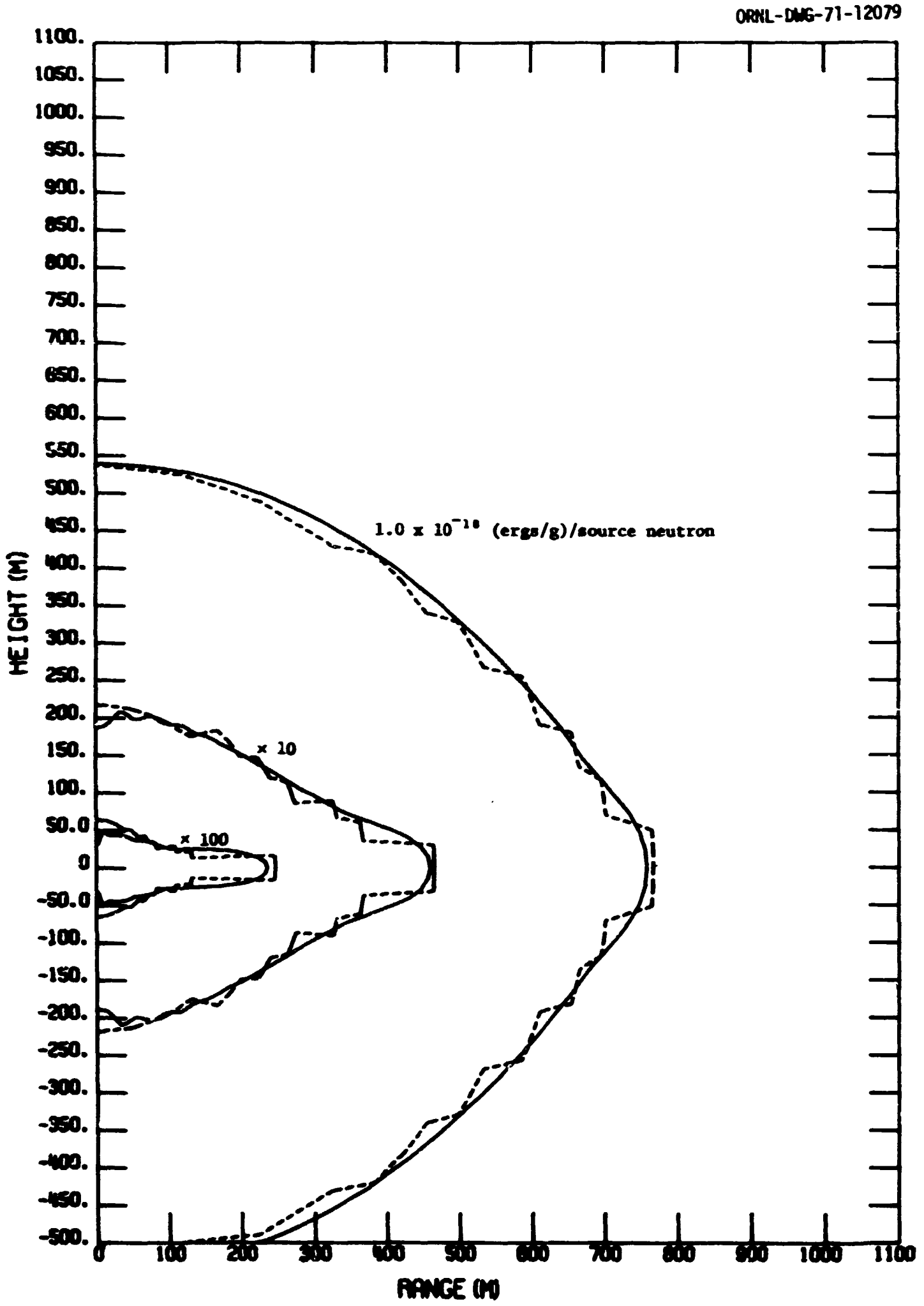

Fig. 3. Neutron Air Isokerma Curves for a 12.2-15-MeV Pancake Source.

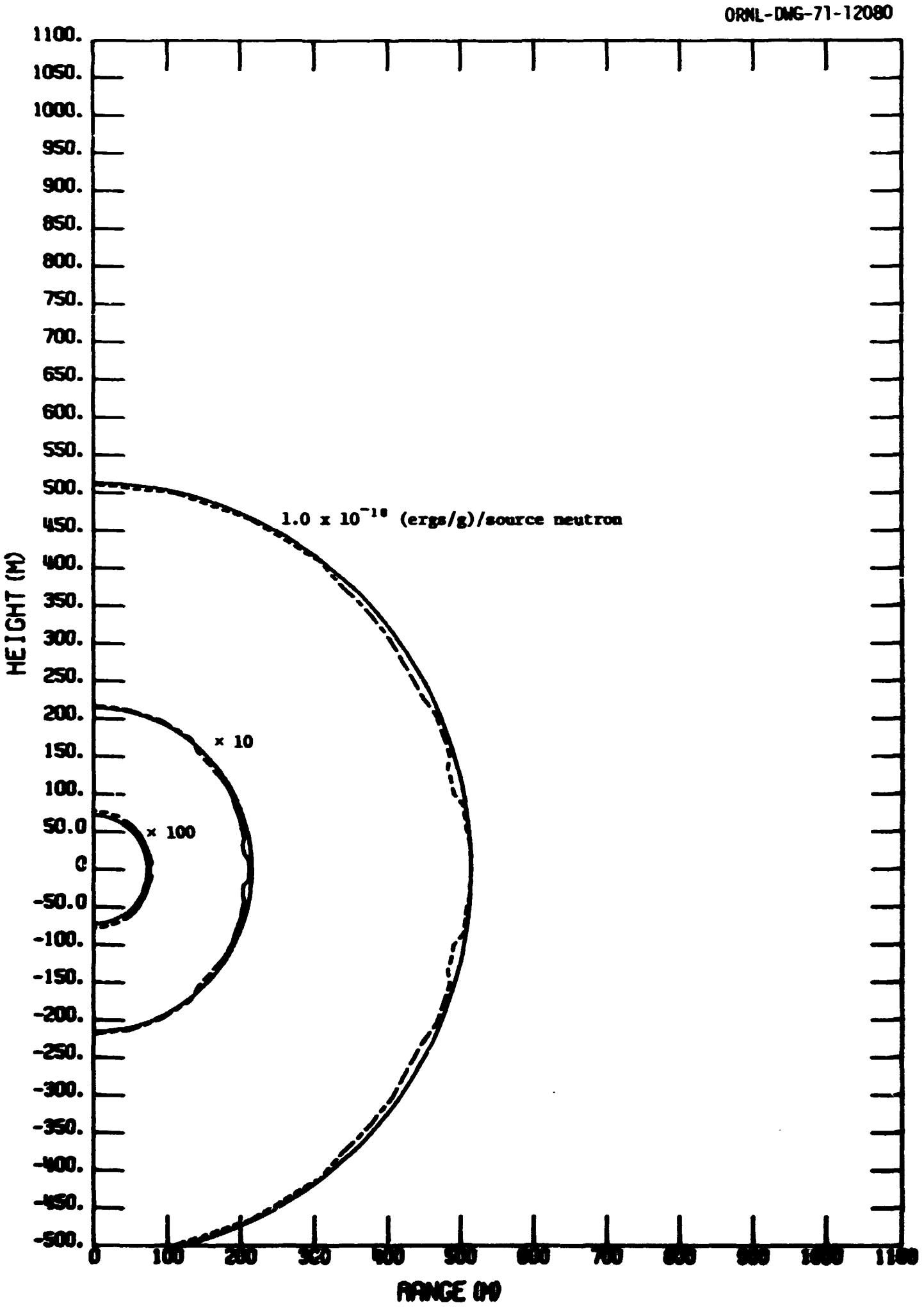

Fig. 4. Neutron Air Isokerma Curves for a Fission Symmetric Source.

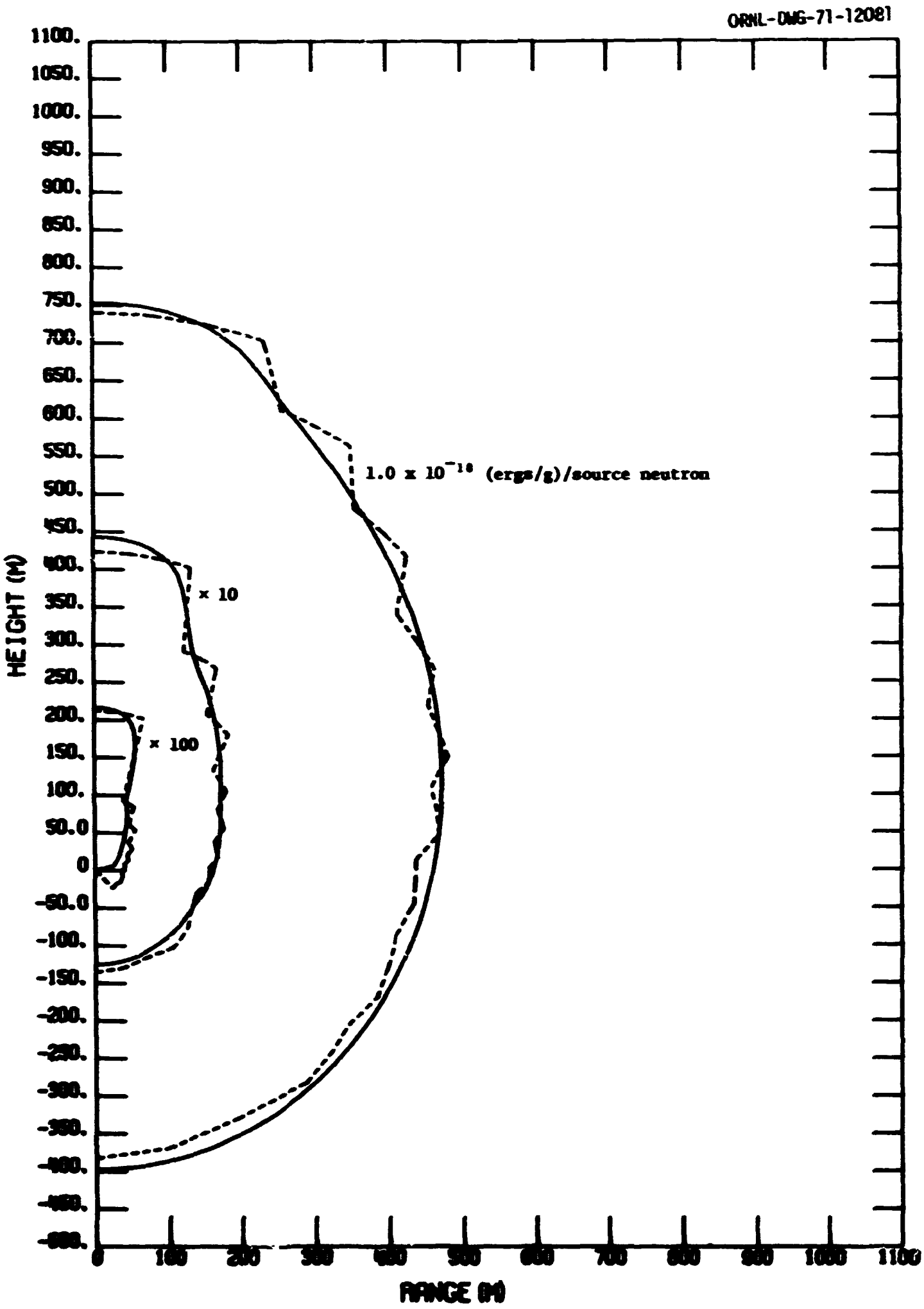

Fig. 5. Neutron Air Isokerma Curves for a Fission Beam Source.

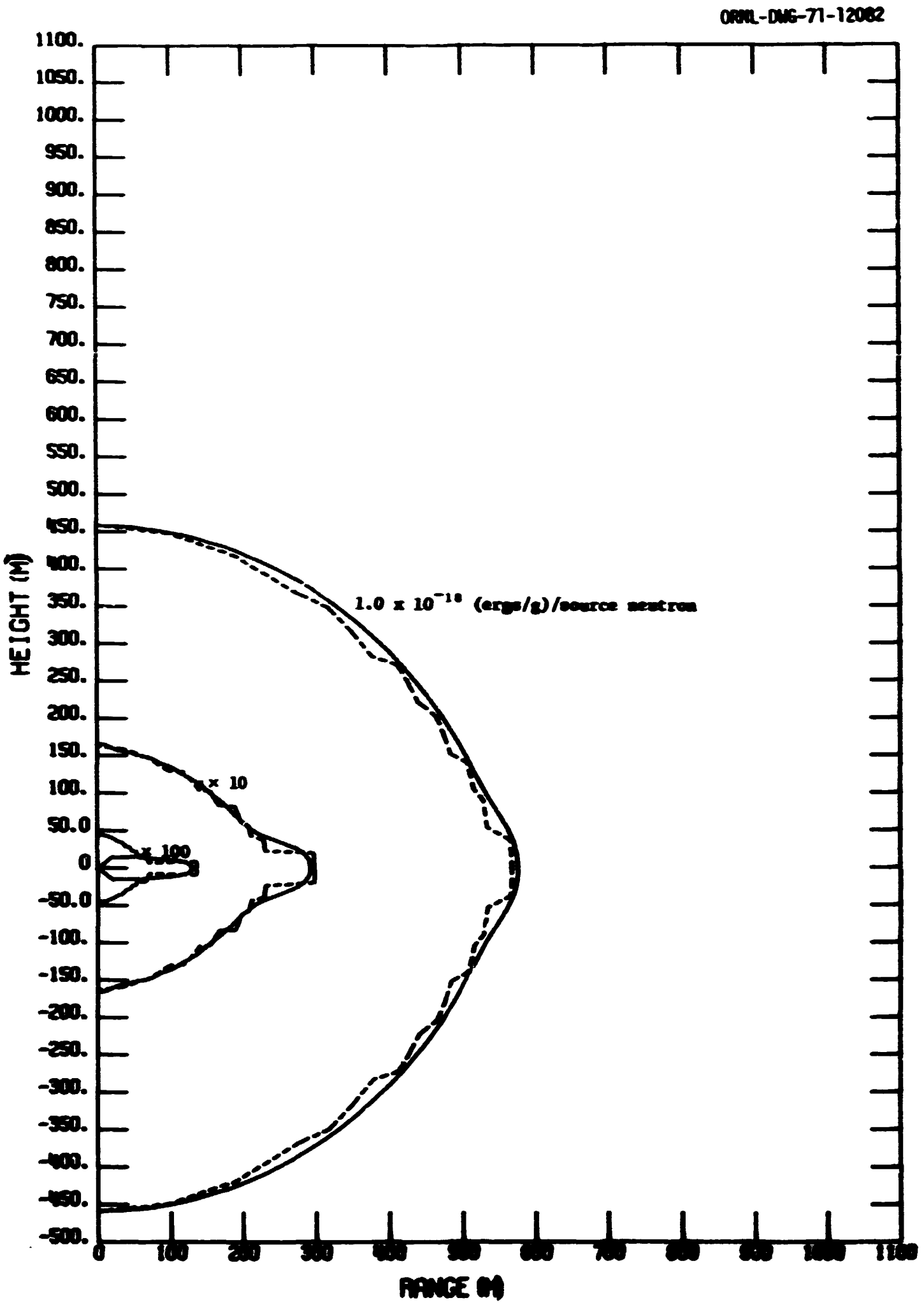

Fig. 6. Neutron Air Isokerma Curves for a Fission Pancake Source.

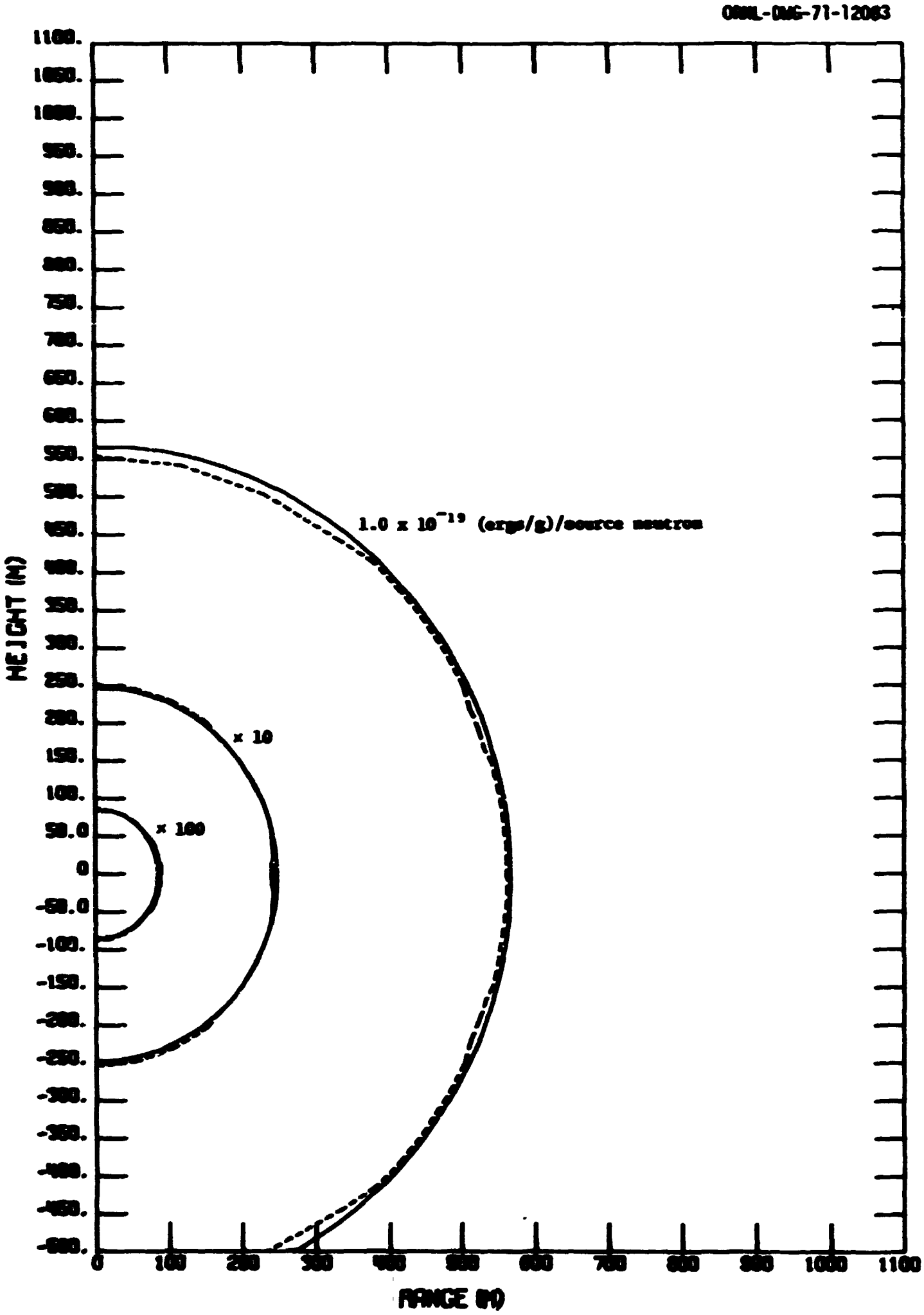

Fig. 7. Neutron Silicon Isokerma Curves for a 12.2-15-MeV Symmetric Source.

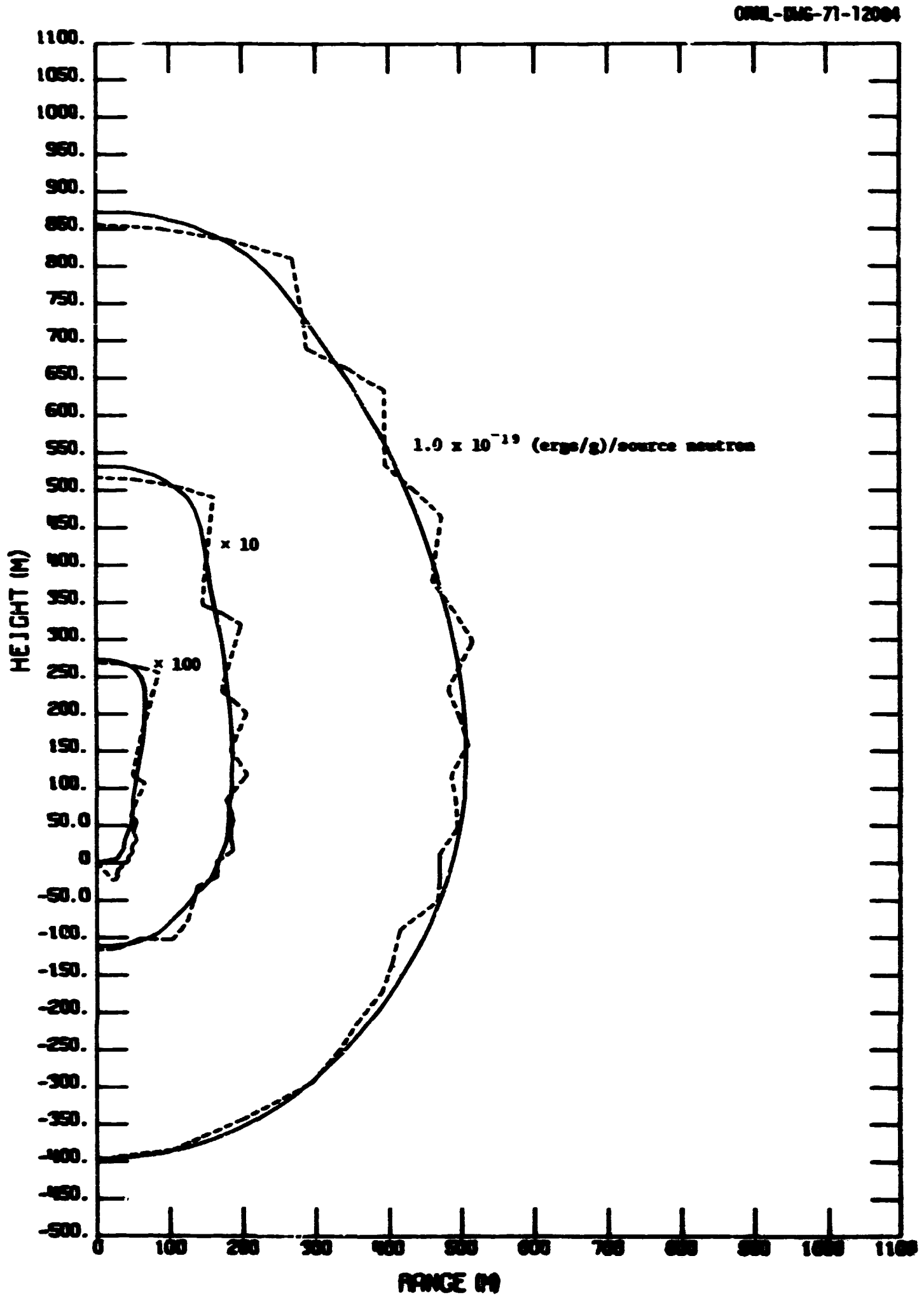

Fig. 8. Neutron Silicon Isokerma Curves for a 12.2-15-MeV Beam Source.

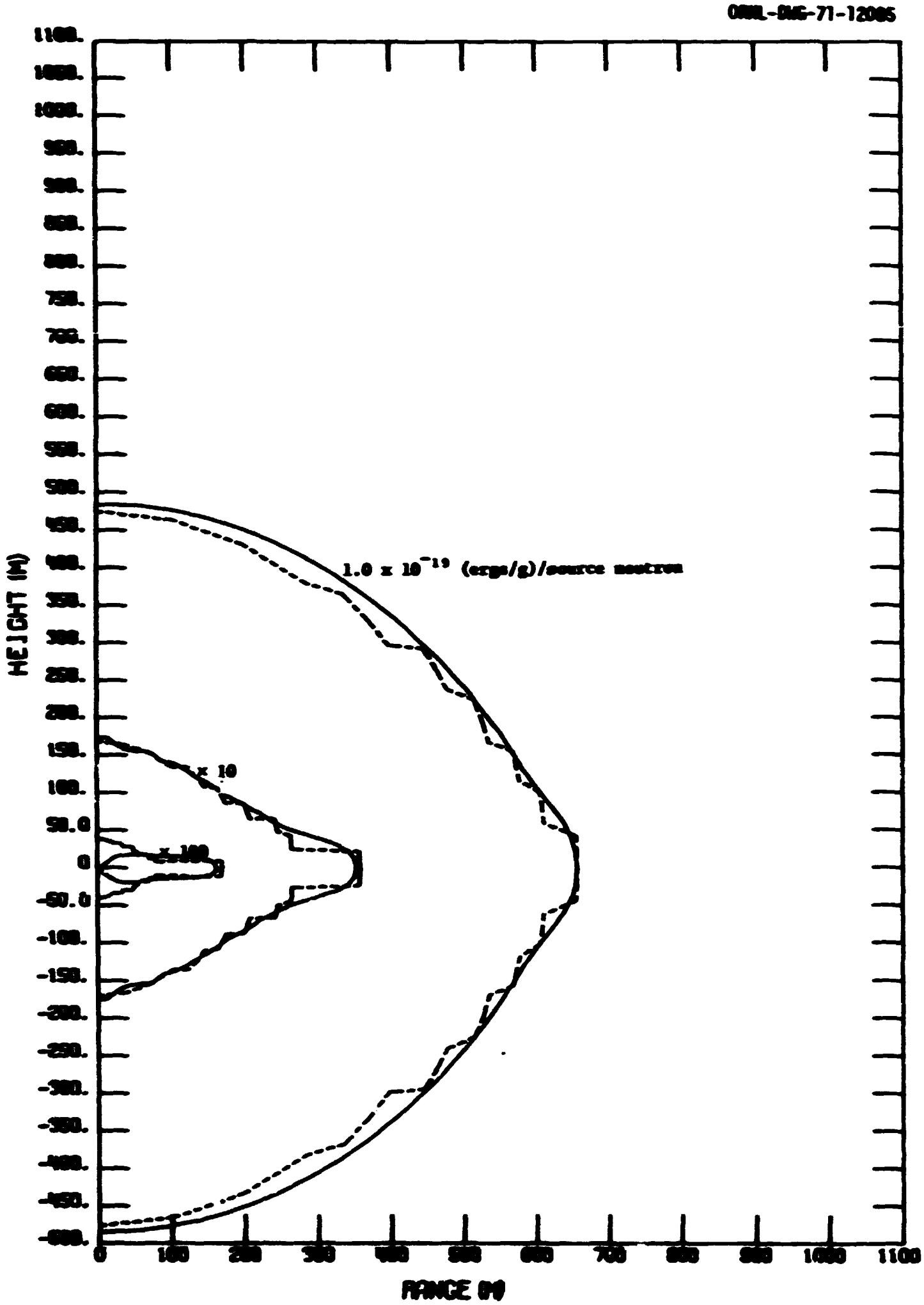

Fig. 9. Neutron Silicon Isokerma Curves for ≥ 12.2-15-MeV Pancake Source.

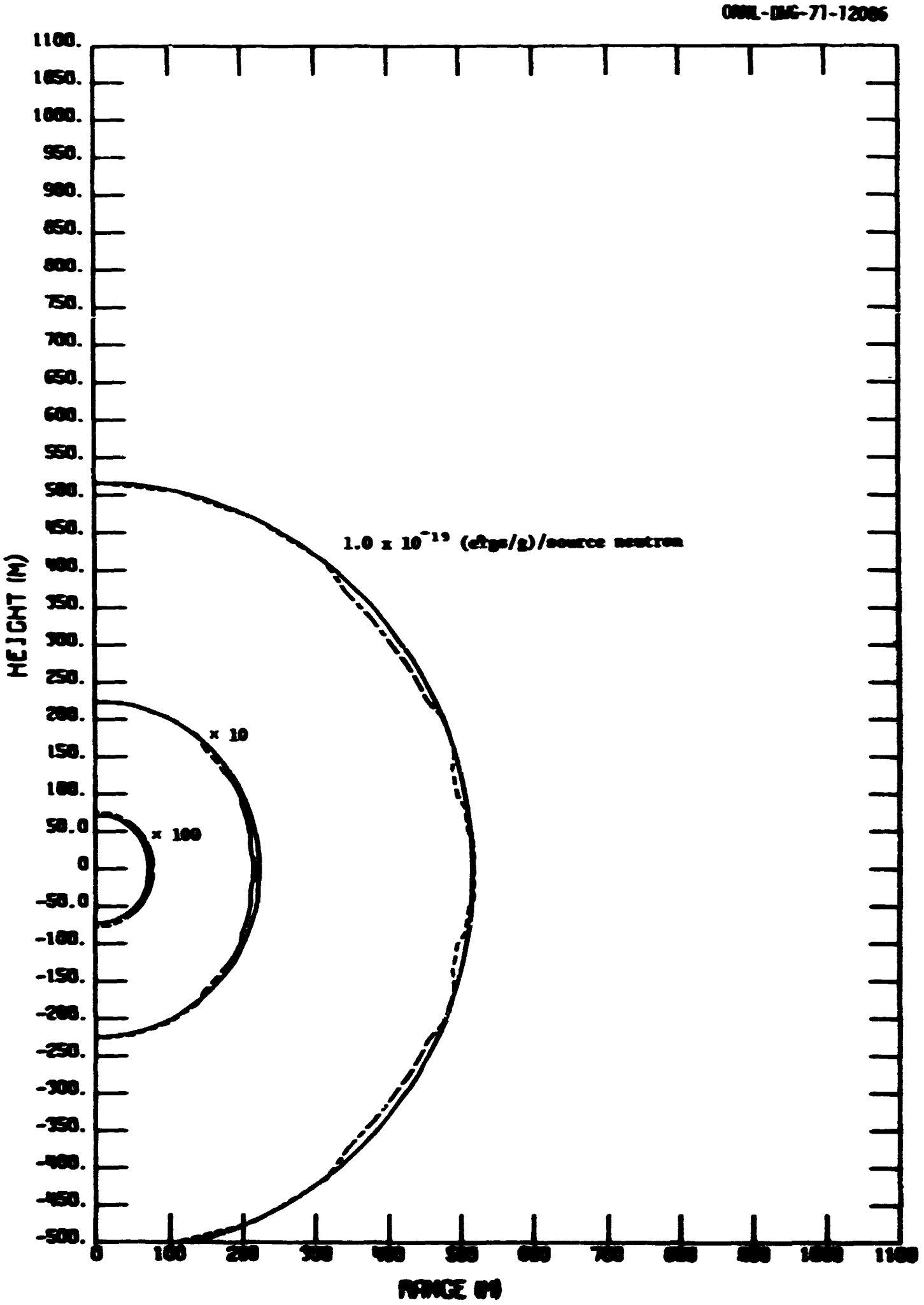

Fig. 10. Neutron Silicon Isokerma Curves for a Fission Symmetric Source.

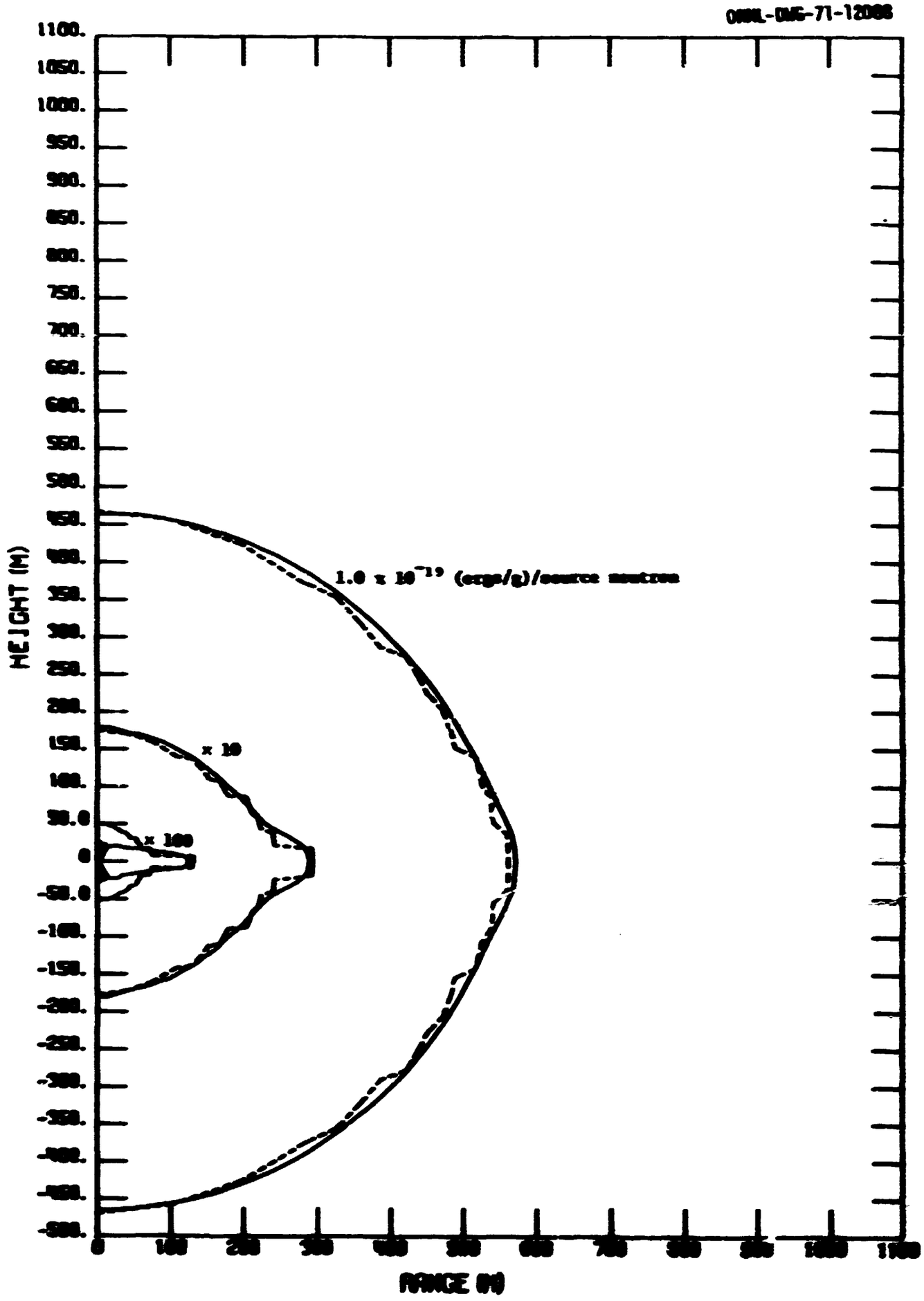

Fig. 12. Neutron Silicon Isotherm Curves for a Fission Pancake Source.

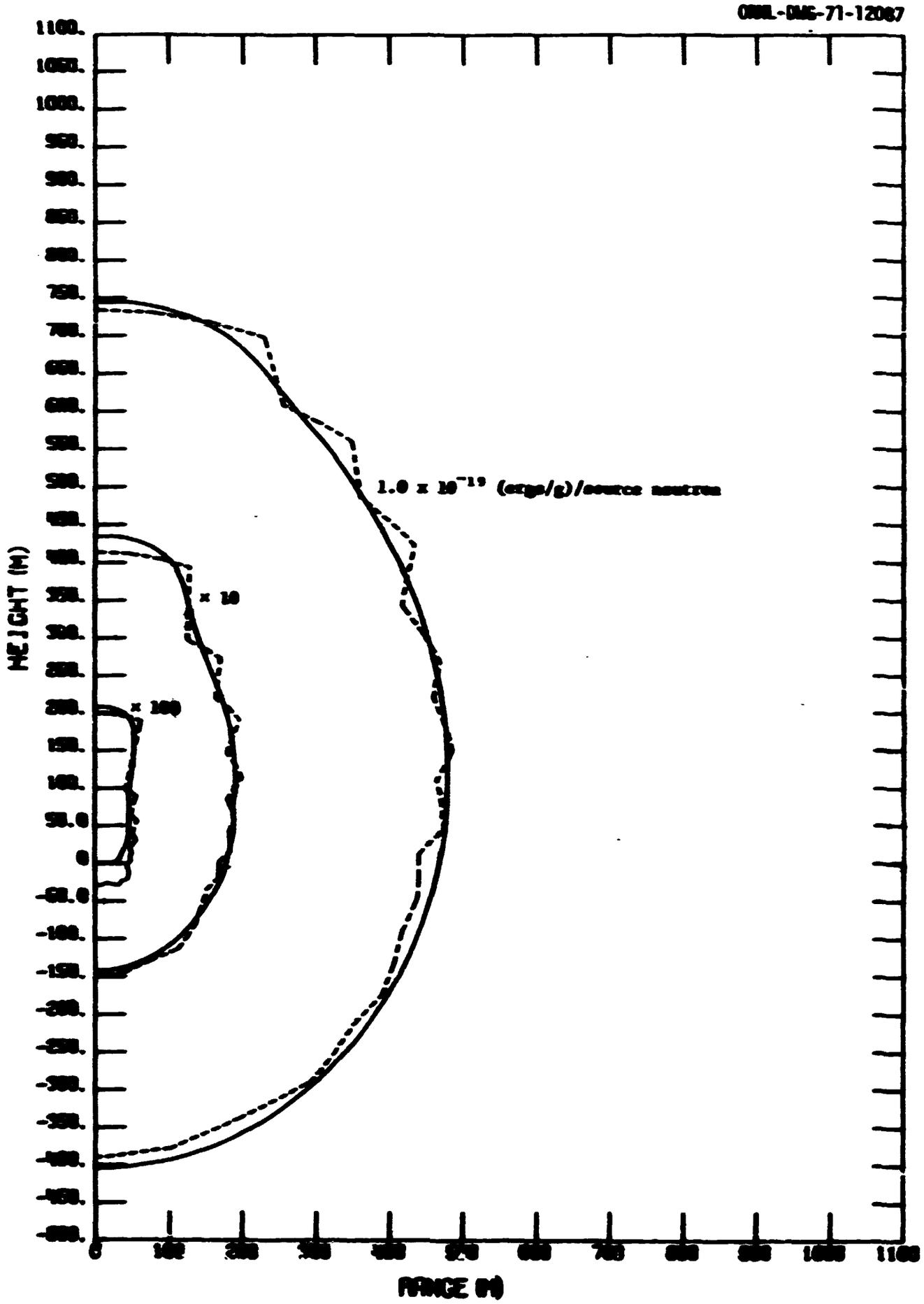

Fig. 11. Neutron Silicon Isokerma Curves for a Fission Beam Source.

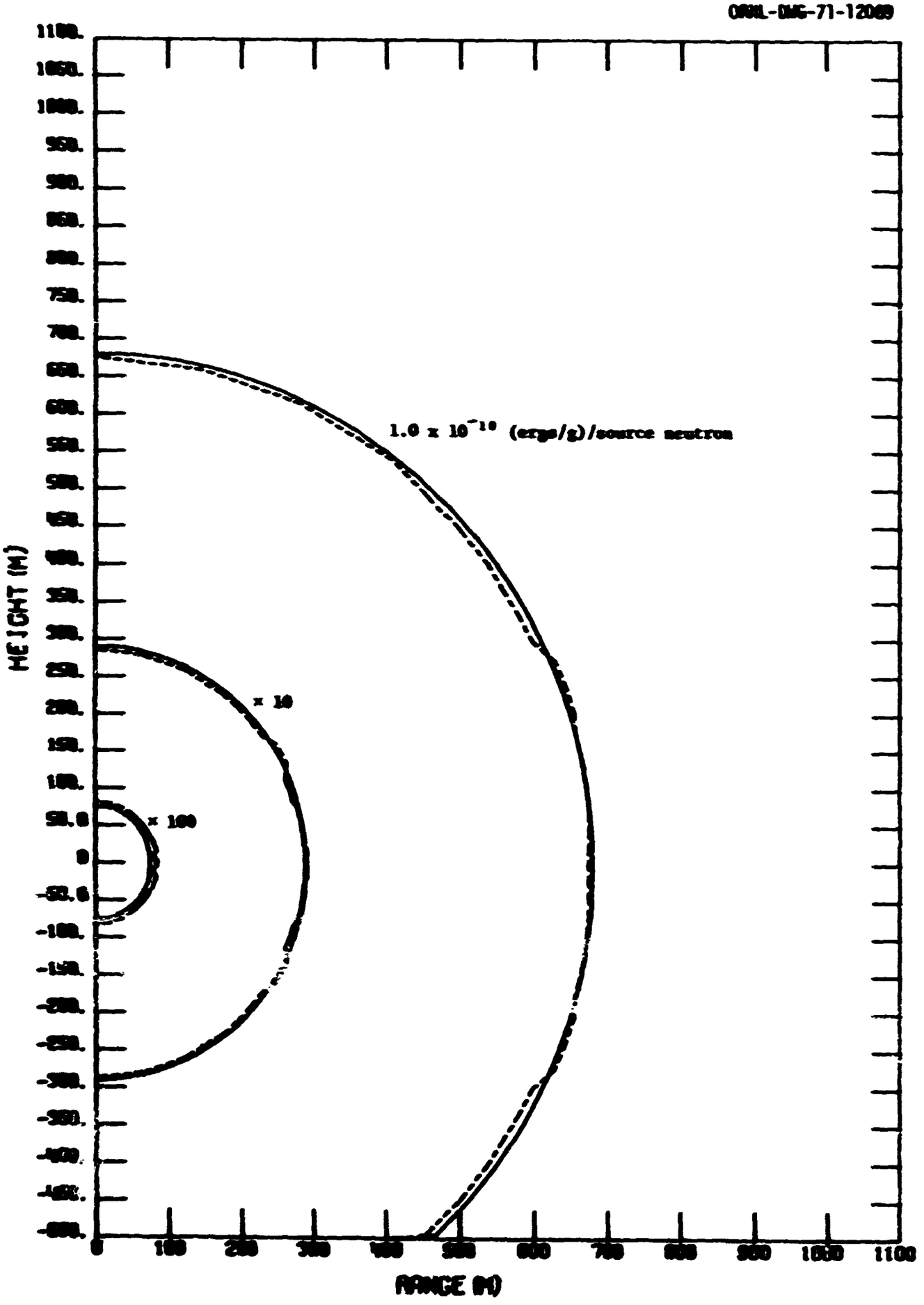

Fig. 13. Gamma-Ray Air Isokerma Curves for a 12.2-15-MeV Symmetric Source.

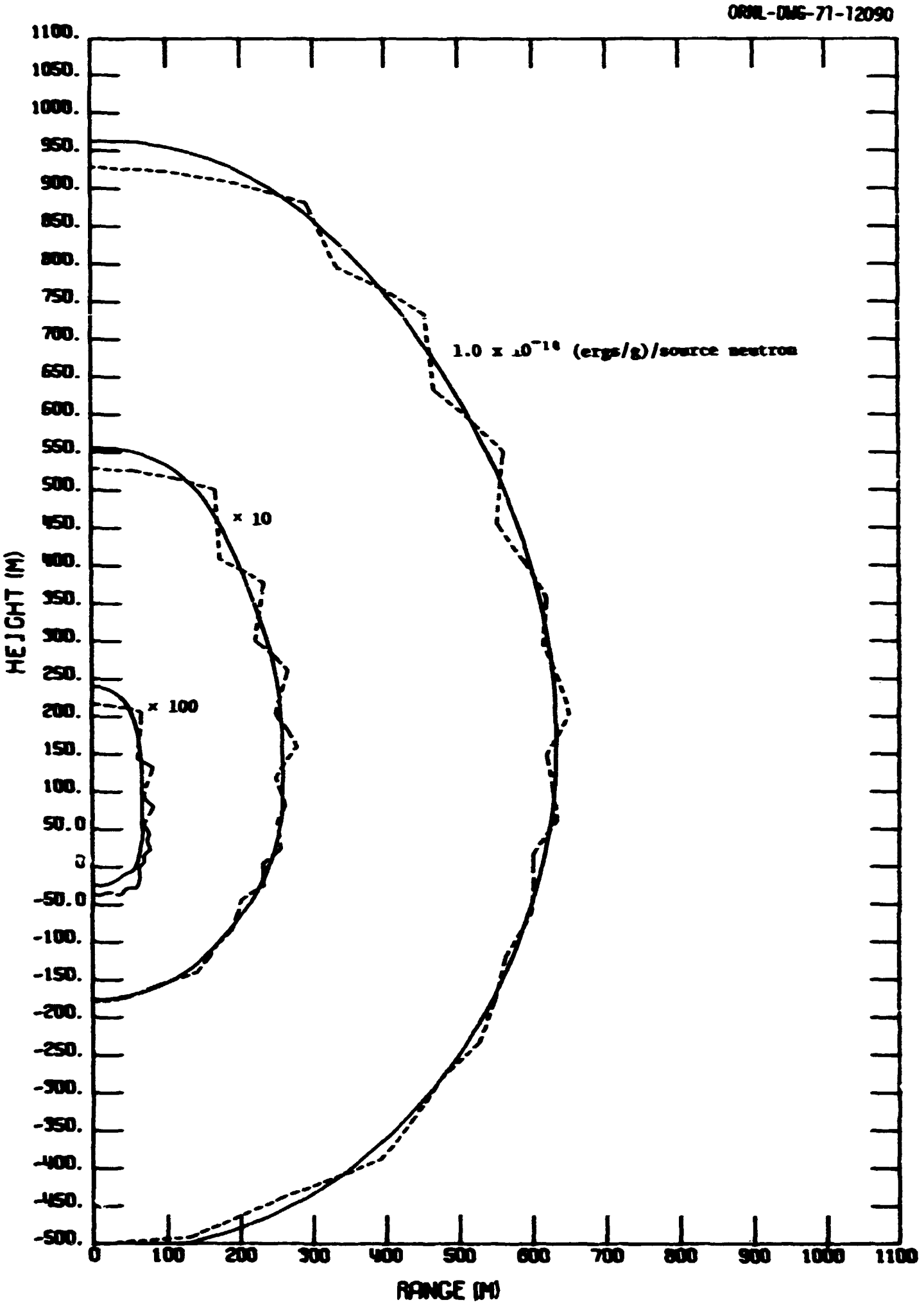

Fig. 14. Gamma-Ray Air Isokerma Curves for a 12.2-15-MeV Beam Source.

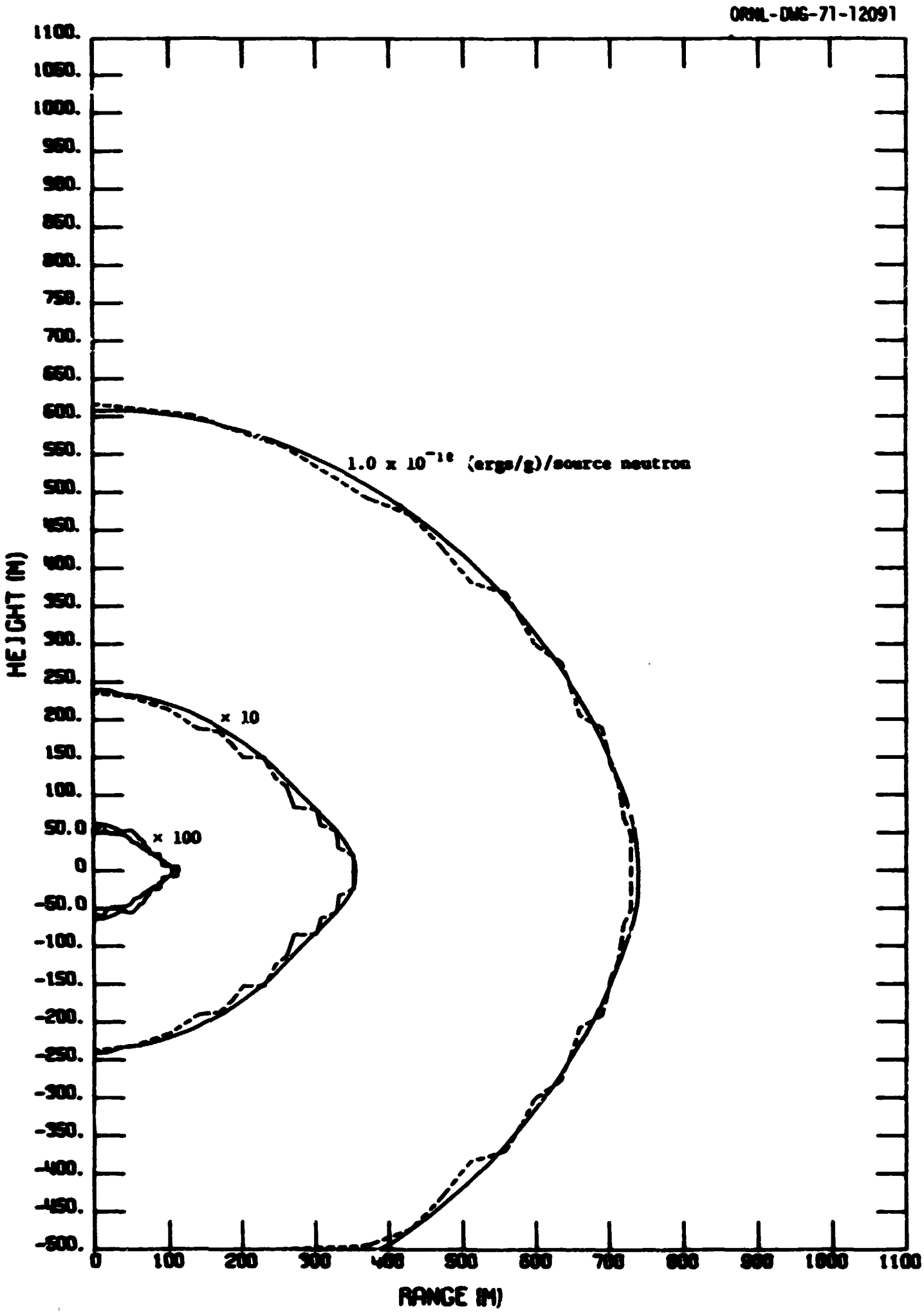

Fig. 15. Gamma-Ray Air Isokerma Curves for a 12.2-15-MeV Pancake Source.

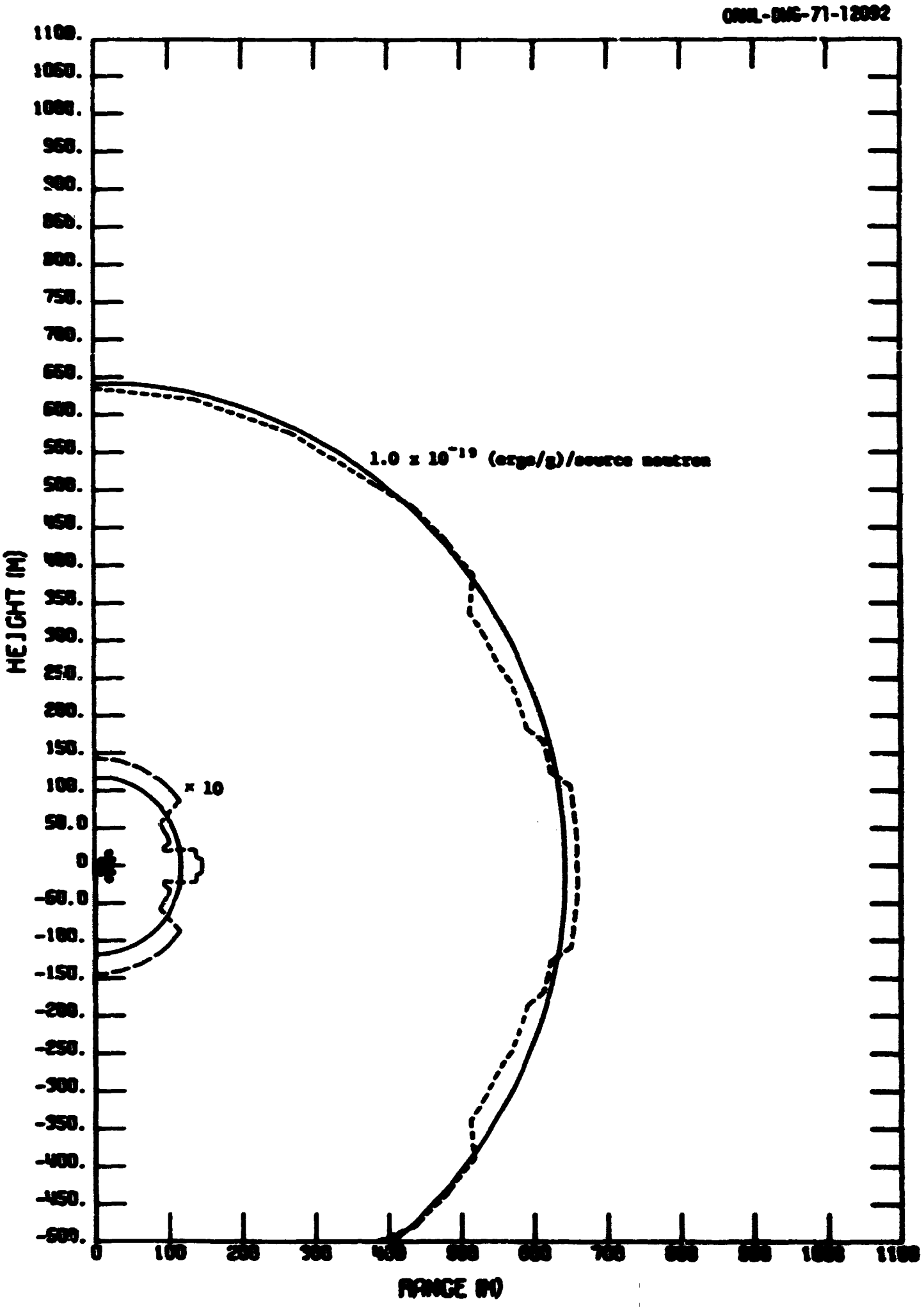

Fig. 16. Gamma-Ray Air Isokerma Curves for a Fission Symmetric Source.

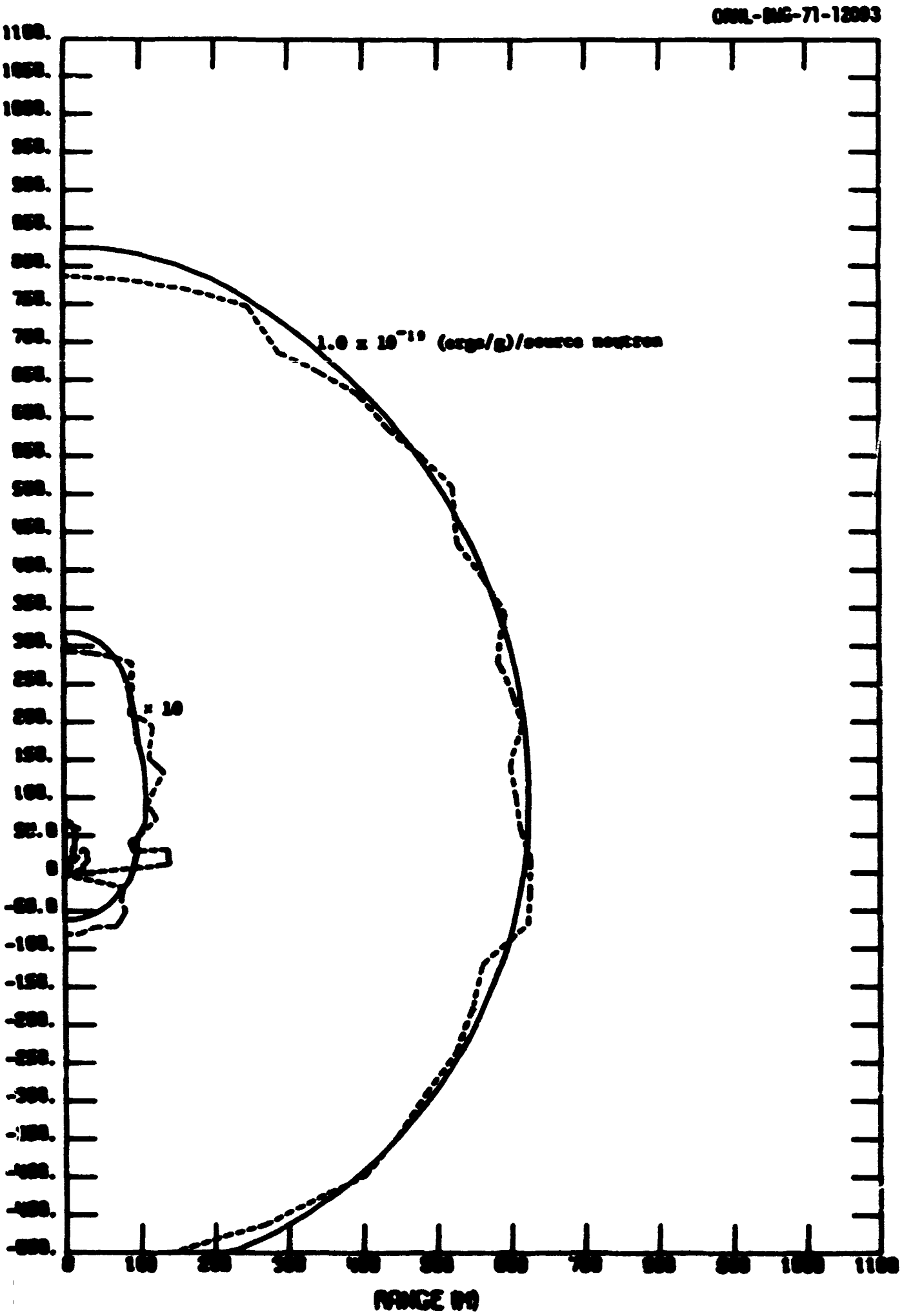

Fig. 17. Gamma-Ray Air Isokerma Curves for a Fission Beam Source.

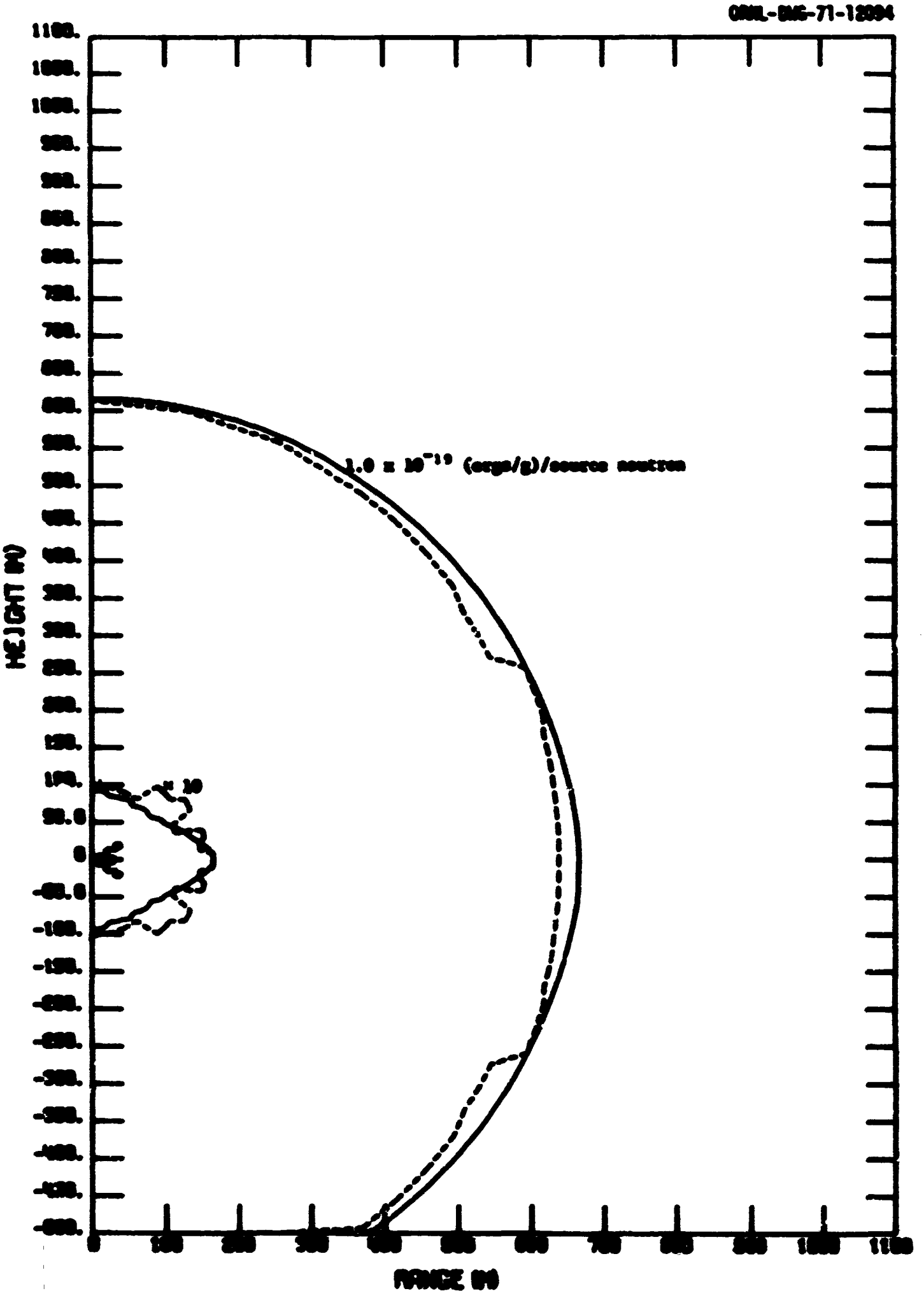

Fig. 18. Gamma-Ray Air Isokerma Curves for a Fission Pancake Source.

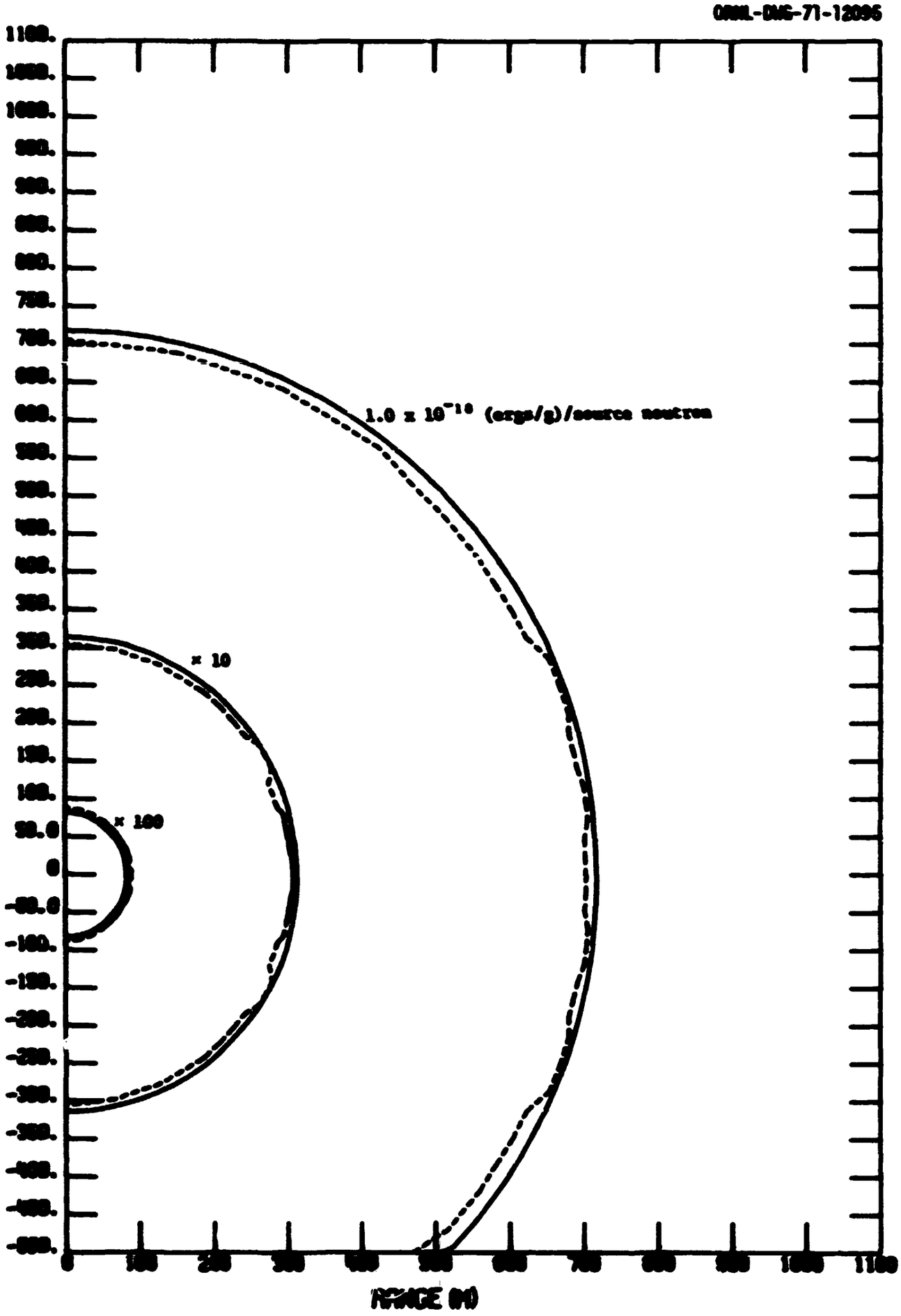

Fig. 19. Gamma-Ray Silicon Isokerma Curves for a 12.2-15-MeV Symmetric Source.

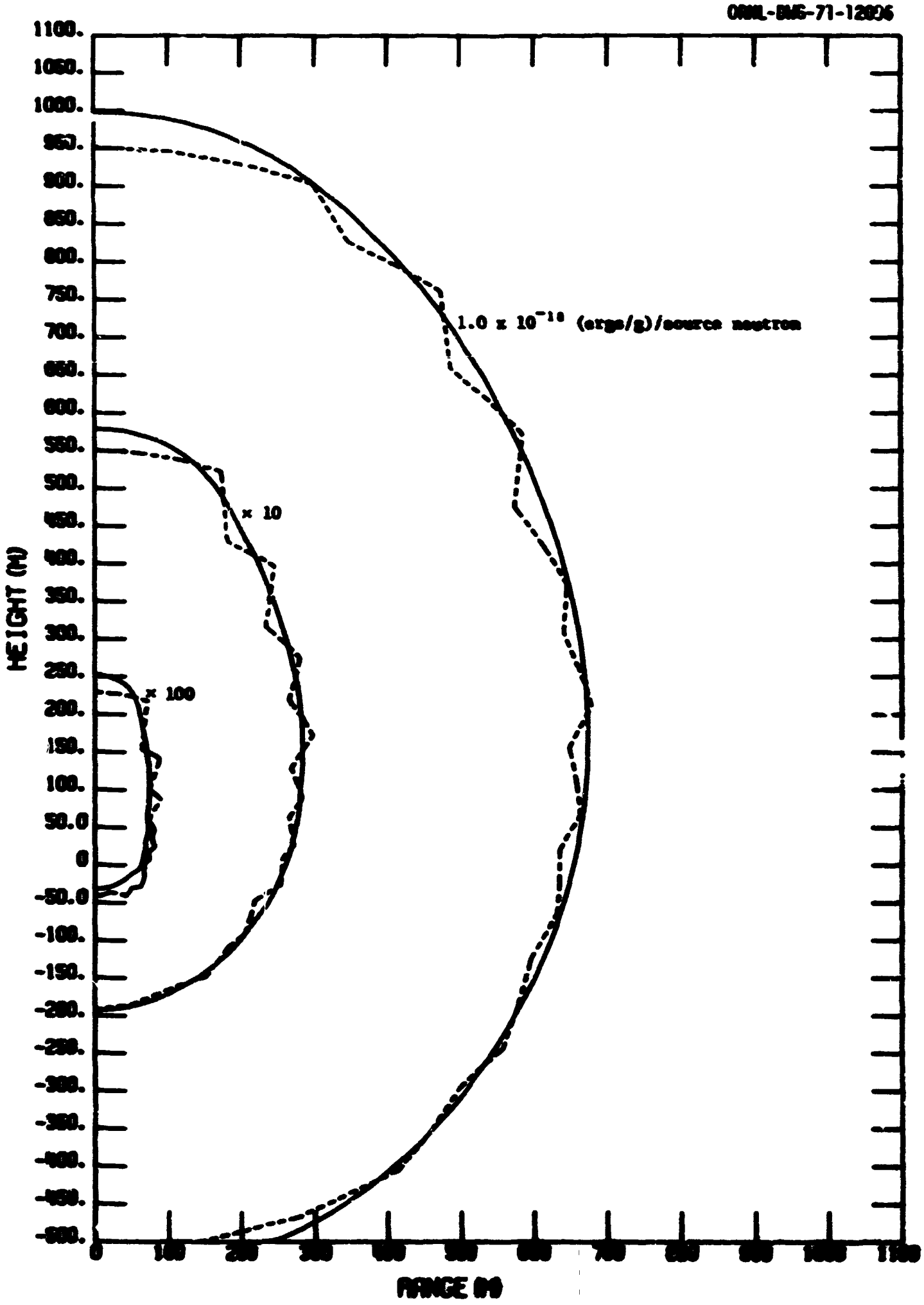

Fig. 20. Gamma-Ray Silicon Isokerma Curves for a 12.2-15-MeV Beam Source.

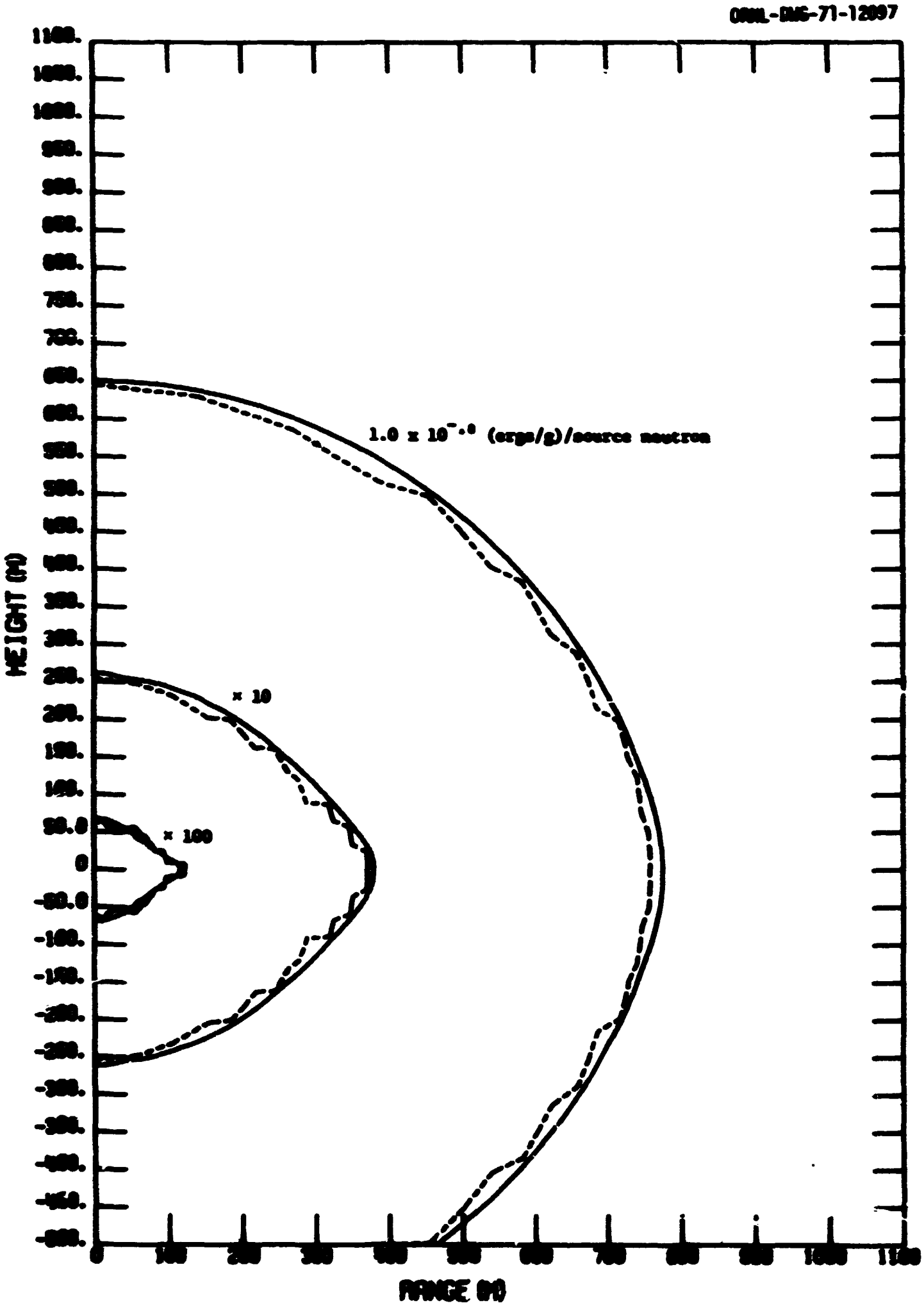

Fig. 21. Gamma-Ray Silicon Isokerma Curves for a 12.2-15-MeV Pancake Source.

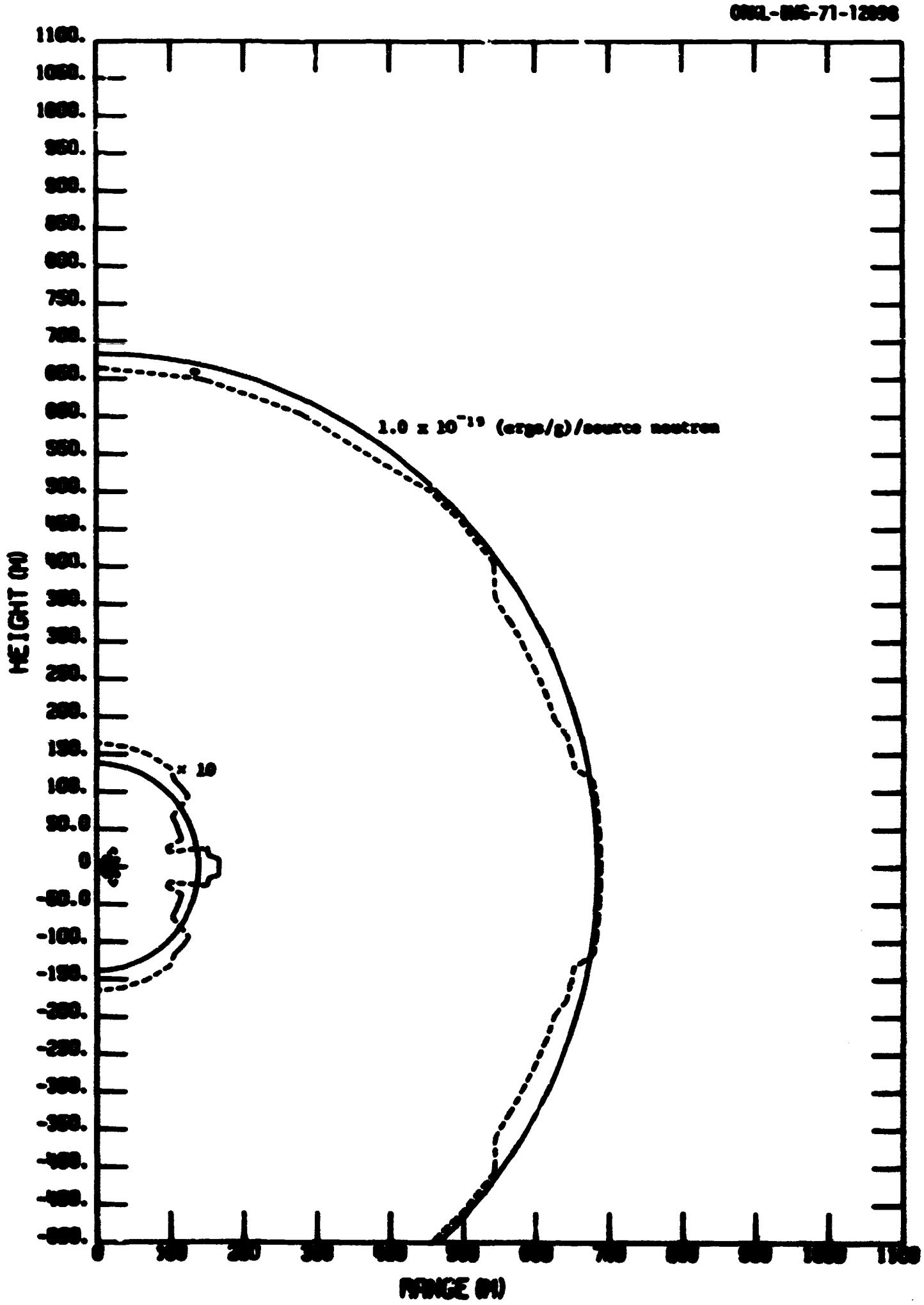

Fig. 22. Gamma-Ray Silicon Isokerma Curves for a Fission Symmetric Source.

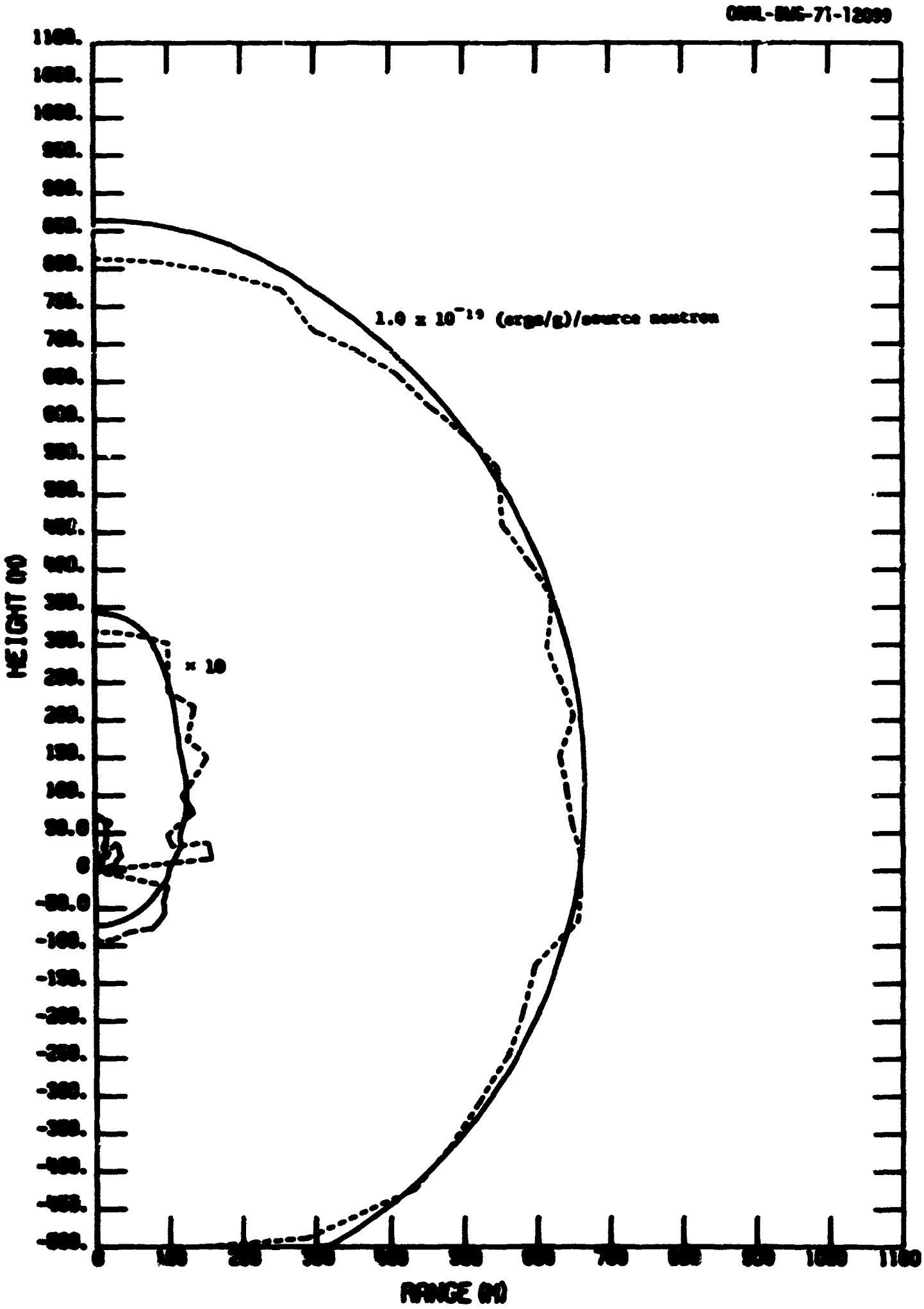

Fig. 23. Gamma-Ray Silicon Isokerma Curves for a Fission Beam Source.

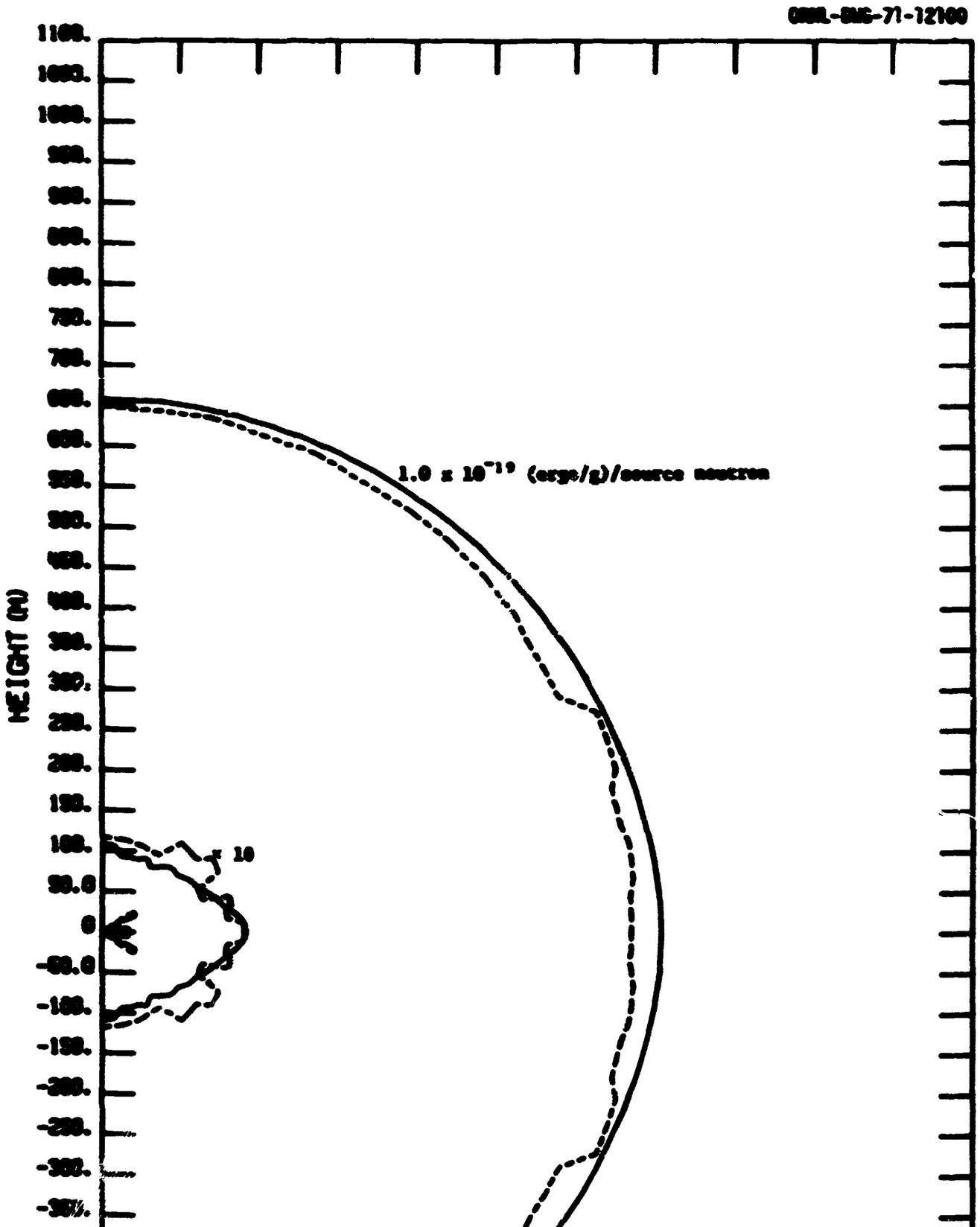

Fig. 24. Gamma-Ray Silicon Isokerma Curves for a Fission Pancake Source.

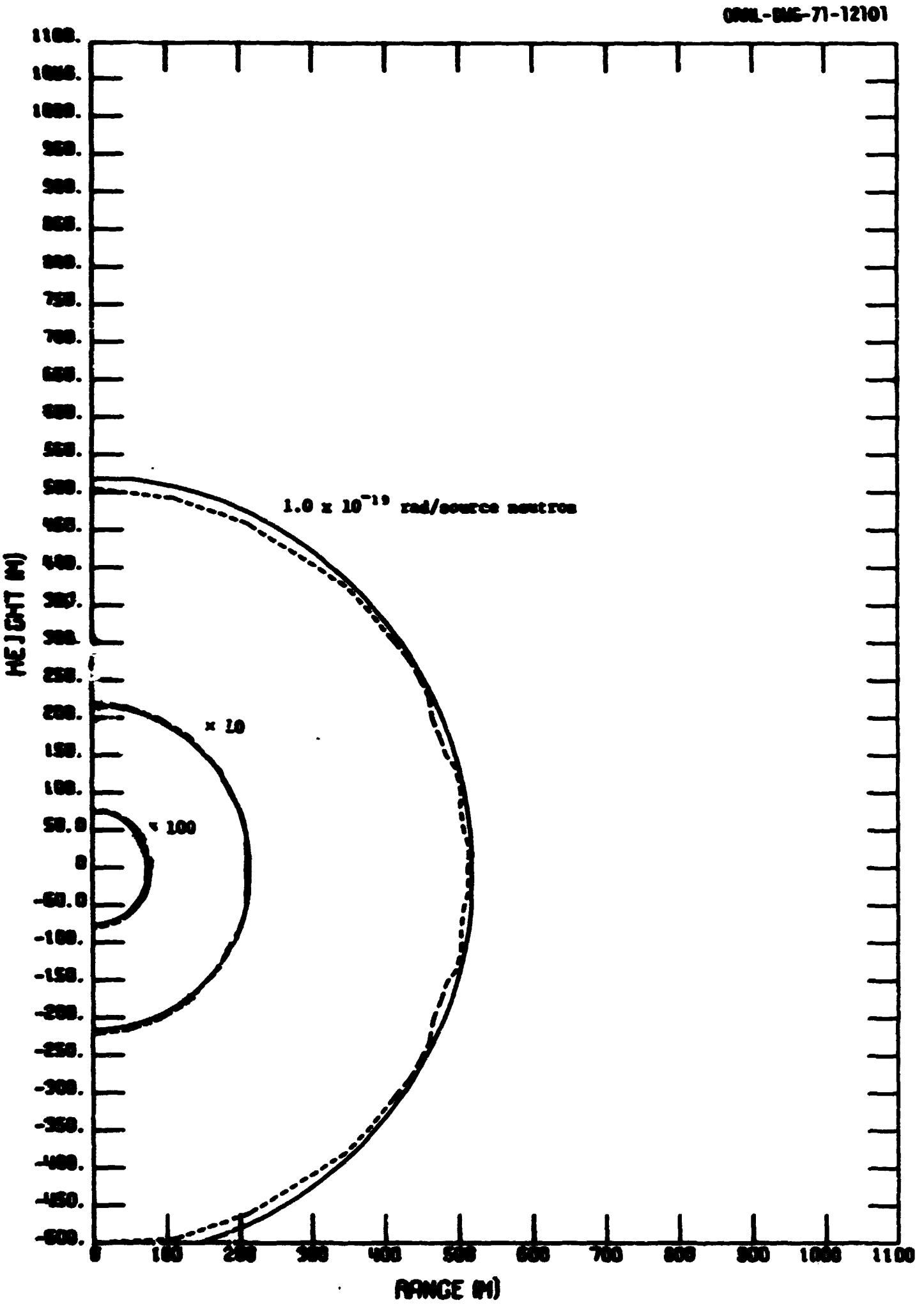

Fig. 25. Neutron Isodose Curves for a 12.2-15-MeV Symmetric Source.

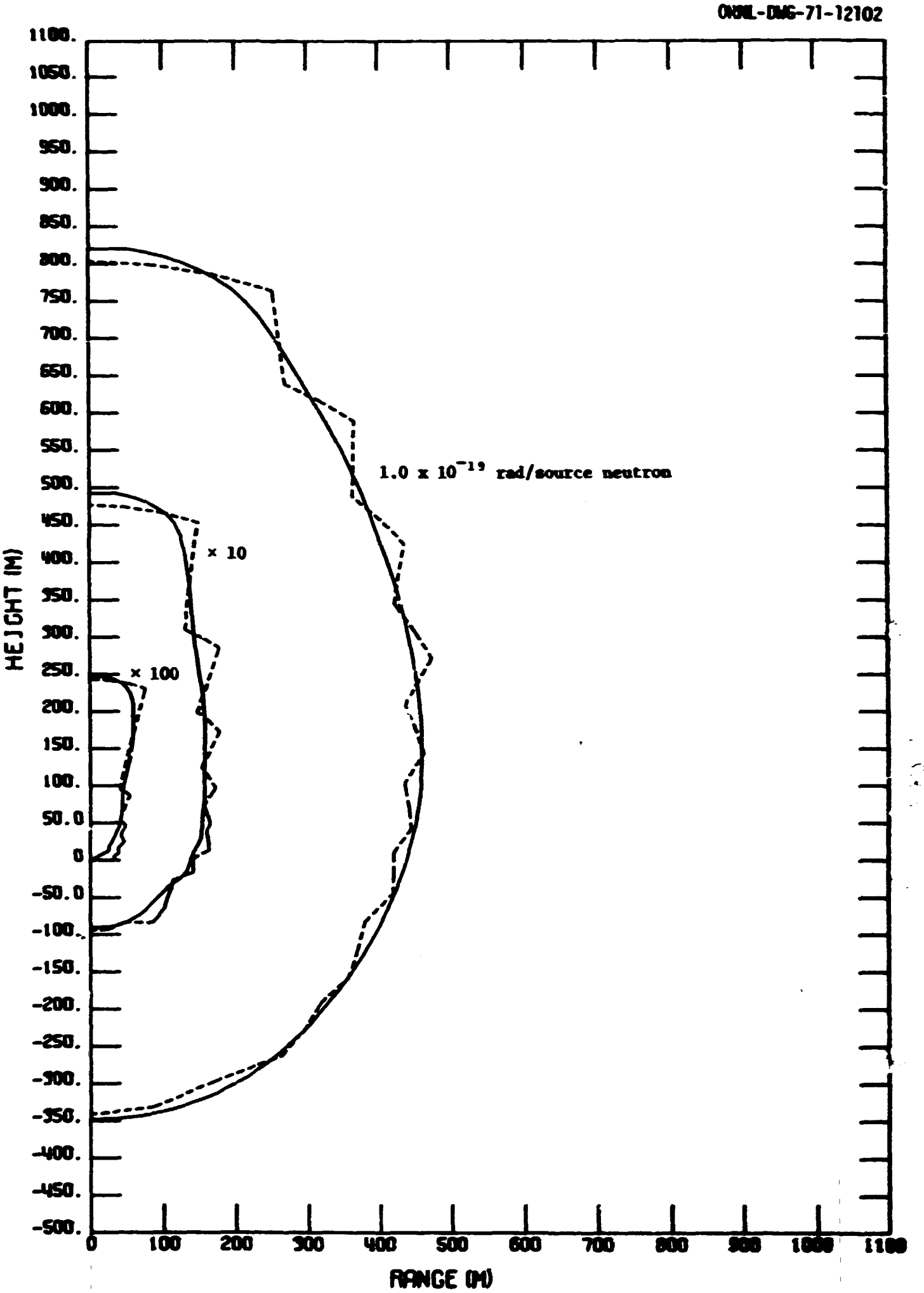

Fig. 26. Neutron Isodose Curves for a 12.2-15-MeV Beam Source.

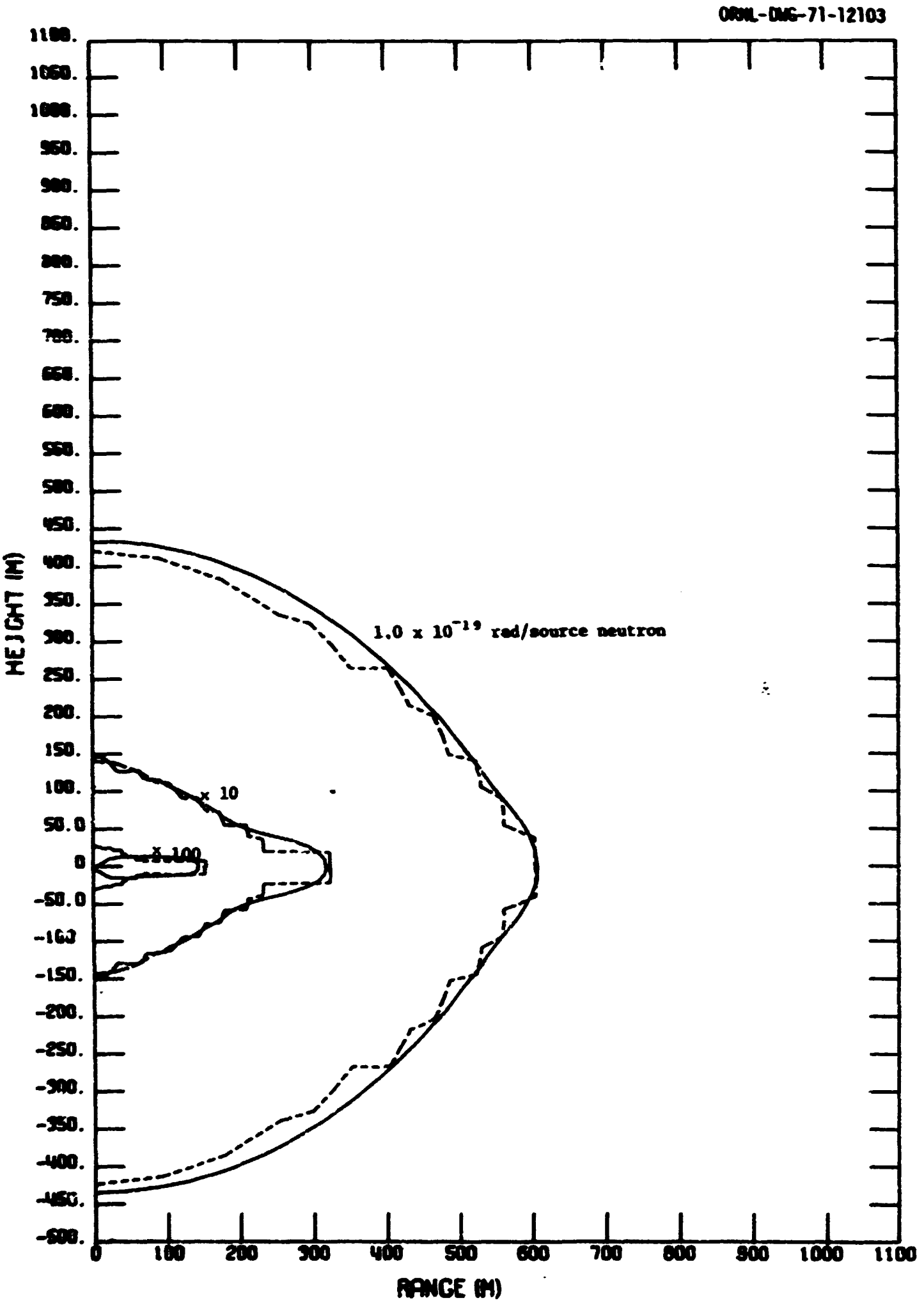

Fig. 27. Neutron Isodose Curves for a 12.2-15-MeV Pancake Source.

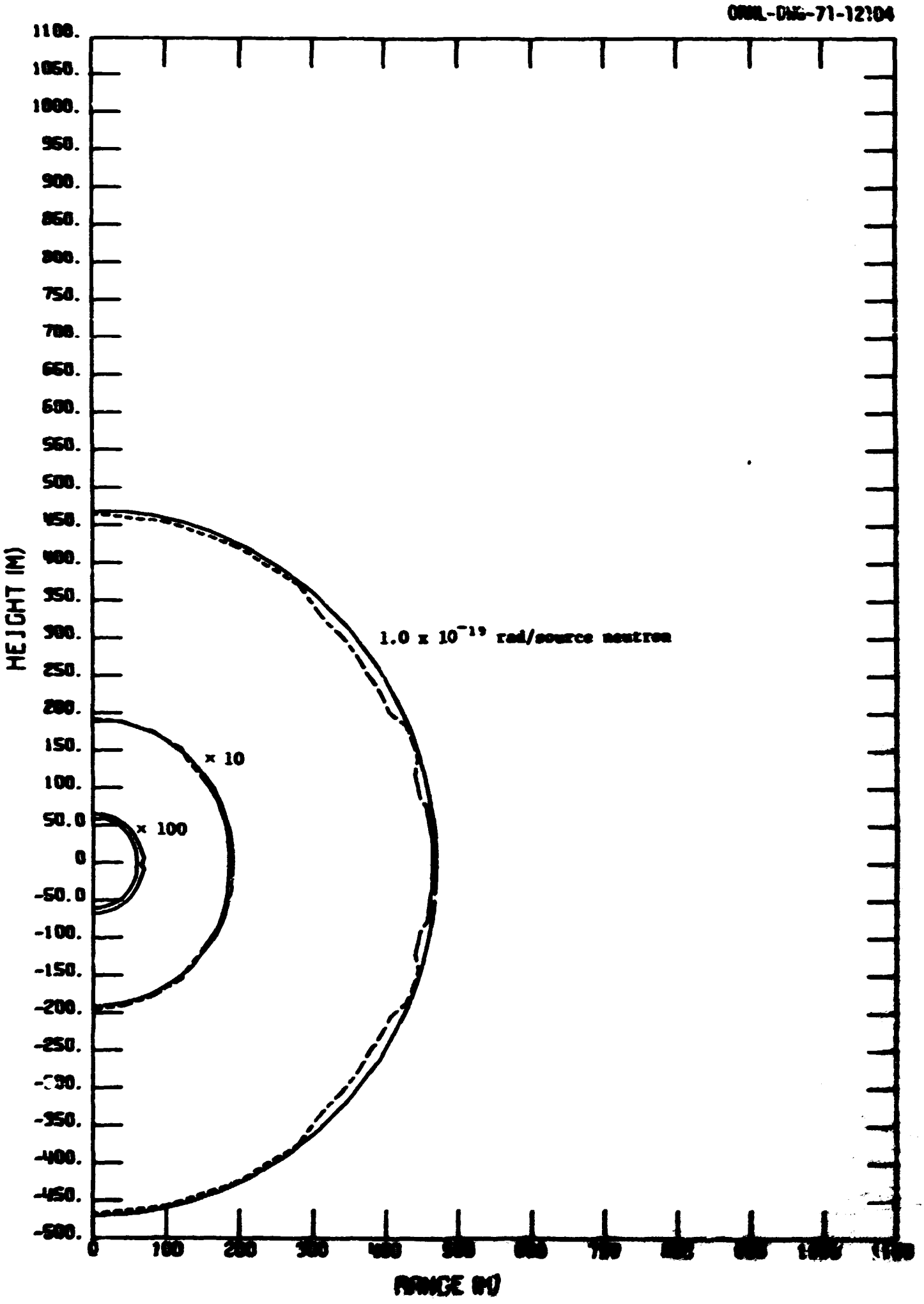

Fig. 28. Neutron Isodose Curves for a Fission Symmetric Source.

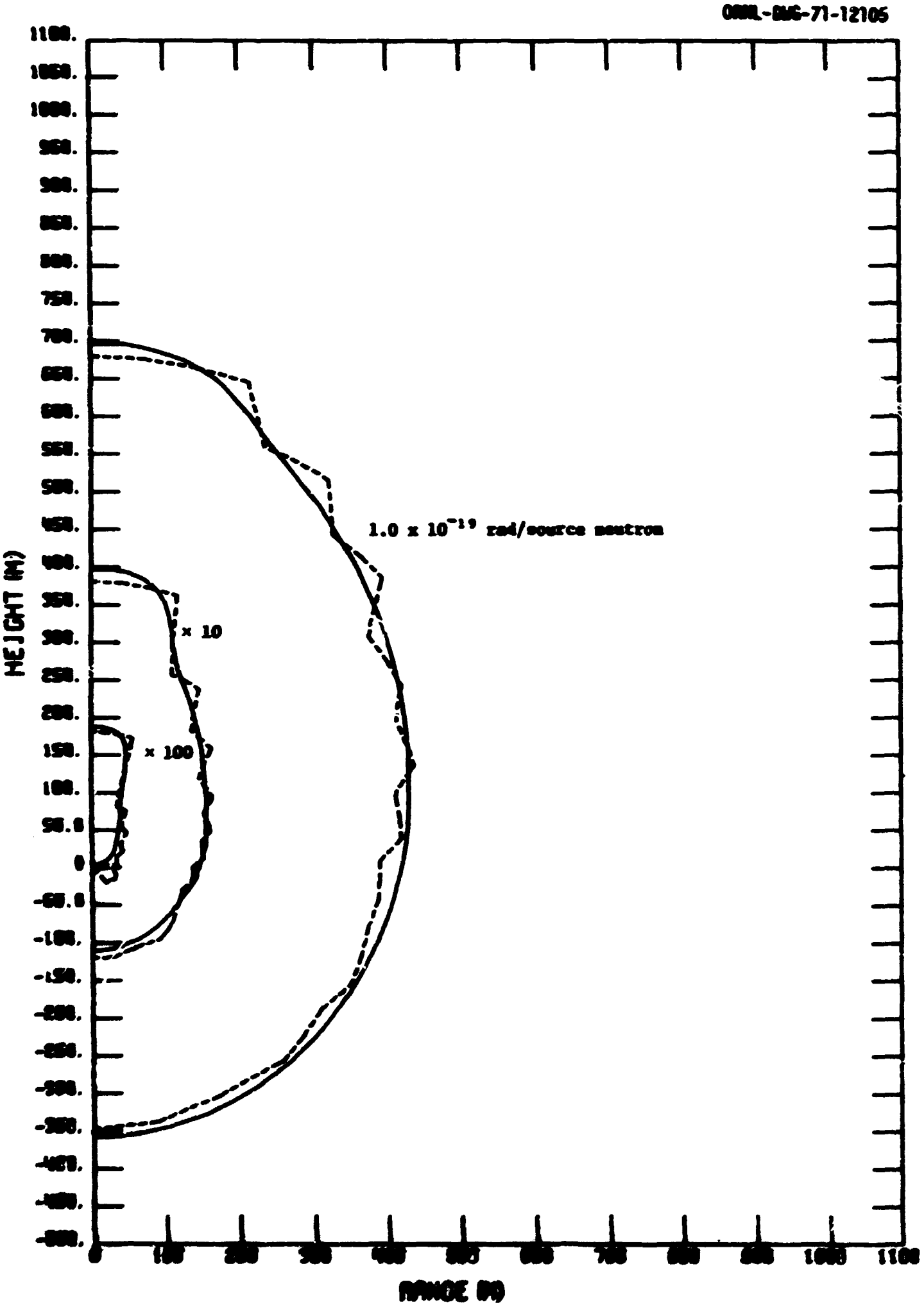

Fig. 29. Neutron Isodose Curves for a Fission Beam Source.

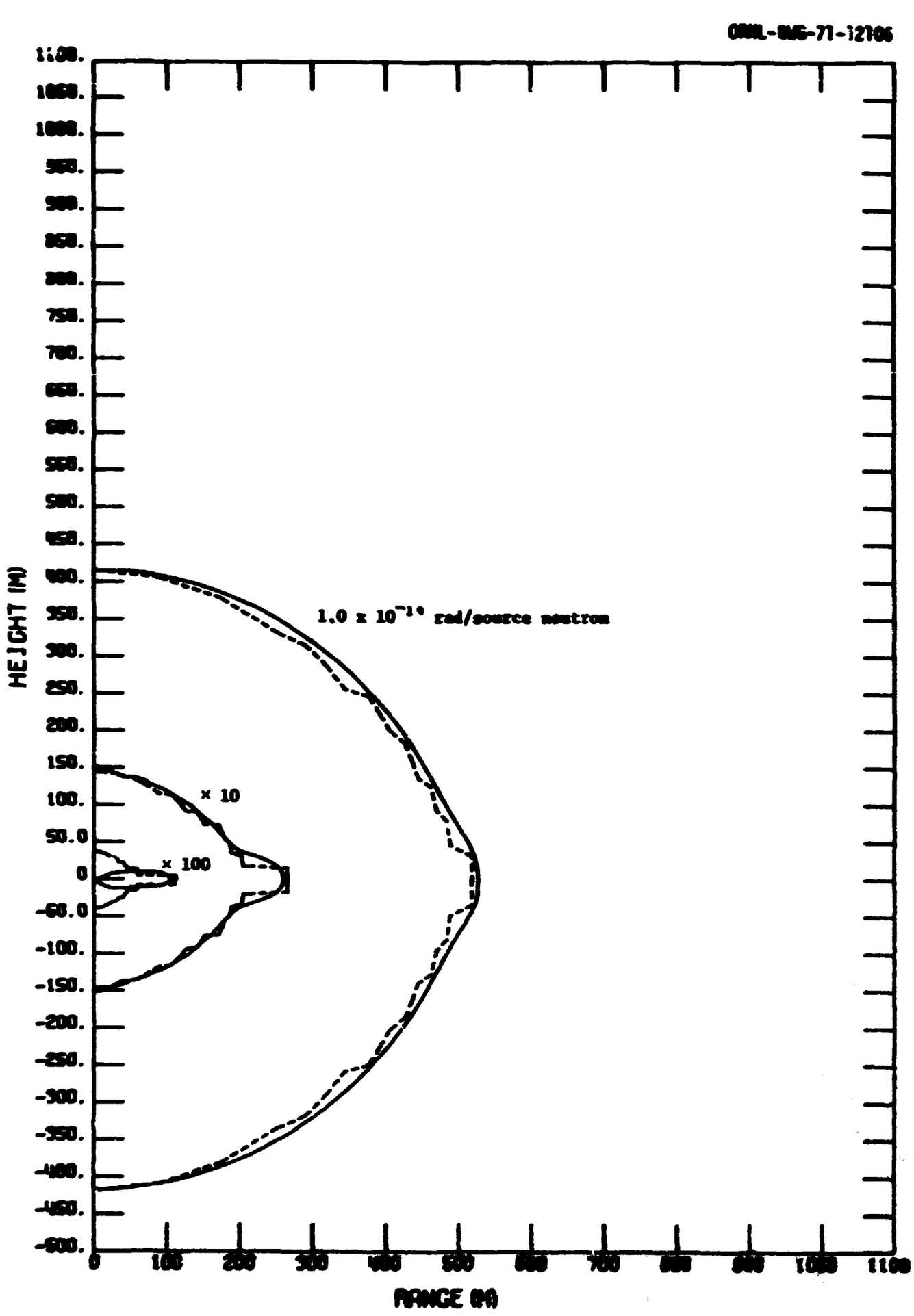

Fig. 30. Neutron Isodose Curves for a Fission Pancake Source.

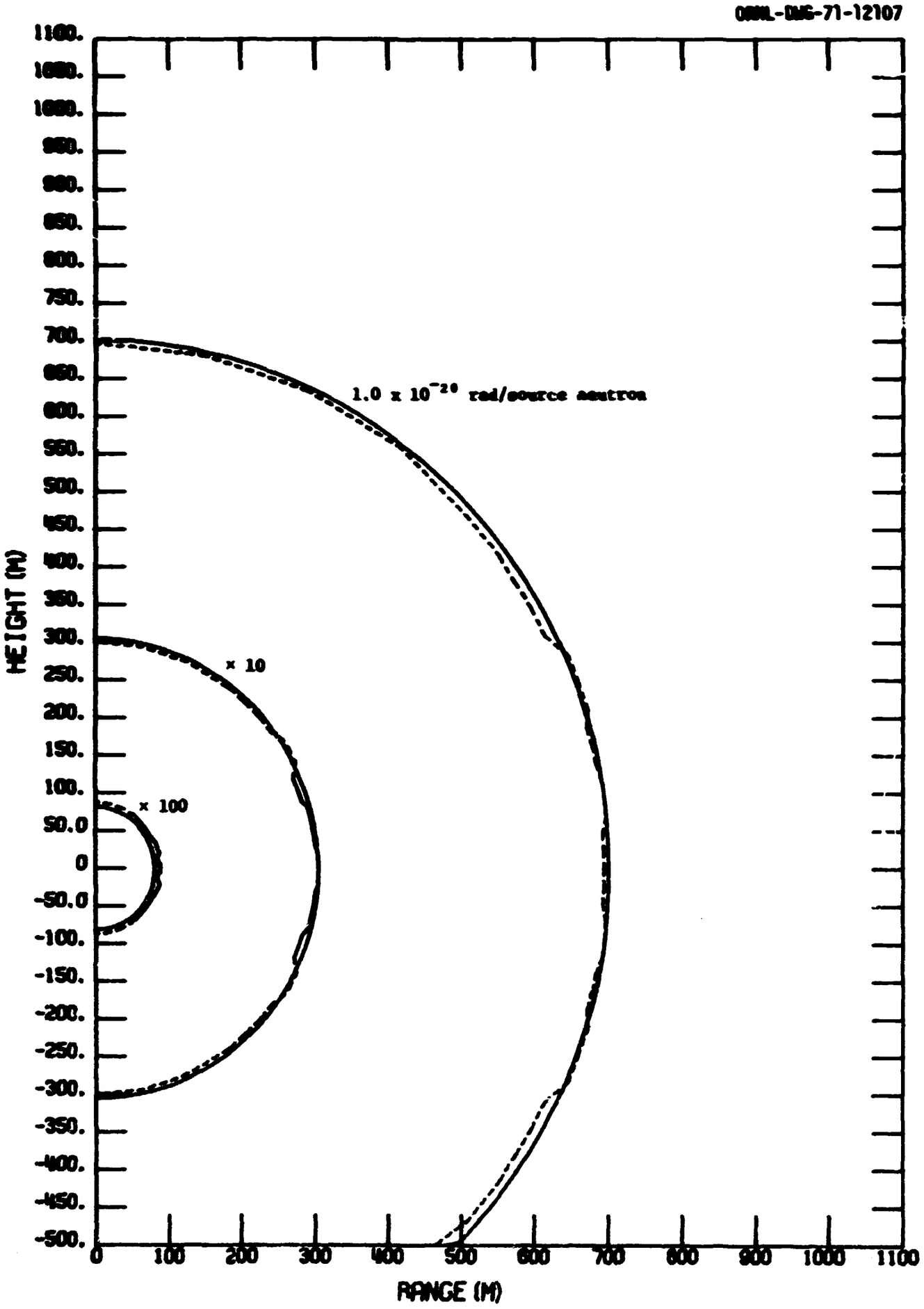

Fig. 31. Gamma-Ray Isodose Curves for a 12.2-15-MeV Symmetric Source.

ORNL-DWG-71-12108

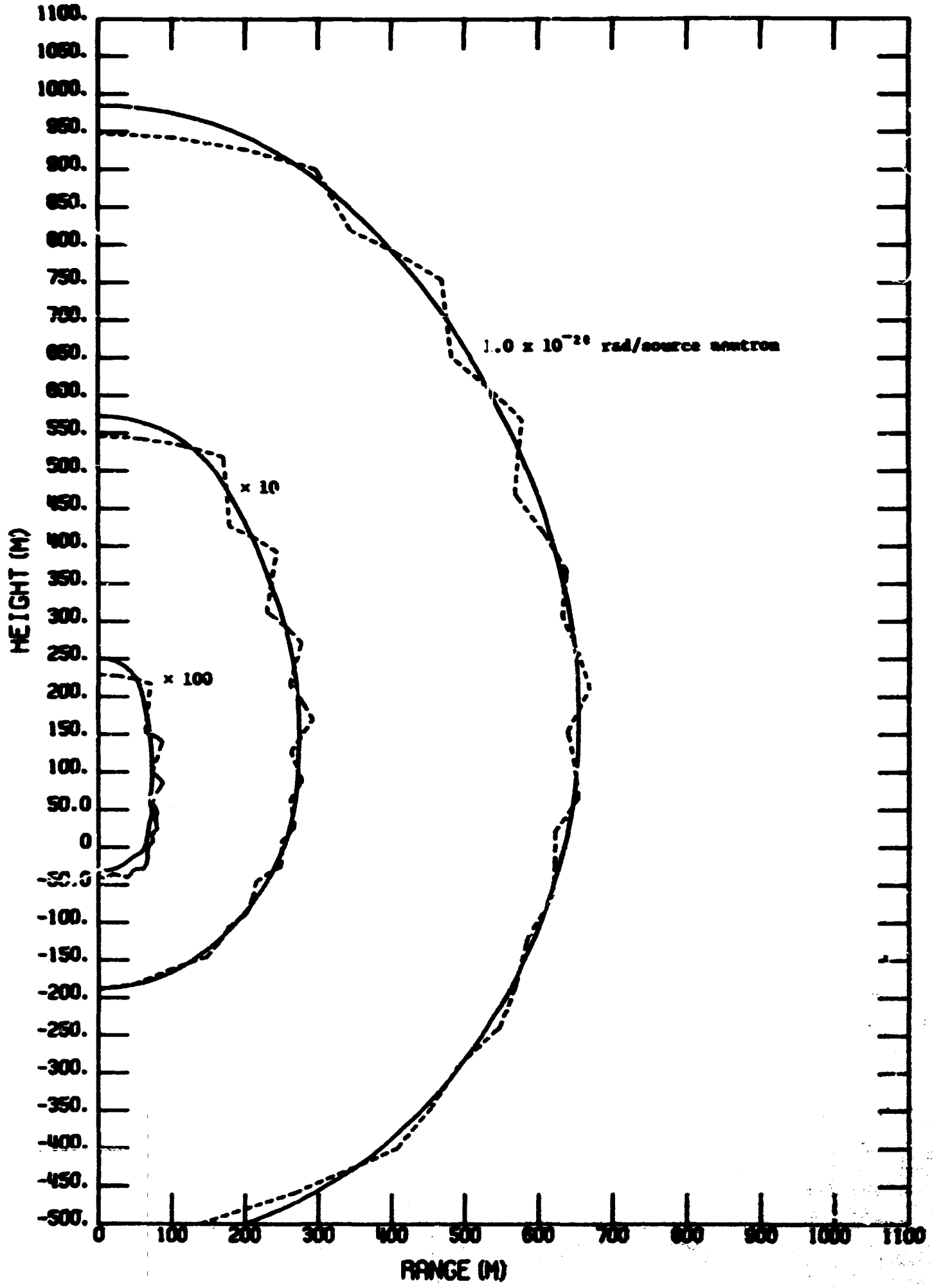

Fig. 32. Gamma-Ray Isodose Curves for a 12.2-15-MeV Beam Source.

ORNL-DWG-71-12109

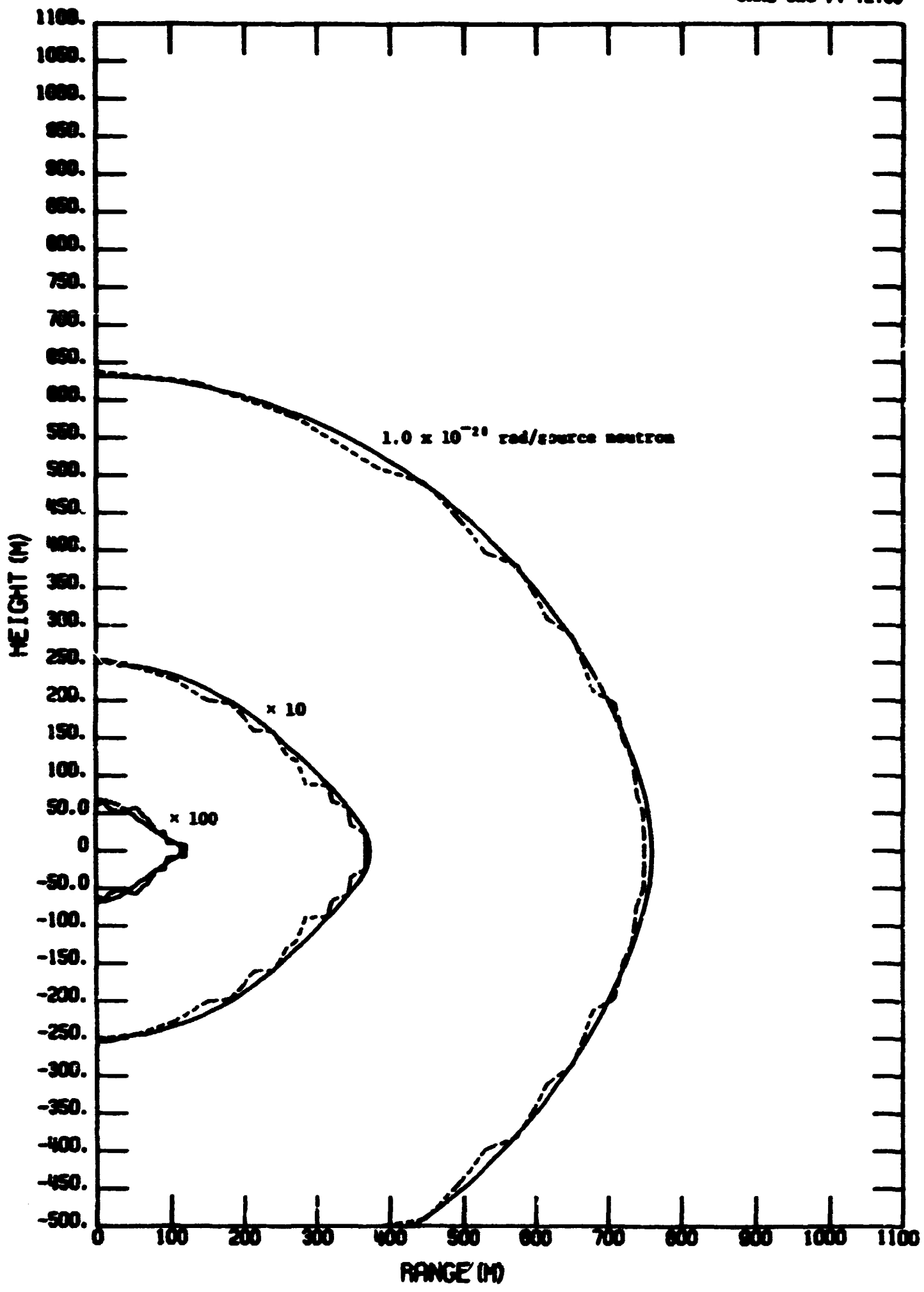

Fig. 33. Gamma-Ray Isodose Curves for a 12.2-15-MeV Pancake Source.

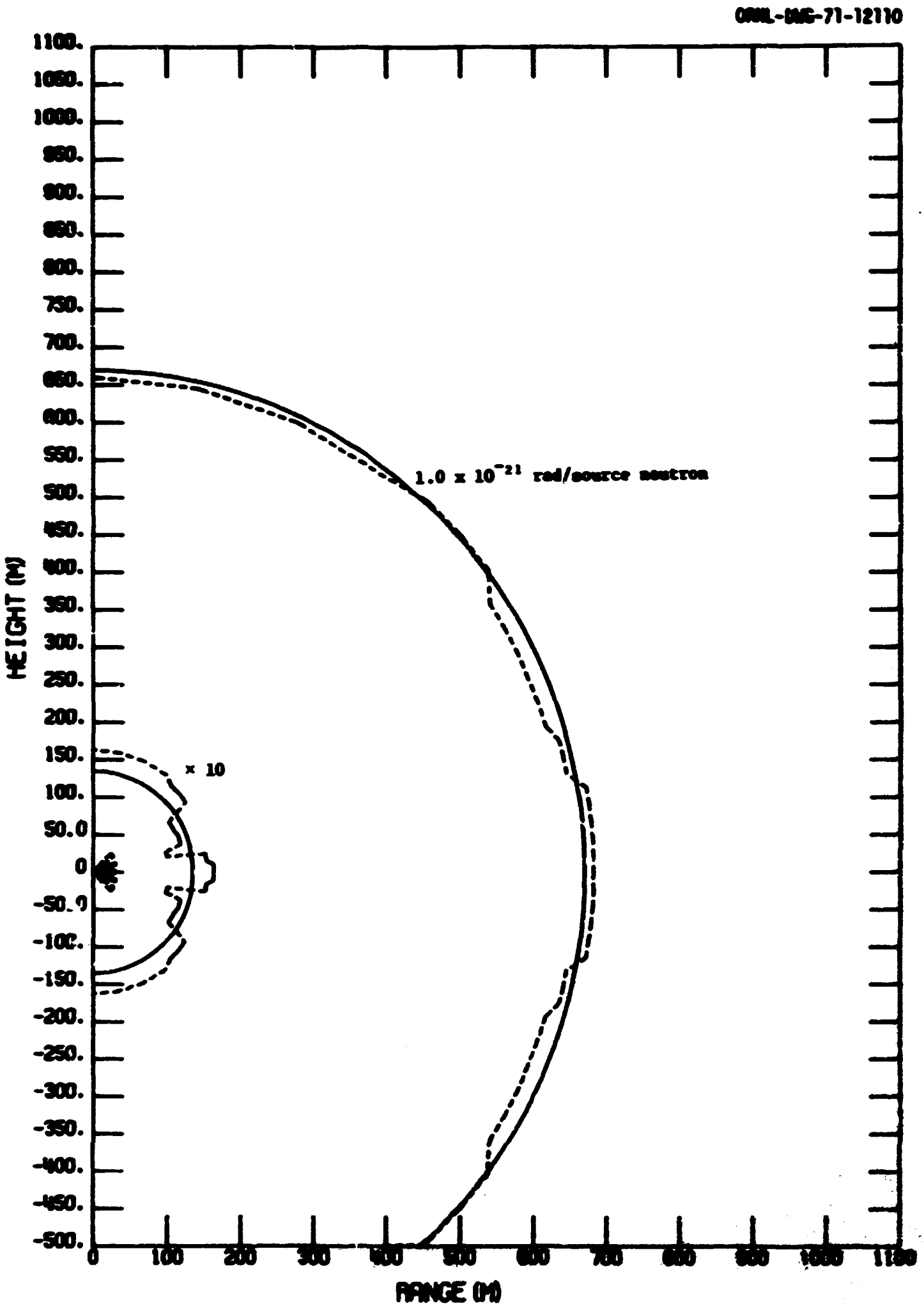

Fig. 34. Gamma-Ray Isodose Curves for a Fission Symmetric Source.

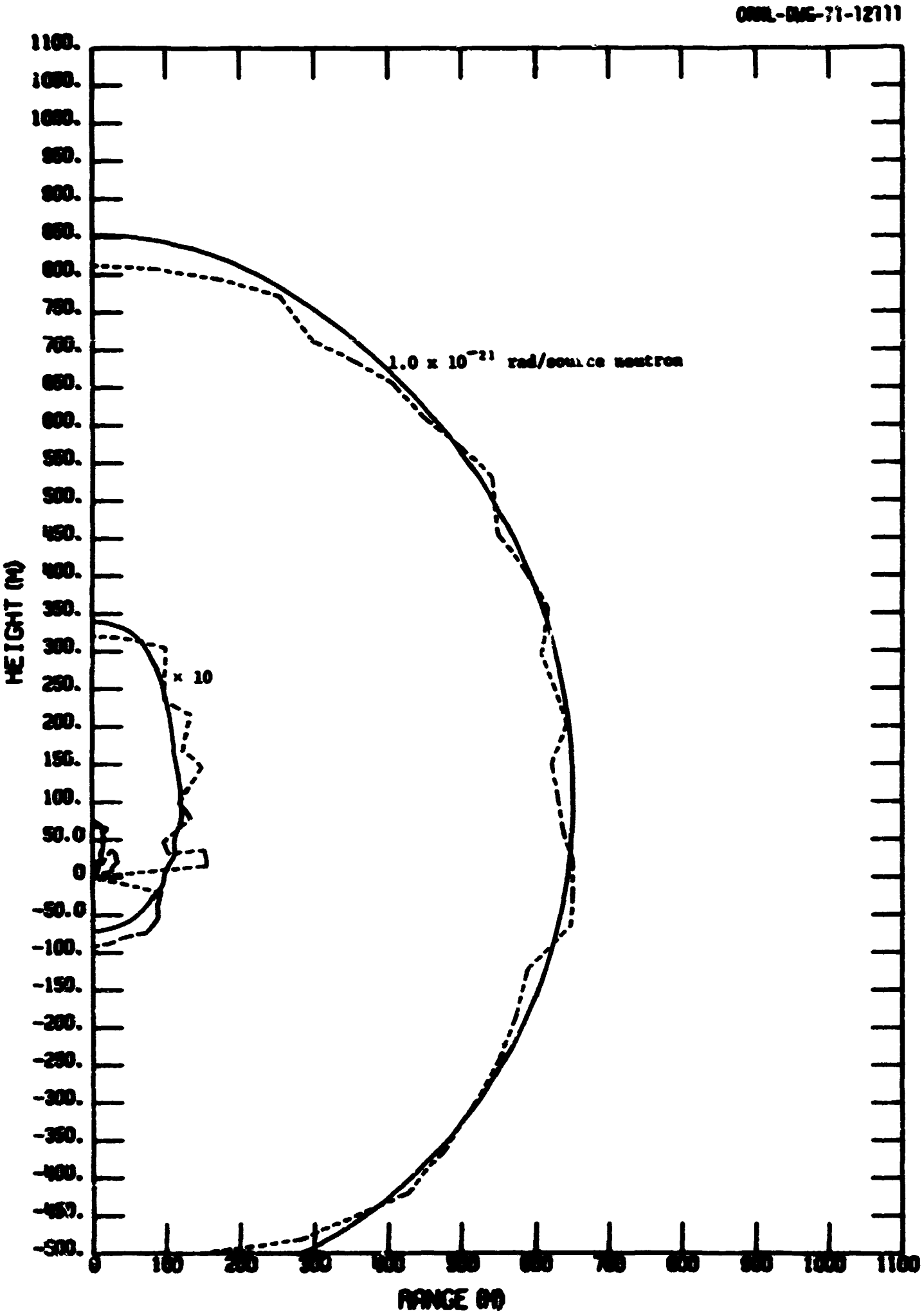

Fig. 35. Gamma-Ray Isodose Curves for a Fission Beam Source.

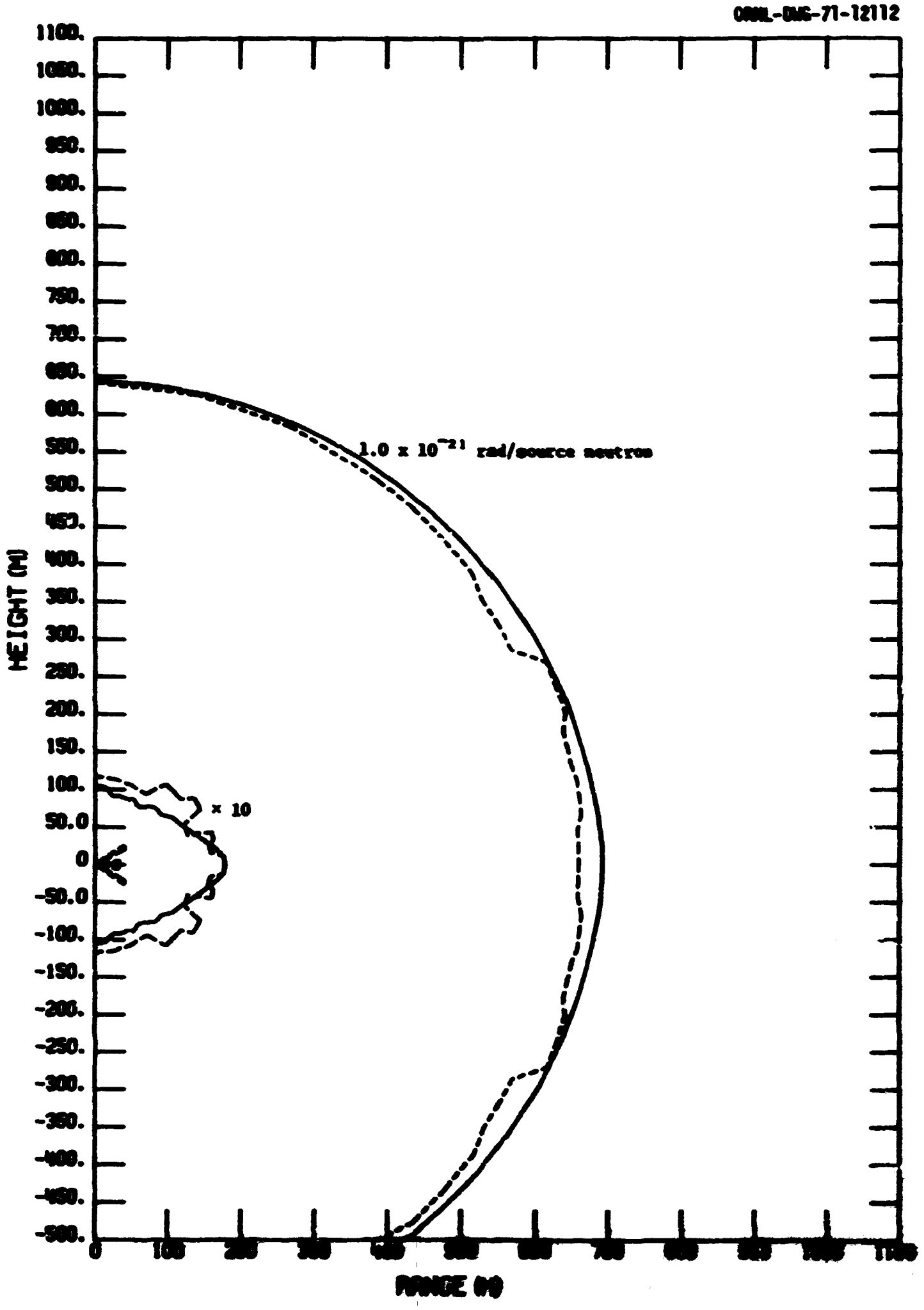

Fig. 36. Gamma-Ray Isodose Curves for a Fission Pancake Source.

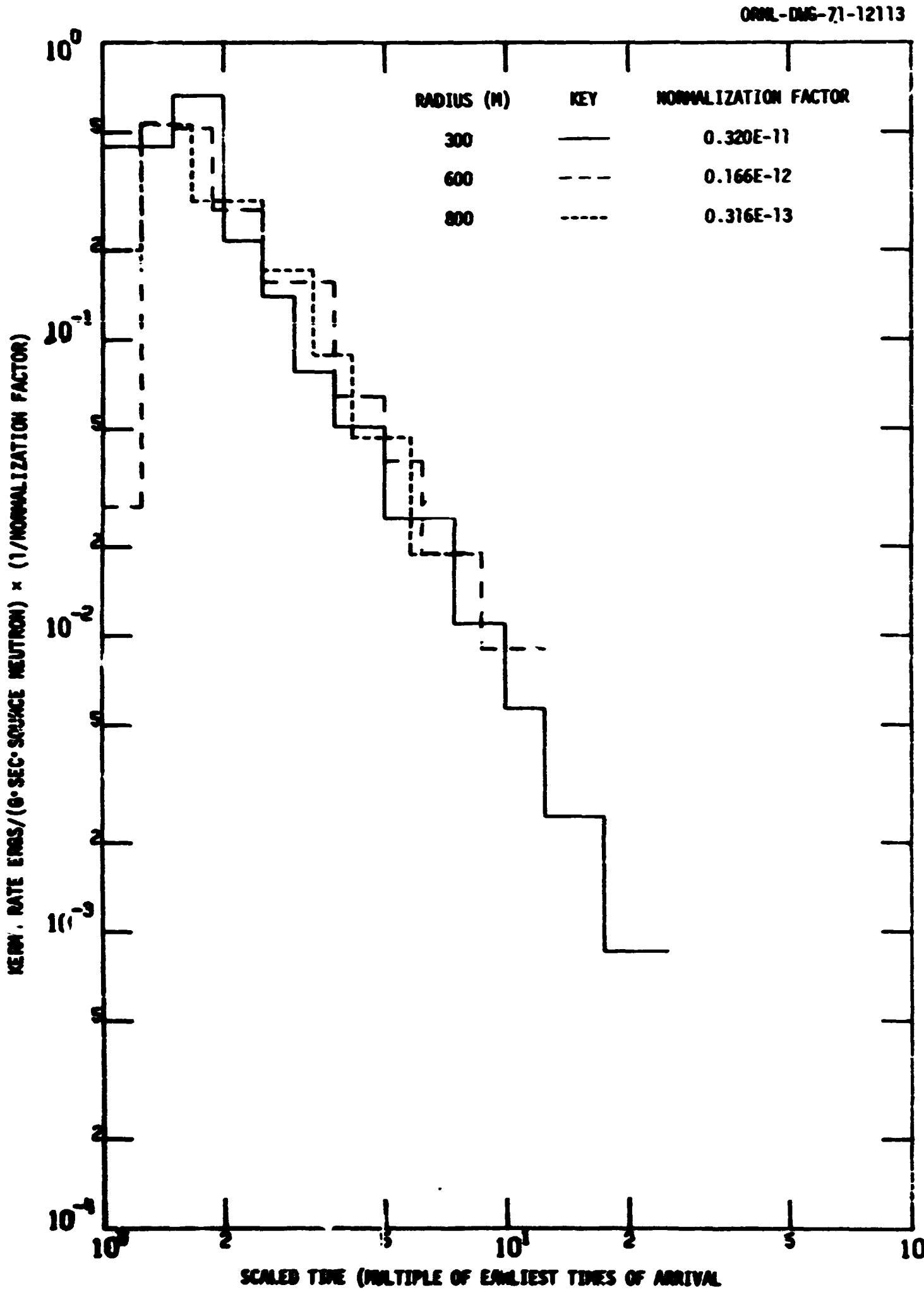

Fig. 37. Time-Dependent Neutron Air Kerma (Scaled) for a 12.2-15-MeV Symmetric Source.

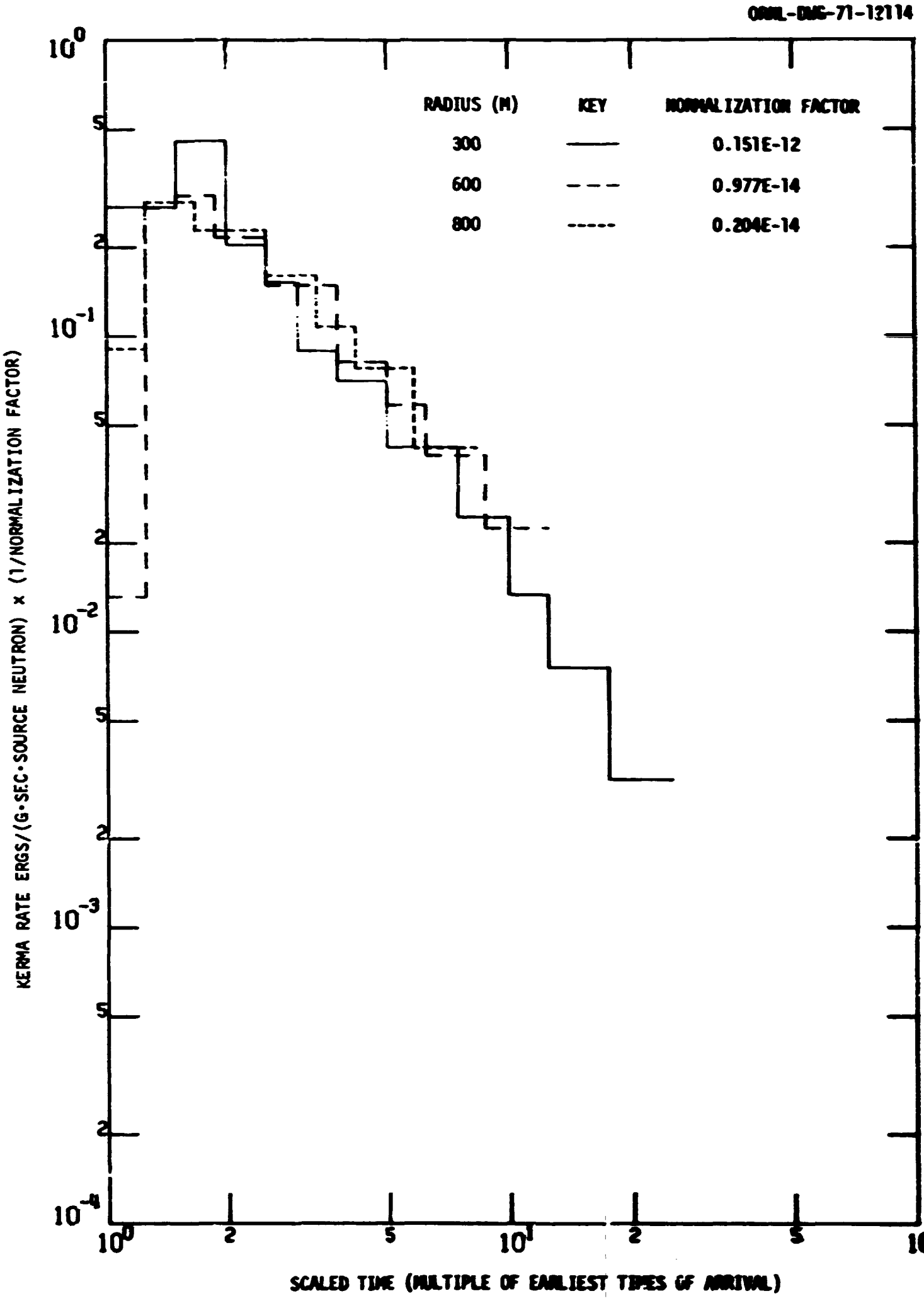

Fig. 38. Time-Dependent Neutron Silicon Kerma (Scaled) for a 12.2-15-MeV Symmetric Source.

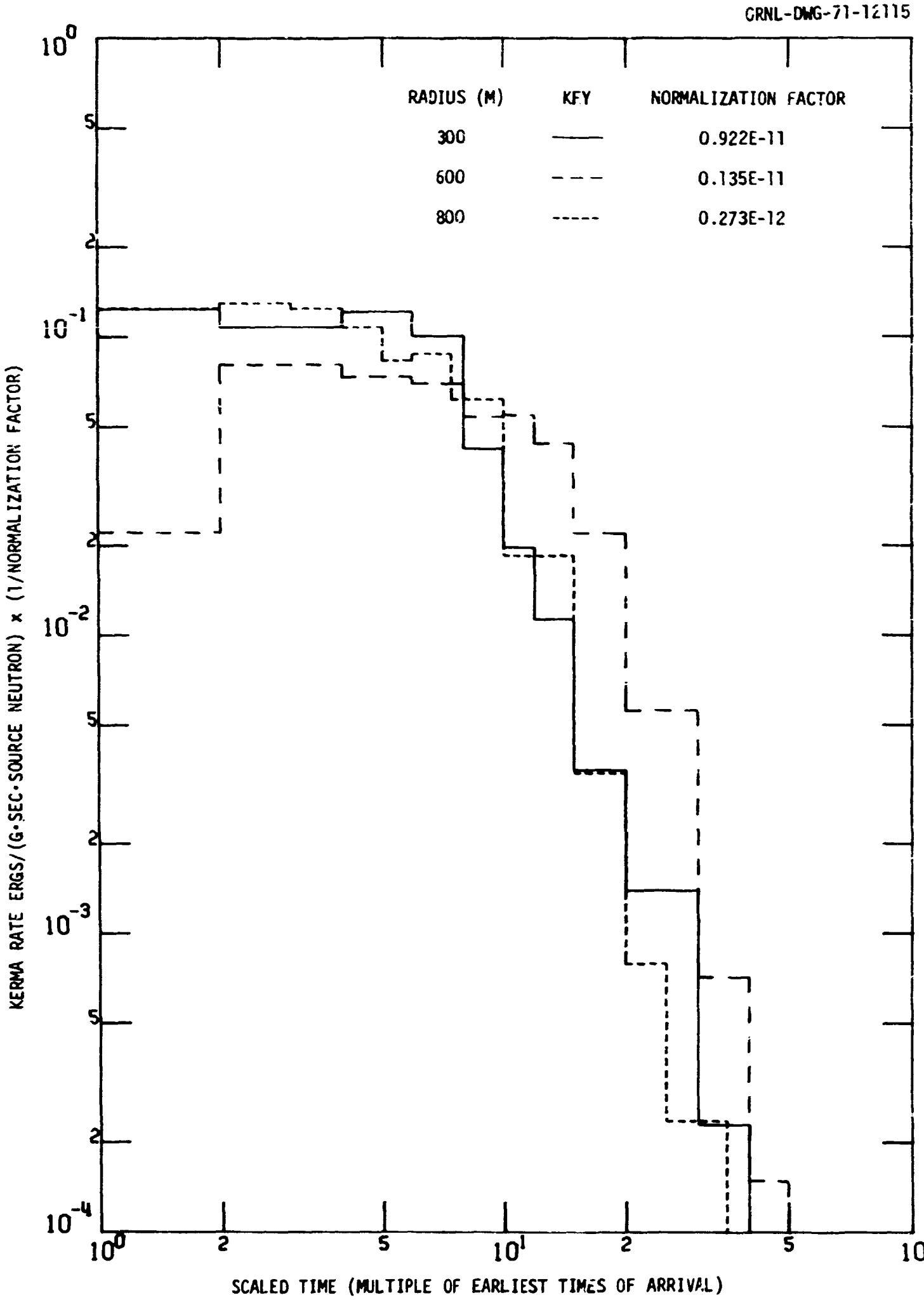

Fig. 39. Time-Dependent Gamma-Ray Air Kerma (Scaled) for a 12.2-15-MeV Symmetric Source.

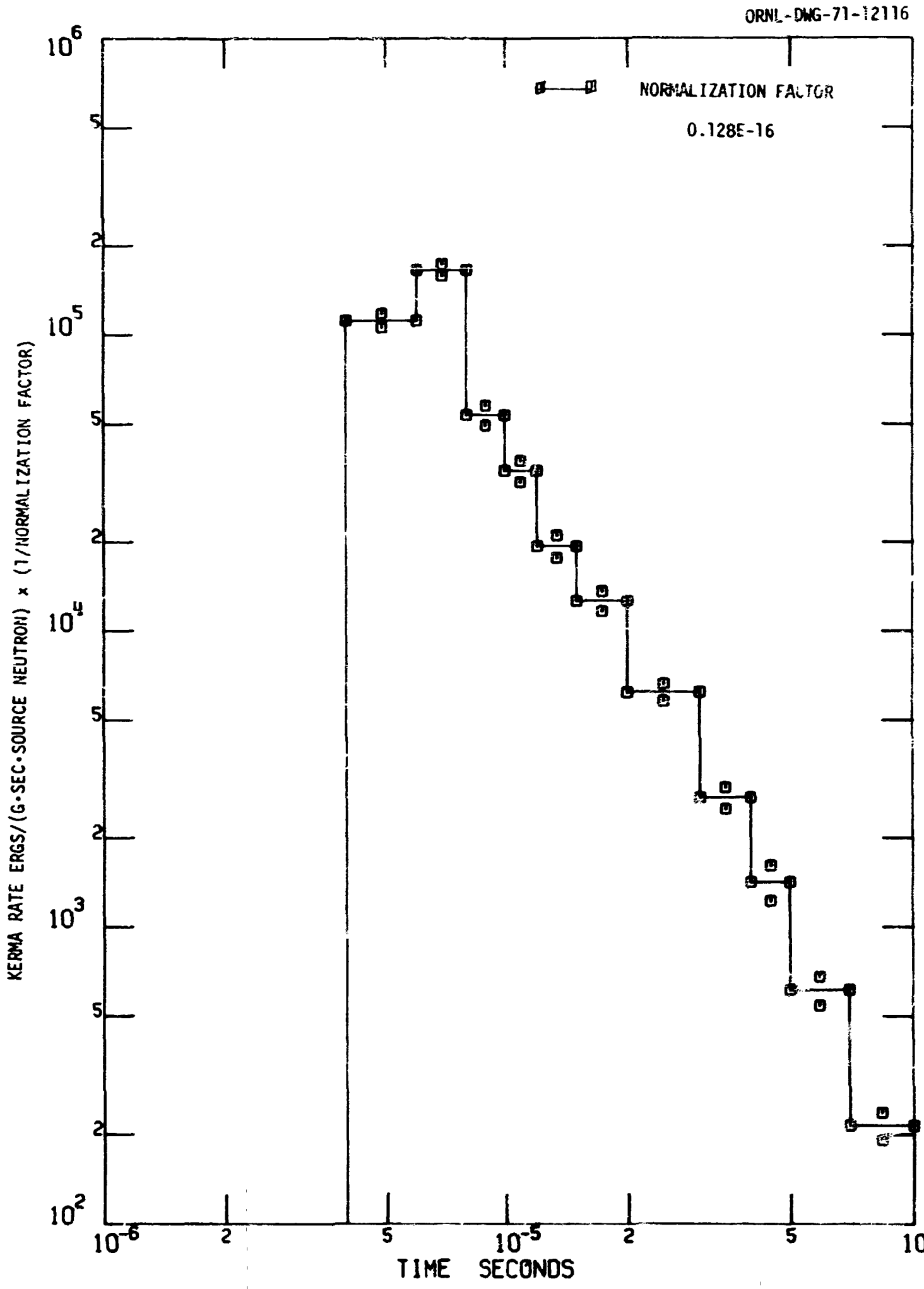

Fig. 40. Time-Dependent Neutron Air Kerma at a Radius of 300 M for a 12.2-15-MeV Symmetric Source.

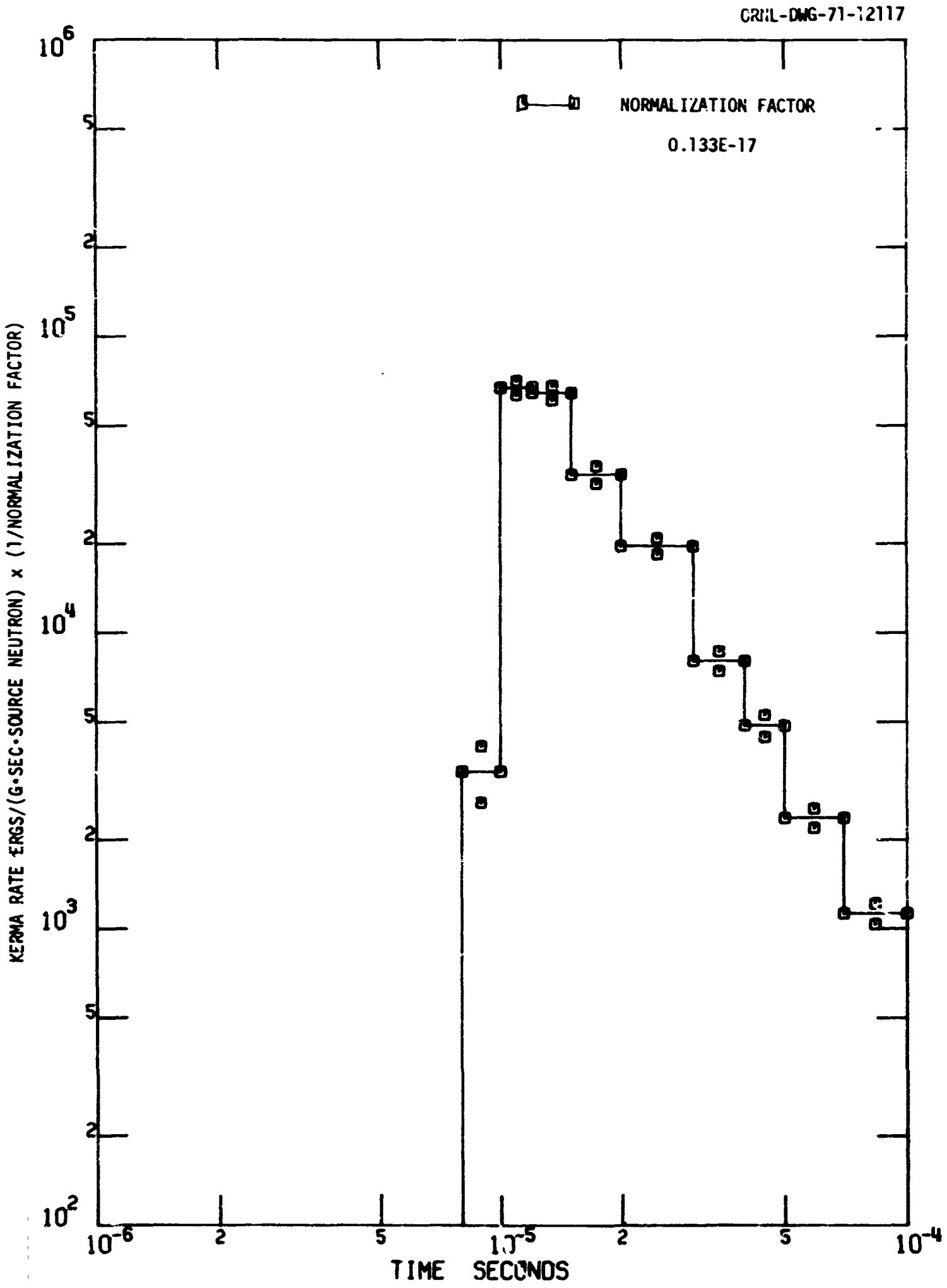

Fig. 41. Time-Dependent Neutron Air Kerma at a Radius of 600 M for a 12.2-15-MeV Symmetric Source.

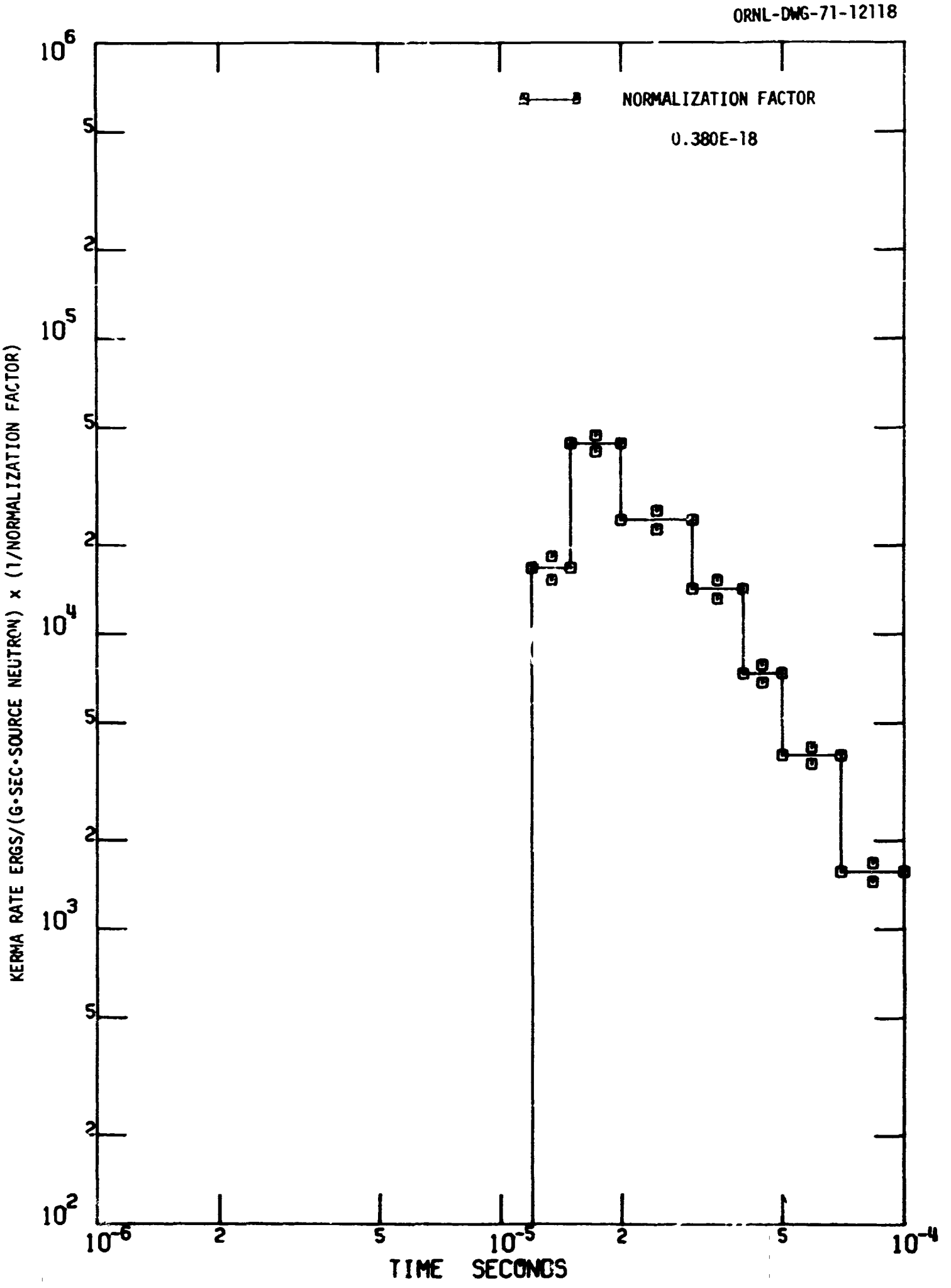

Fig. 42. Time-Dependent Neutron Air Kerma at a Radius of 800 M for a 12.2-15-MeV Symmetric Source.

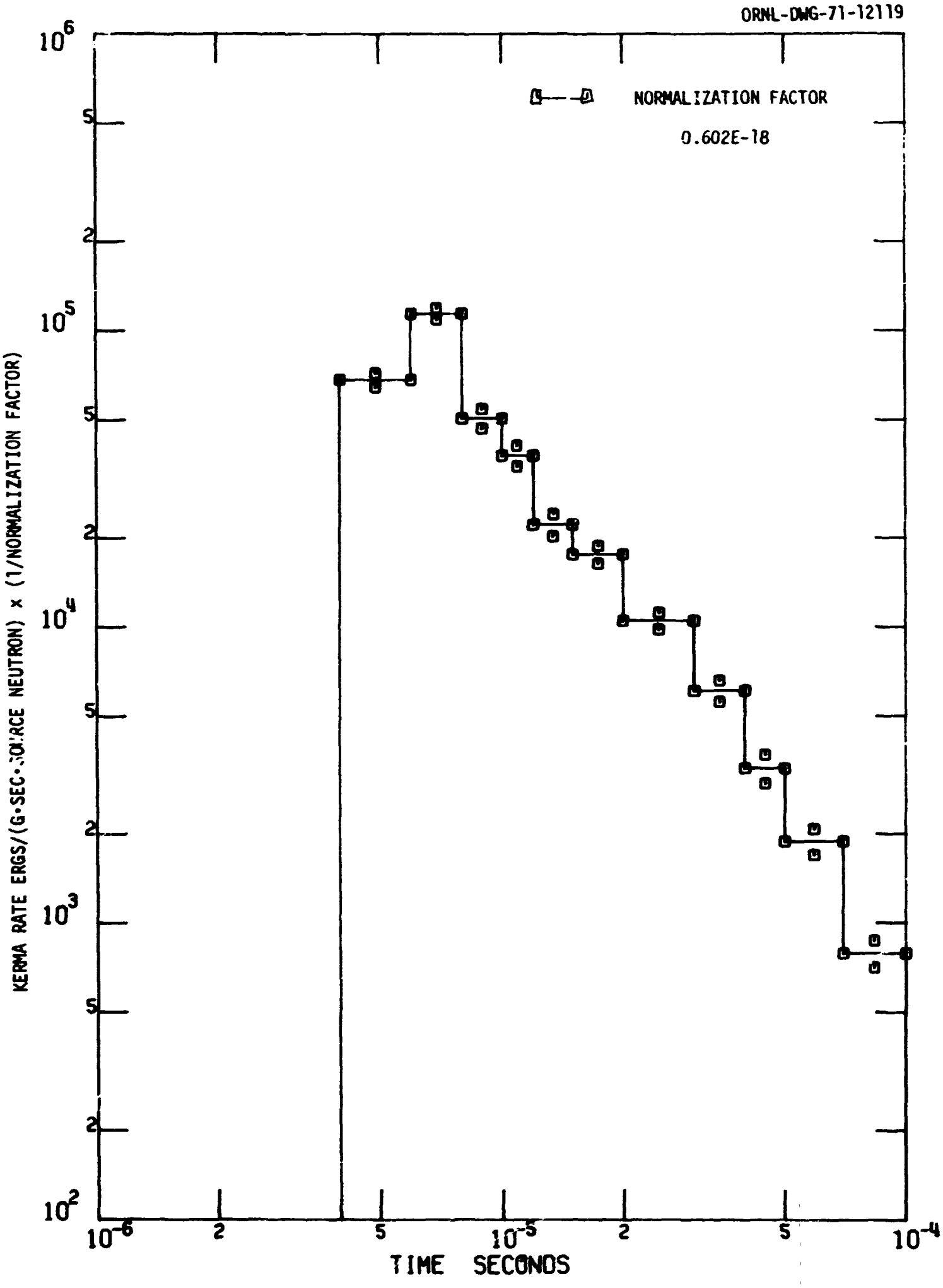

Fig. 43. Time-Dependent Neutron Silicon Kerma at a Radius of 300 M for a 12.2-15 MeV-Symmetric Source.

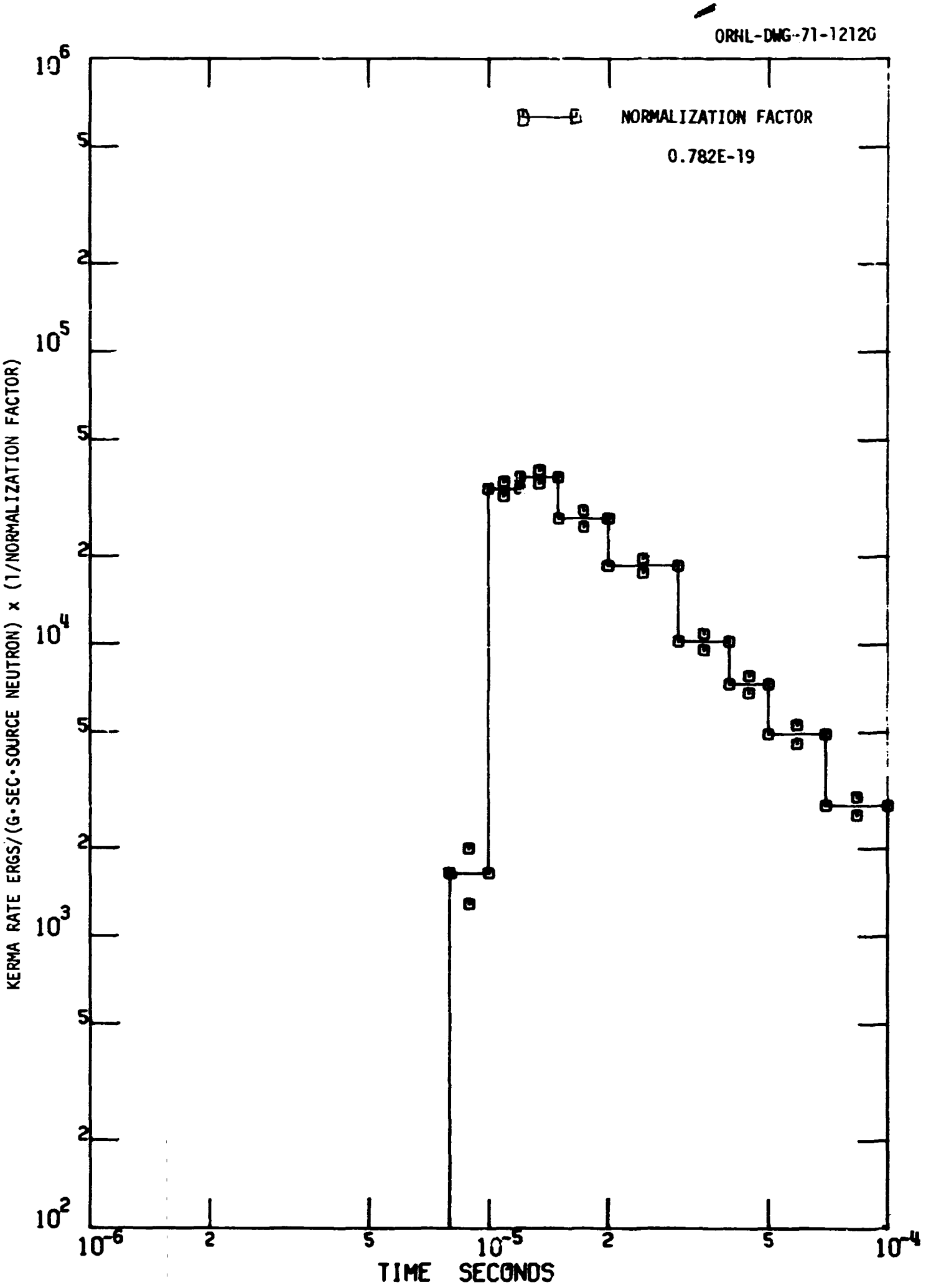

Fig. 44. Time-Dependent Neutron Silicon Kerma at a Radius of 600 M for a 12.2-15-MeV Symmetric Source.

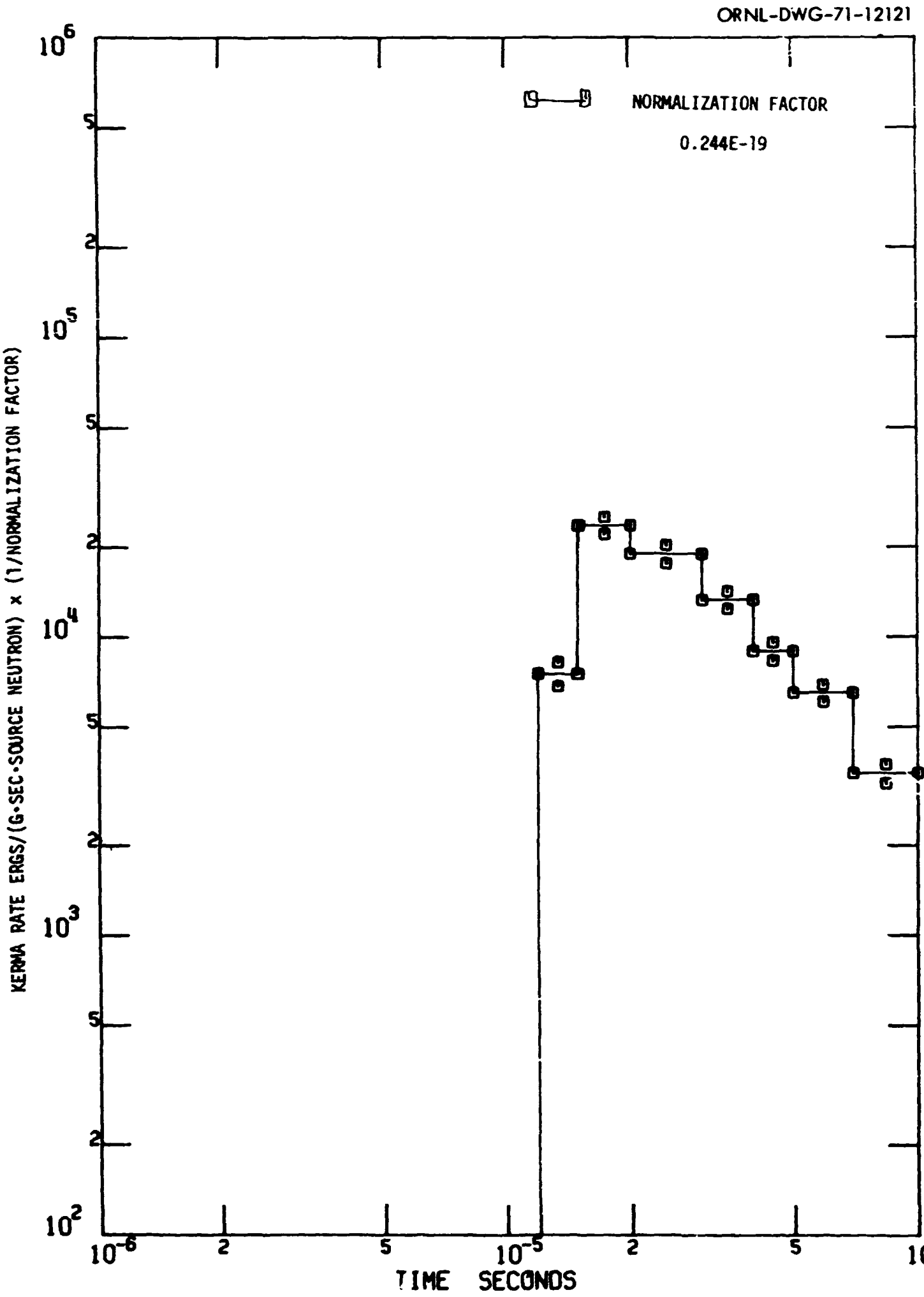

Fig. 45. Time-Dependent Neutron Silicon Kerma at a Radius of 800 M for a 12.2-15-MeV Symmetric Source.

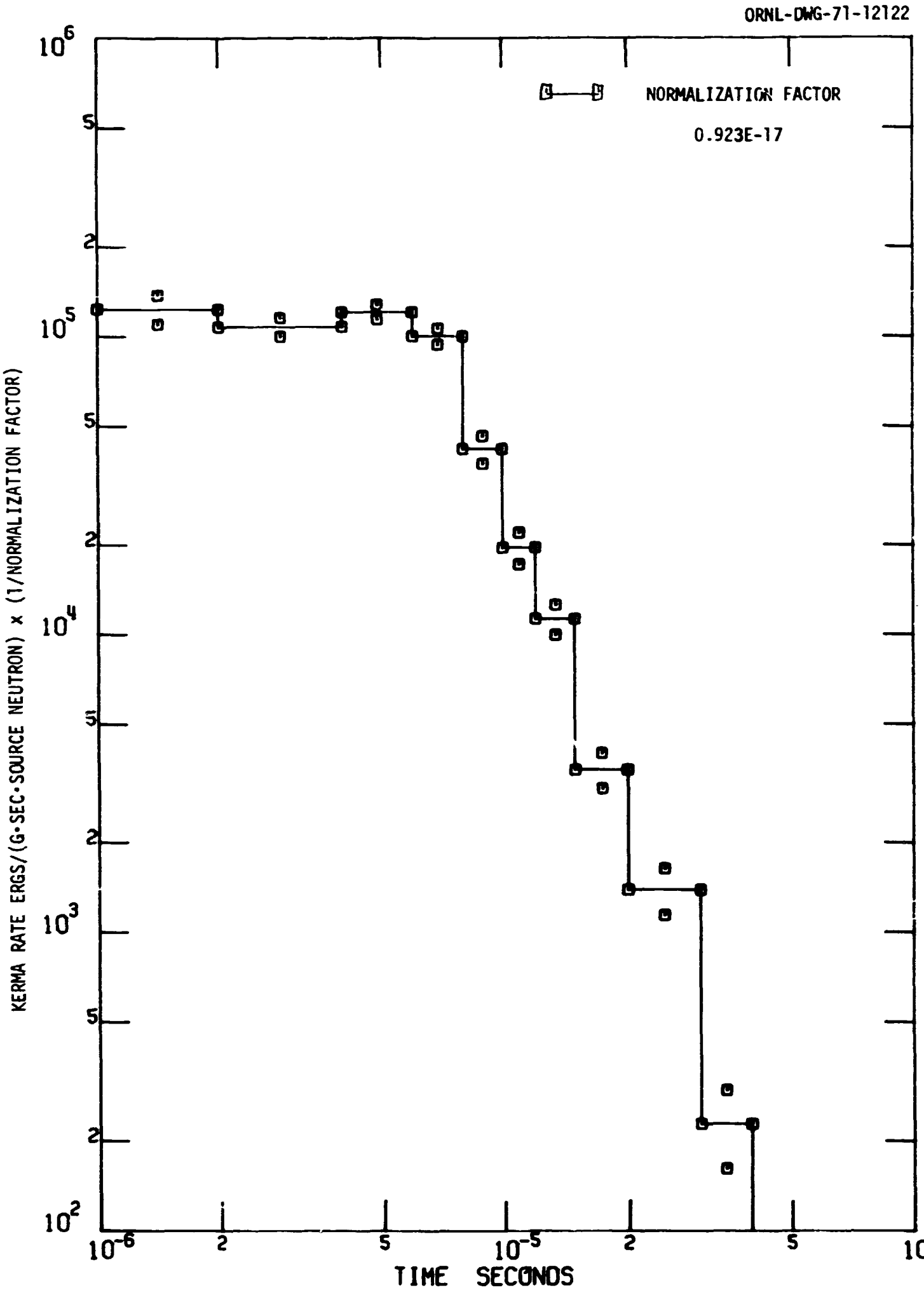

Fig. 46. Time-Dependent Gamma-Ray Air Kerma at a Radius of 300 M for a 12.2-15-MeV Symmetric Source.

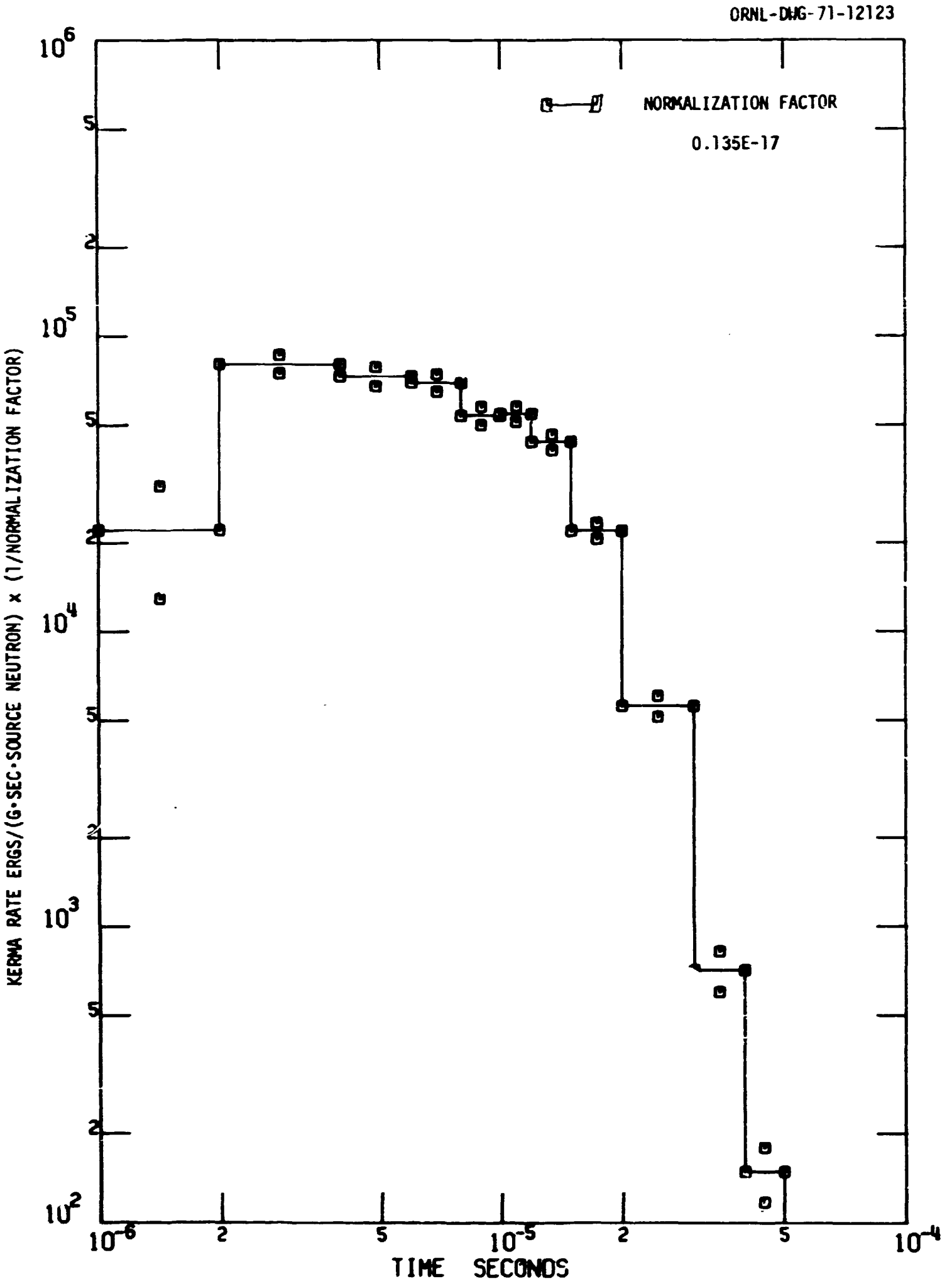

Fig. 47. Time-Dependent Gamma-Ray Air Kerma at a Radius of 600 M for a 12.2-15-MeV Symmetric Source.

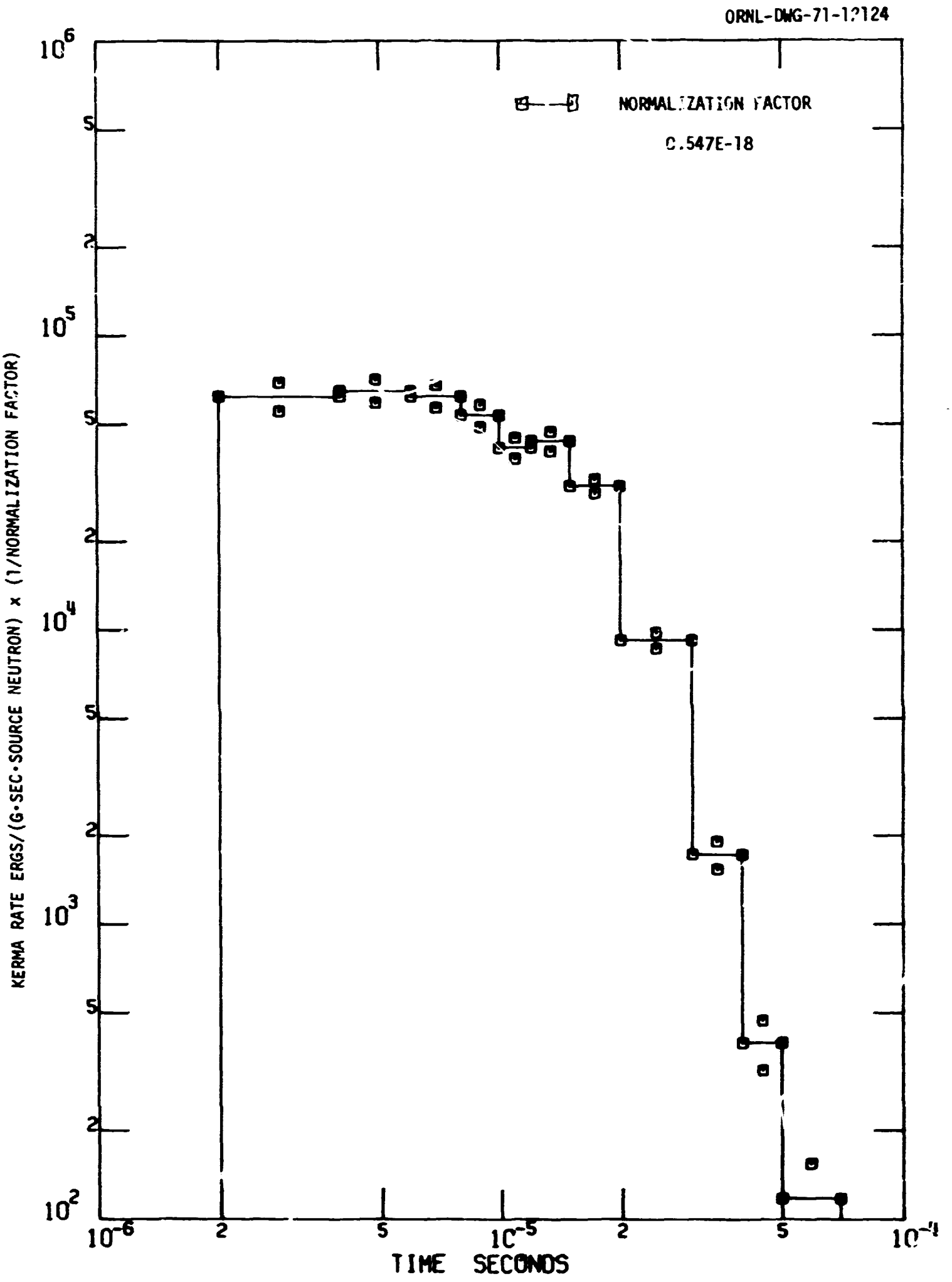

Fig. 48. Time-Dependent Gamma-Ray Air Kerma at a Radius of 800 M for a 12.2-15-MeV Symmetric Source.

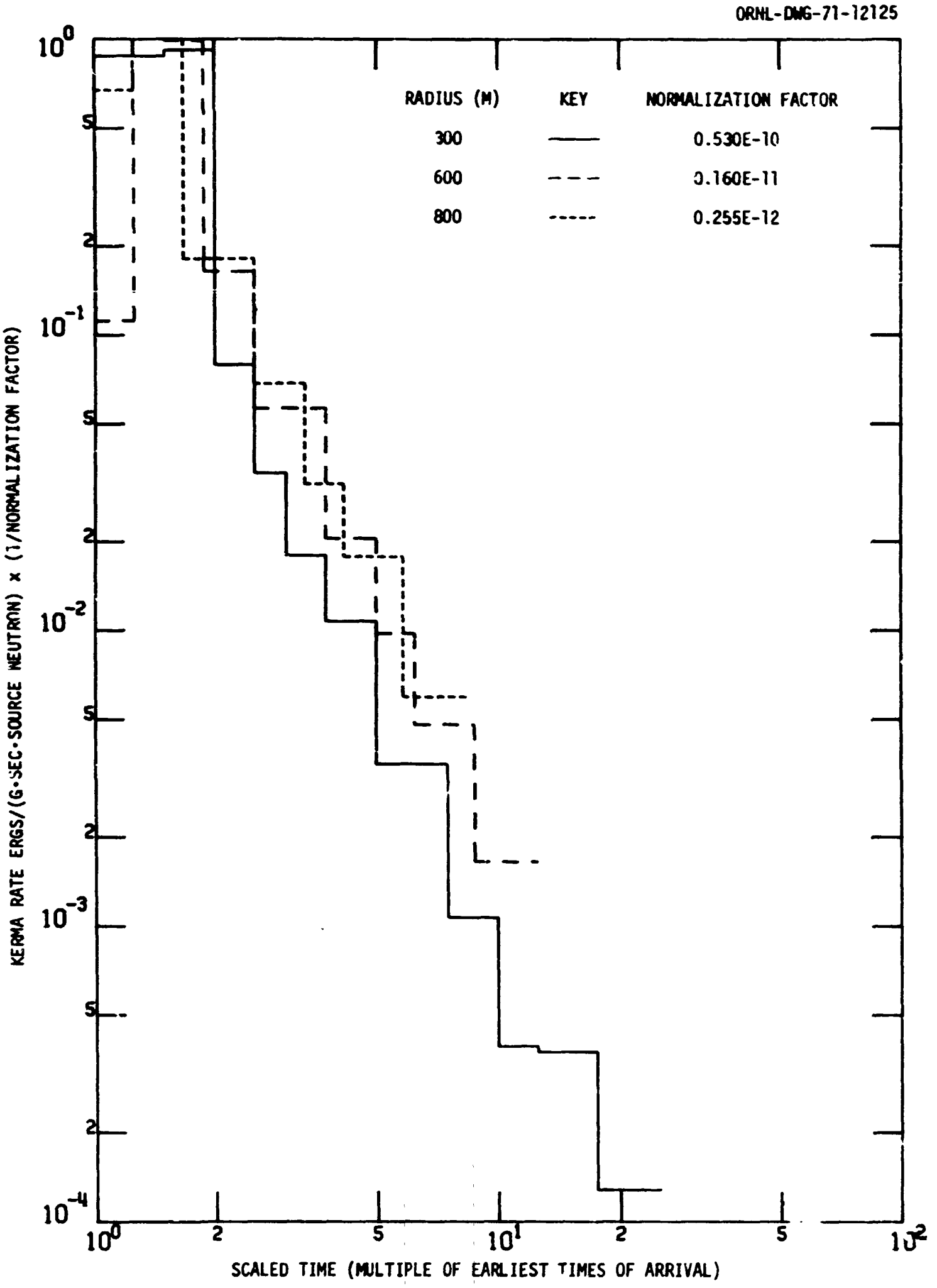

Fig. 49. Time-Dependent Neutron Air Kerma (Scaled) in the Source Direction for a 12.2-15-MeV Beam Source.

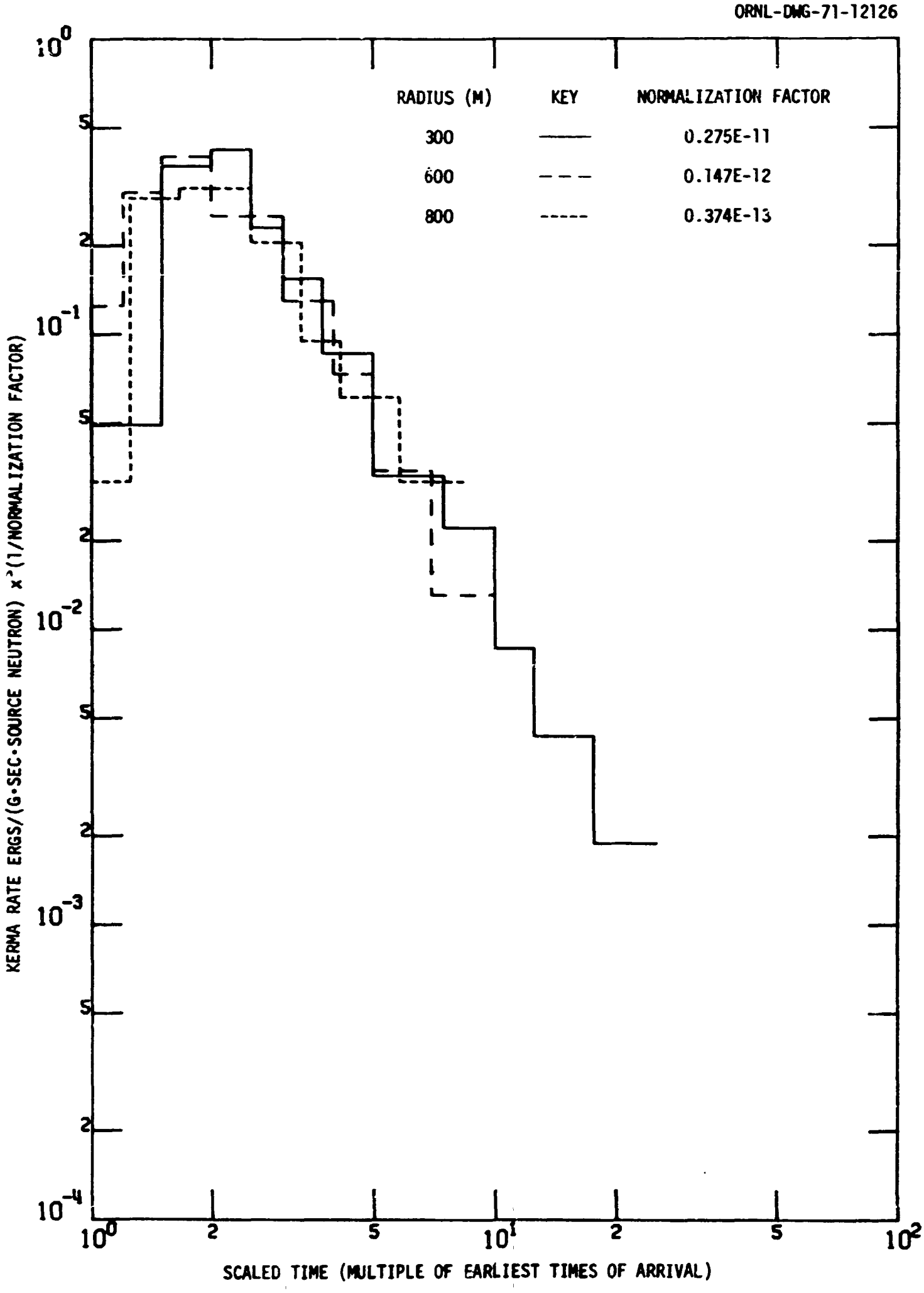

Fig. 50. Time-Dependent Neutron Air Kerma (Scaled) in a Direction at 50 deg from the Source Direction for a 12.2-15-MeV Beam Source.

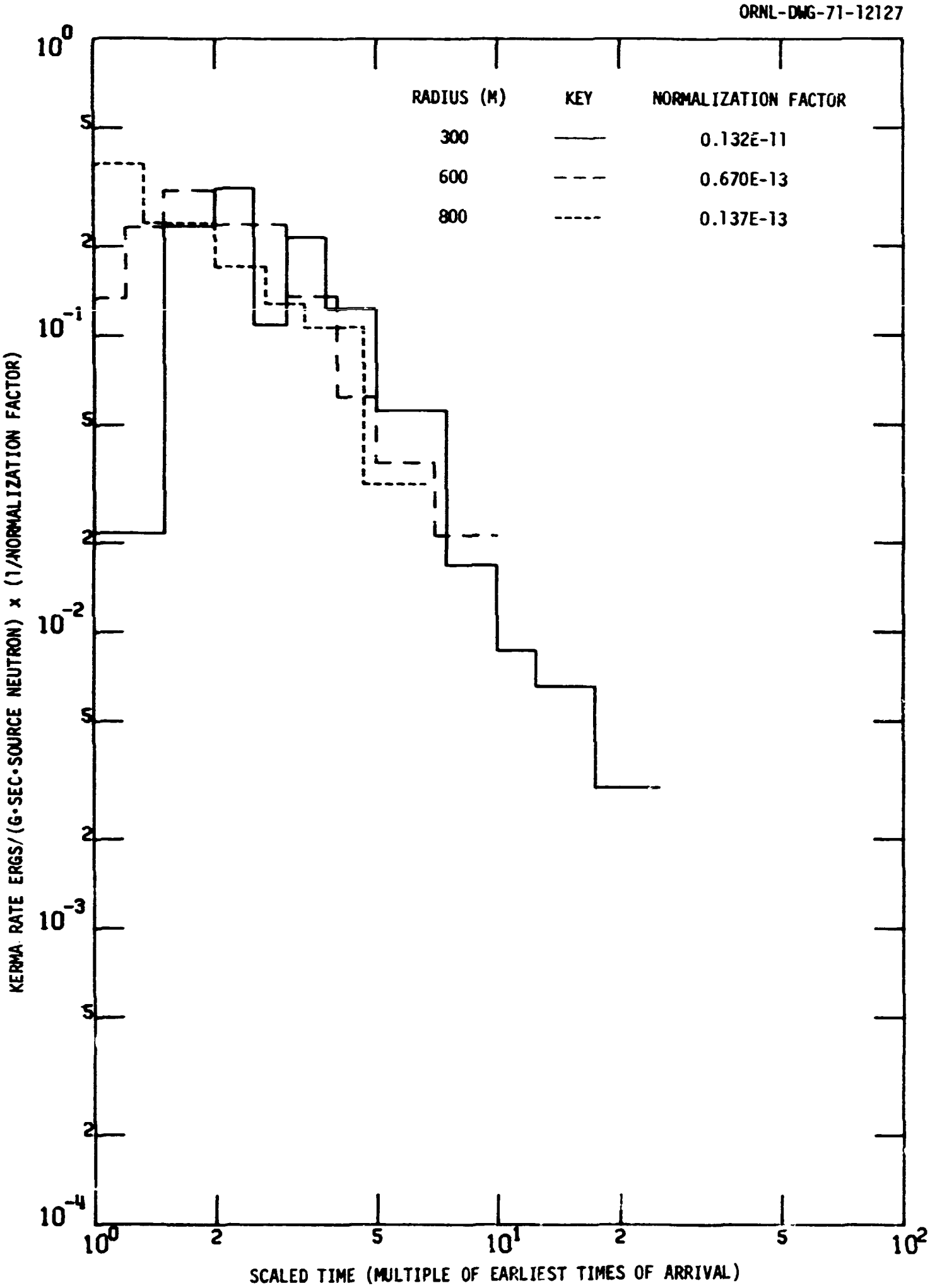

Fig. 51. Time-Dependent Neutron Air Kerma (Scaled) in a Direction Normal to the Source Direction for a 12.2-15-MeV Beam Source.

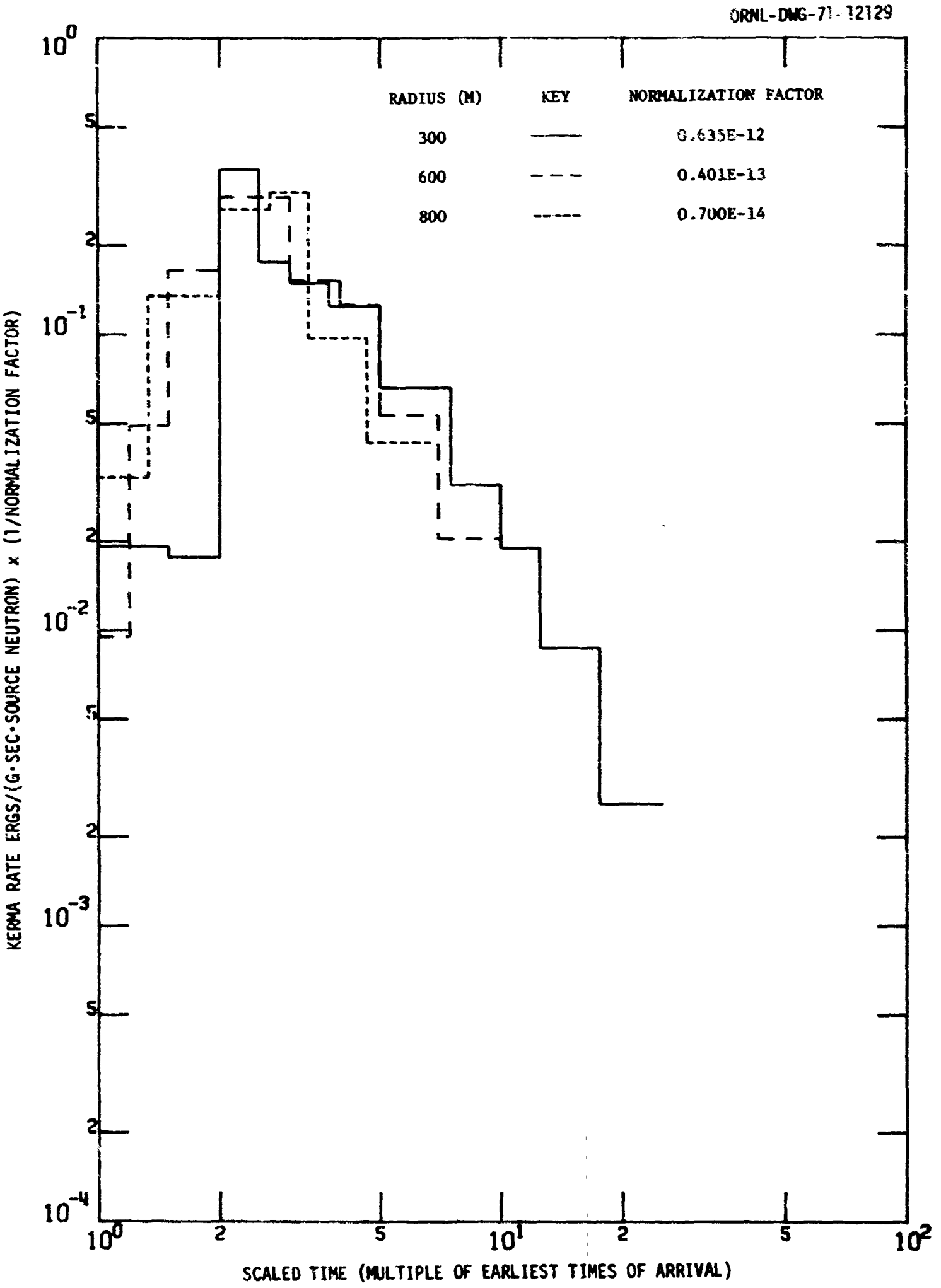

Fig. 52. Time-Dependent Neutron Air Kerma (Scaled) in a Direction at 150 deg from the Source Direction for a 12.2-15-MeV Beam Source.

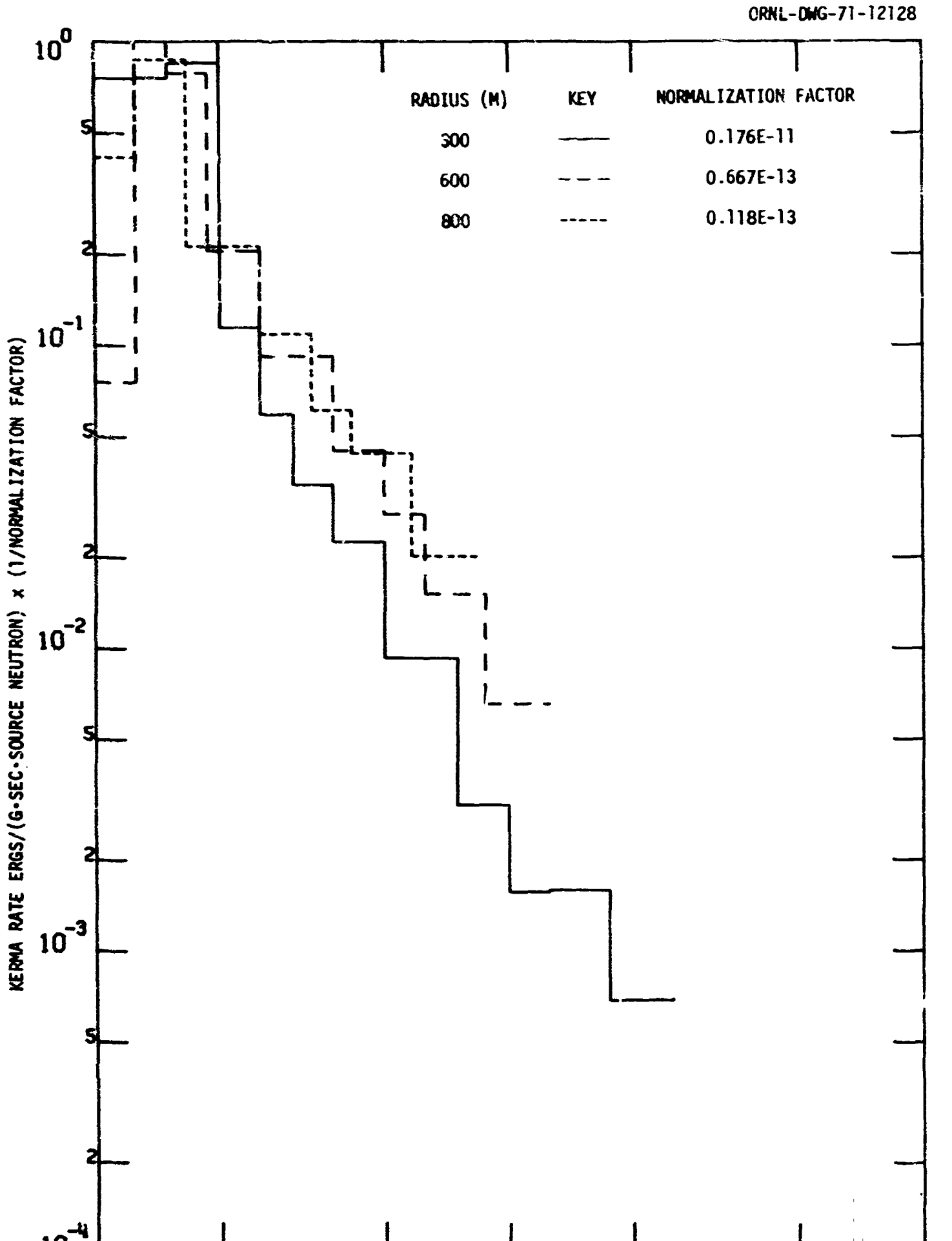

Fig. 53. Time-Dependent Neutron Silicon Kerma (Scaled) in the Source Direction for a 12.2-15-MeV Beam Source.

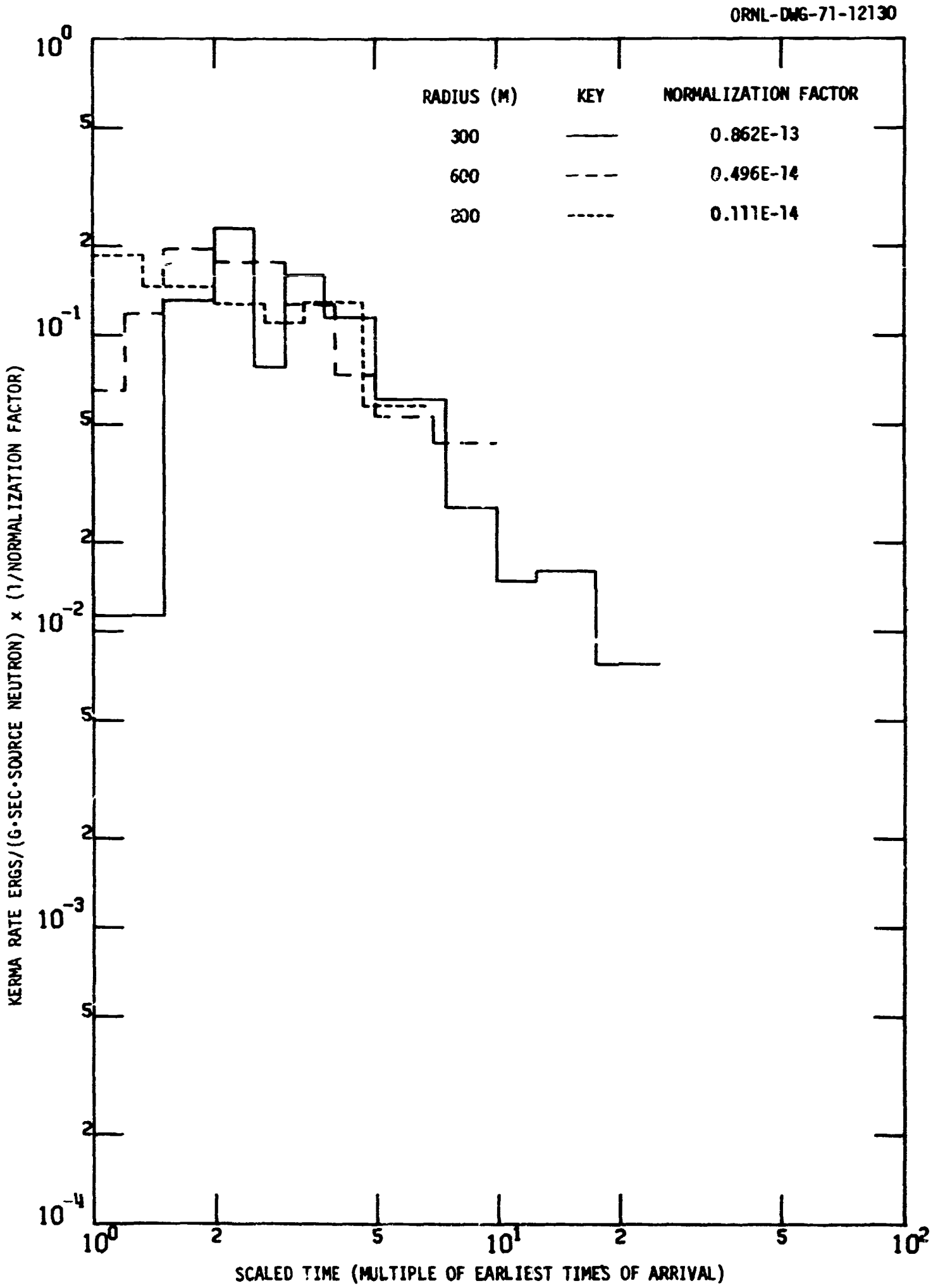

Fig. 54. Time-Dependent Neutron Silicon Kerma (Scaled) in a Direction Normal to the Source Directions for a 12.2-15-MeV Beam Source.

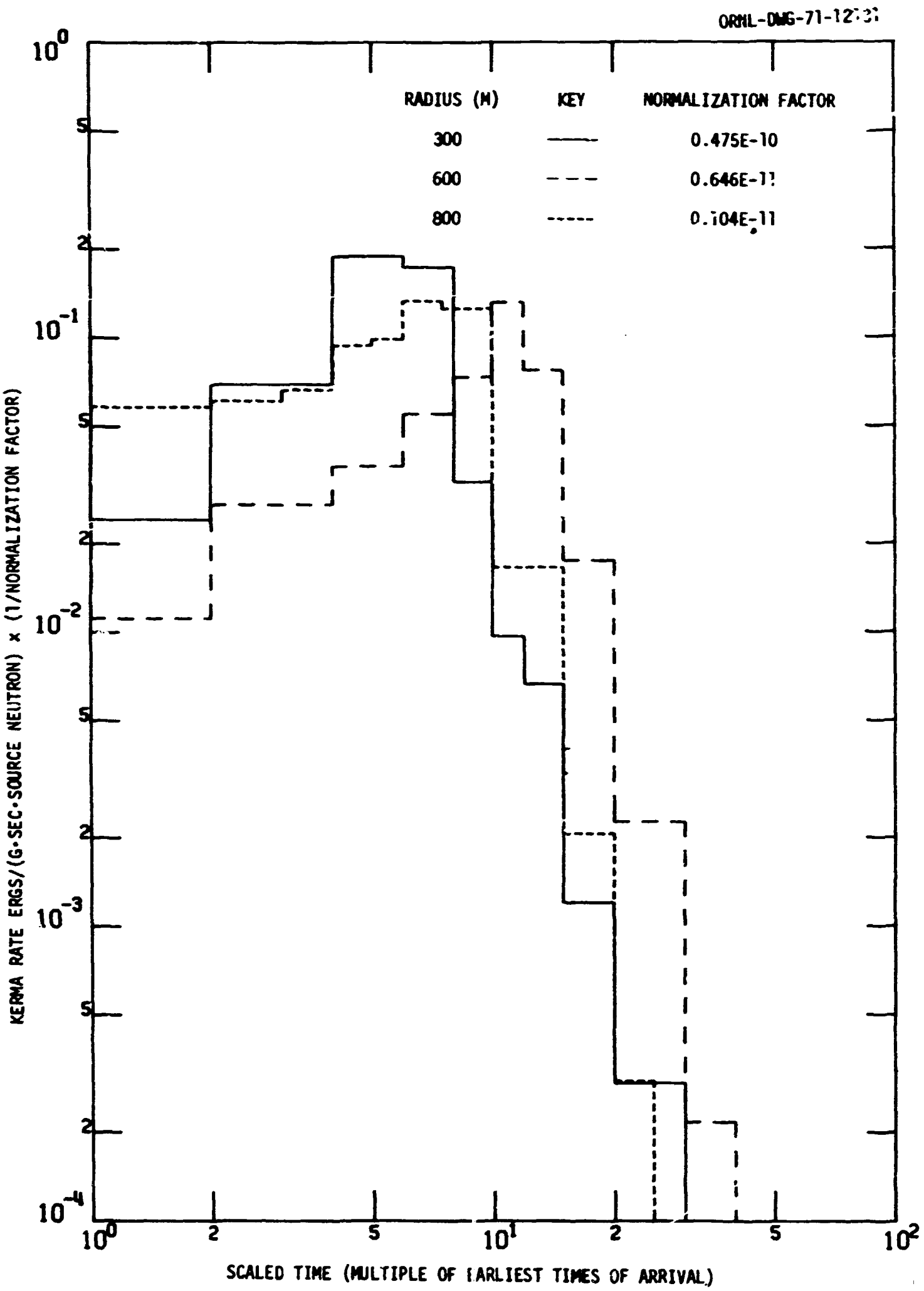

Fig. 55. Time-Dependent Gamma-Ray Air Kerma (Scaled) in the Source Direction for a 12.2-15-MeV Beam Source.

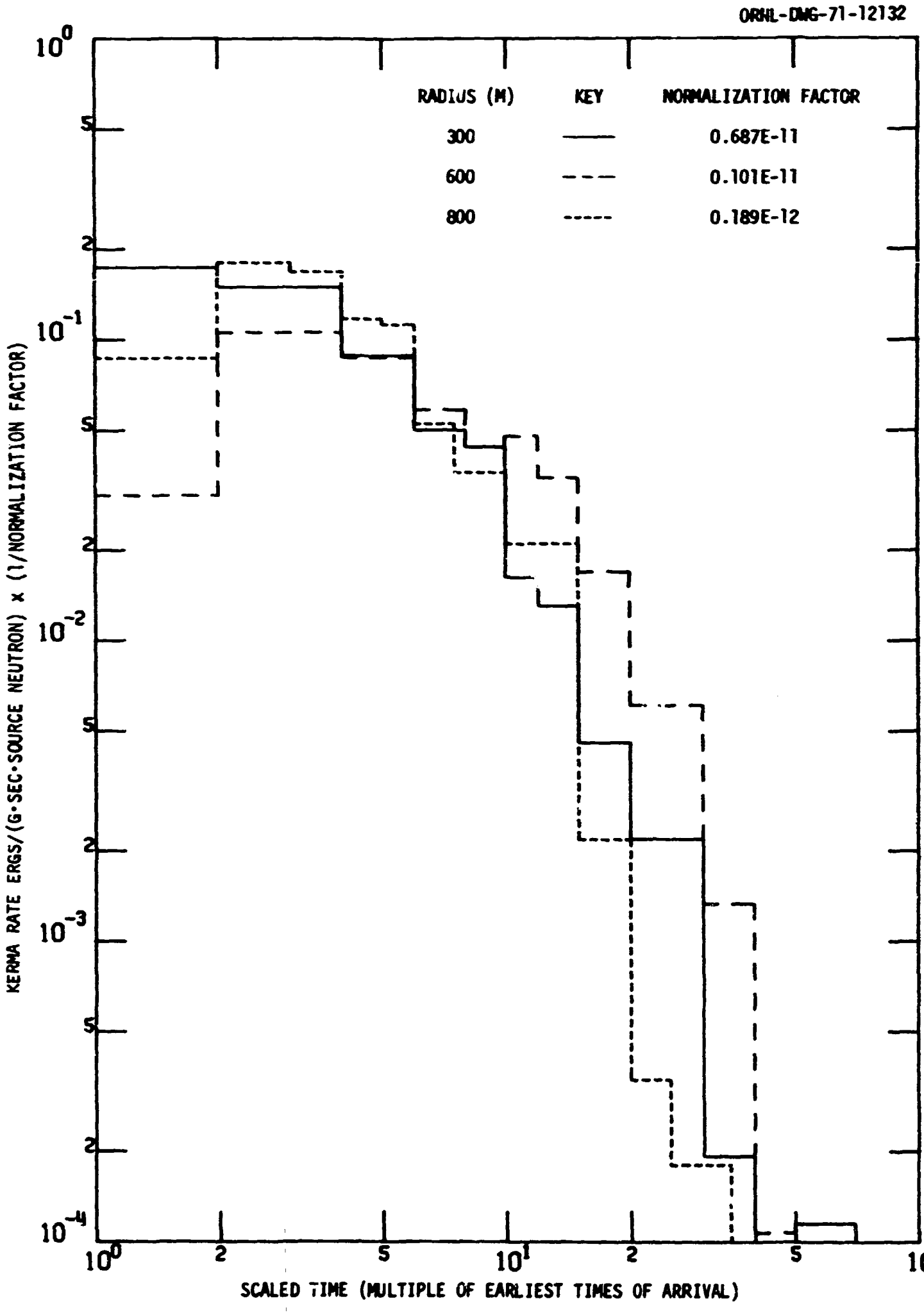

Fig. 56. Time-Dependent Gamma-Ray Air Kerma (Scaled) in a Direction Normal to the Source Direction for a 12.2-15-MeV Beam Source.

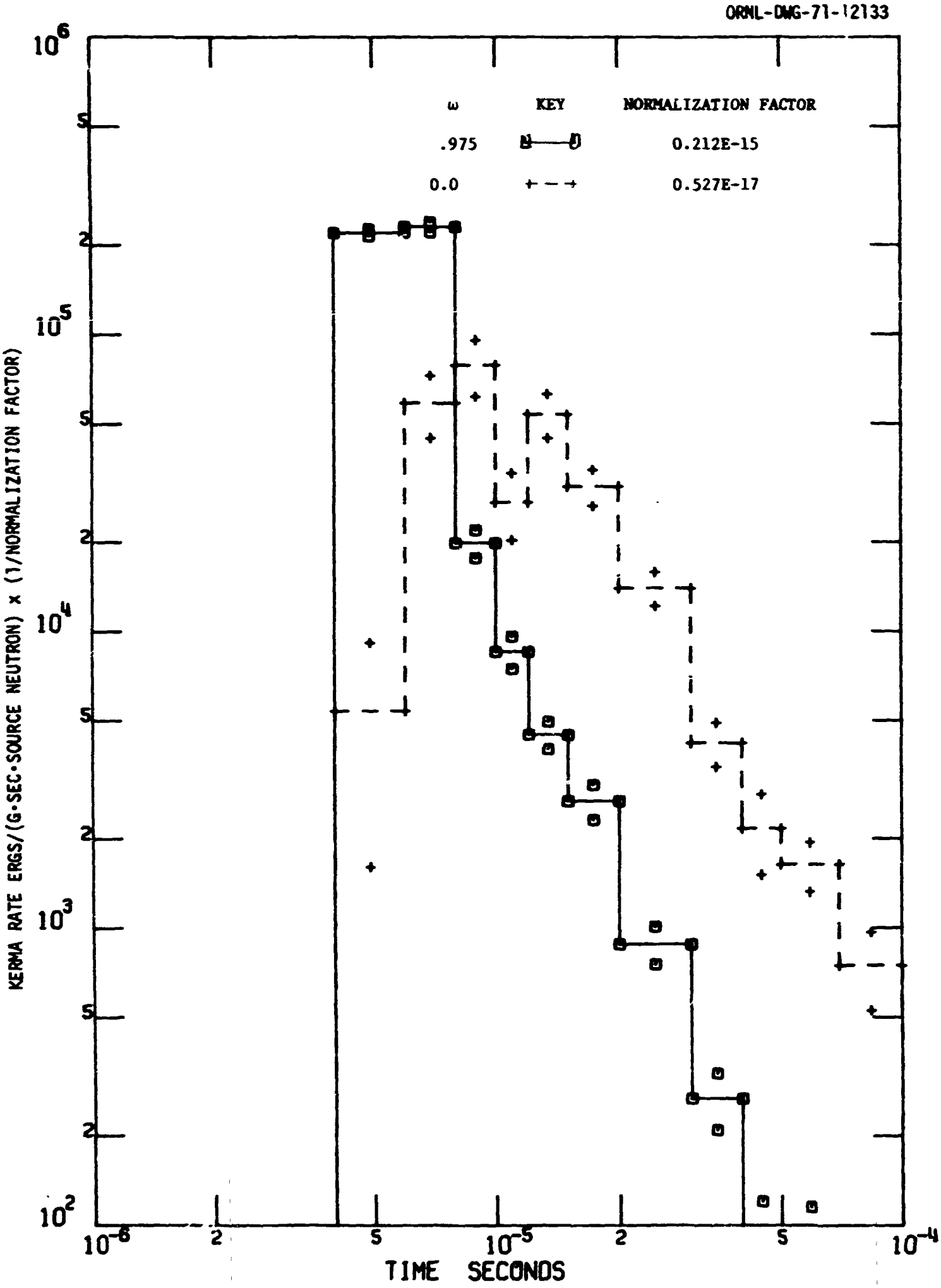

Fig. 57. Time-Dependent Neutron Air Kerma at a Radius of 300 M in the Directions Both Normal to and the Same as the Source Direction for a 12.2–15-MeV Beam Source.

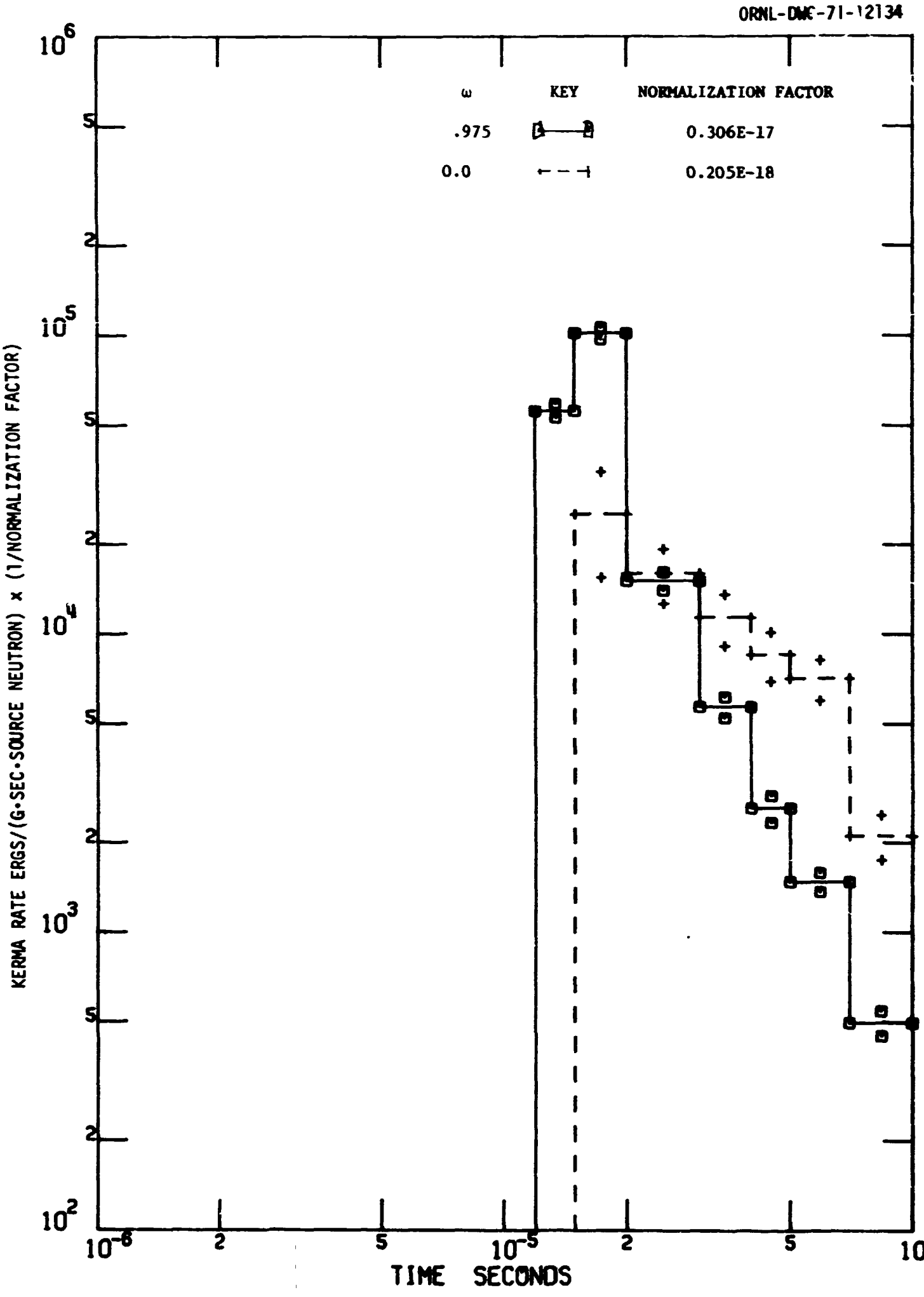

Fig. 58. Time-Dependent Neutron Air Kerma at a Radius of 800 M in the Directions Both Normal to and the Same as the Source Direction for a 12.2-15-MeV Beam Source.

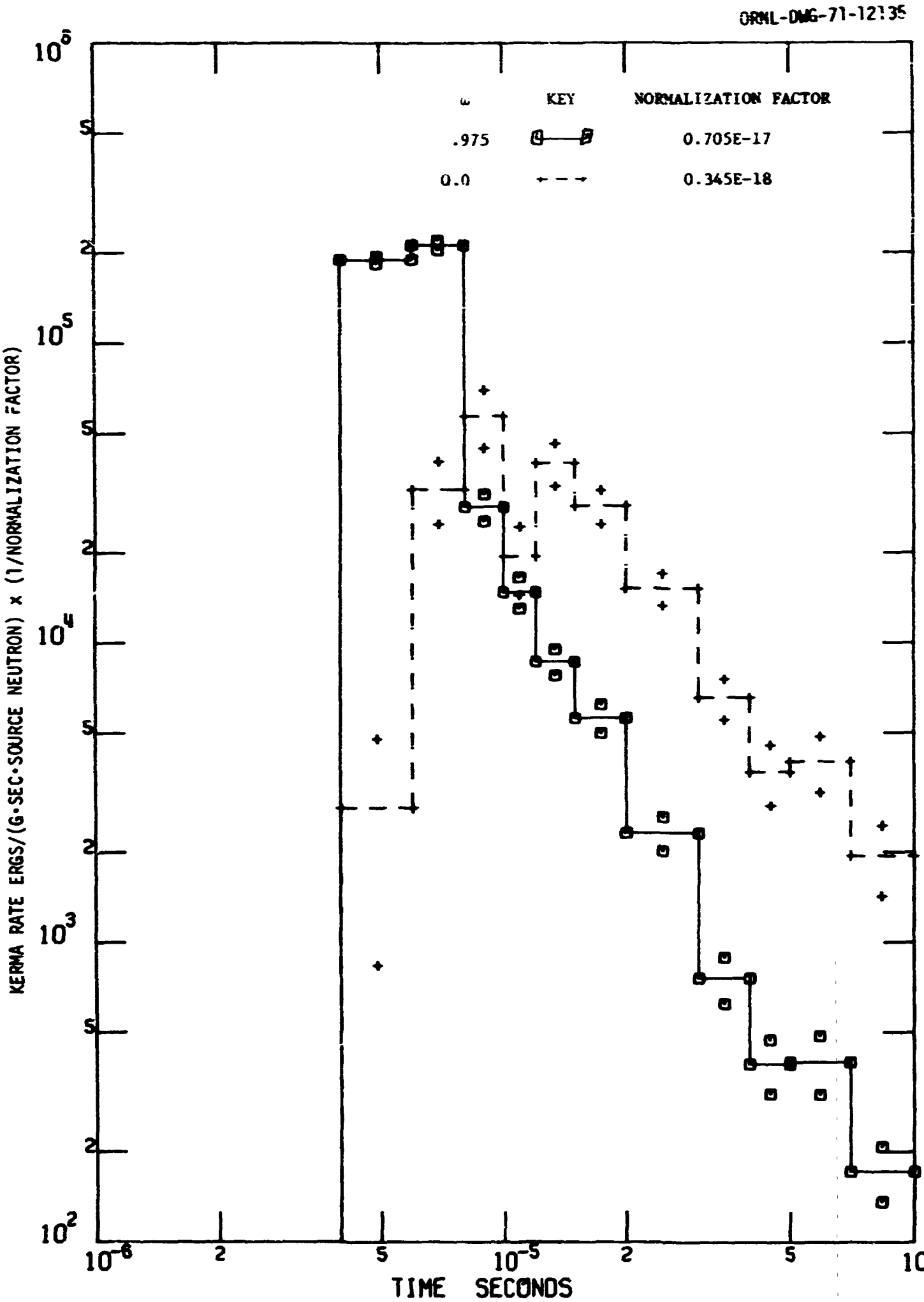

Fig. 59. Time-Dependent Neutron Silicon Kerma at a Radius of 300 M in the Directions Both Normal to and the Same as the Source Direction for a 12.2-15-MeV Beam Source.

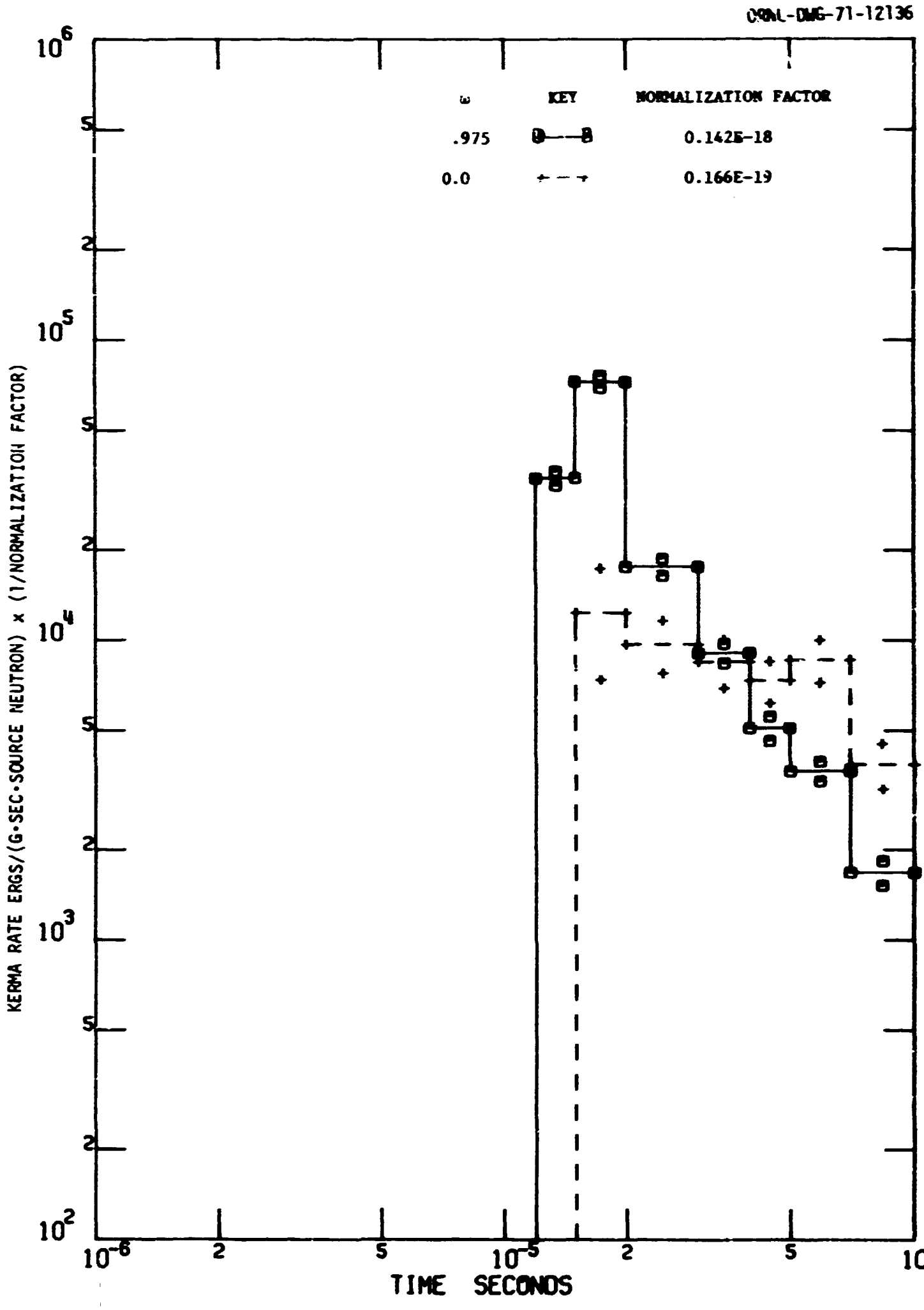

Fig. 60. Time-Dependent Neutron Silicon Kerma at a Radius of 800 M in the Directions Both Normal to and the Same as the Source Direction for a 12.2-15-MeV Beam Source.

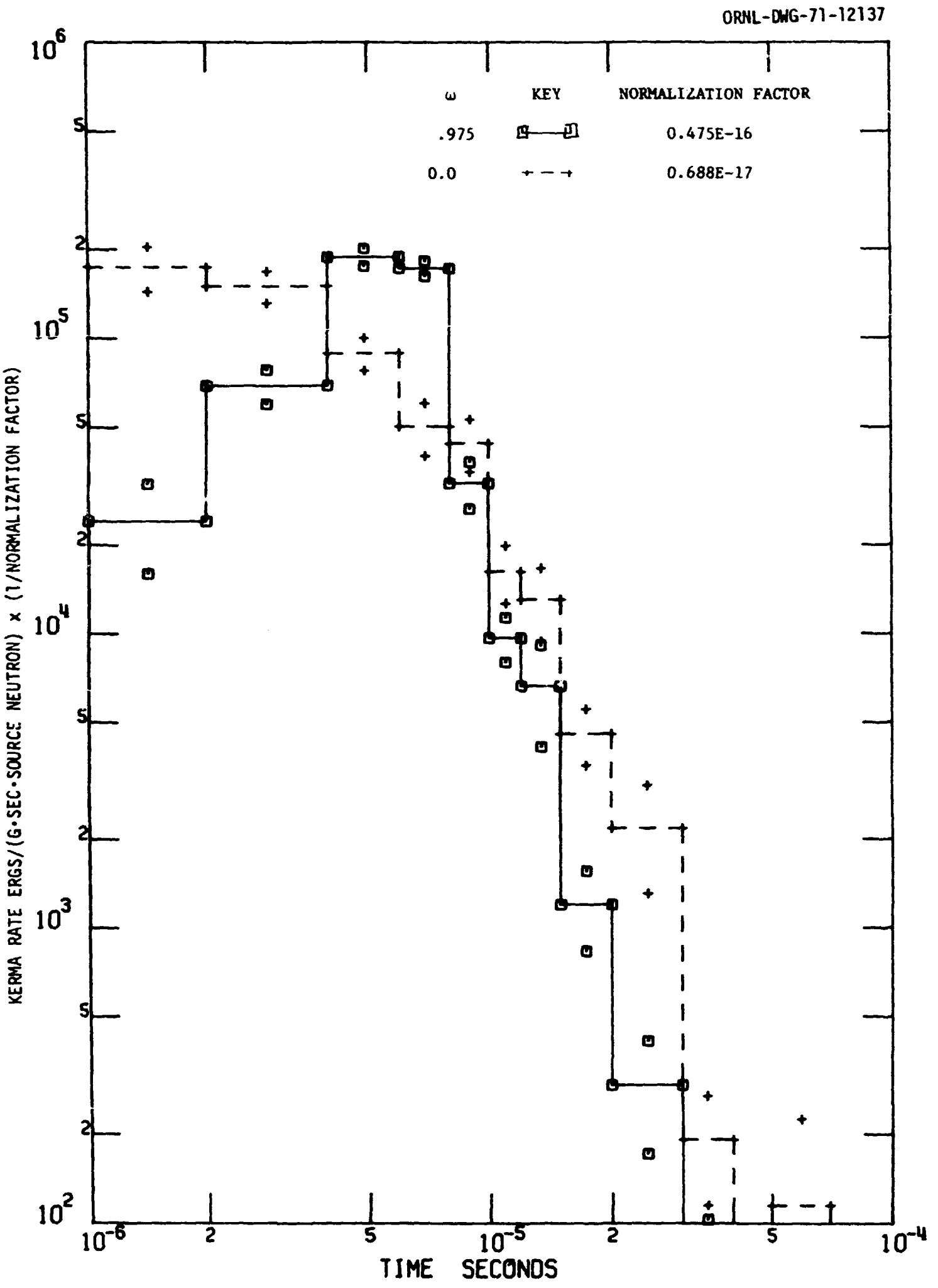

Fig. 61. Time-Dependent Gamma-Ray Air Kerma at a Radius of 300 M in the Directions Both Normal to and the Same as the Source Direction for a 12.2-15-MeV Beam Source.

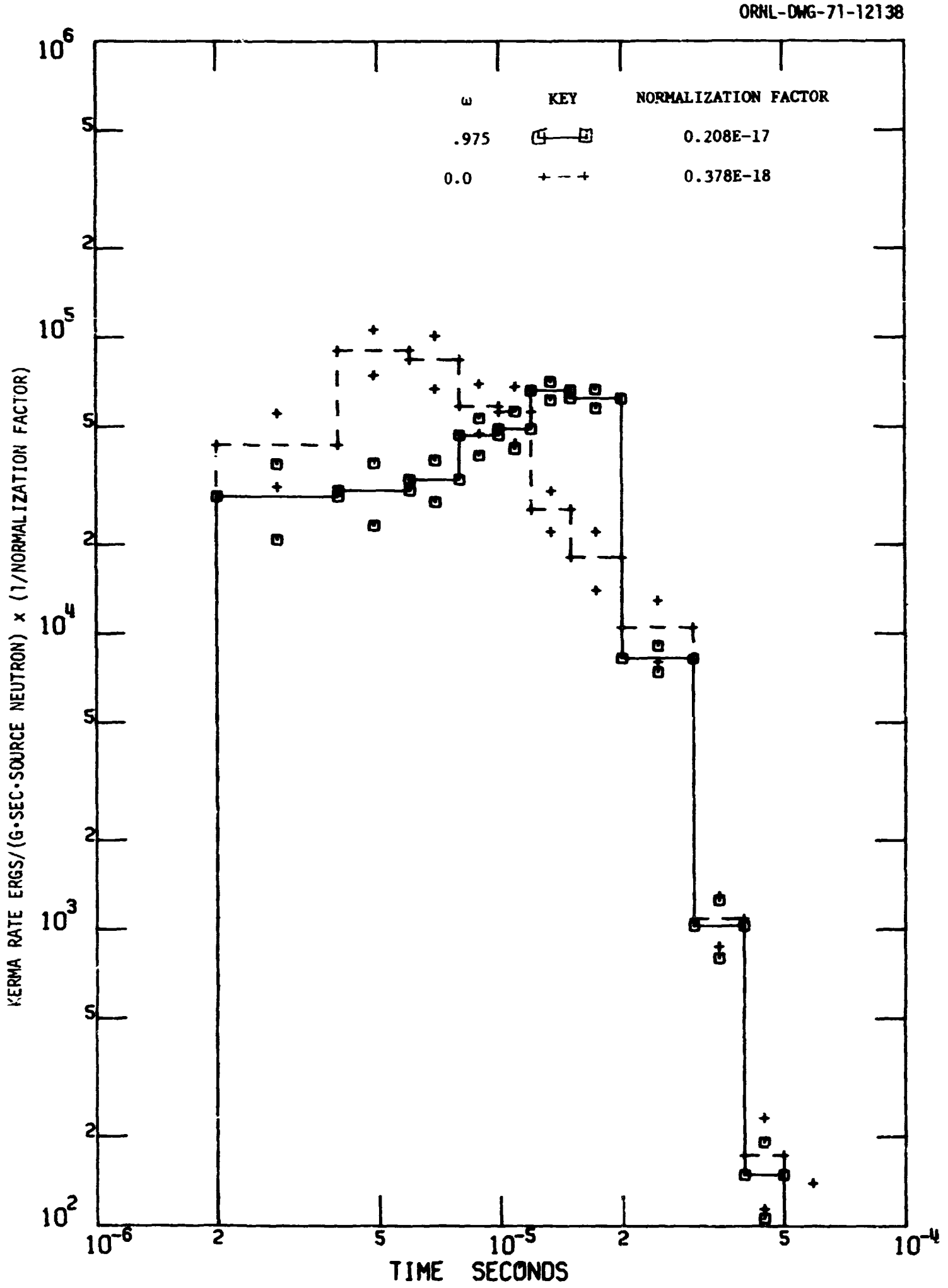

Fig. 62. Time-Dependent Gamma-Ray Air Kerma at a Radius of 800 M in the Directions Both Normal to and the Same as the Source Direction for a 12.2-15 MeV-Beam Source.

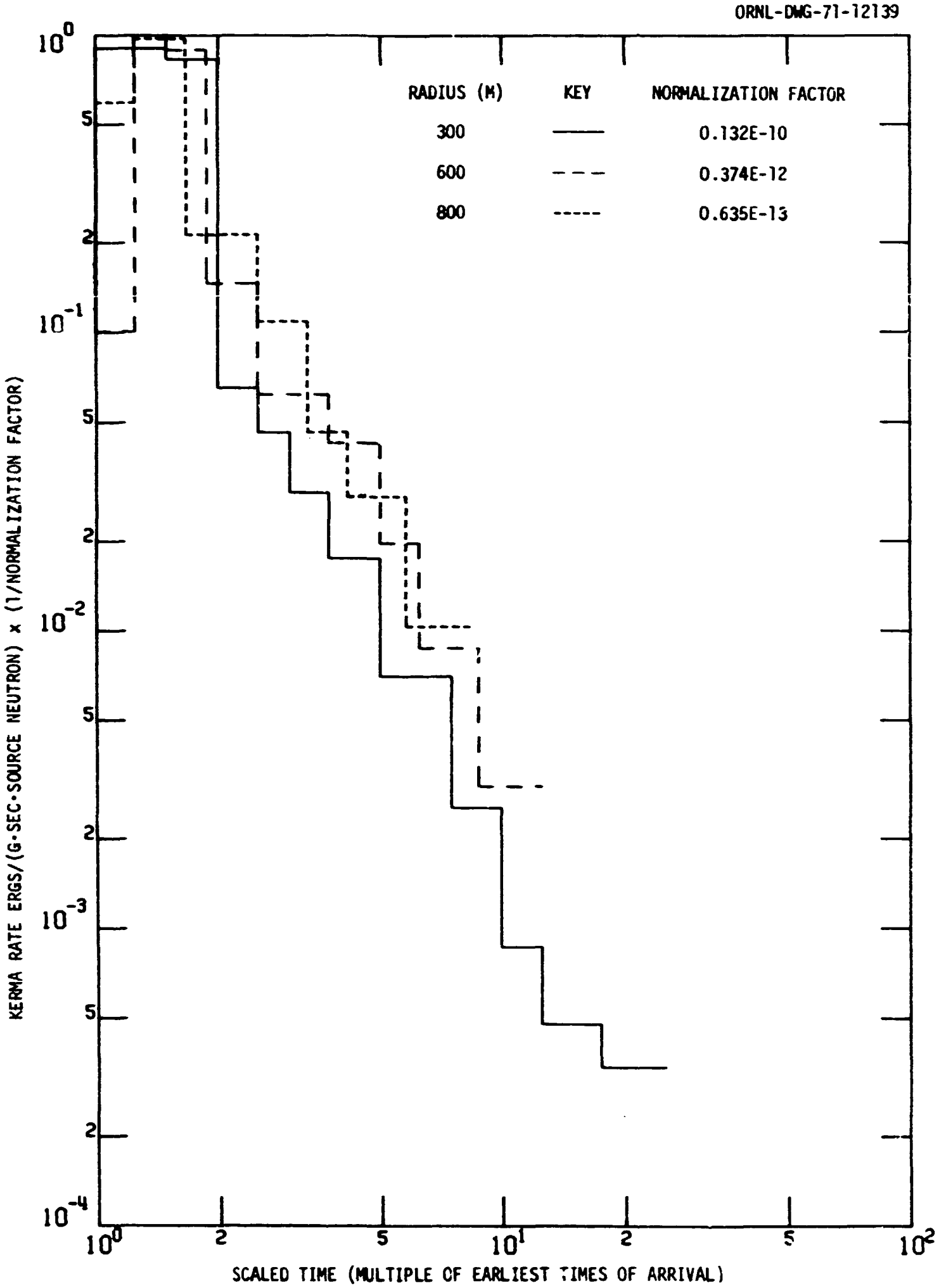

Fig. 63. Time-Dependent Neutron Air Kerma (Scaled) in the Source Plane for a 12.2-15-MeV Pancake Source.

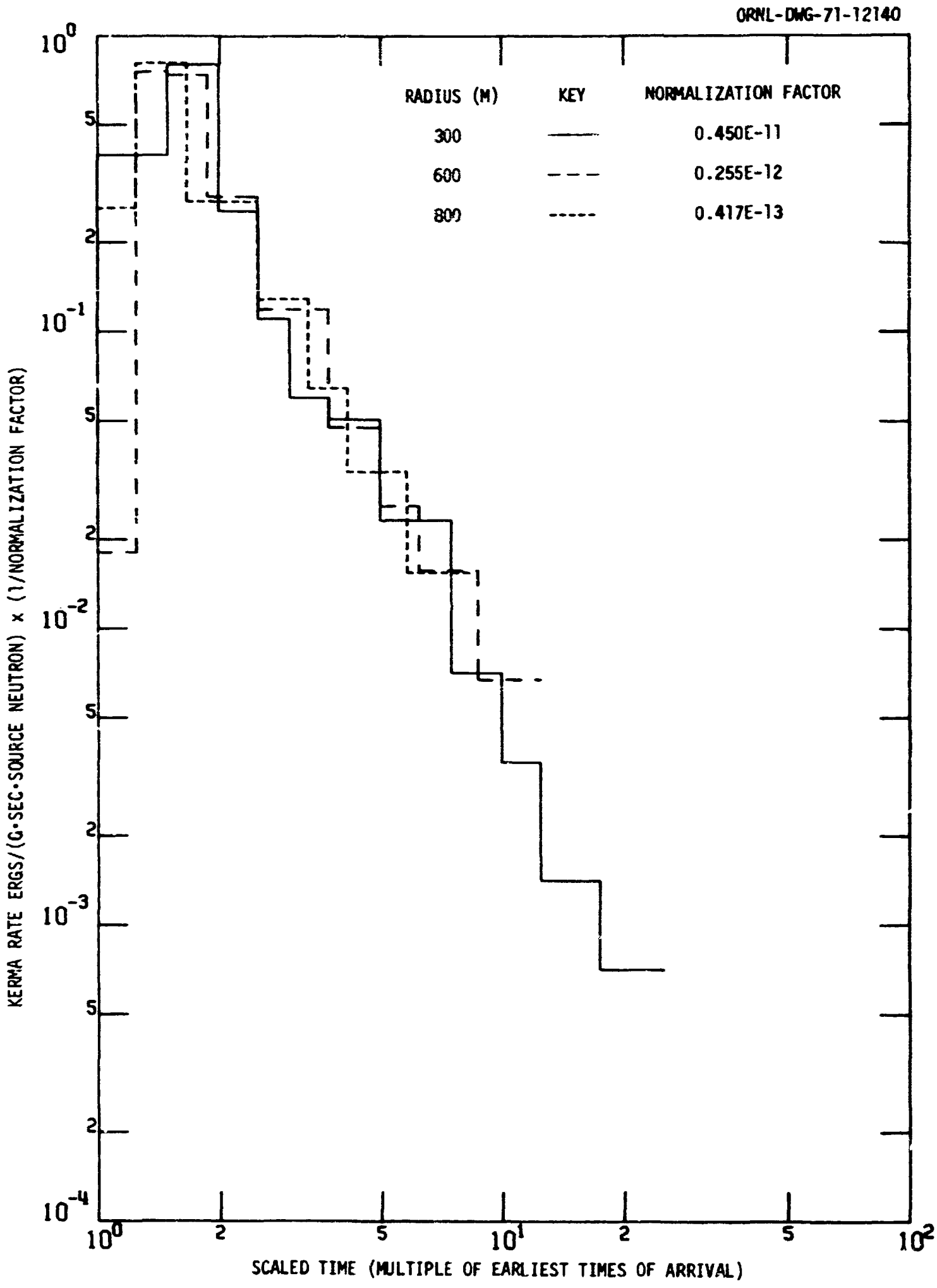

Fig. 64. Time-Dependent Neutron Air Kerma (Scaled) in the Direction at 10 deg from the Source Plane for a 12.2-15 MeV Pancake Source

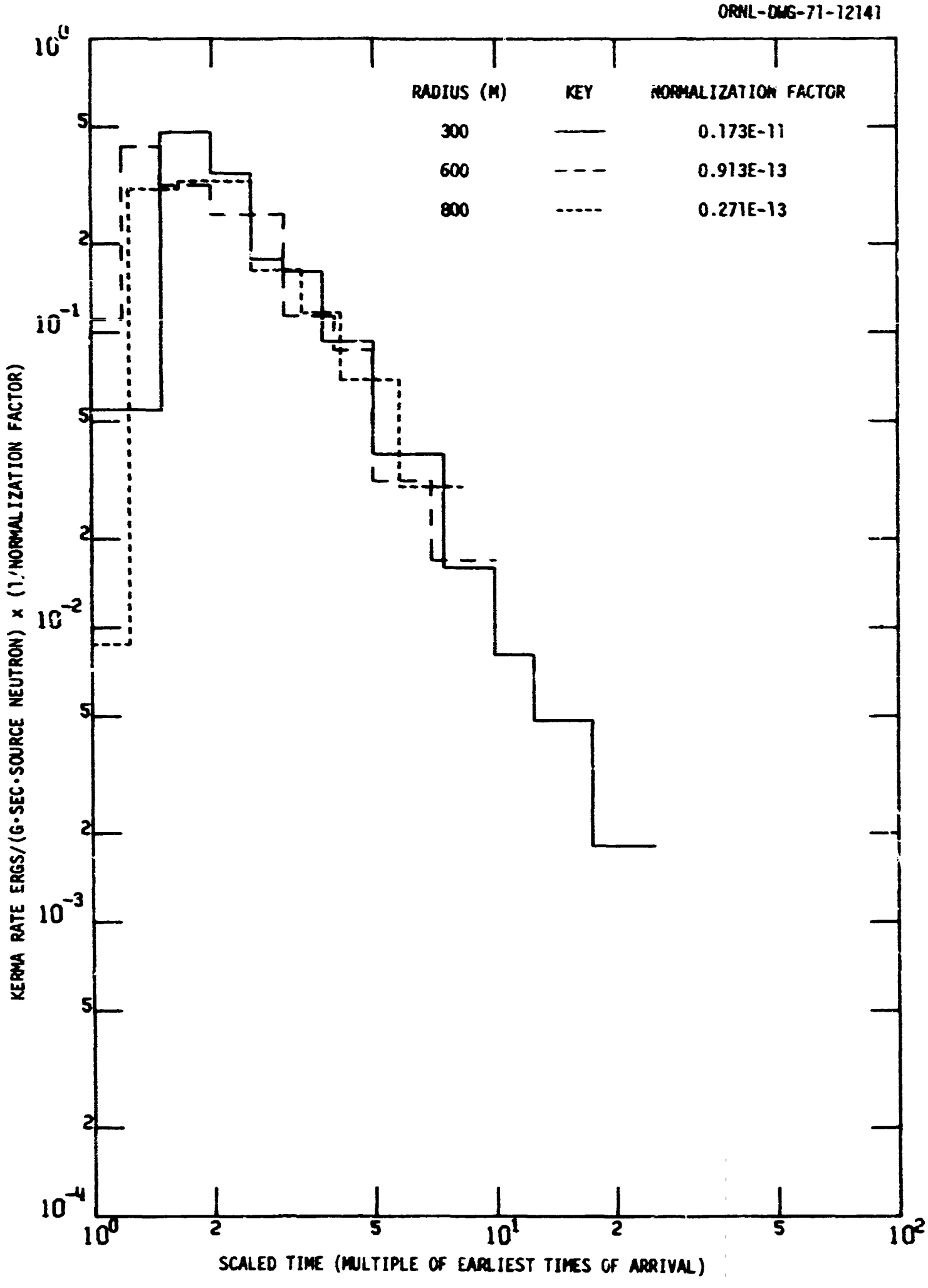

Fig. 65. Time-Dependent Neutron Air Kerma (Scaled) in a Direction at 30 deg from the Source Plane for a 12.2-15-MeV Pancake Source.

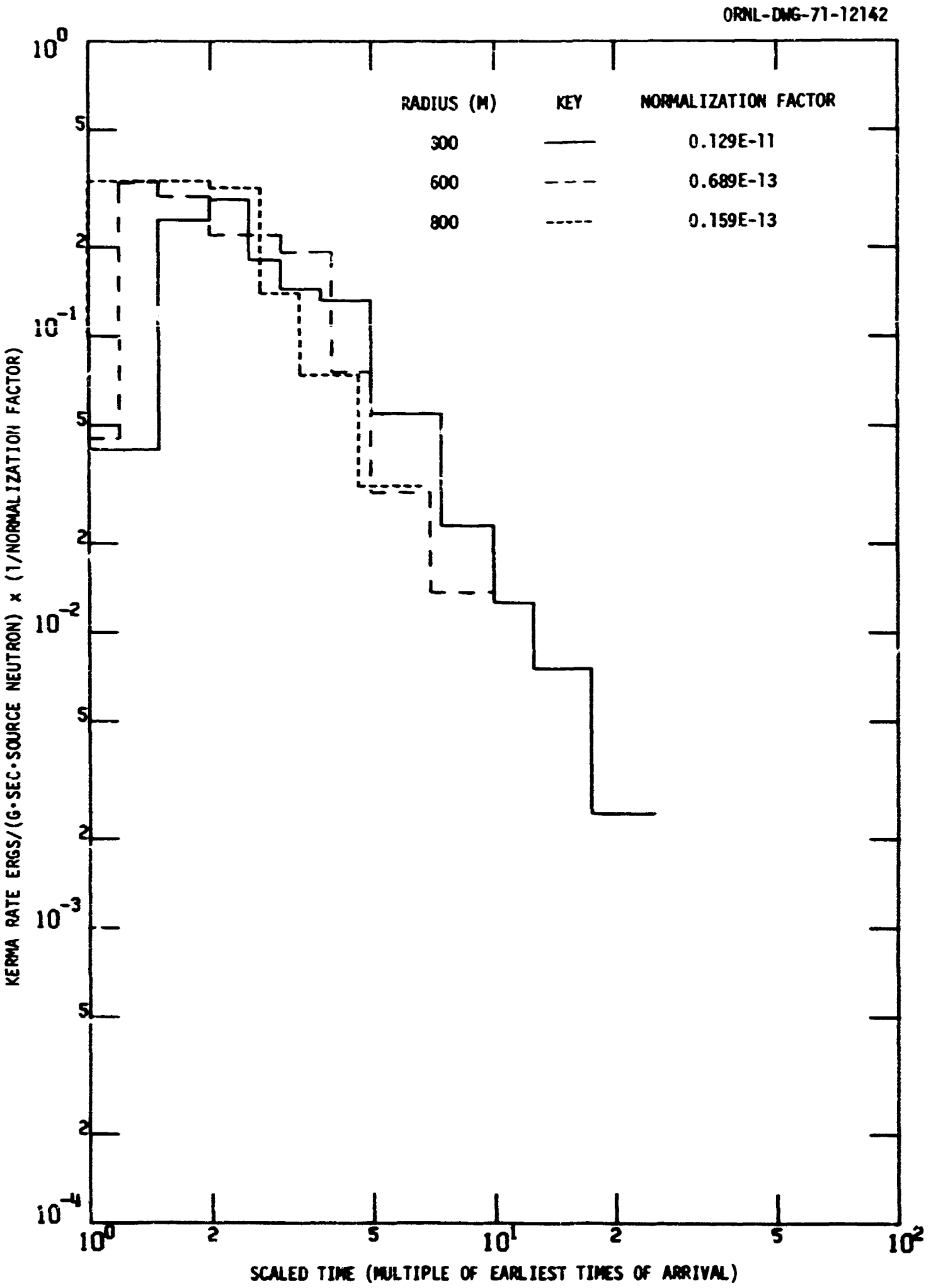

Fig. 66. Time-Dependent Neutron Air Kerma (Scaled) in a Direction at 70 deg from the Source Plane for a 12.2-15-MeV Pancake Source.

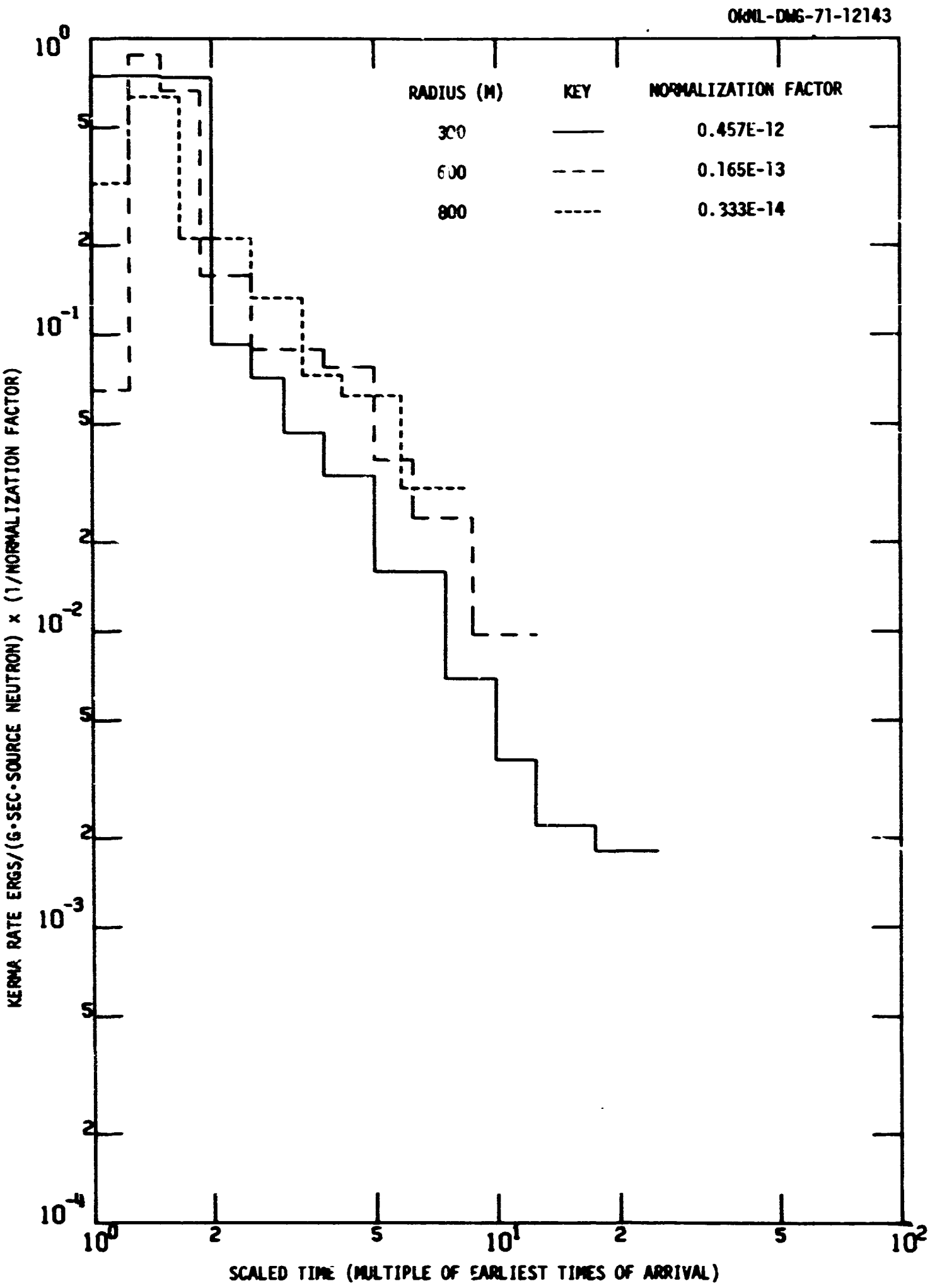

Fig. 67. Time-Dependent Neutron Silicon Kerma (Scaled) in the Source Plane for a 12.2-15-MeV Pancake Source.

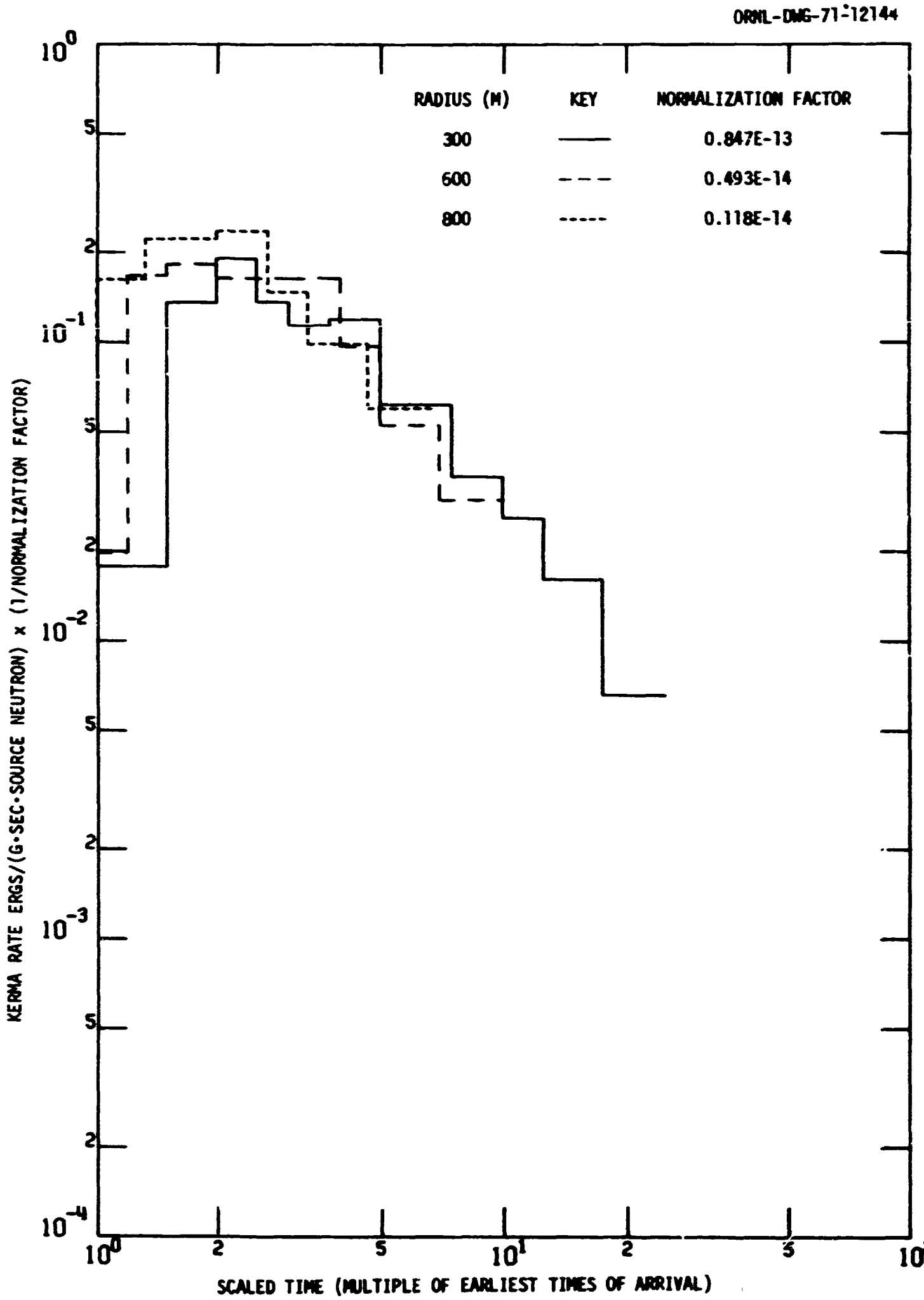

Fig. 68. Time-Dependent Neutron Silicon Kerma (Scaled) in a Direction at 70 deg from the Source Plane for a 12.2-15-MeV Pancake Source.

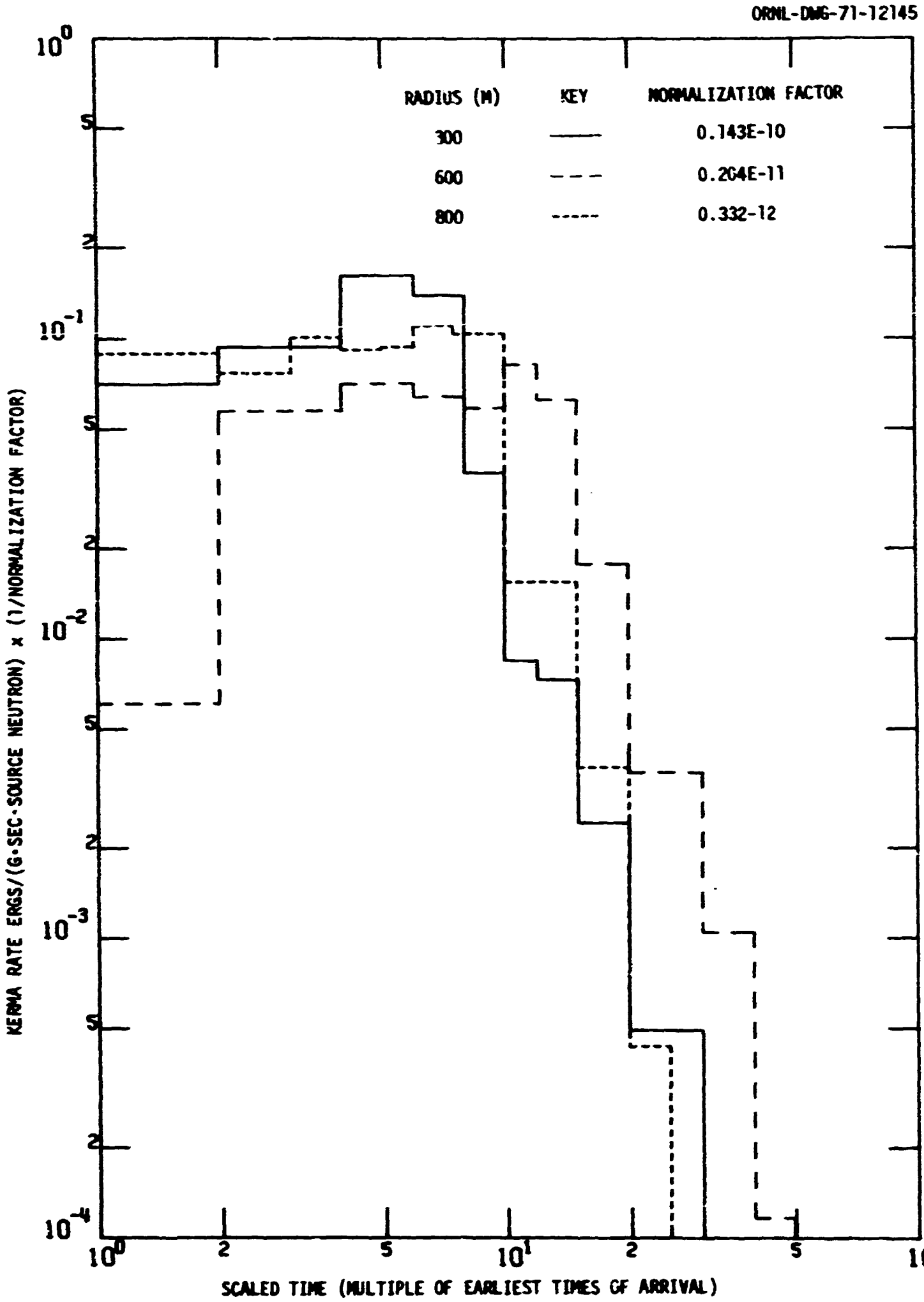

Fig. 69. Time-Dependent Gamma-Ray Air Kerma (Scaled) in the Source Plane for a 12.2-15-MeV Pancake Source.

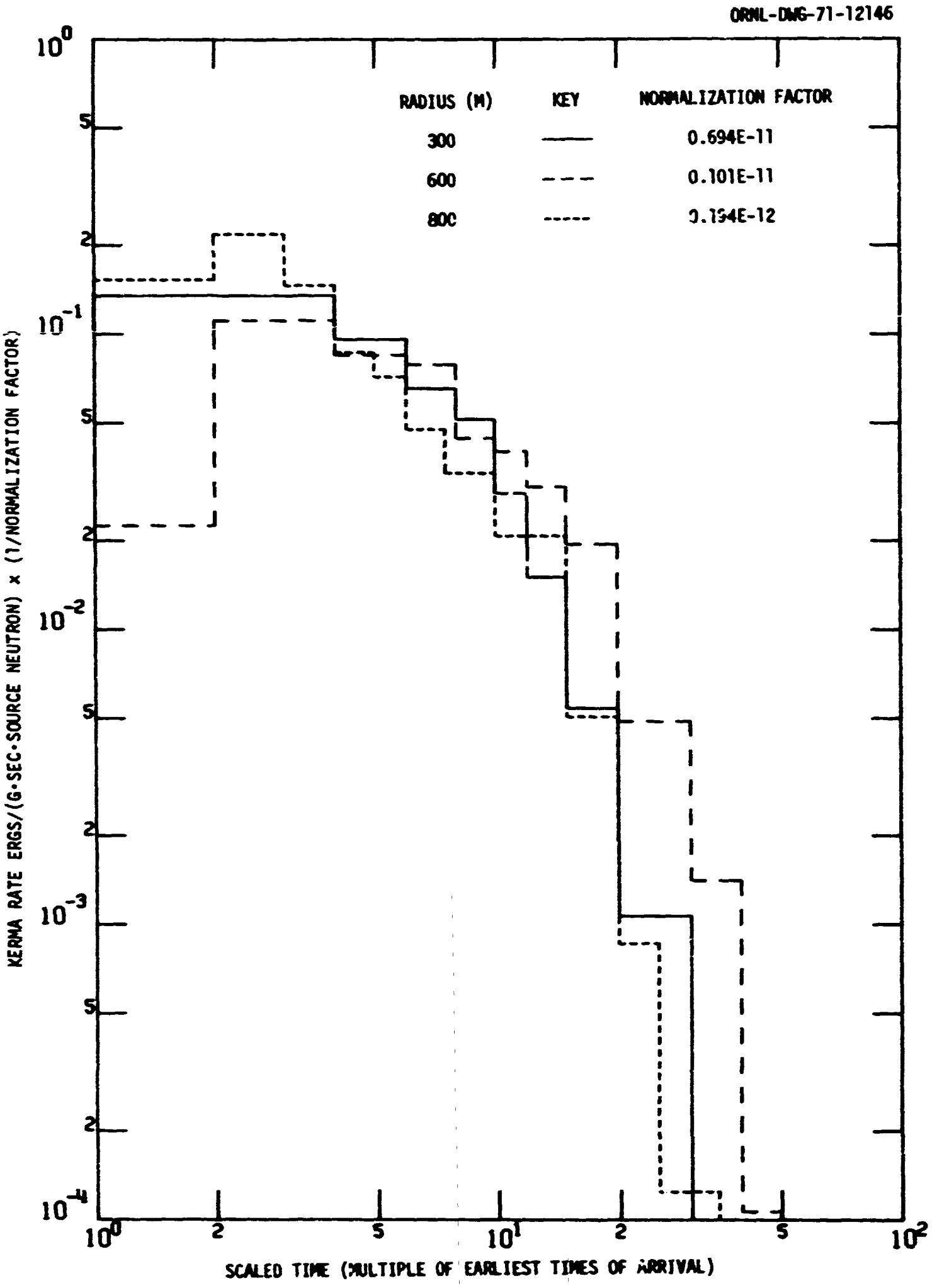

Fig. 70. Time-Dependent Gamma-Ray Air Kerma (Scaled) in a Direction at 70 deg from the Source Plane for a 12.2-15-MeV Pancake Source.

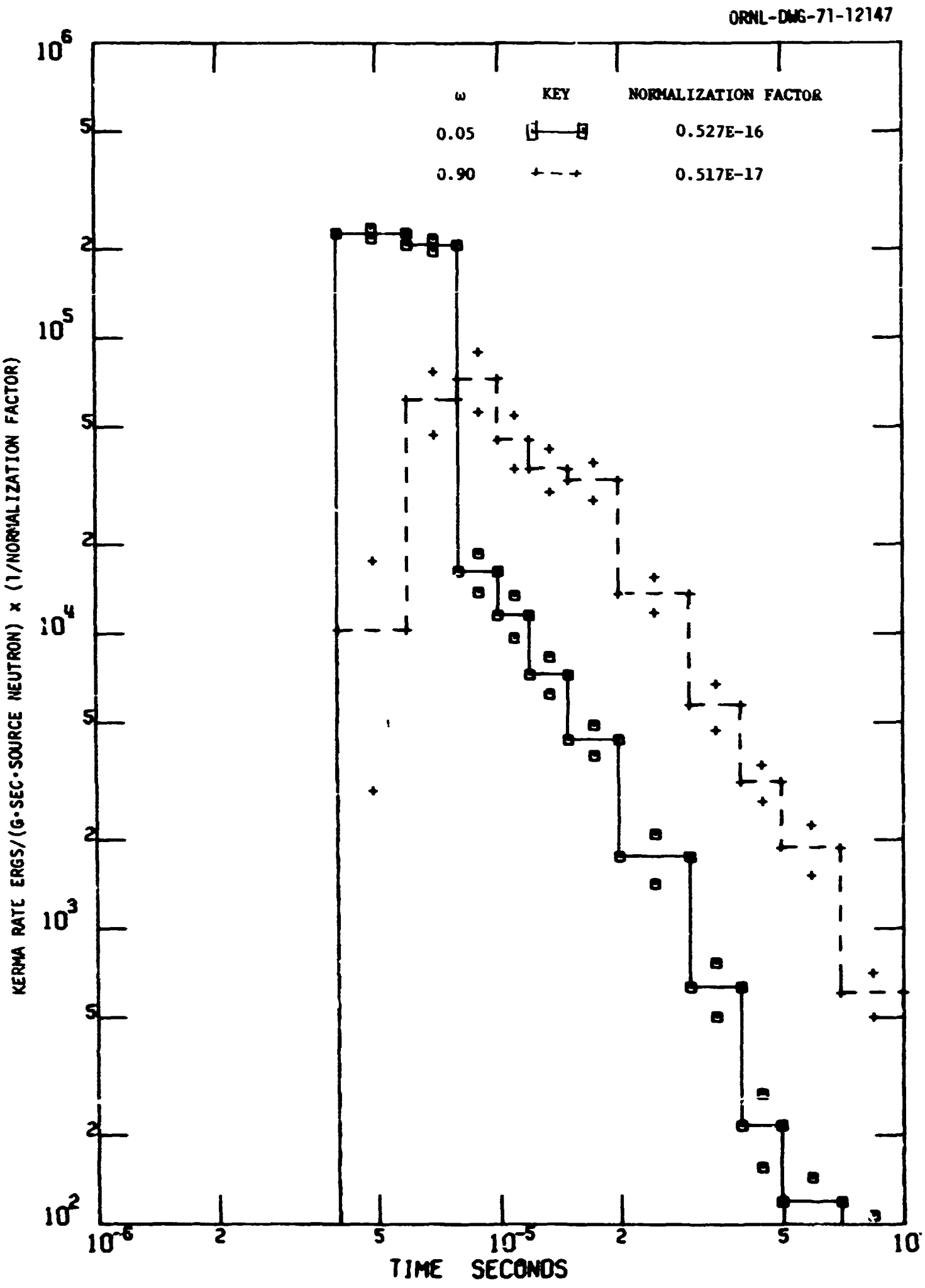

Fig. 71. Time-Dependent Neutron Air Kerma at a Radius of 300 M Both in the Source and at 70 deg from the Source Plane for a 12.2-15-MeV Pancake Source.

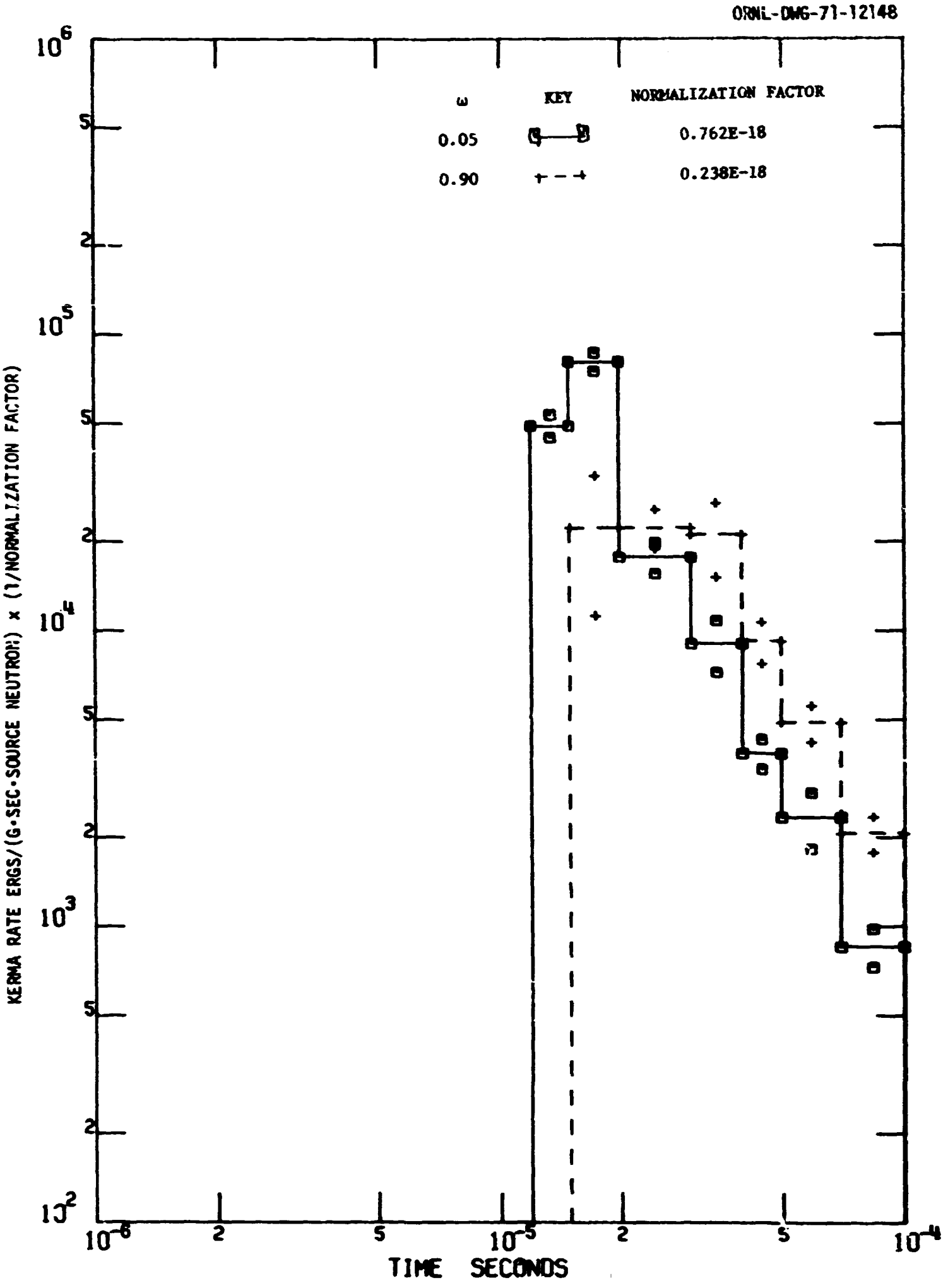

Fig. 72. Time-Dependent Neutron Air Kerma at a Radius of 800 M Both in the Source Plane and at 70 deg from the Source Plane for a 12.2-15-MeV Pancake Source.

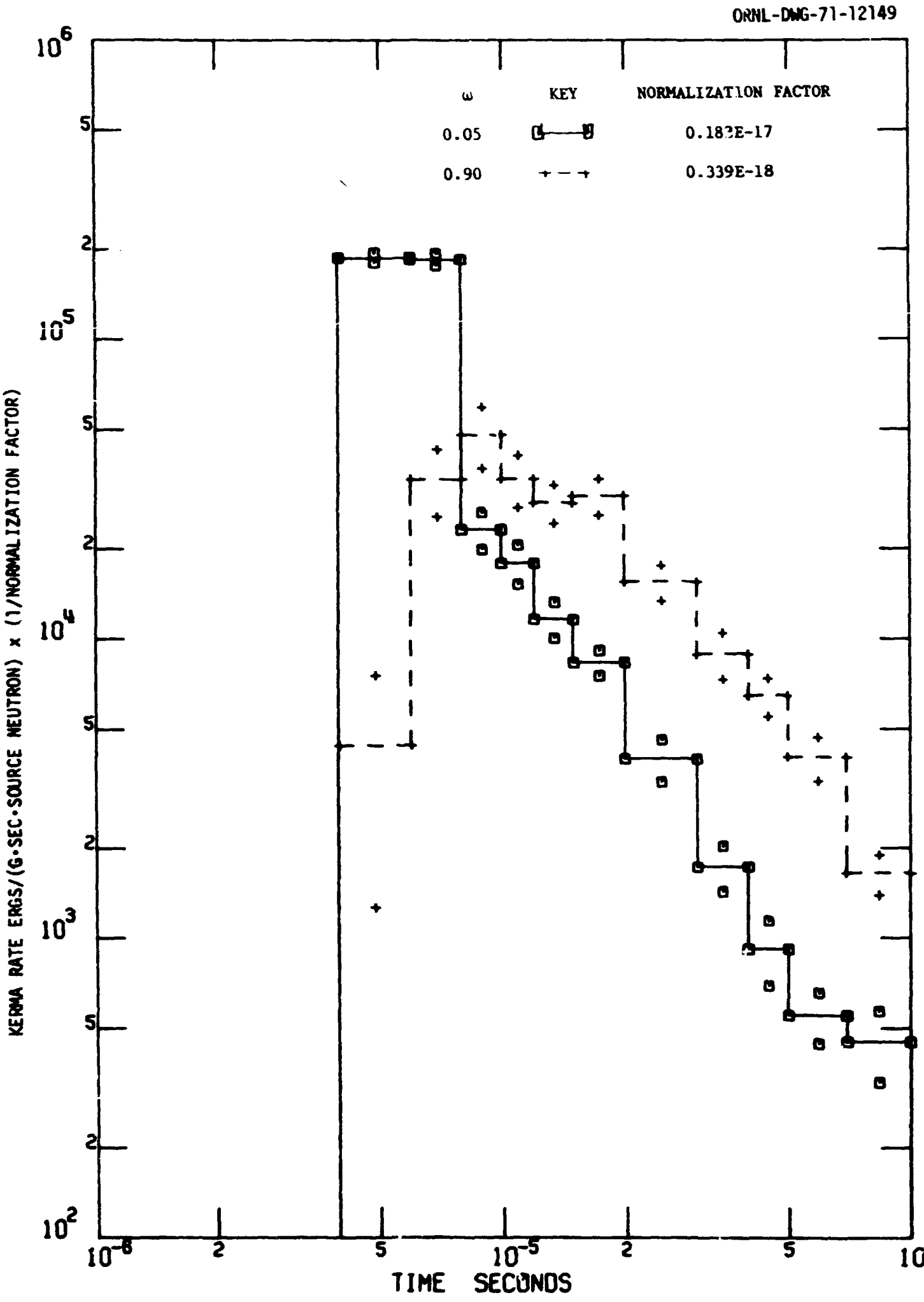

Fig. 73. Time-Dependent Neutron Silicon Kerma at a Radius of 300 M Both in the Source Plane and at 70 deg from the Source Plane for a 12.2-15-MeV Pancake Source.

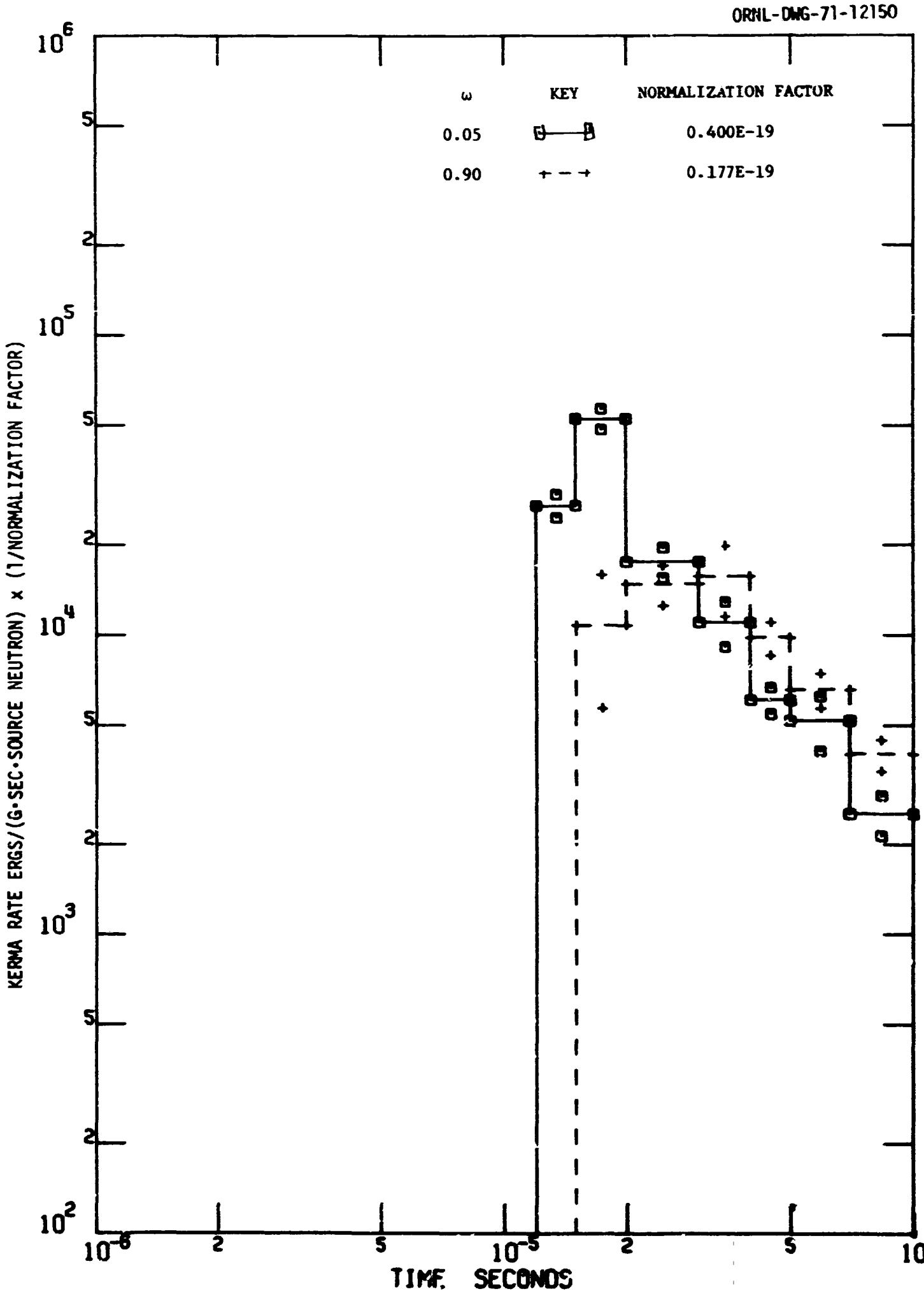

Fig. 74. Time-Dependent Neutron Silicon Kerma at a Radius of 800 M Both in the Source Plane and at 70 deg from the Source Plane for a 12.2-15-MeV Pancake Source.

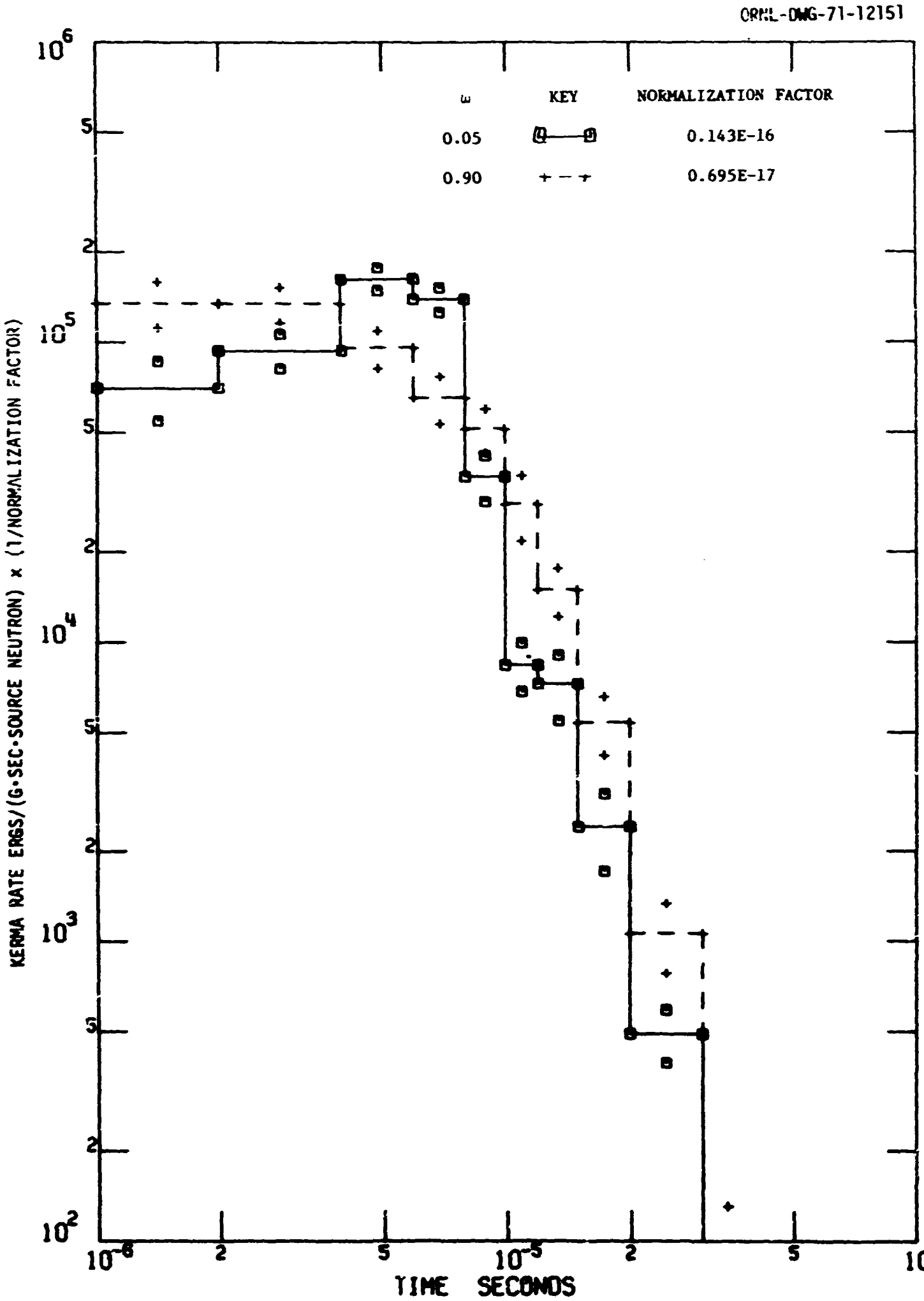

Fig. 75. Time-Dependent Gamma-Ray Air Kerma at a Radius of 300 M Both in the Source Plane and at 70 deg from the Source Plane for a 12.2-15-MeV Pancake Source.

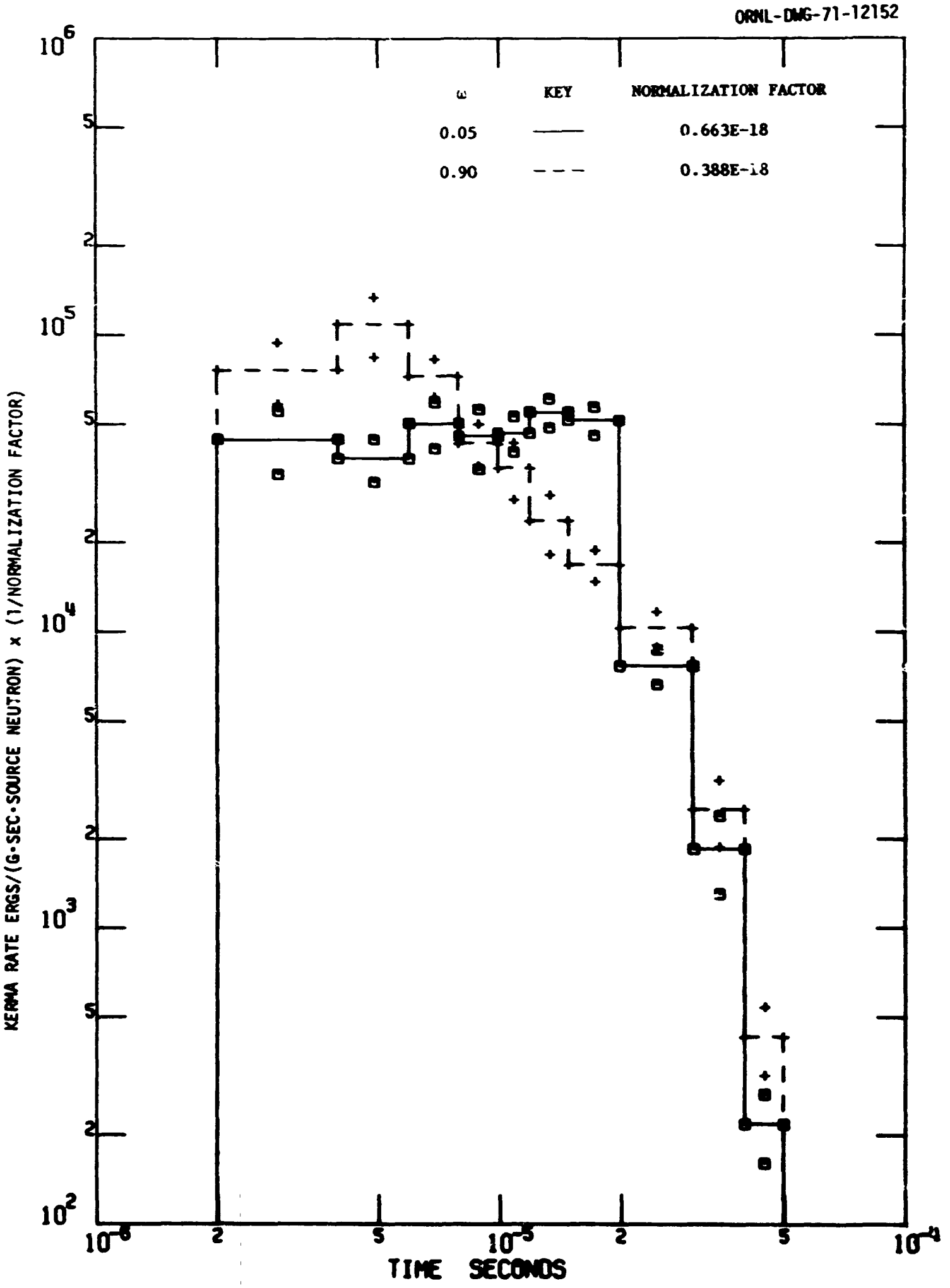

Fig. 76. Time-Dependent Gamma-Ray Air Kerma at a Radius of 800 M Both in the Source Plane and at 70 deg from the Source Plane for a 12.2-15-MeV Pancake Source.

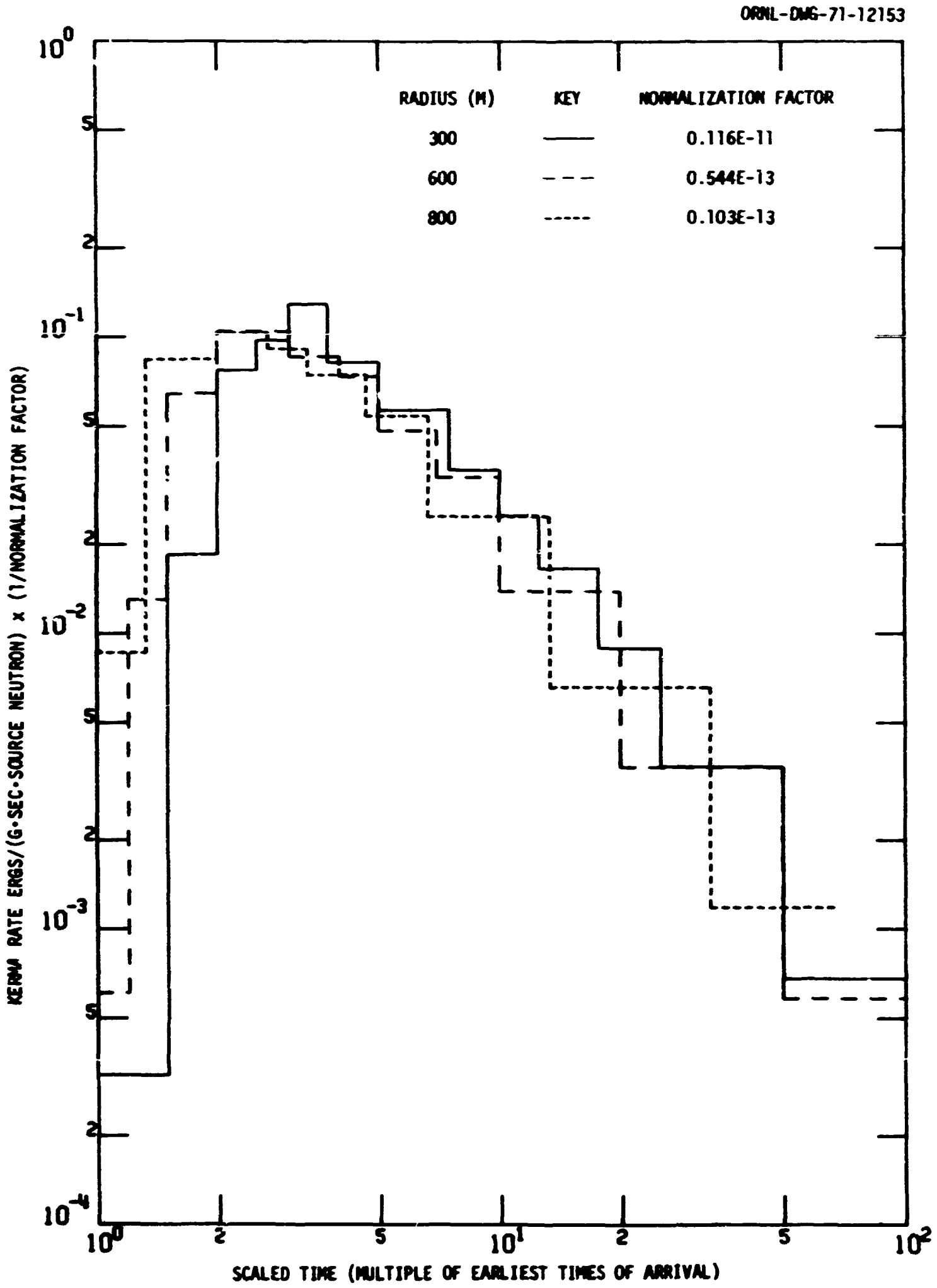

Fig. 77. Time-Dependent Neutron Air Kerma (Scaled) for a Fission Symmetric Source.

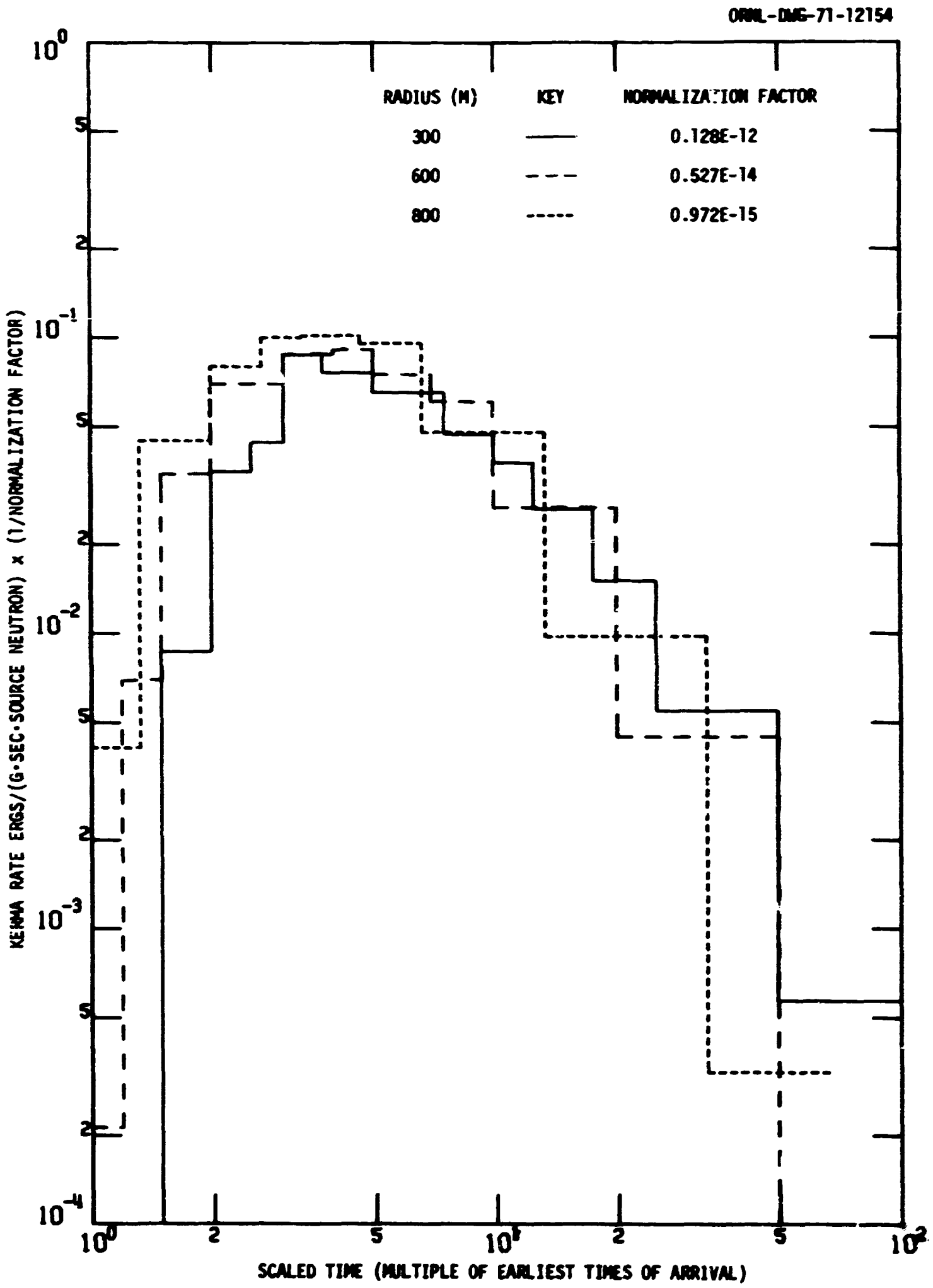

Fig. 78. Time-Dependent Neutron Silicon Kerma (Scaled) for a Fission Symmetric Source.

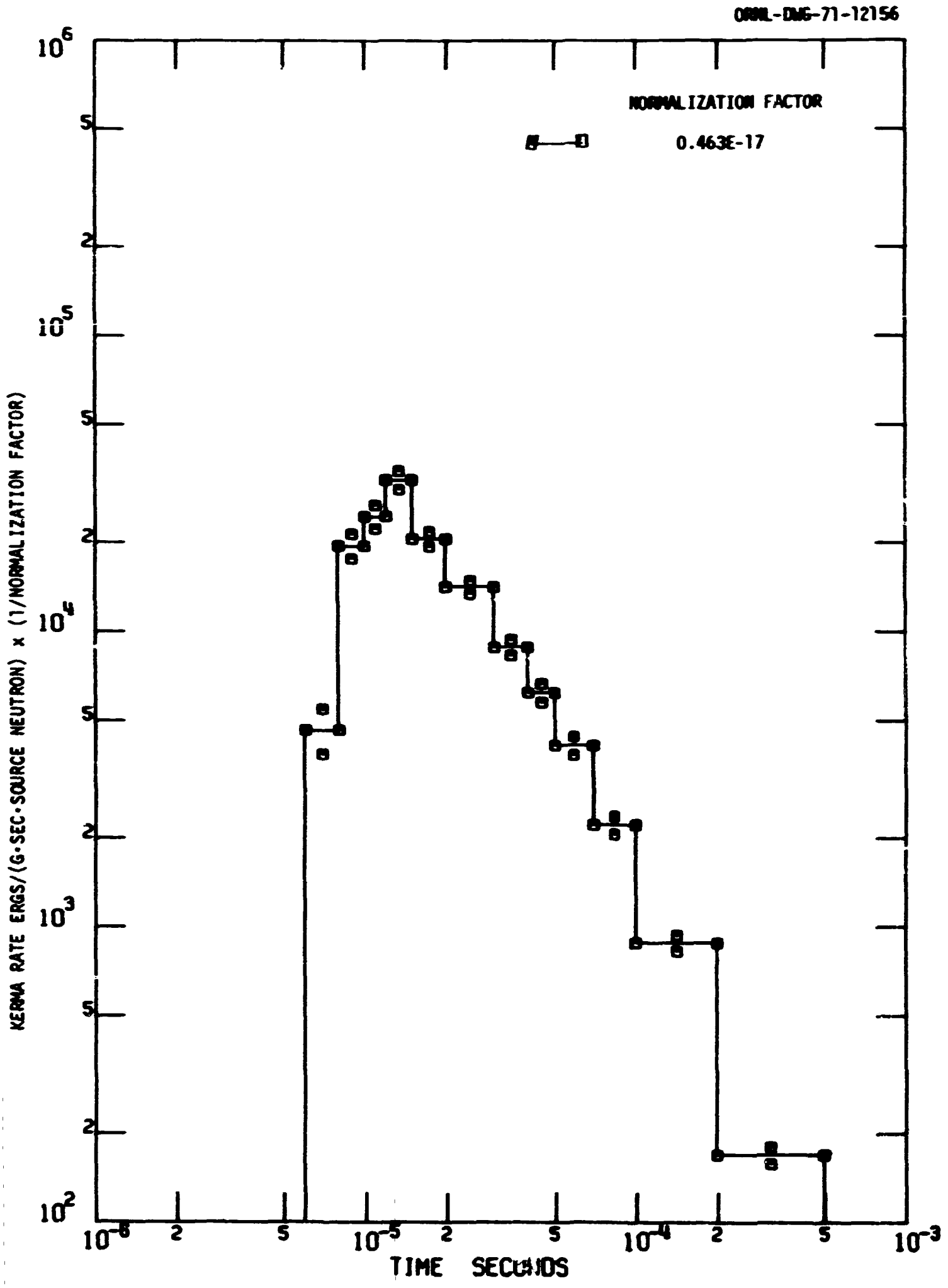

Fig. 80. Time-Dependent Neutron Air Kerma at a Radius of 300 M for a Fission Symmetric Source.

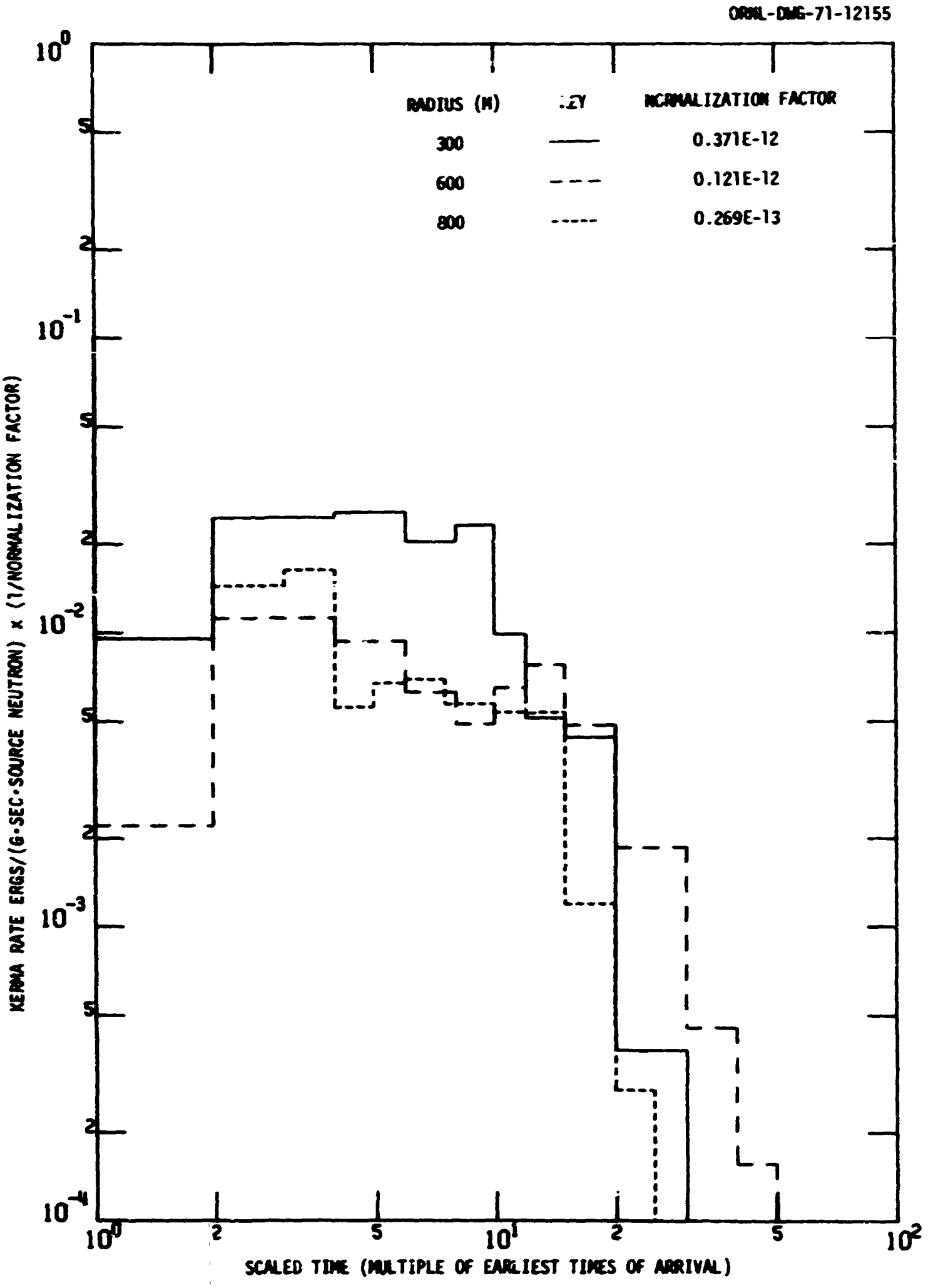

Fig. 79. Time-Dependent Gamma-Ray Air Kerma (Scaled) for a Fission Symmetric Source.

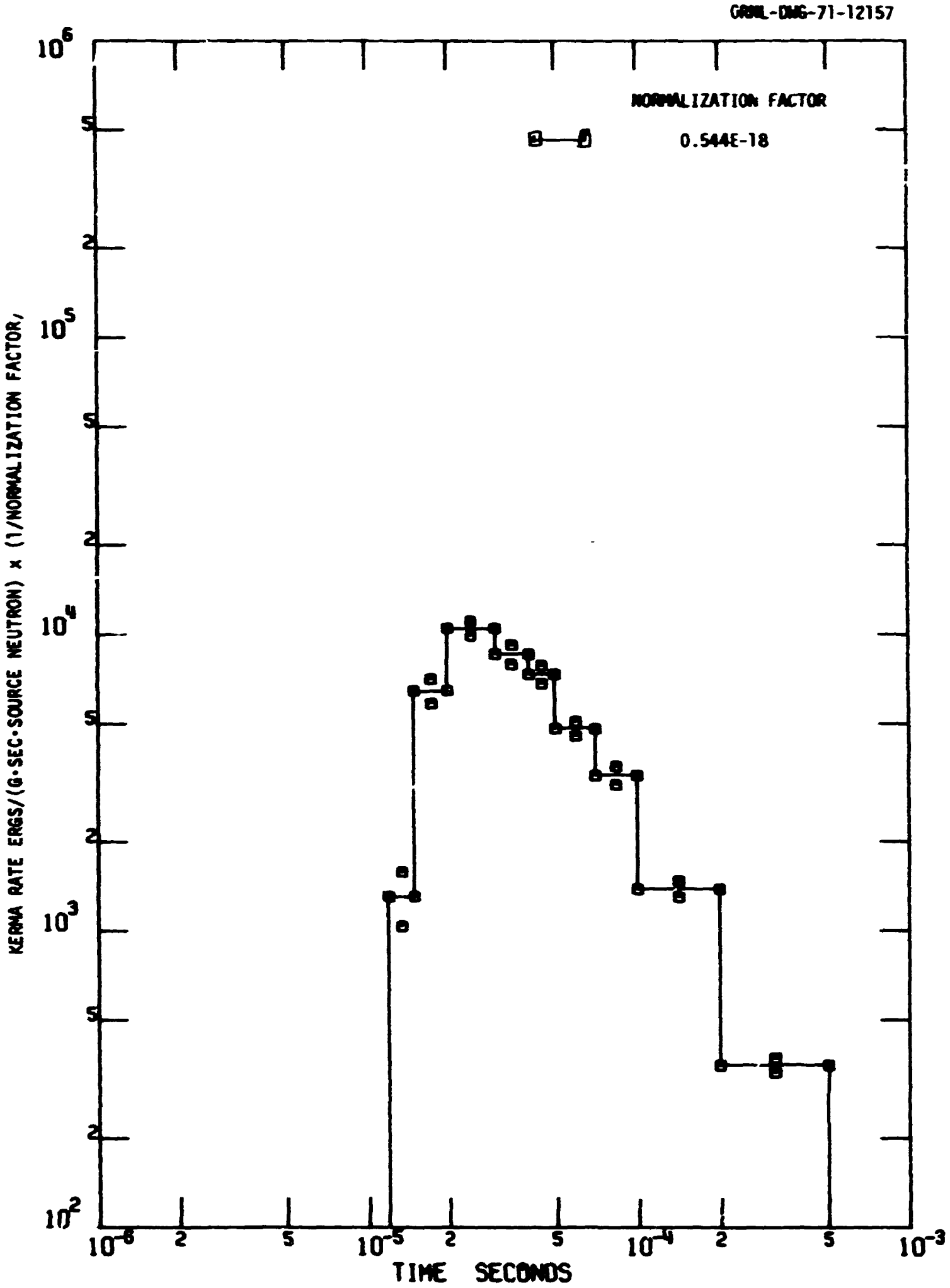

Fig. 81. Time-Dependent Neutron Air Kerma at a Radius of 600 M for a Fission Symmetric Source.

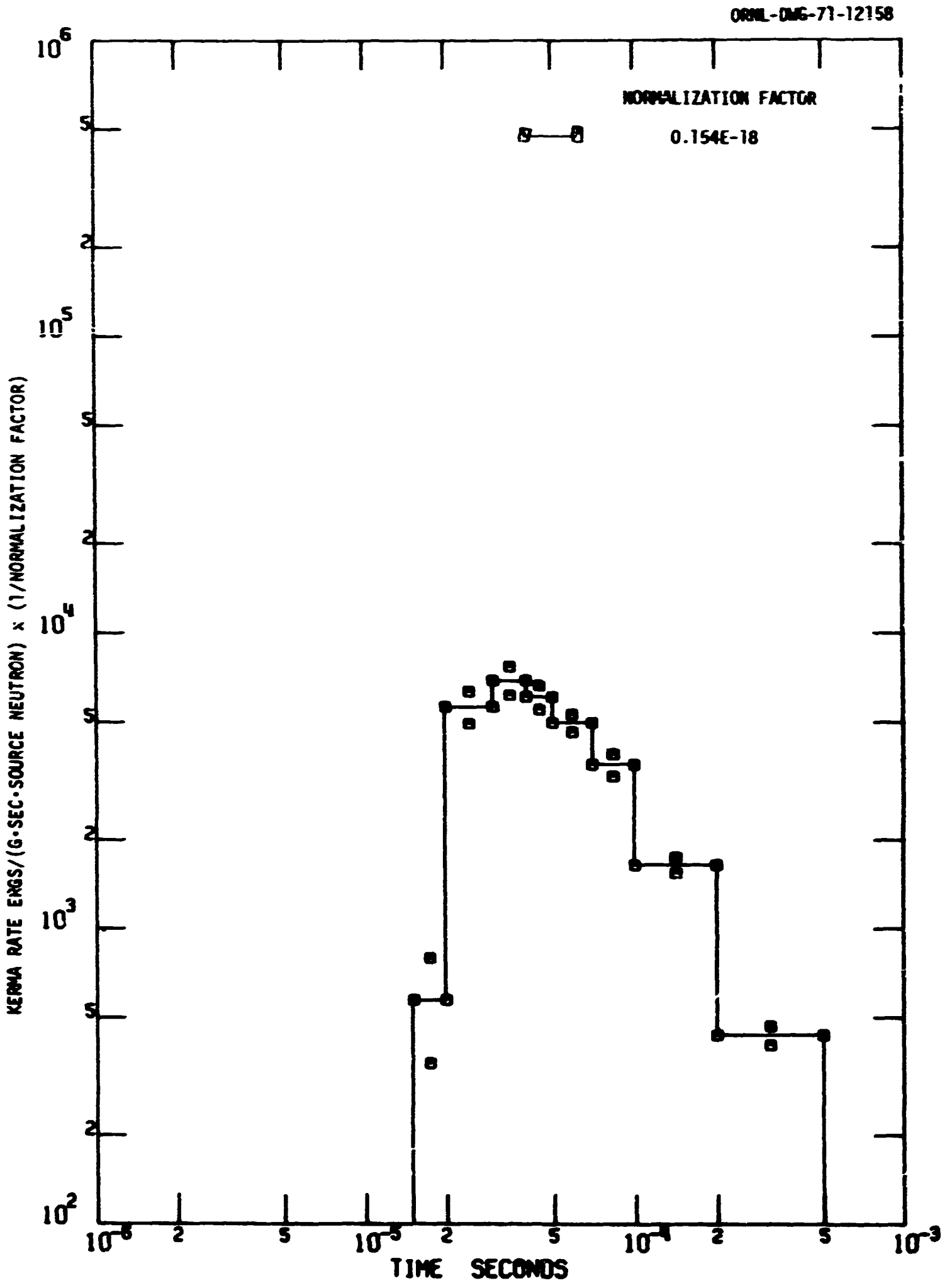

Fig. 82. Time-Dependent Neutron Air Kerma at a Radius of 800 M for a Fission Symmetric Source.

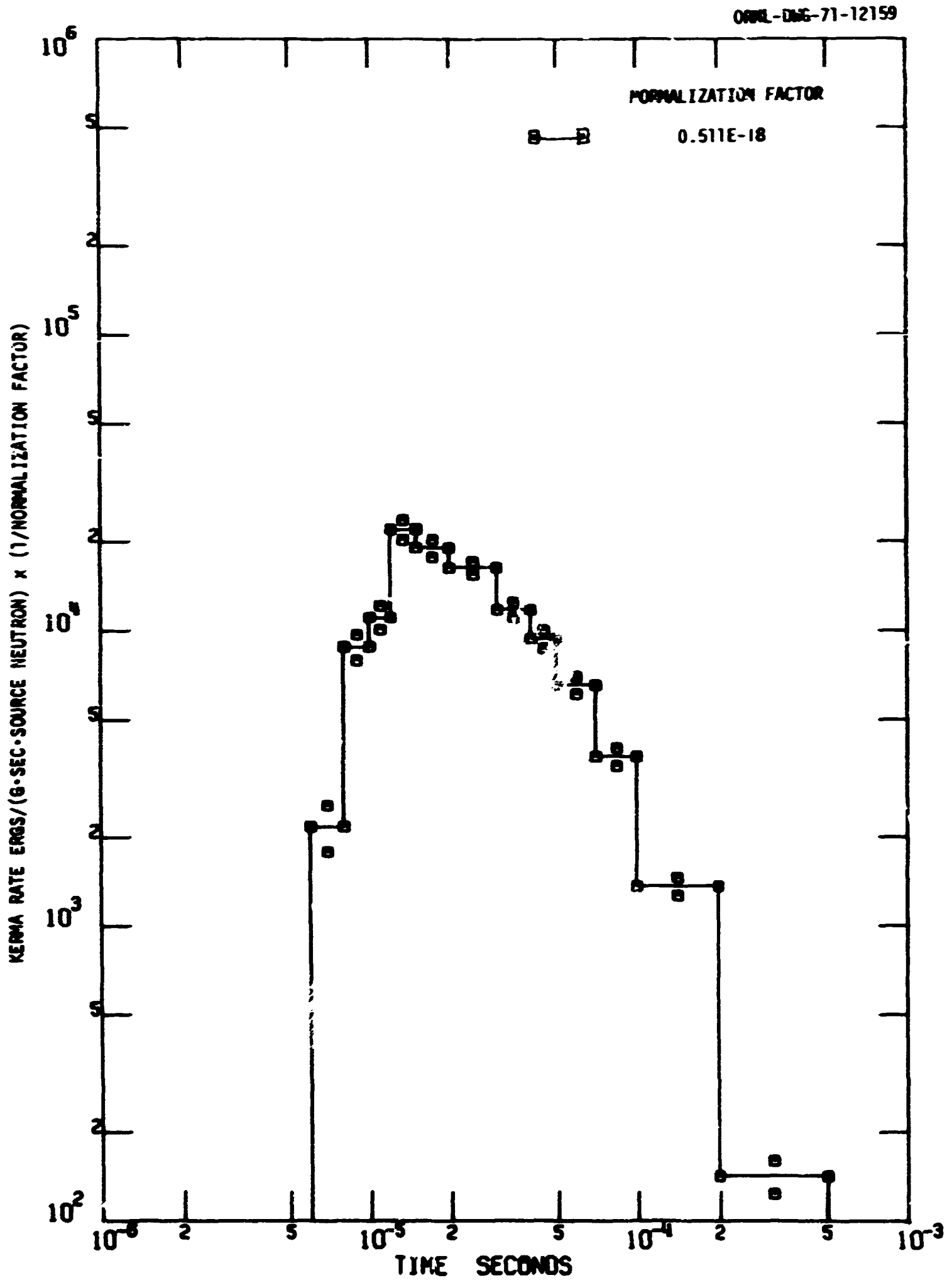

Fig. 83. Time-Dependent Neutron Silicon Kerma at a Radius of 300 M for a Fission Symmetric Source.

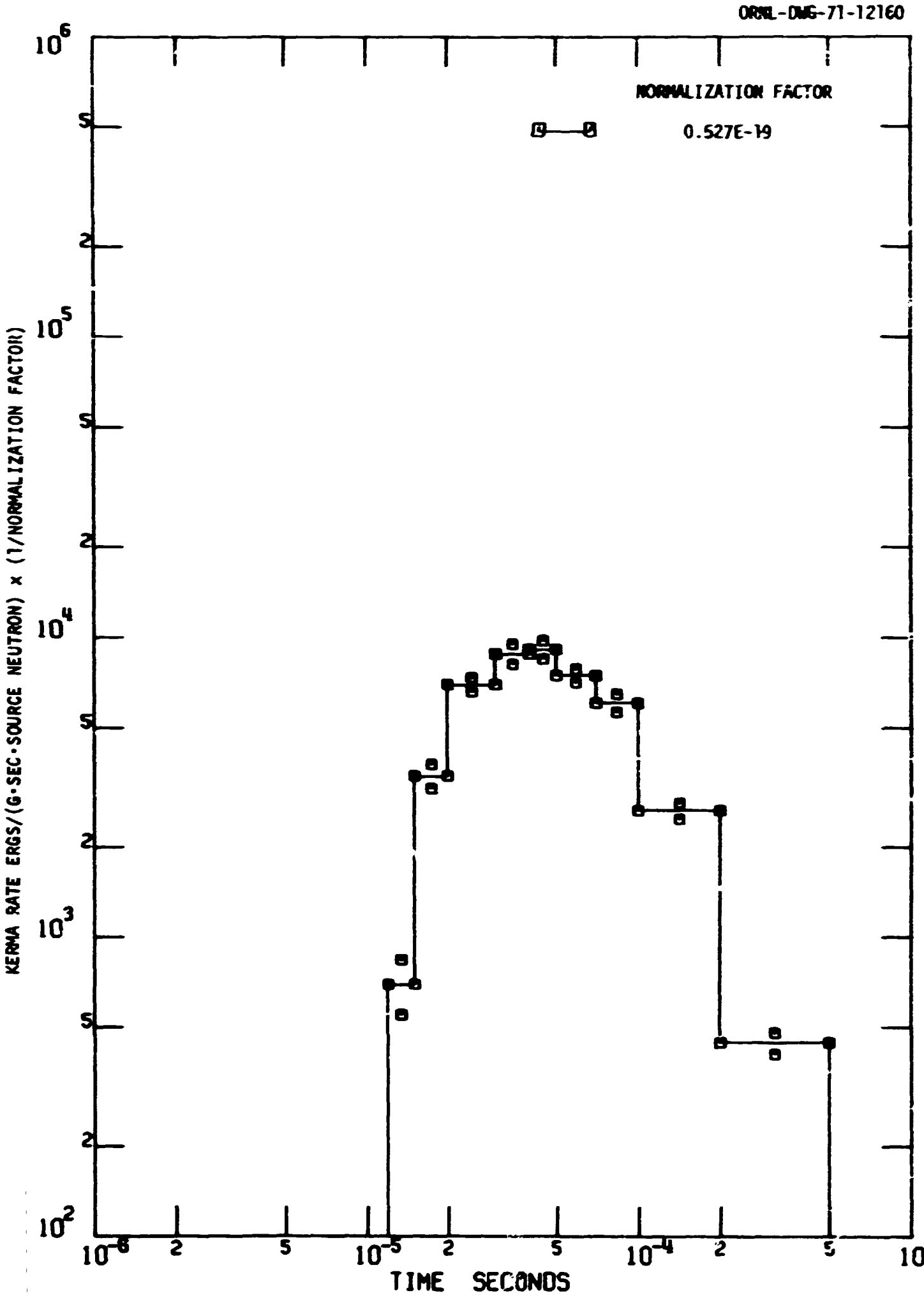

Fig. 84. Time-Dependent Neutron Silicon Kerma at a Radius of 600 M for a Fission Symmetric Source.

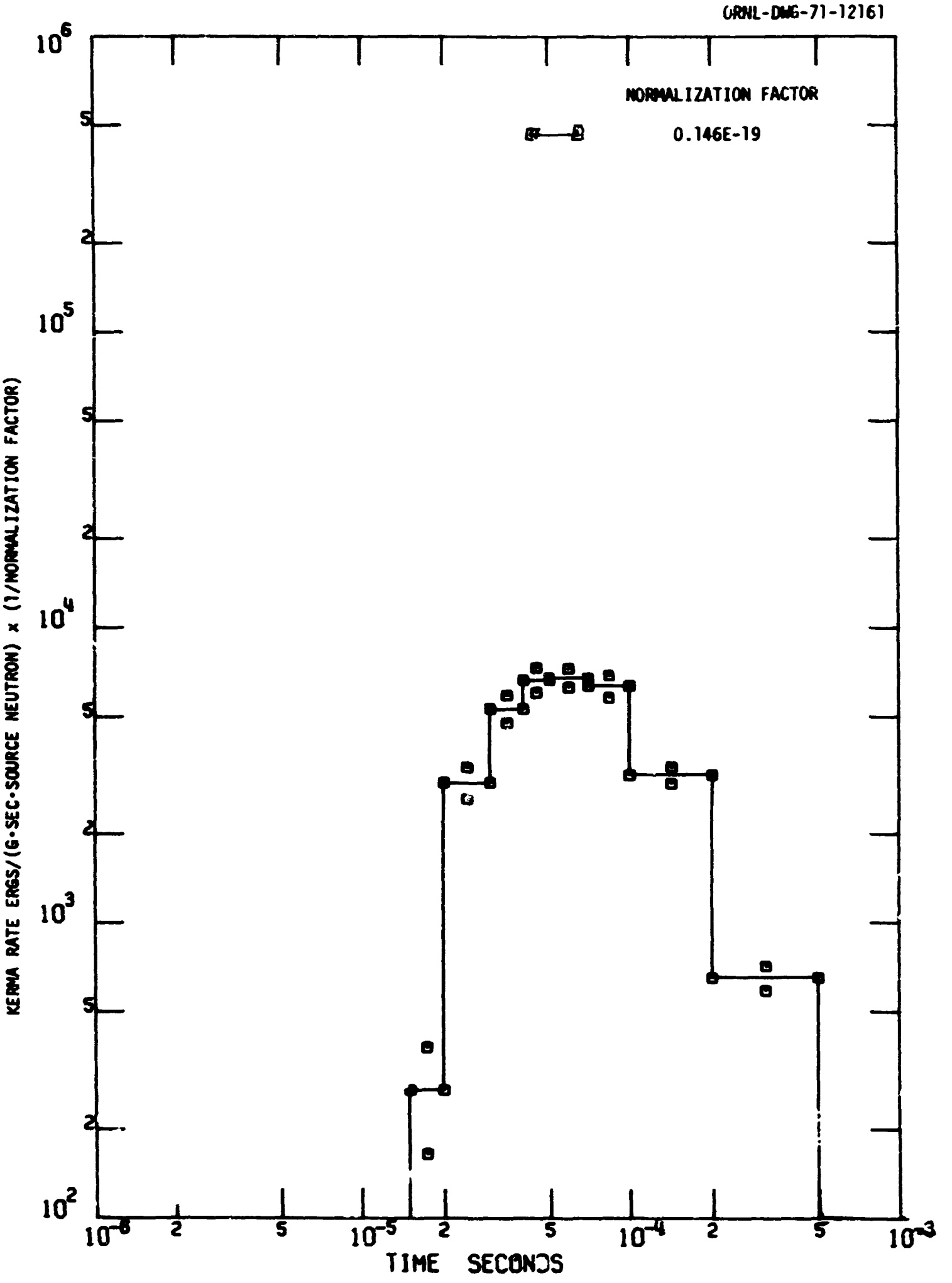

Fig. 85. Time-Dependent Neutron Silicon Kerma at a Radius of 800 M for a Fission Symmetric Source.

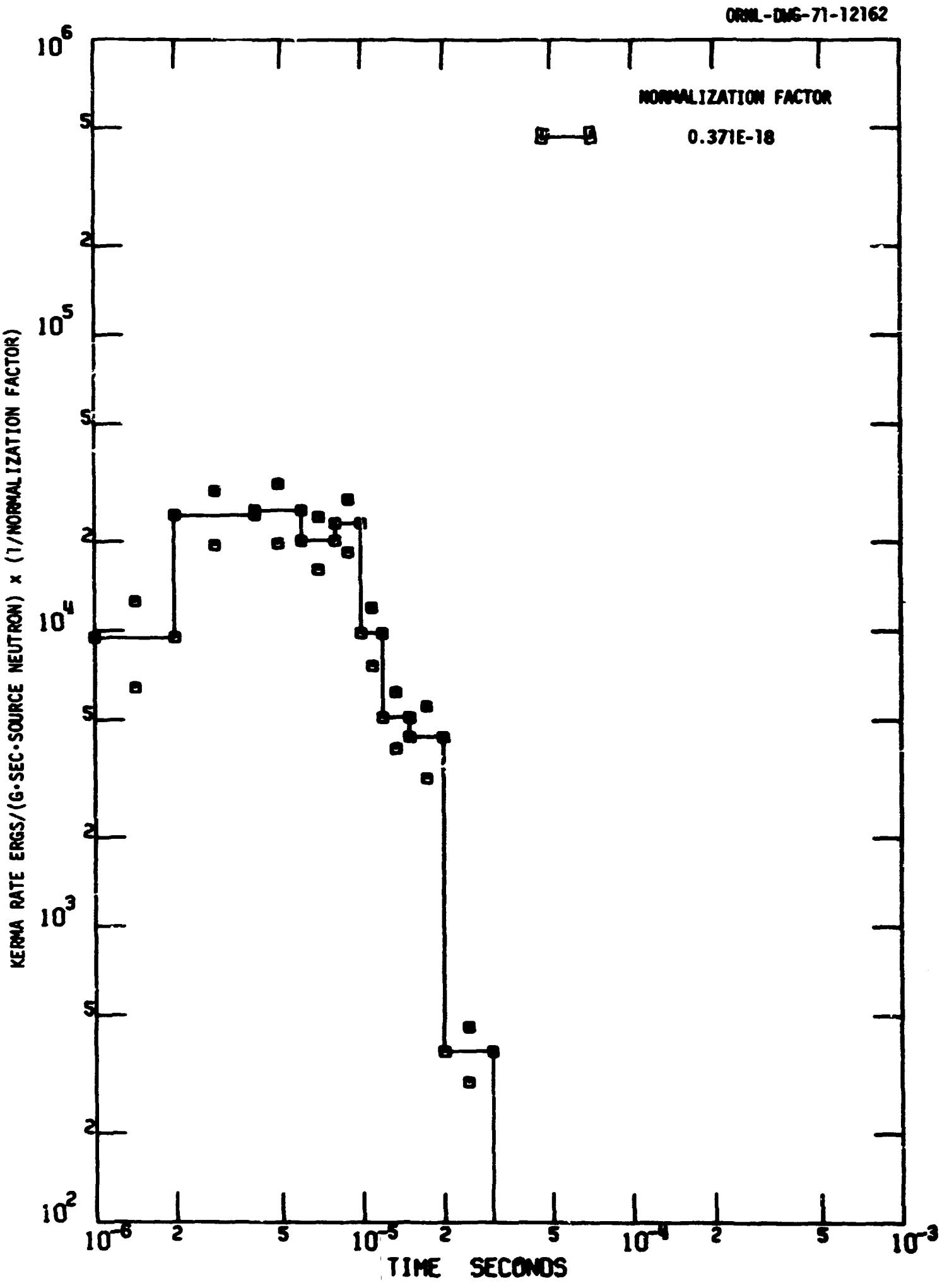

Fig. 86. Time-Dependent Gamma-Ray Air Kerma at a Radius of 300 M for a Fission Symmetric Source.

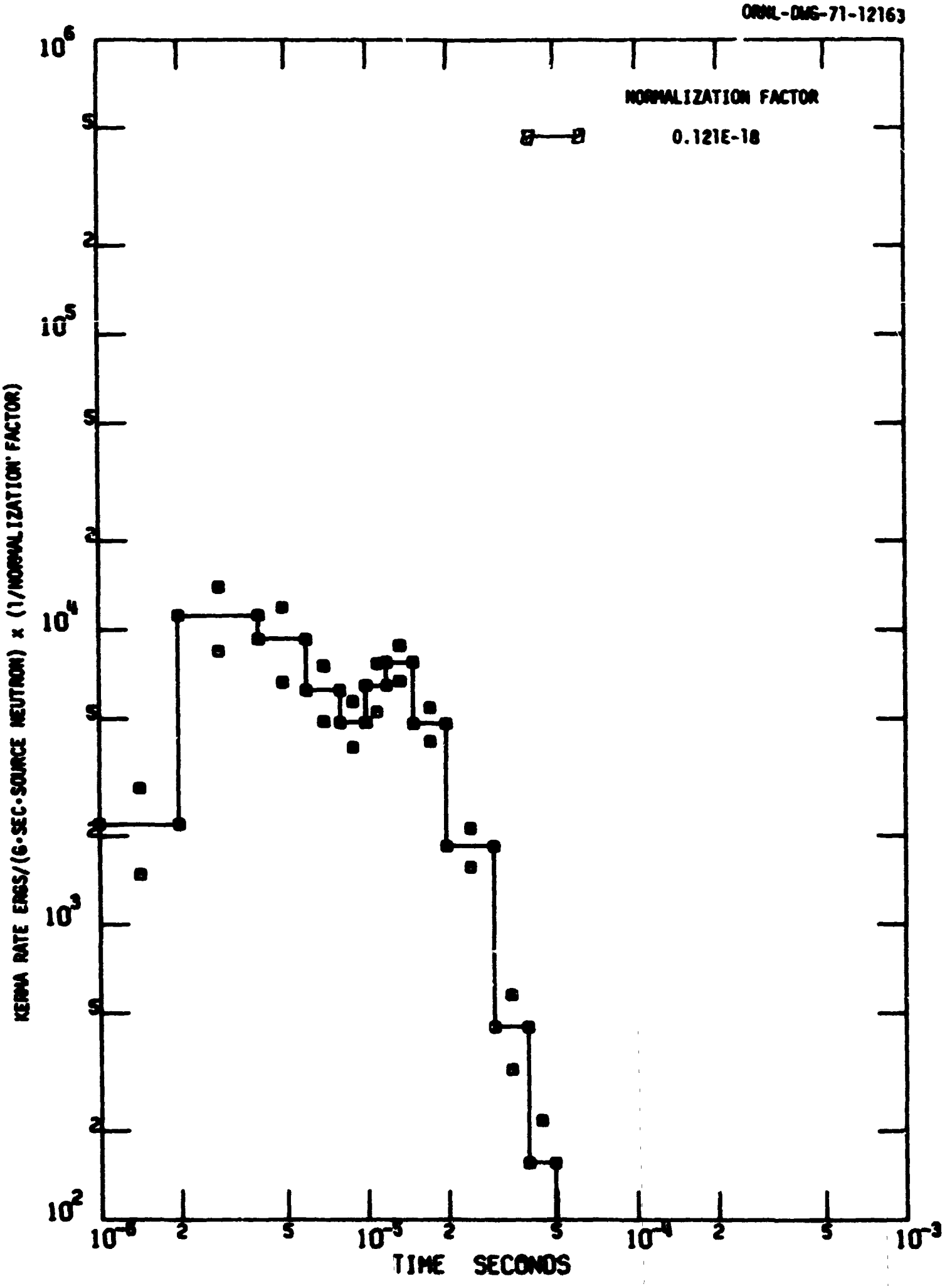

Fig. 87. Time-Dependent Gamma-Ray Air Kerma at a Radius of 600 M for a Fission Symmetric Source.

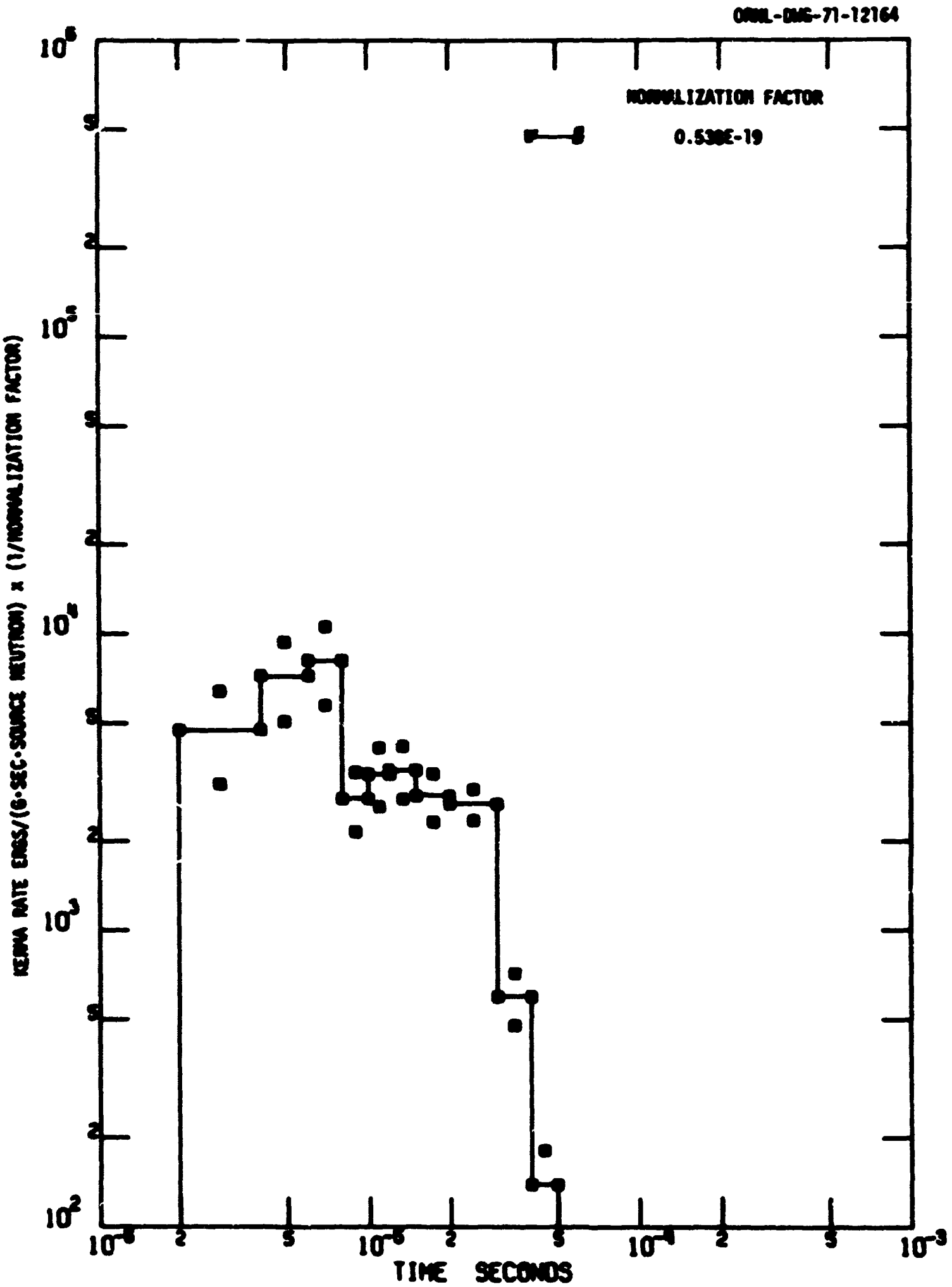

Fig. 88. Time-Dependent Gamma-Ray Air Kerma at a Radius of 800 M for a Fission Symmetric Source.

ORNL-DWG-71-12165

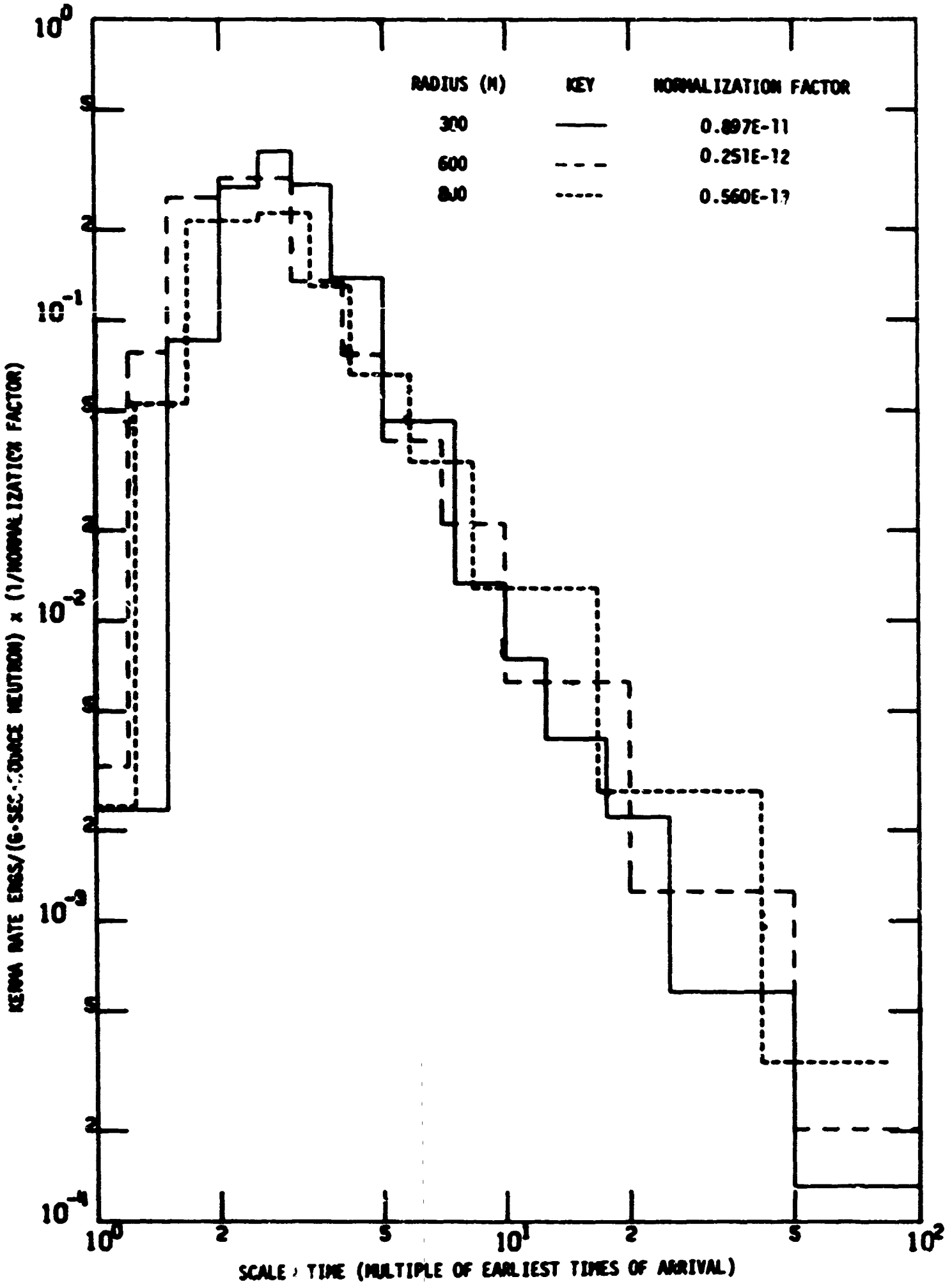

Fig. 89. Time-Dependent Neutron Air Kerma (Scaled) in the Source Direction for a Fission Beam Source.

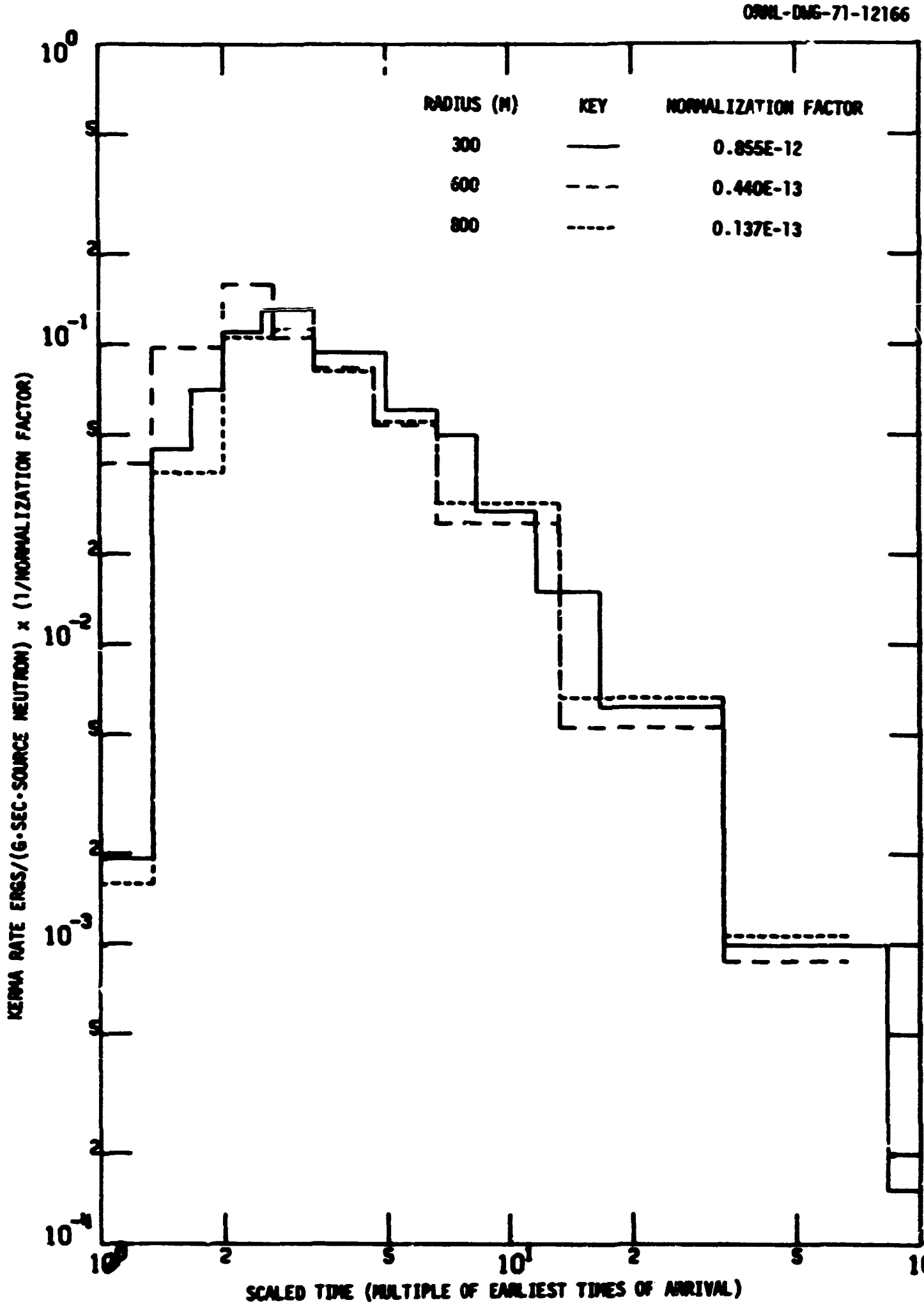

Fig. 90. Time-Dependent Neutron Air Kerma (Scaled) in a Direction at 50 deg from the Source Direction for a Fission Beam Source.

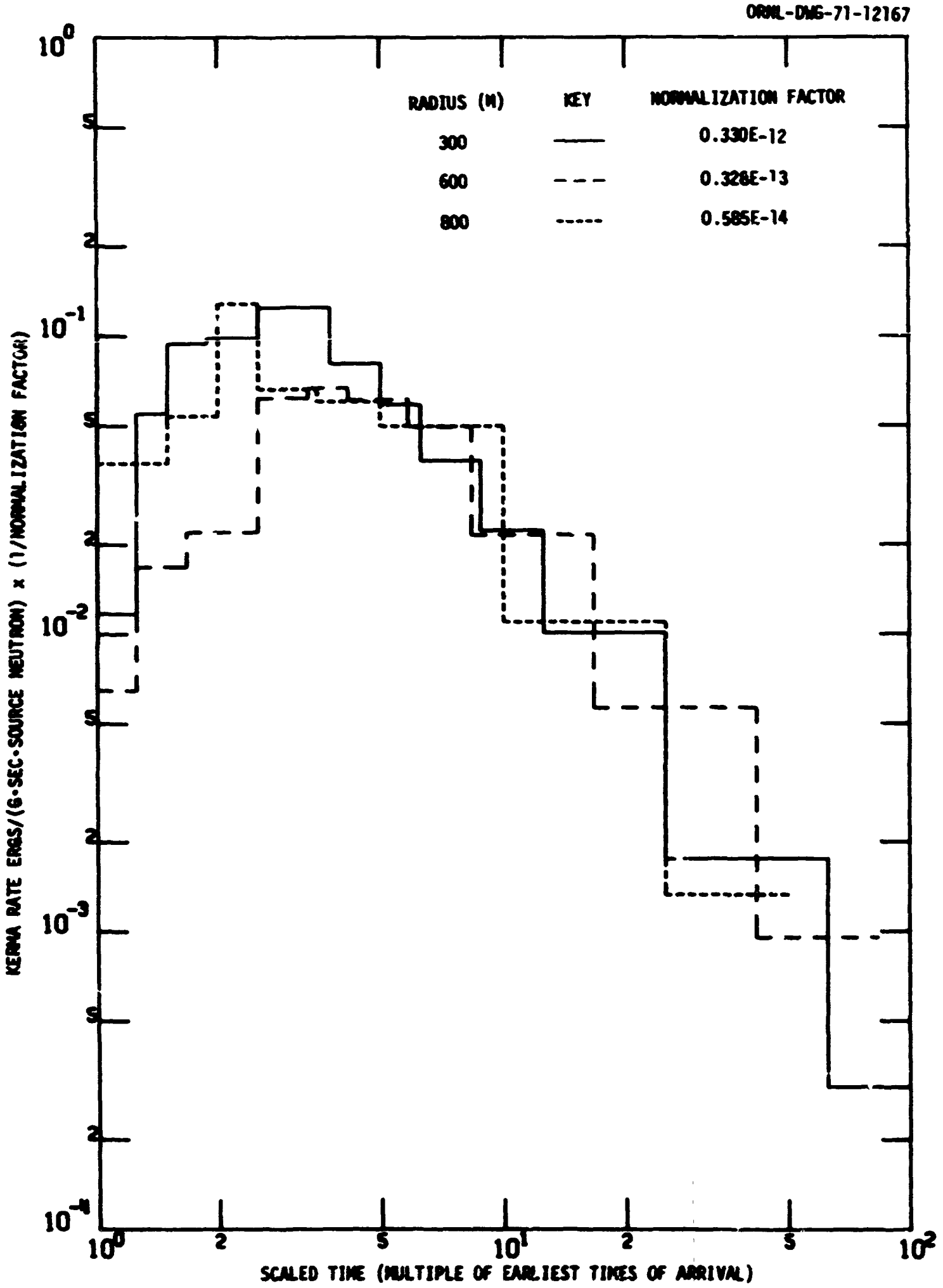

Fig. 91. Time-Dependent Neutron Air Kerma (Scaled) in a Direction Normal to the Source Direction for a Fission Beam Source.

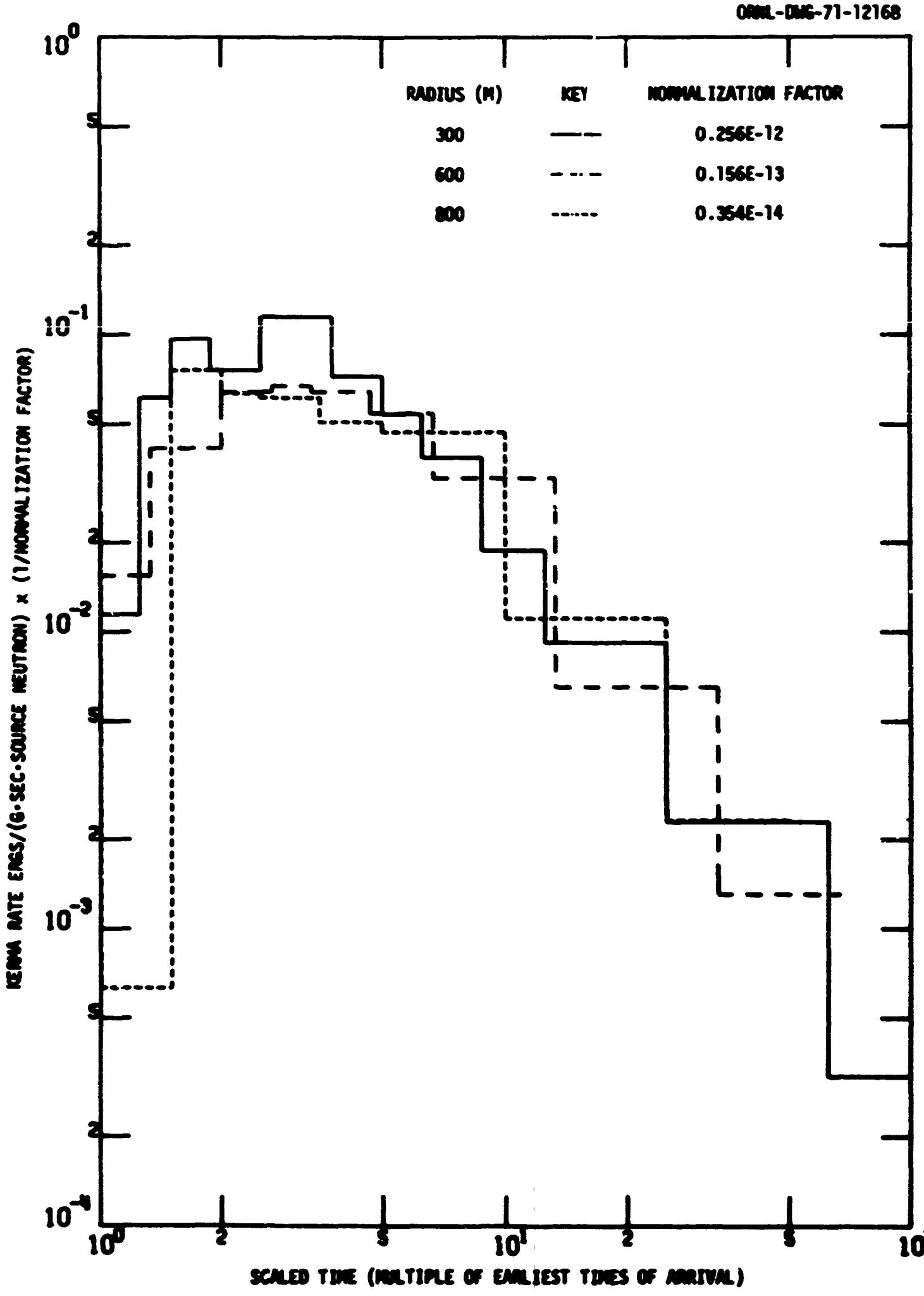

Fig. 92. Time-Dependent Neutron Air Kerma (Scaled) in a Direction at 150 deg from the Source Direction for a Fission Beam Source.

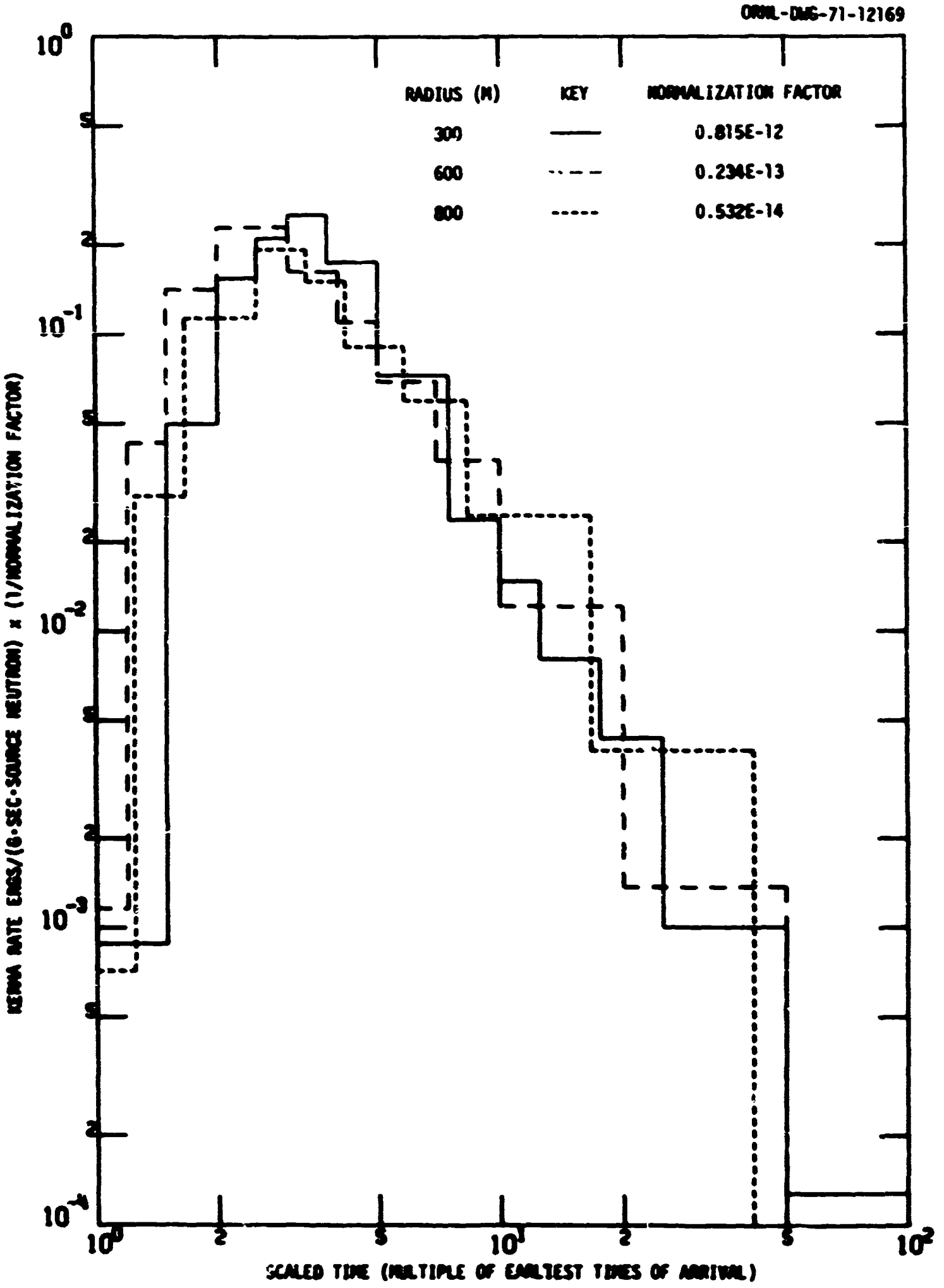

Fig. 93. Time-Dependent Neutron Silicon Kerma (Scaled) in the Source Direction for a Fission Beam Source.

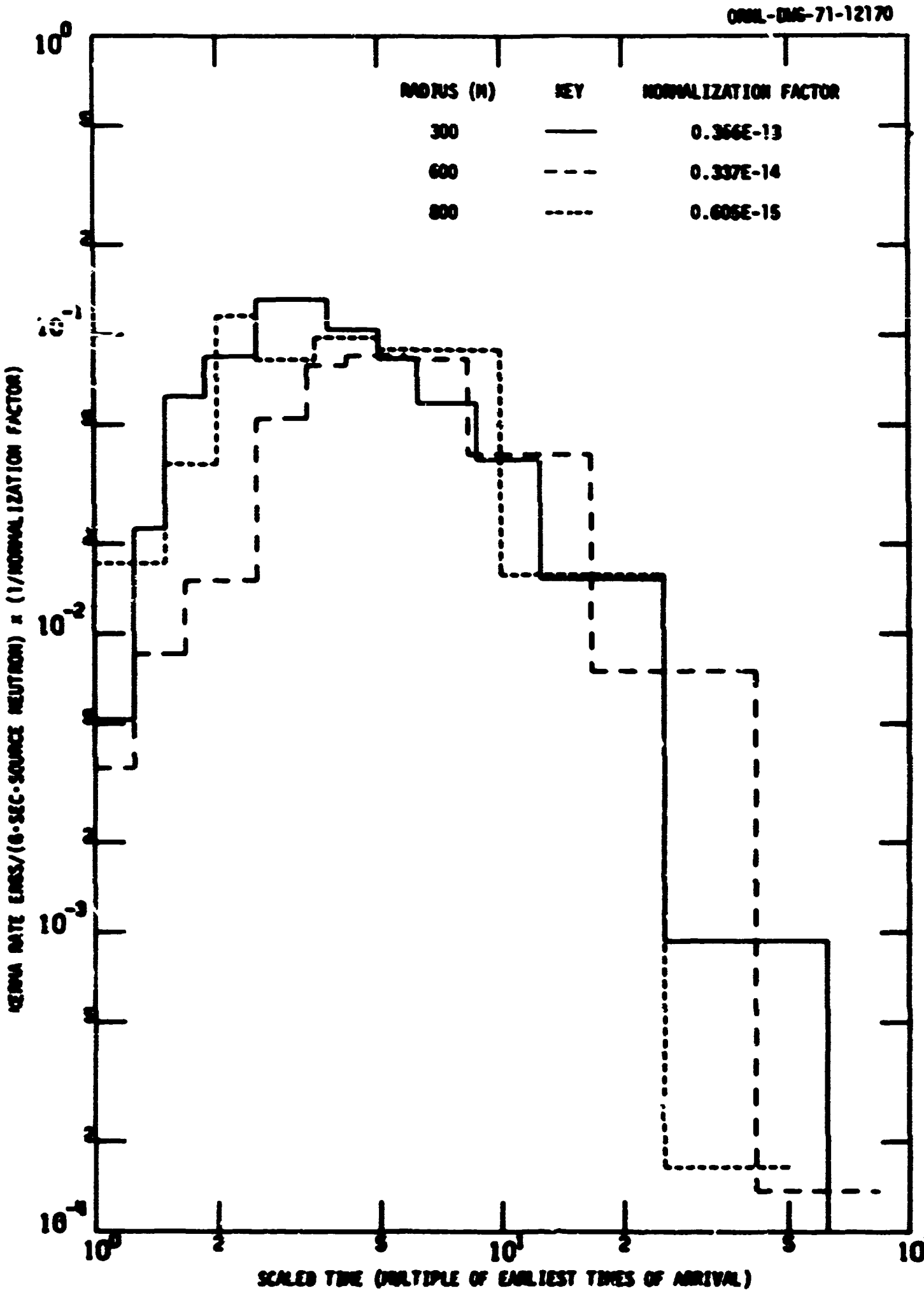

Fig. 94. Time-Dependent Neutron Silicon Kerma (Scaled) in a Direction Normal to the Source Direction for a Fission Beam Source.

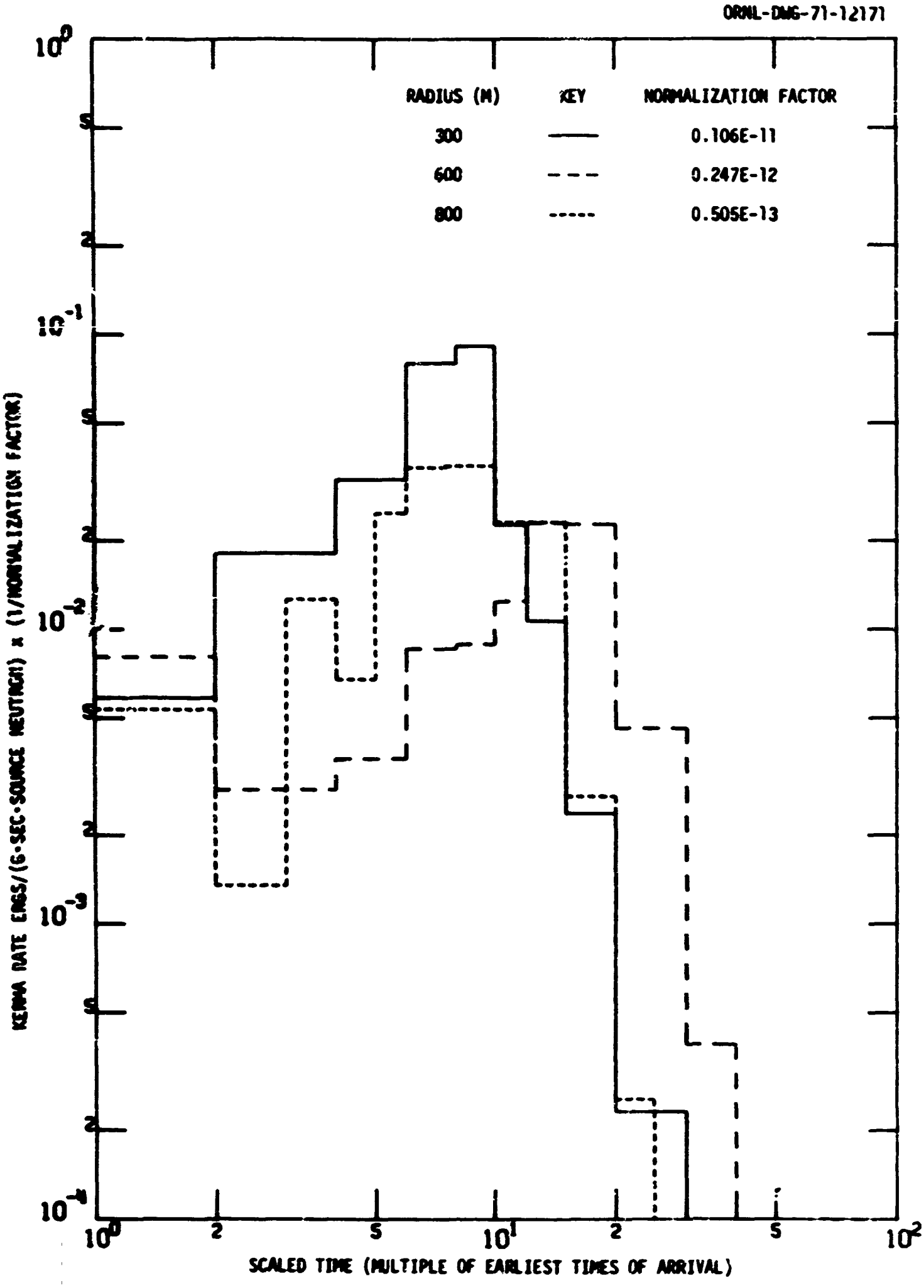

Fig. 95. Time-Dependent Gamma-Ray Air Kerma (Scaled) in the Source Direction for a Fission Beam Source.

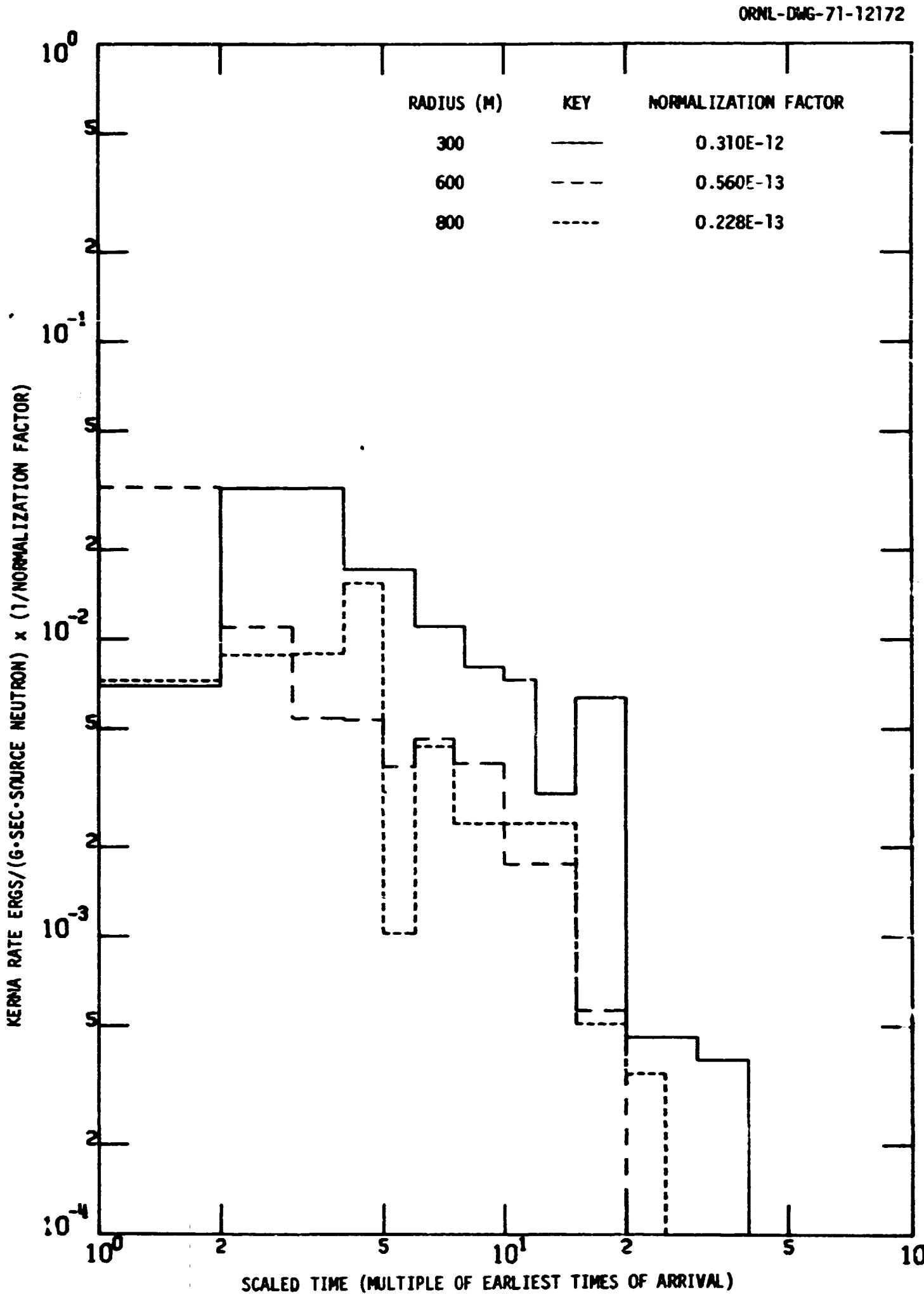

Fig. 96. Time-Dependent Gamma-Ray Air Kerma (Scaled) in a Direction Normal to the Source Direction for a Fission Beam Source.

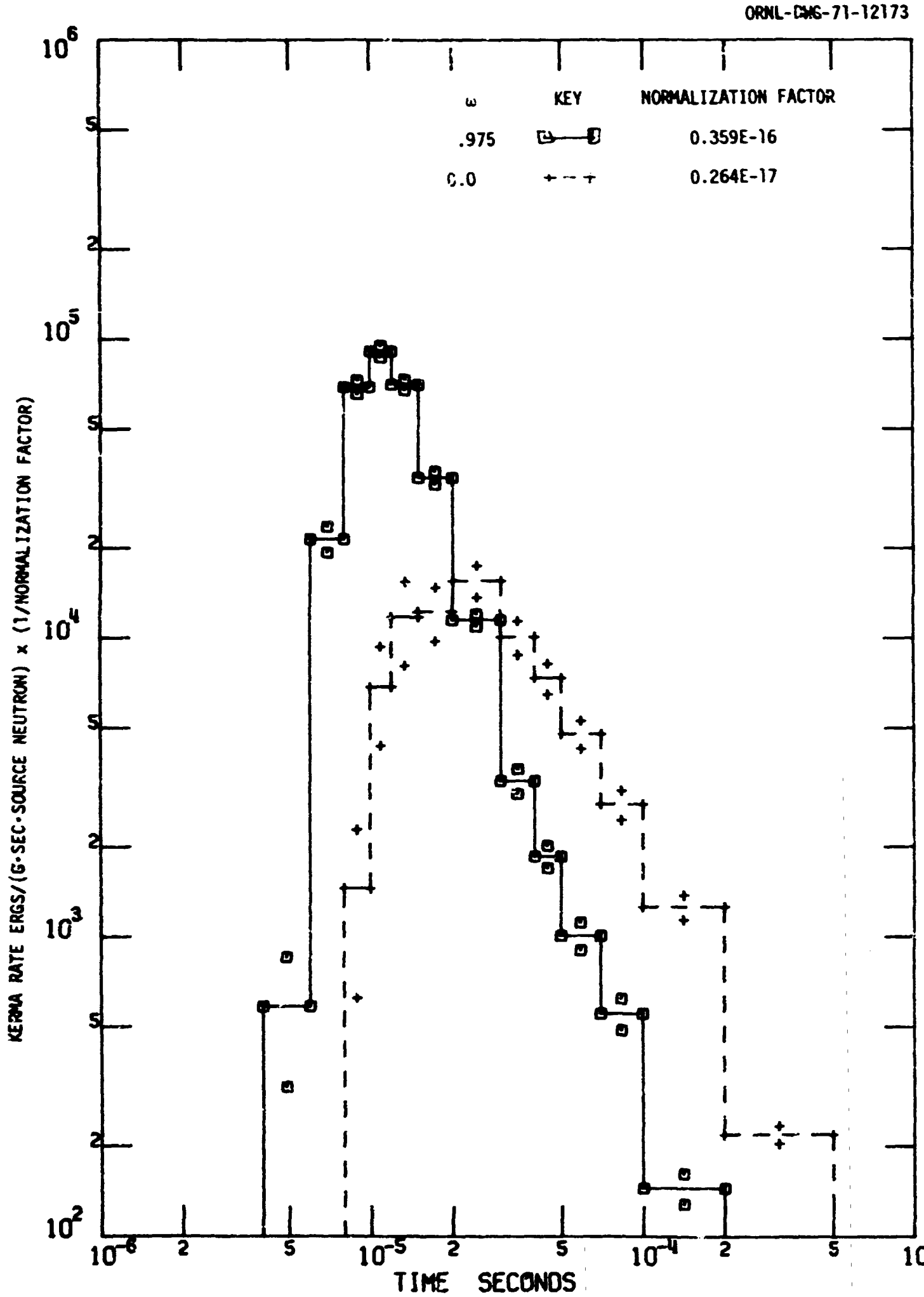

Fig. 97. Time-Dependent Neutron Air Kerma at a Radius of 300 M in the Directions Both Normal to and the Same as the Source Direction for a Fission Beam Source.

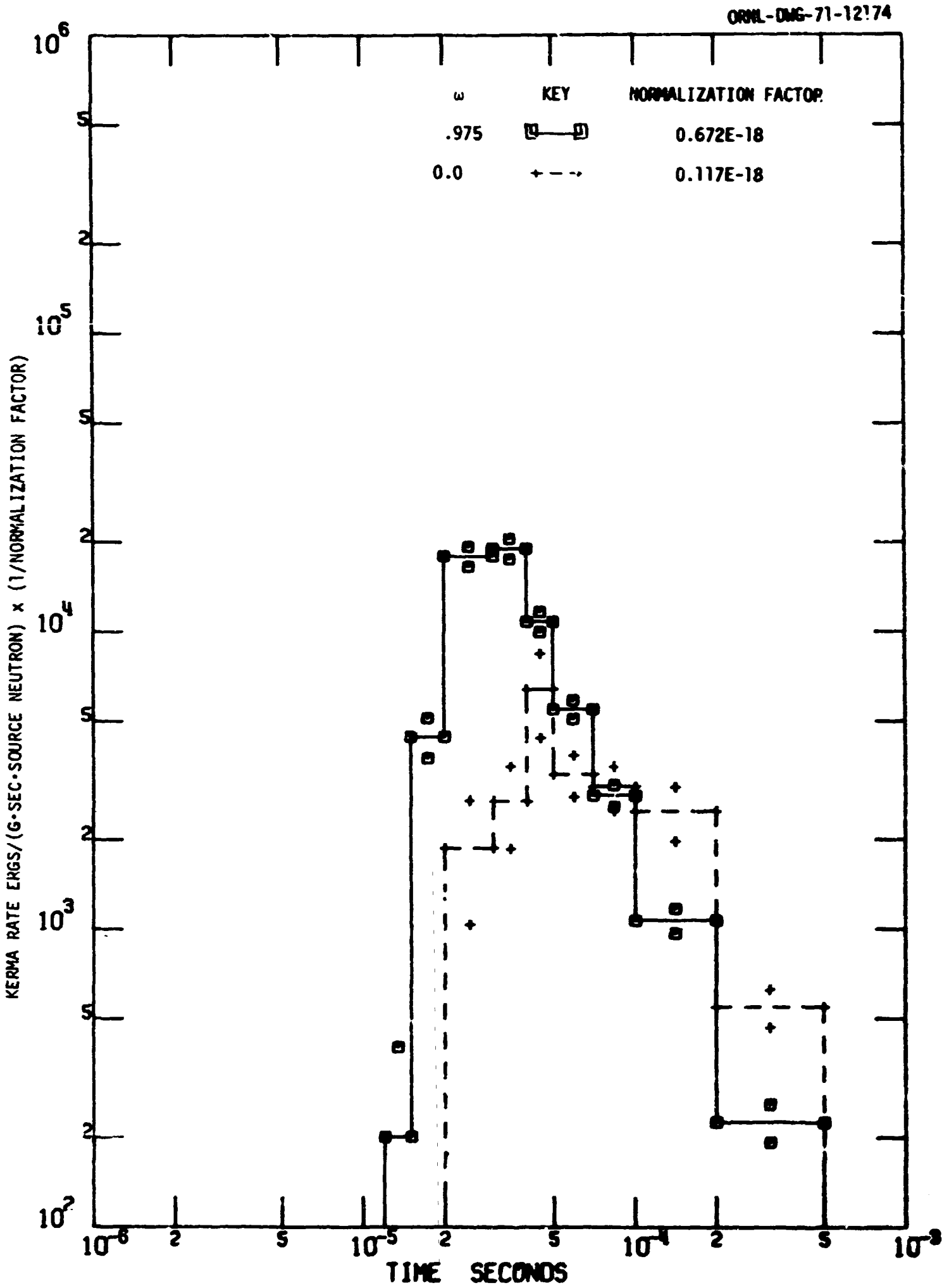

Fig. 98. Time-Dependent Neutron Air Kerma at a Radius of 800 M in the Directions Both Normal to and the Same as the Source Direction for a Fission Beam Source.

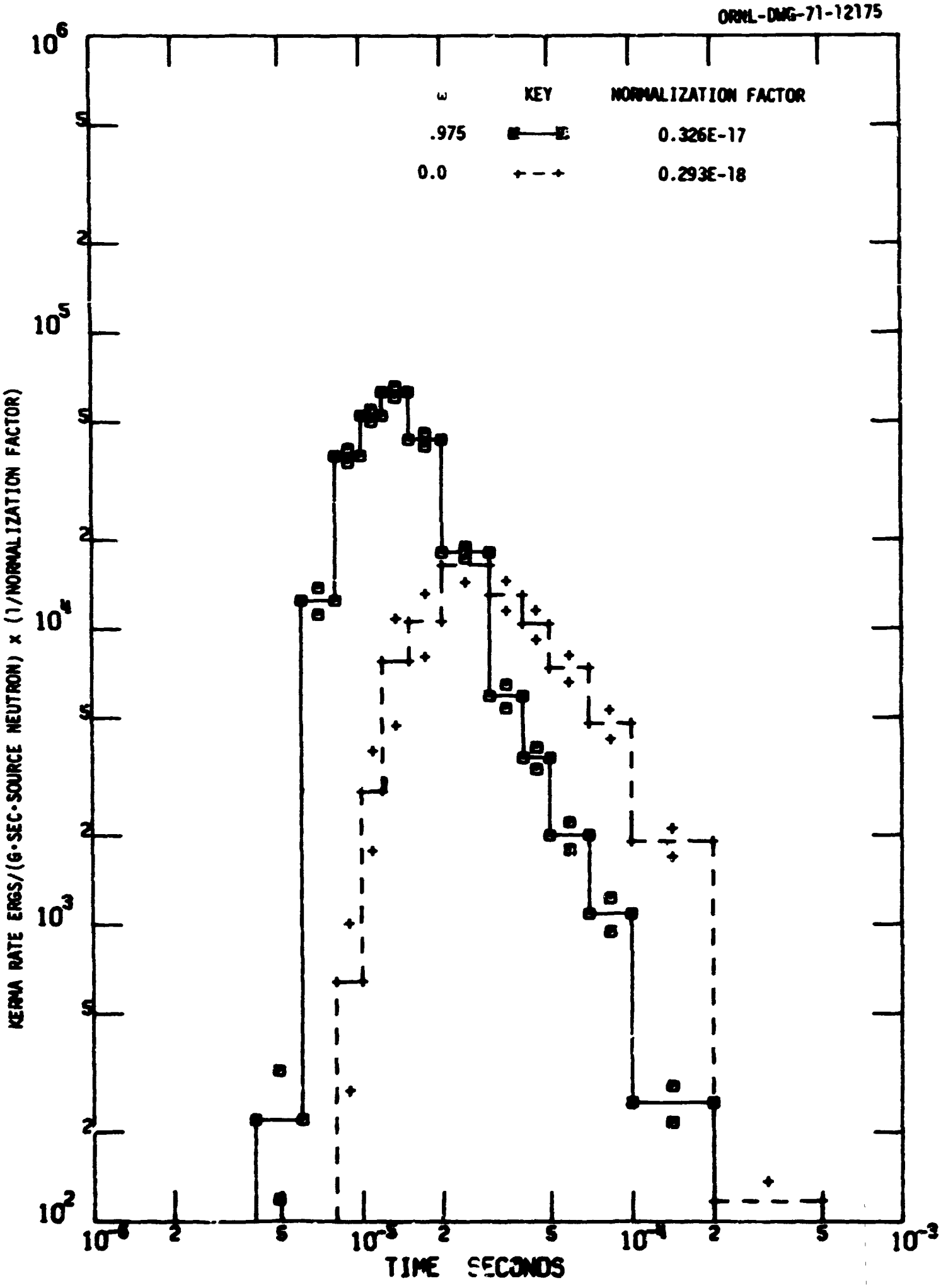

Fig. 99. Time-Dependent Neutron Silicon Kerma at a Radius of 300 M in the Directions Both Normal to and the Same as the Source Direction for a Fission Beam Source.

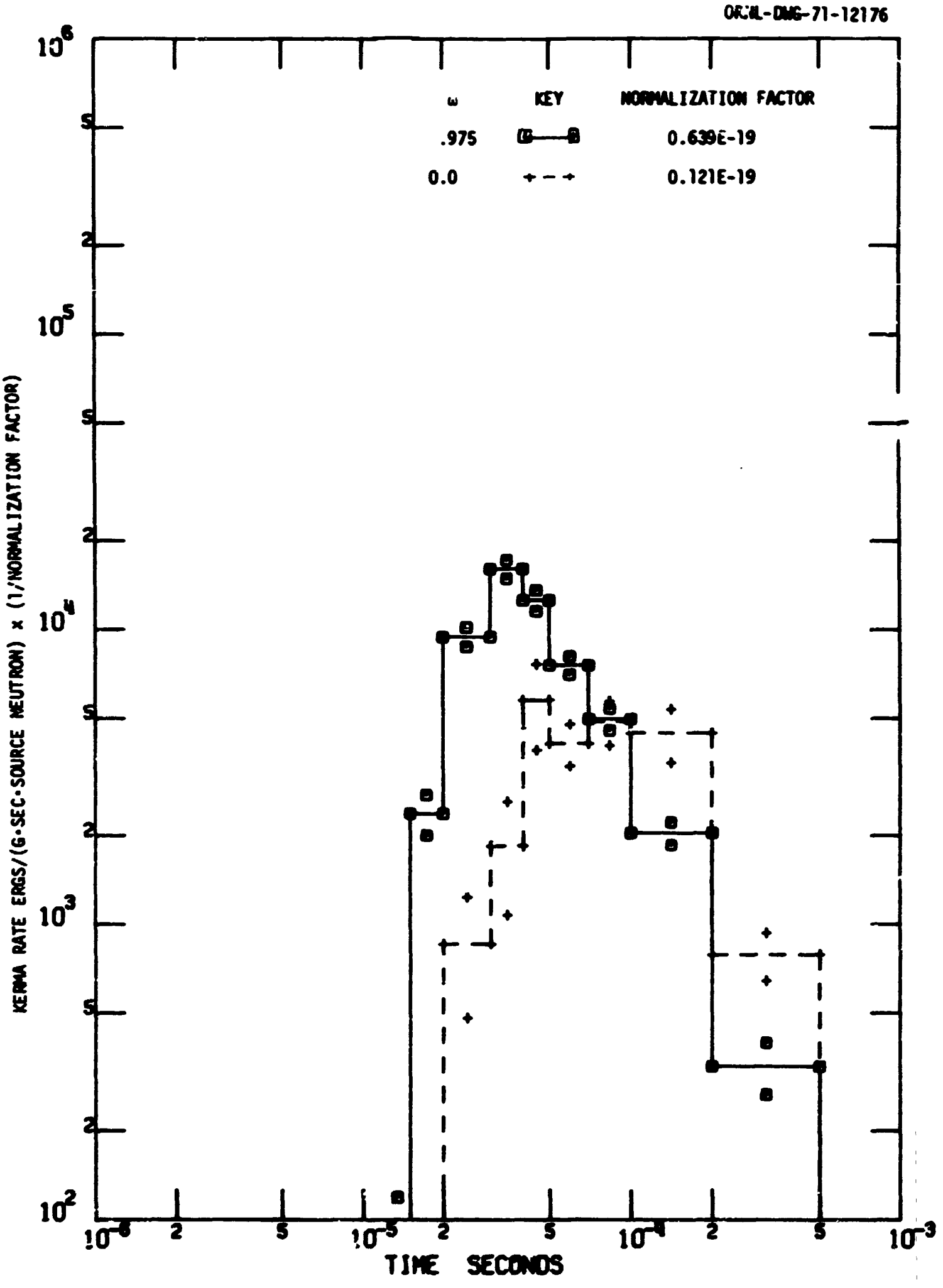

Fig. 100. Time-Dependent Neutron Silicon Kerma at a Radius of 800 M in the Directions Both Normal to and the Same as the Source Direction for a Fission Beam Source.

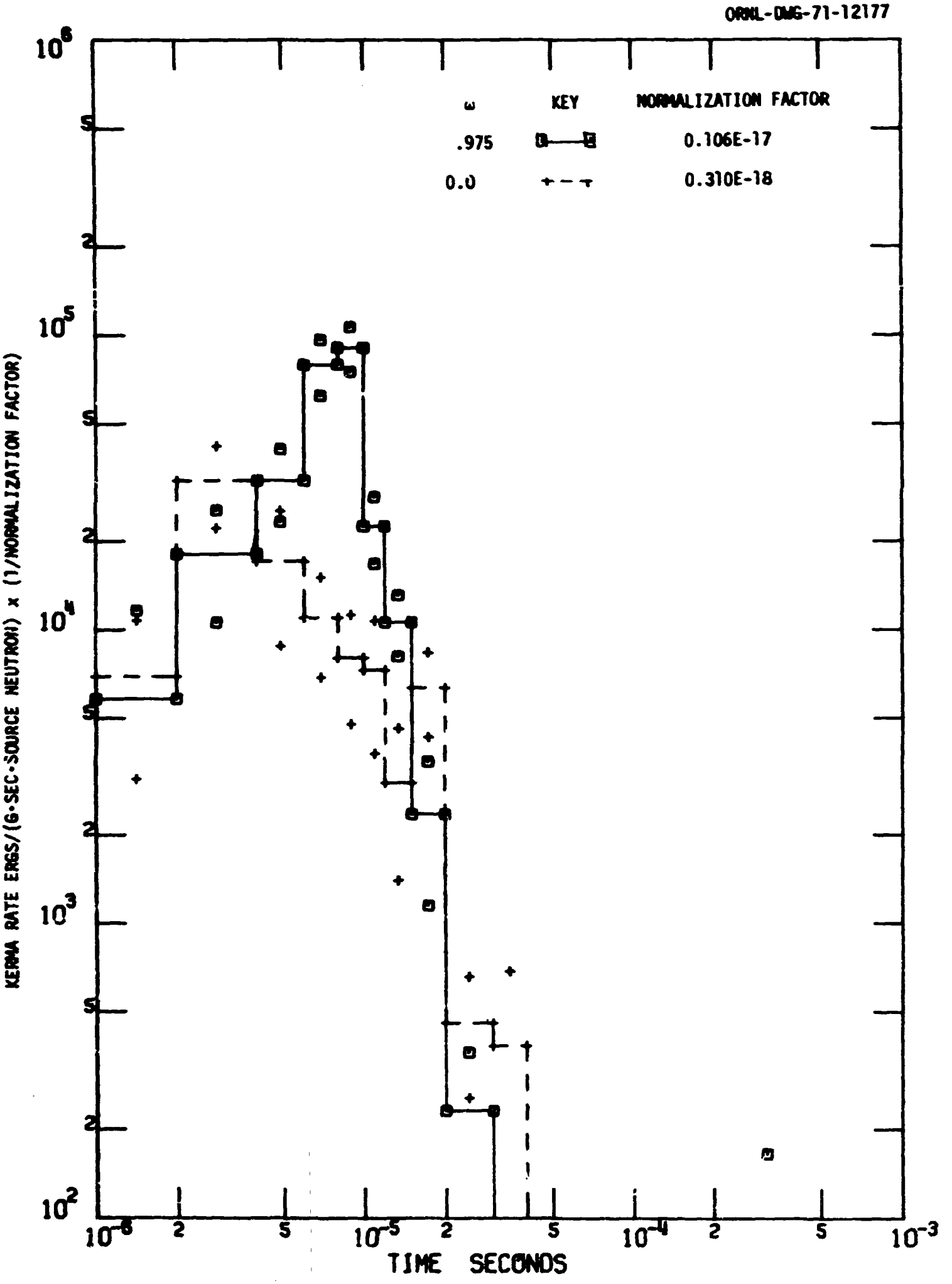

Fig. 101. Time-Dependent Gamma-Ray Air Kerma at a Radius of 300 M in the Directions Both Normal to and the Same as the Source Direction for a Fission Beam Source.

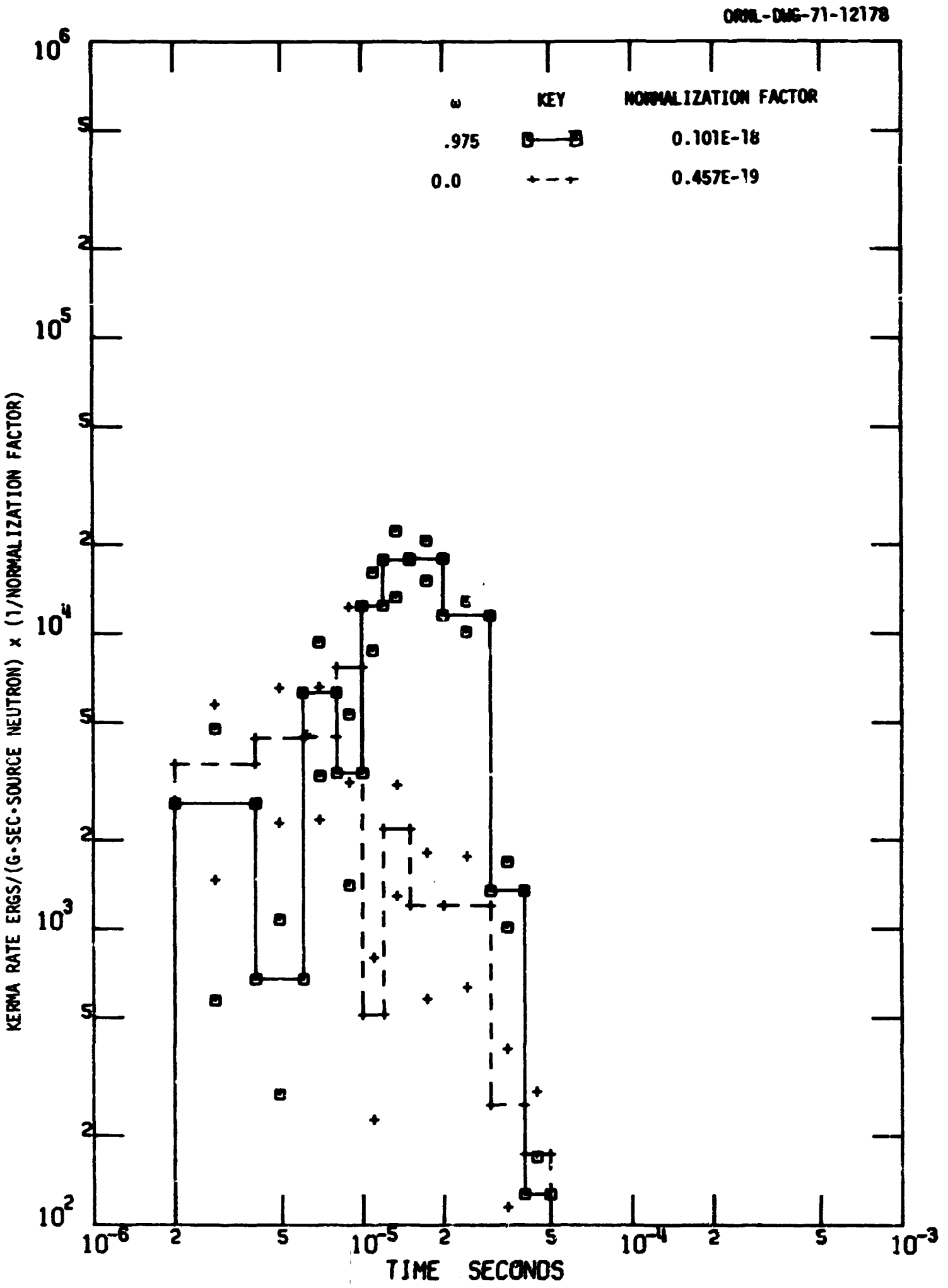

Fig. 102. Time-Dependent Gamma-Ray Air Kerma at a Radius of 800 M in the Directions Both Normal to and the Same as the Source Direction for a Fission Beam Source.

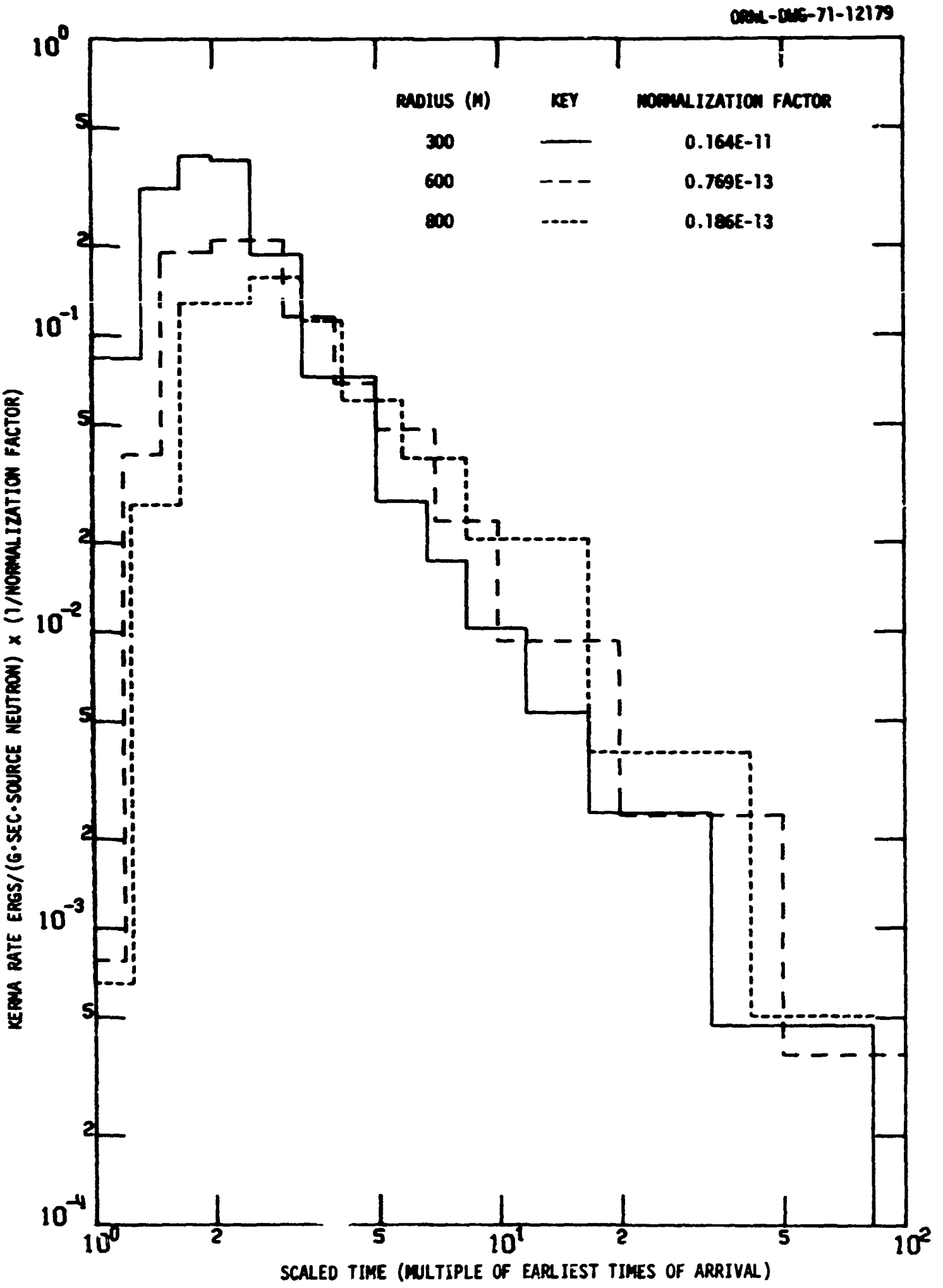

Fig. 103. Time-Dependent Neutron Air Kerma (Scaled) in the Source Plane for a Fission Pancake Source.

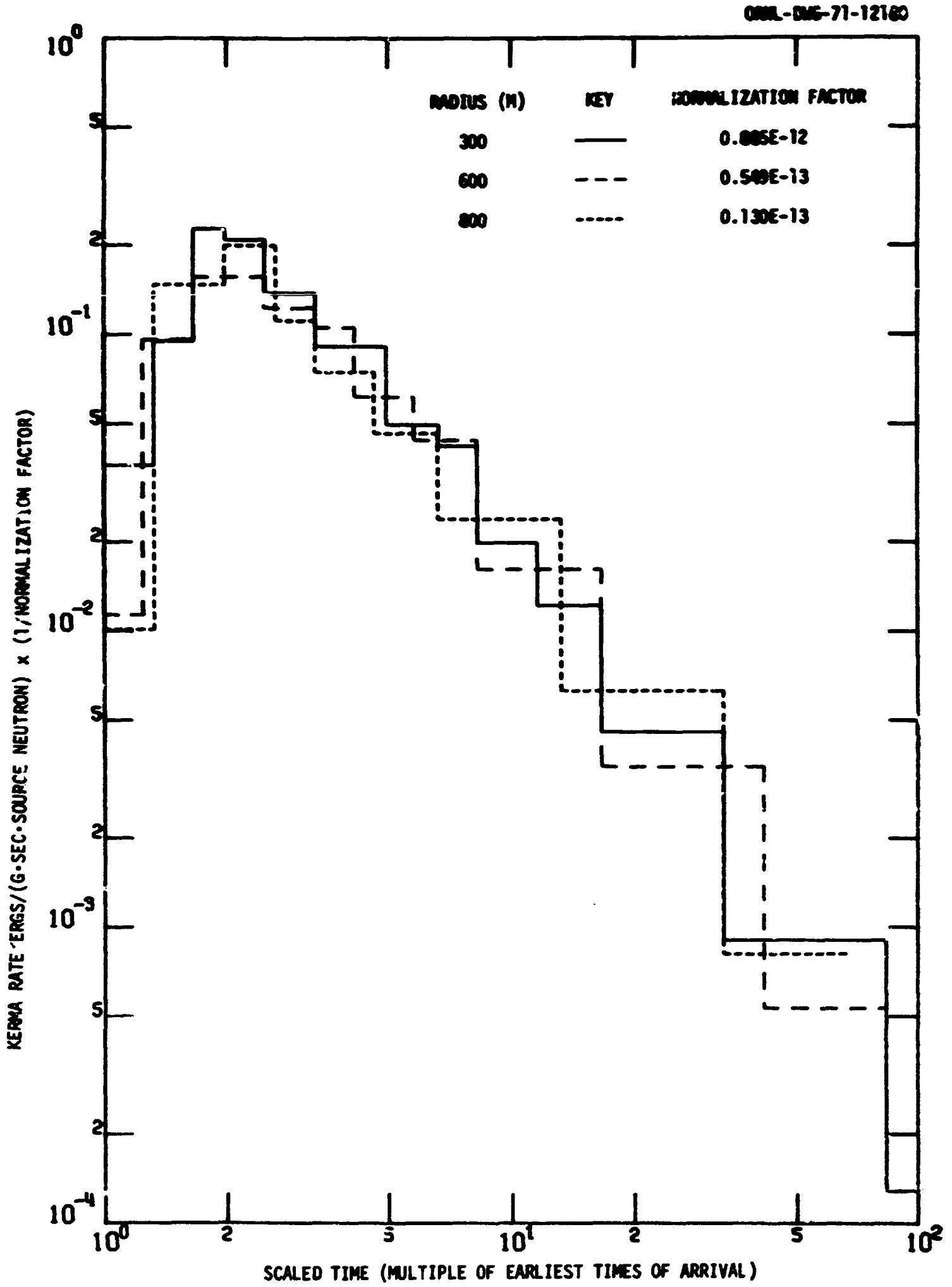

Fig. 104. Time-Dependent Neutron Air Kerma (Scaled) in a Direction at 10 deg from the Source Plane for a 12.2-15 MeV-Fission Pancake Source.

ORNL-DWG-71-12181

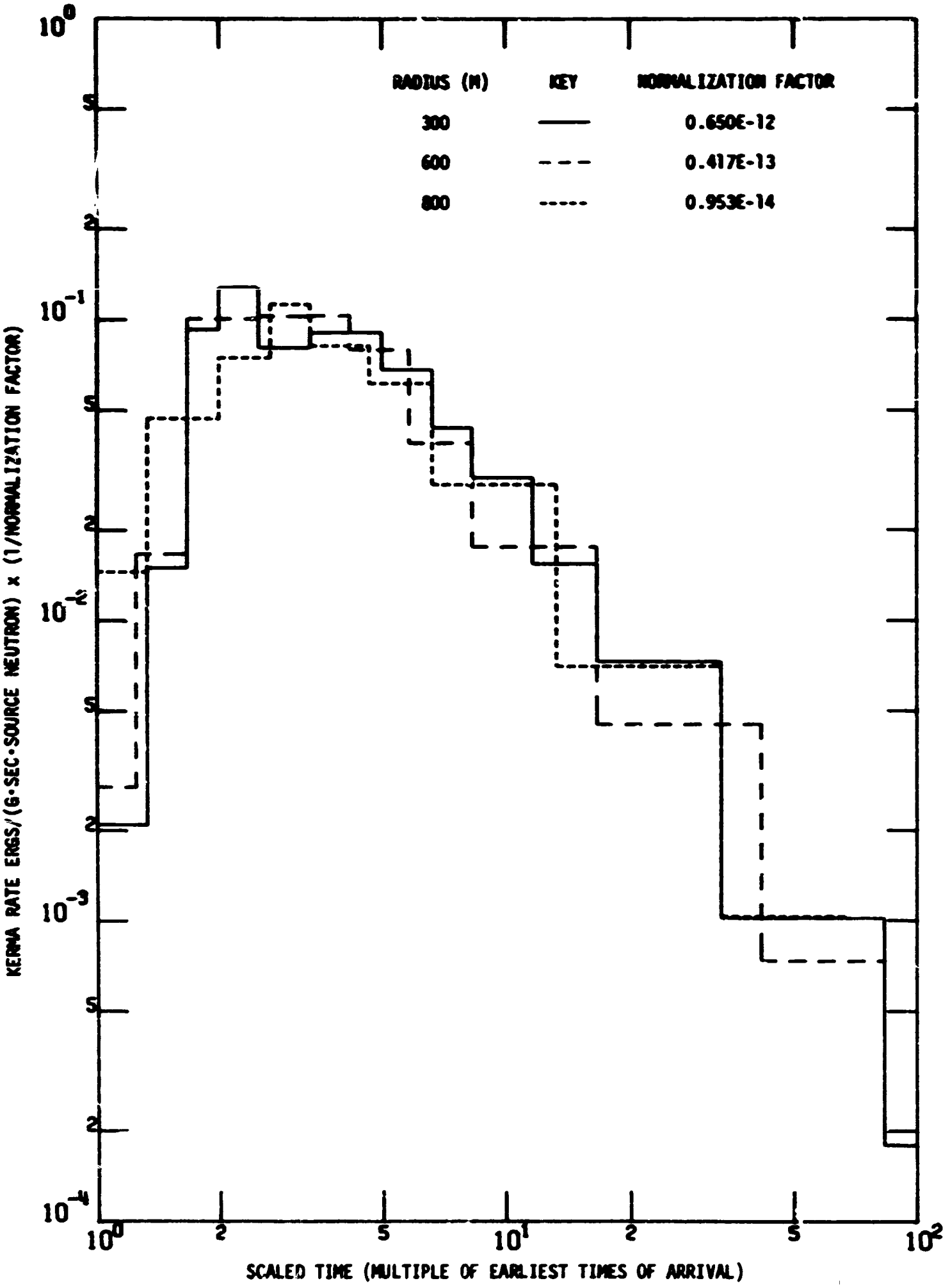

Fig. 105. Time-Dependent Neutron Air Kerma (Scaled) in a Direction at 30 deg from the Source Plane for a Fission Pancake Source.

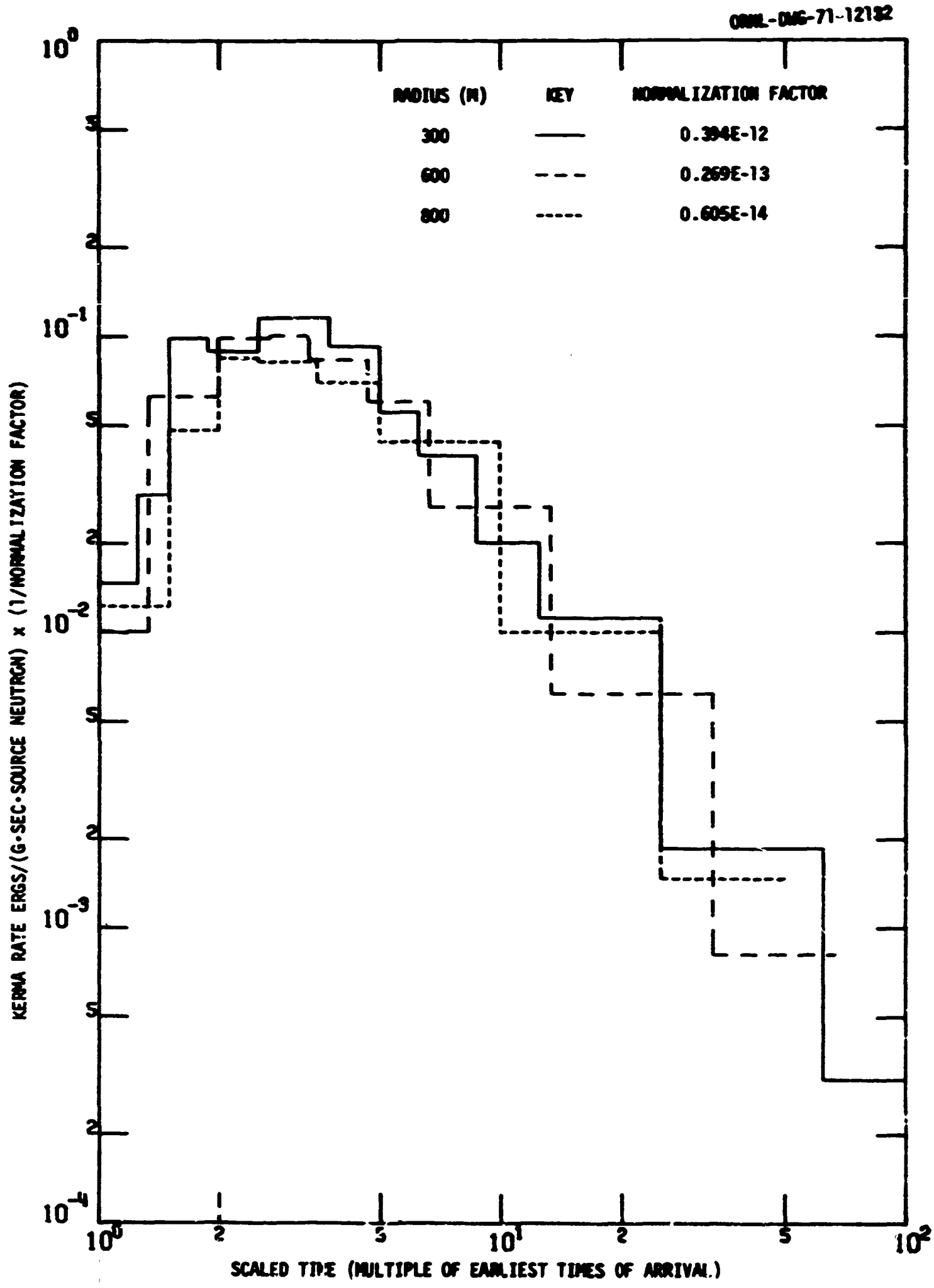

Fig. 106. Time-Dependent Neutron Air Kerma (Scaled) in a Direction at 70 deg from the Source Plane for a Fission Pancake Source.

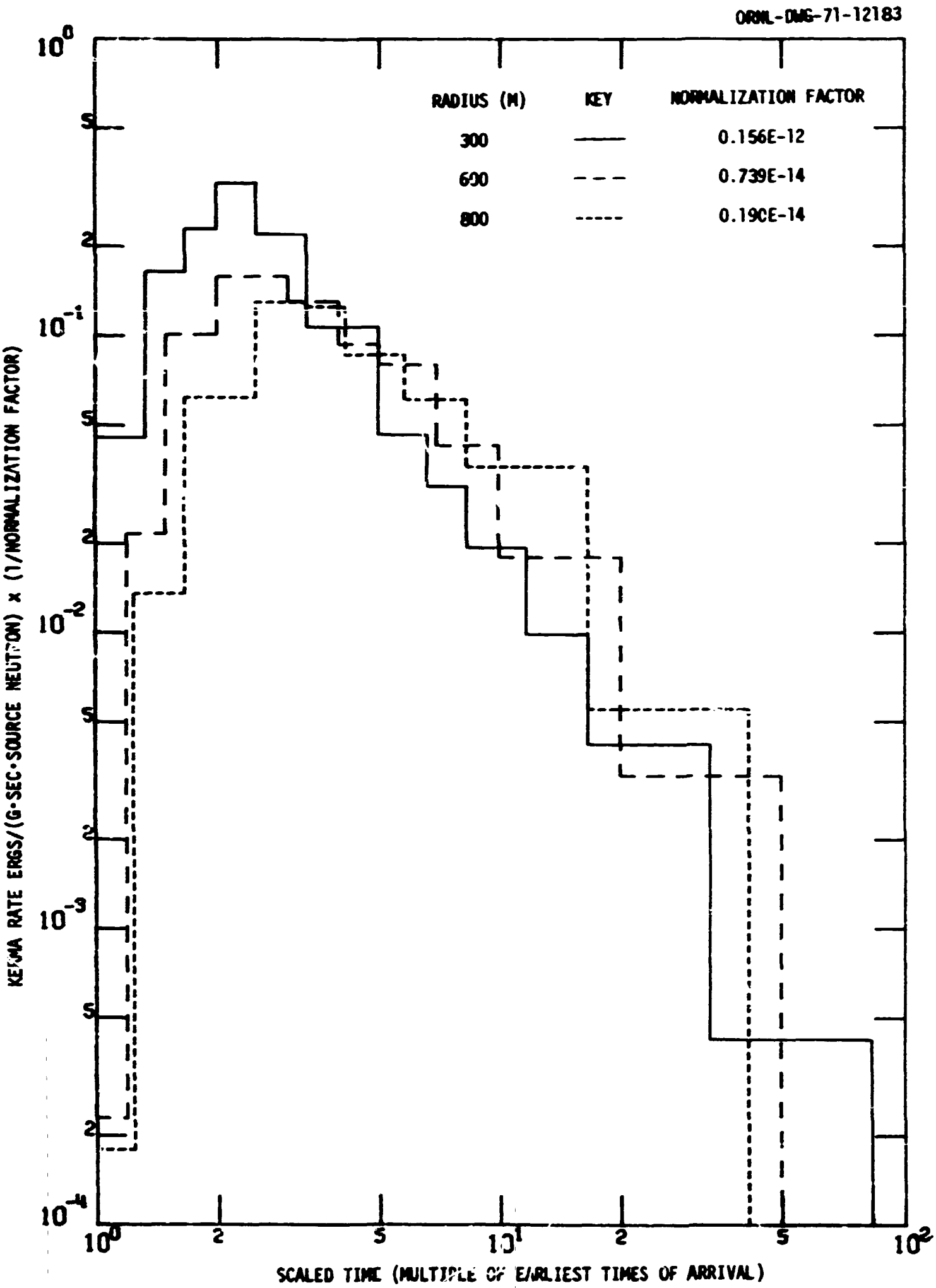

Fig. 107. Time-Dependent Neutron Silicon Kerma (Scaled) in the Source Plane for a Fission Pancake Source.

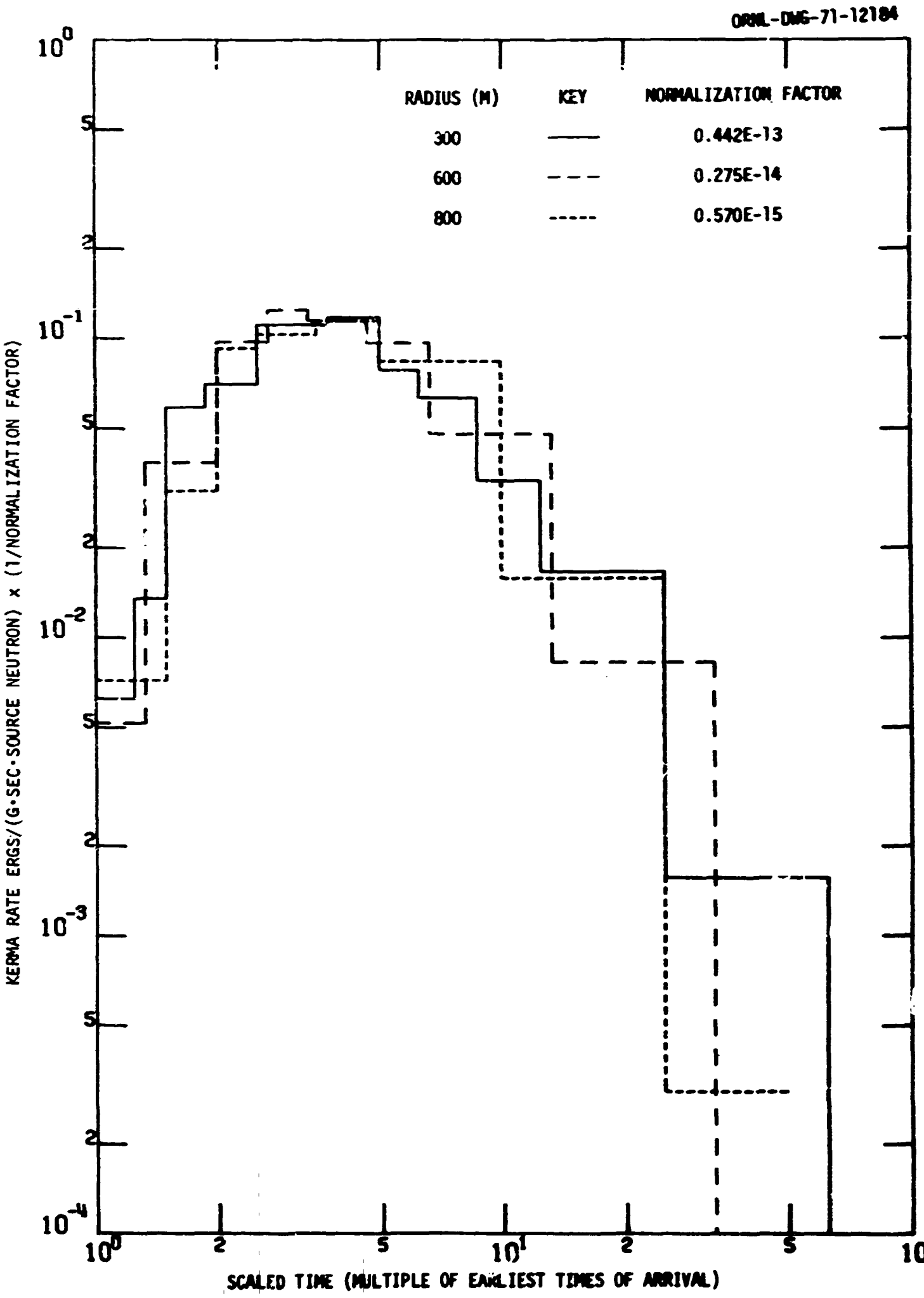

Fig. 108. Time-Dependent Neutron Silicon Kerma (Scaled) in a Direction at 70 deg from the Source Plane for a Fission Pancake Source.

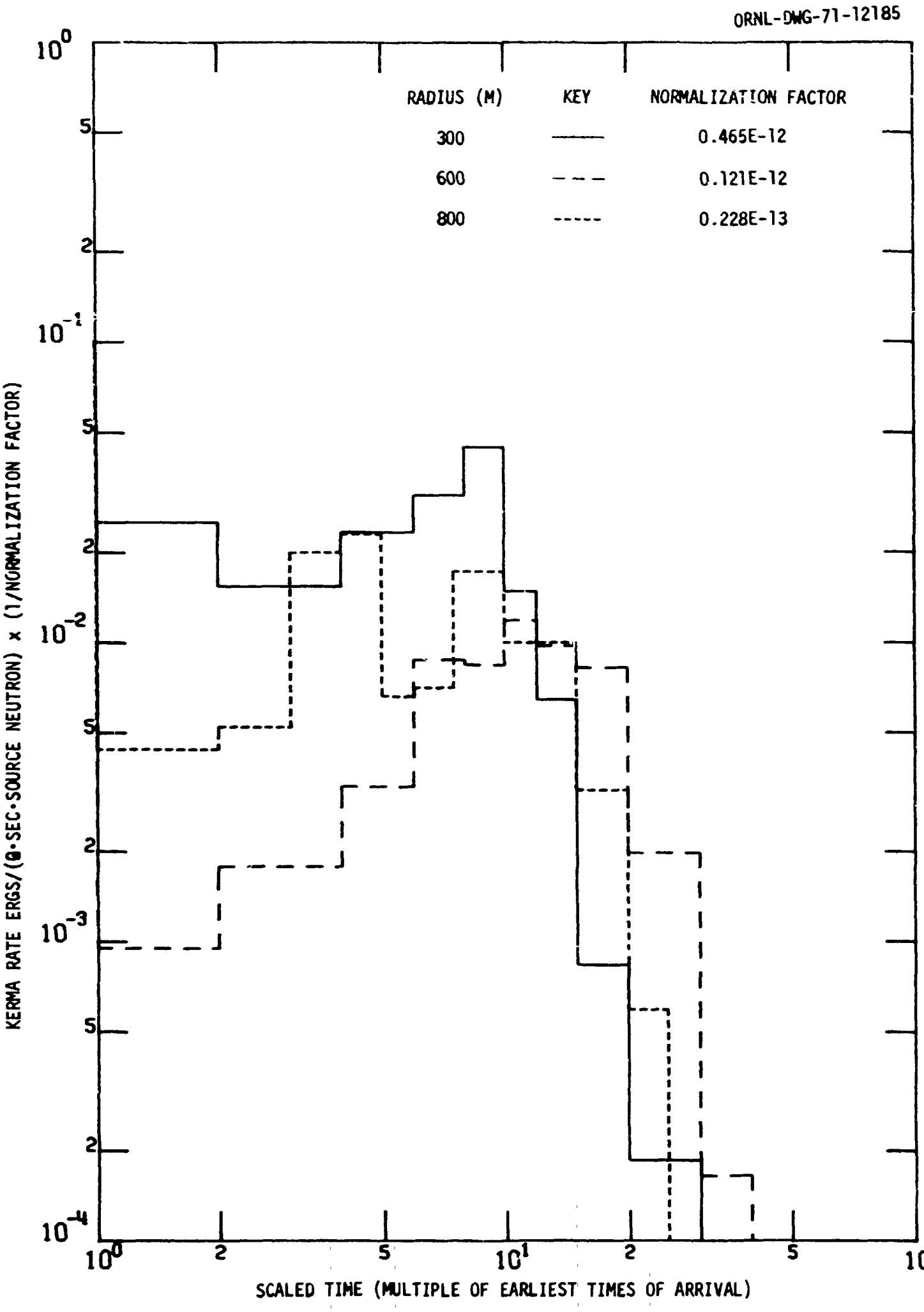

Fig. 109. Time-Dependent Gamma-Ray Air Kerma (Scaled) in the Source Plane for a Fission Pancake Source.

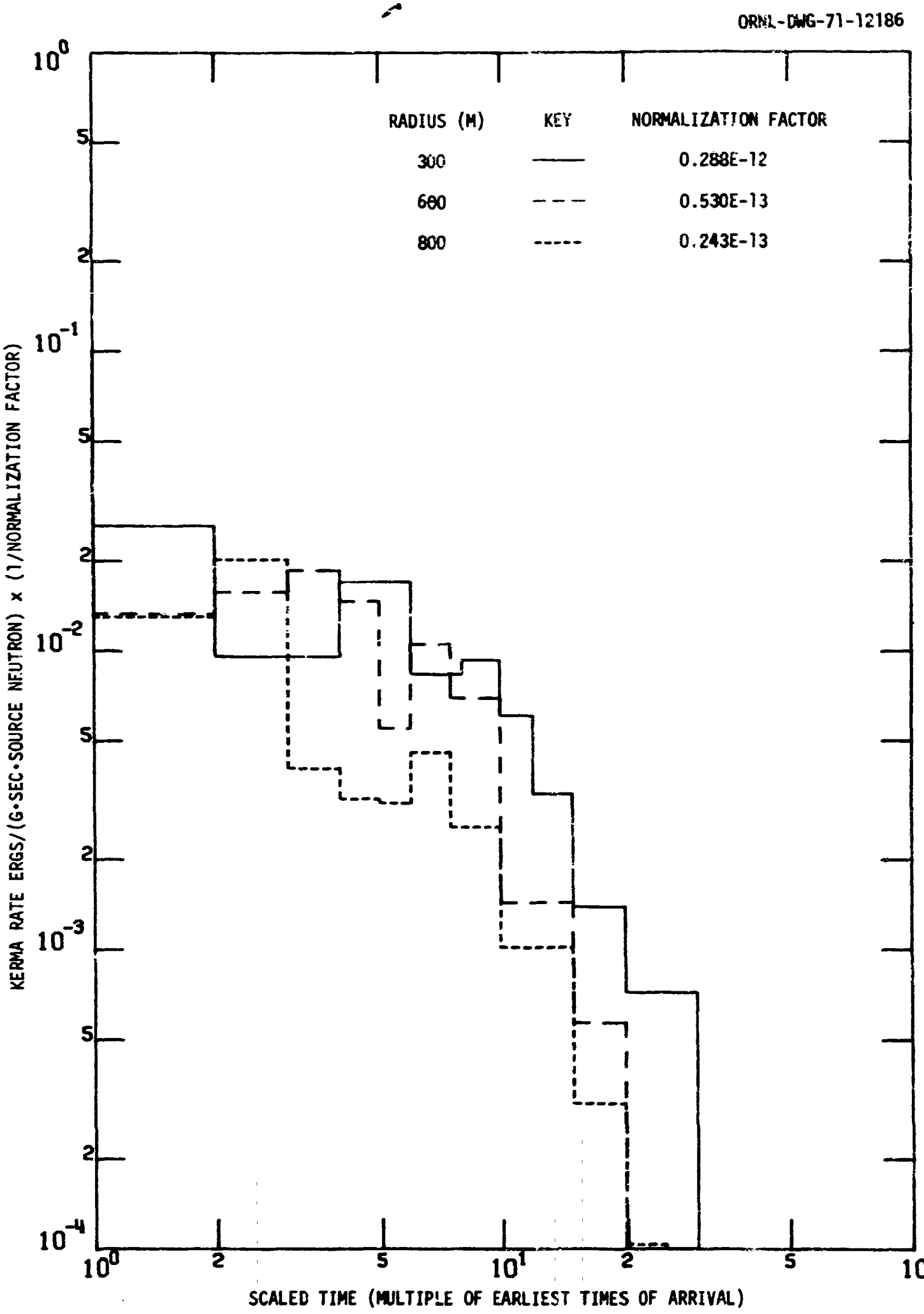

Fig. 110. Time-Dependent Gamma-Ray Air Kerma (Scaled) in a Direction at 70 deg from the Source Plane for a Fission Pancake Source.

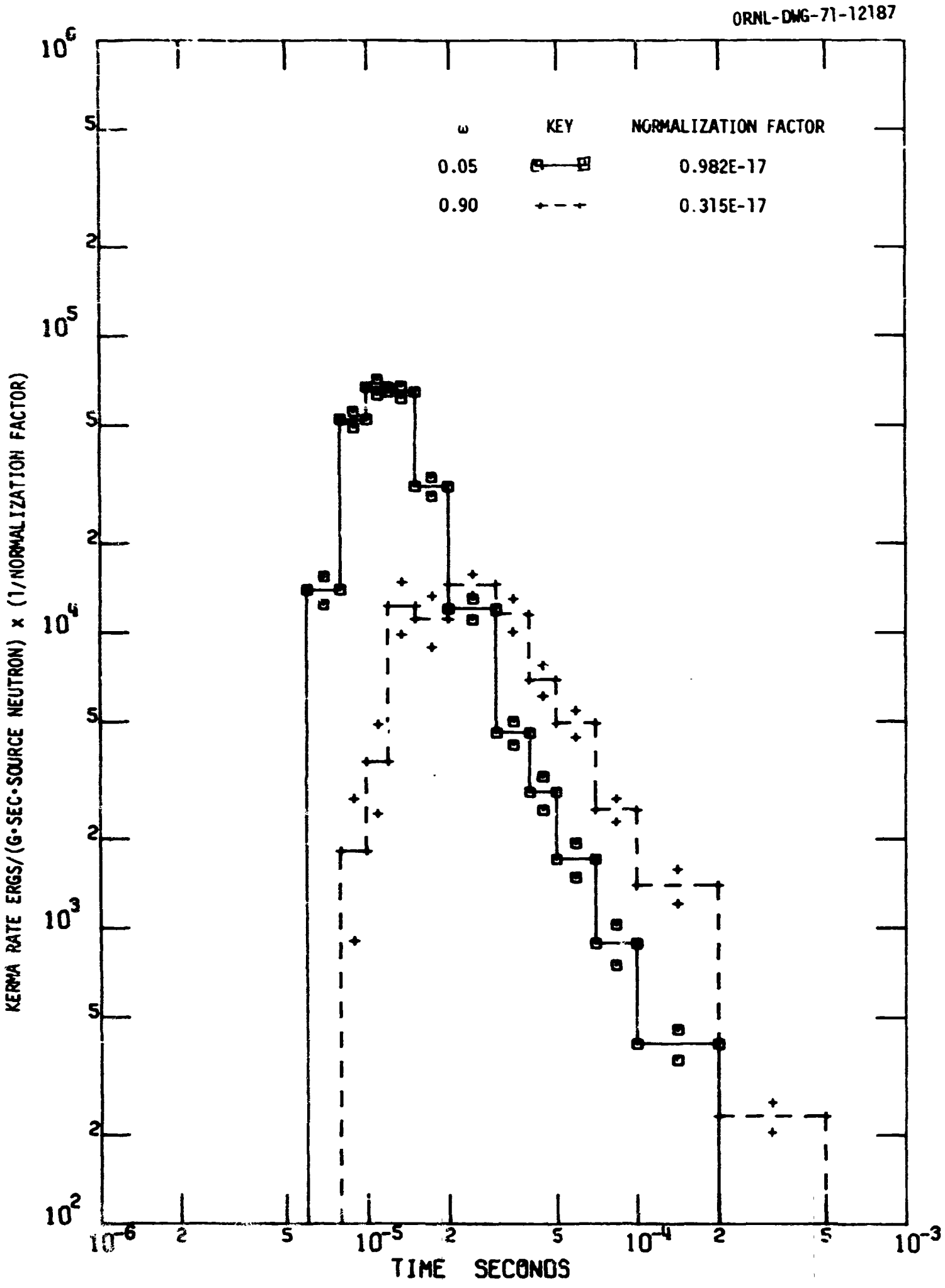

Fig. 111. Time-Dependent Neutron Air Kerma at a Radius of 300 M Both in the Source Plane and at 70 deg from the Source Plane for a Fission Pancake Source.

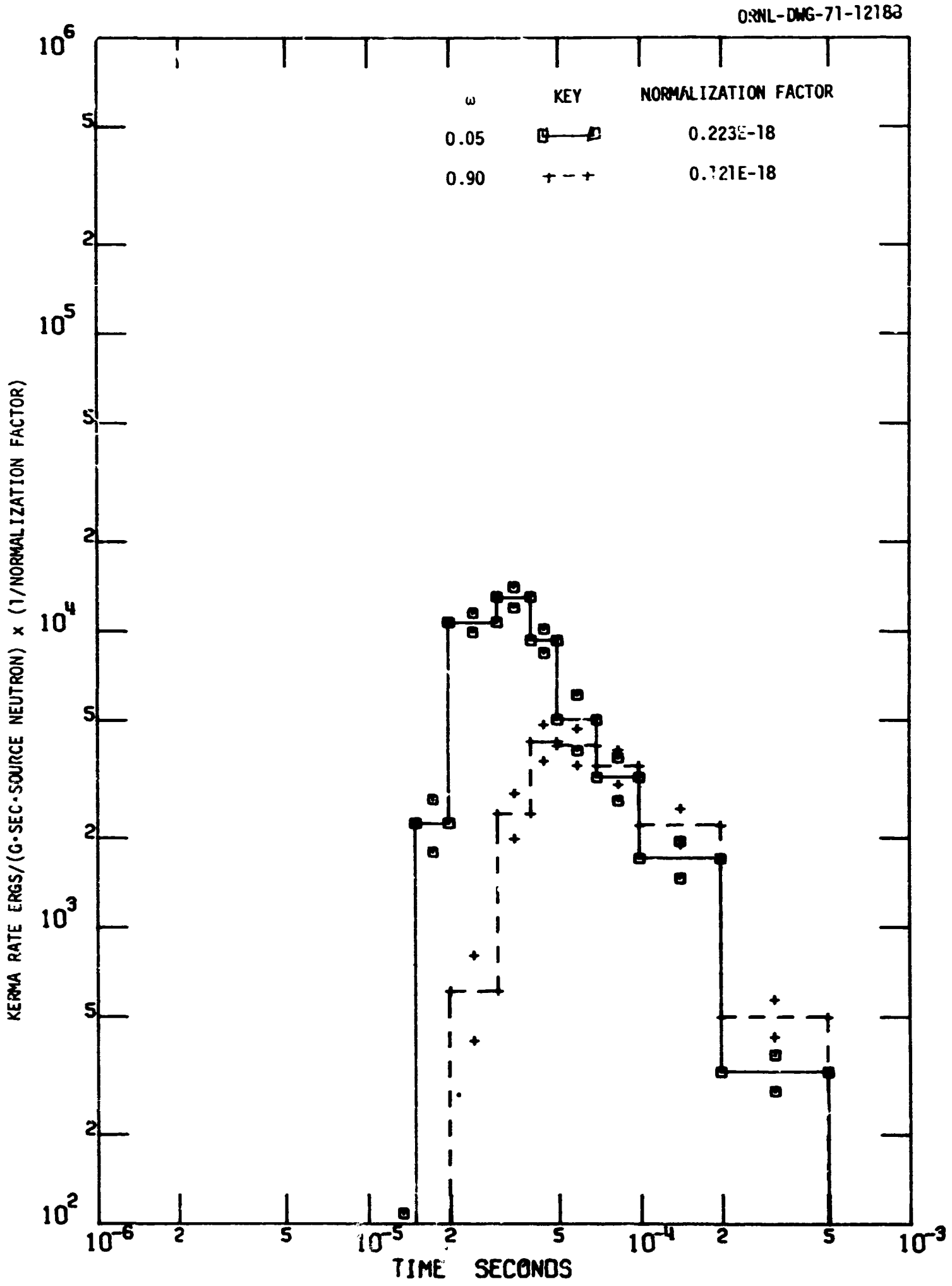

Fig. 112. Time-Dependent Neutron Air Kerma at a Radius of 800 M Both in the Source Plane and at 70 deg from the Source Plane for a Fission Pancake Source.

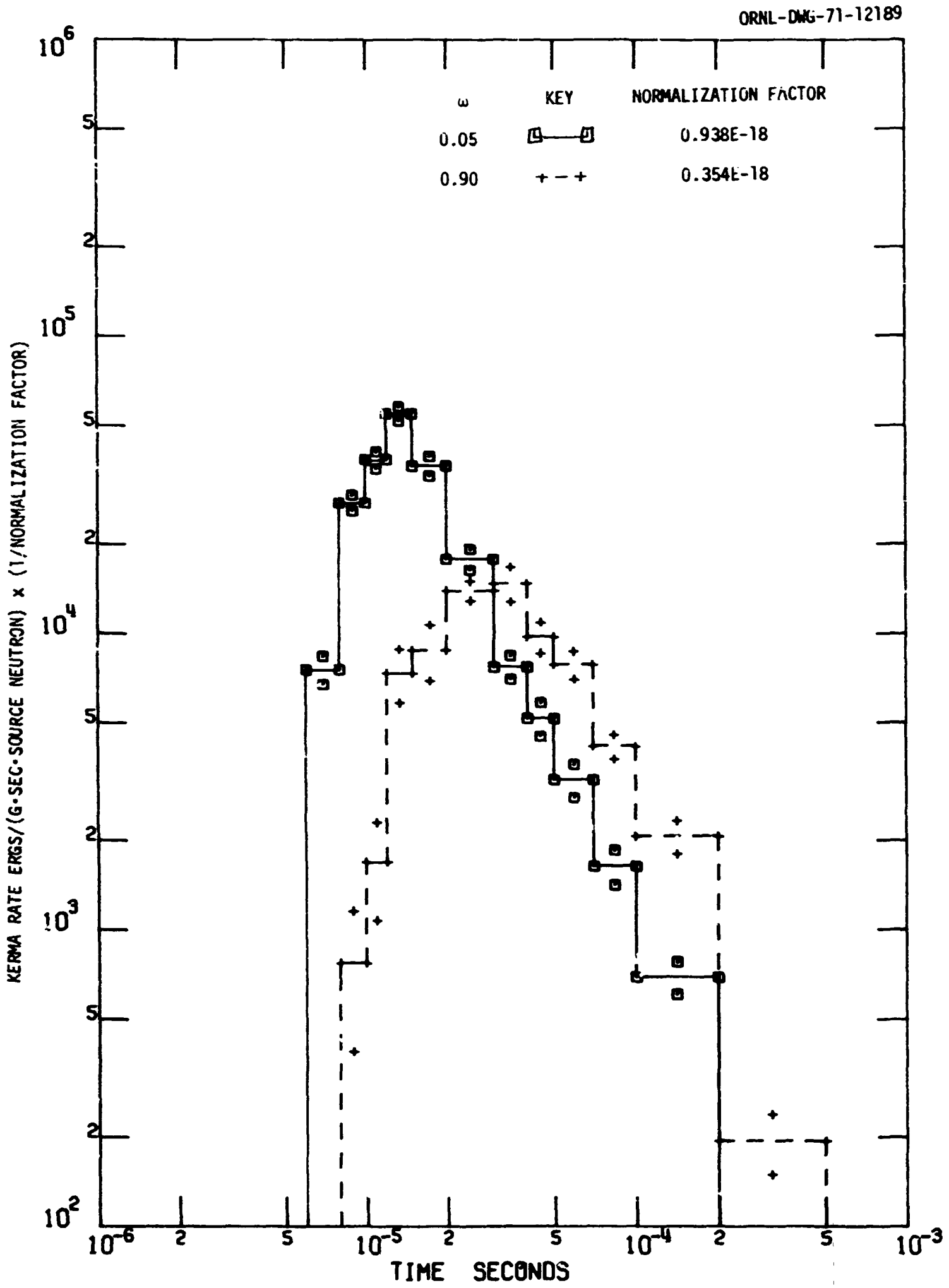

Fig. 113. Time-Dependent Neutron Silicon Kerma at a Radius of 300 M Both in the Source Plane and at 70 deg from the Source Plane for a Fission Pancake Source.

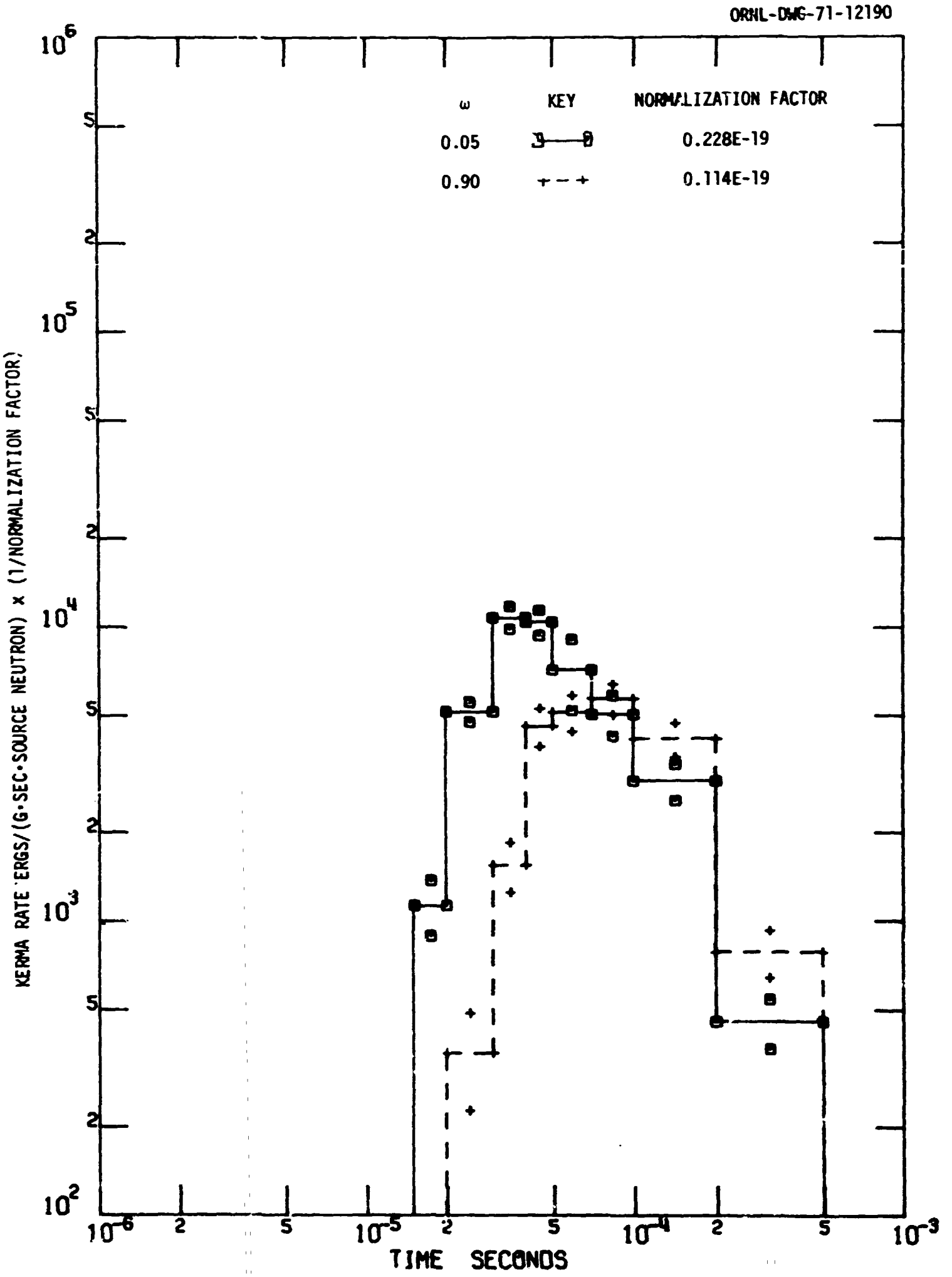

Fig. 114. Time-Dependent Neutron Silicon Kerma at a Radius of 800 M Both in the Source Plane and at 70 deg from the Source Plane for a Fission Pancake Source.

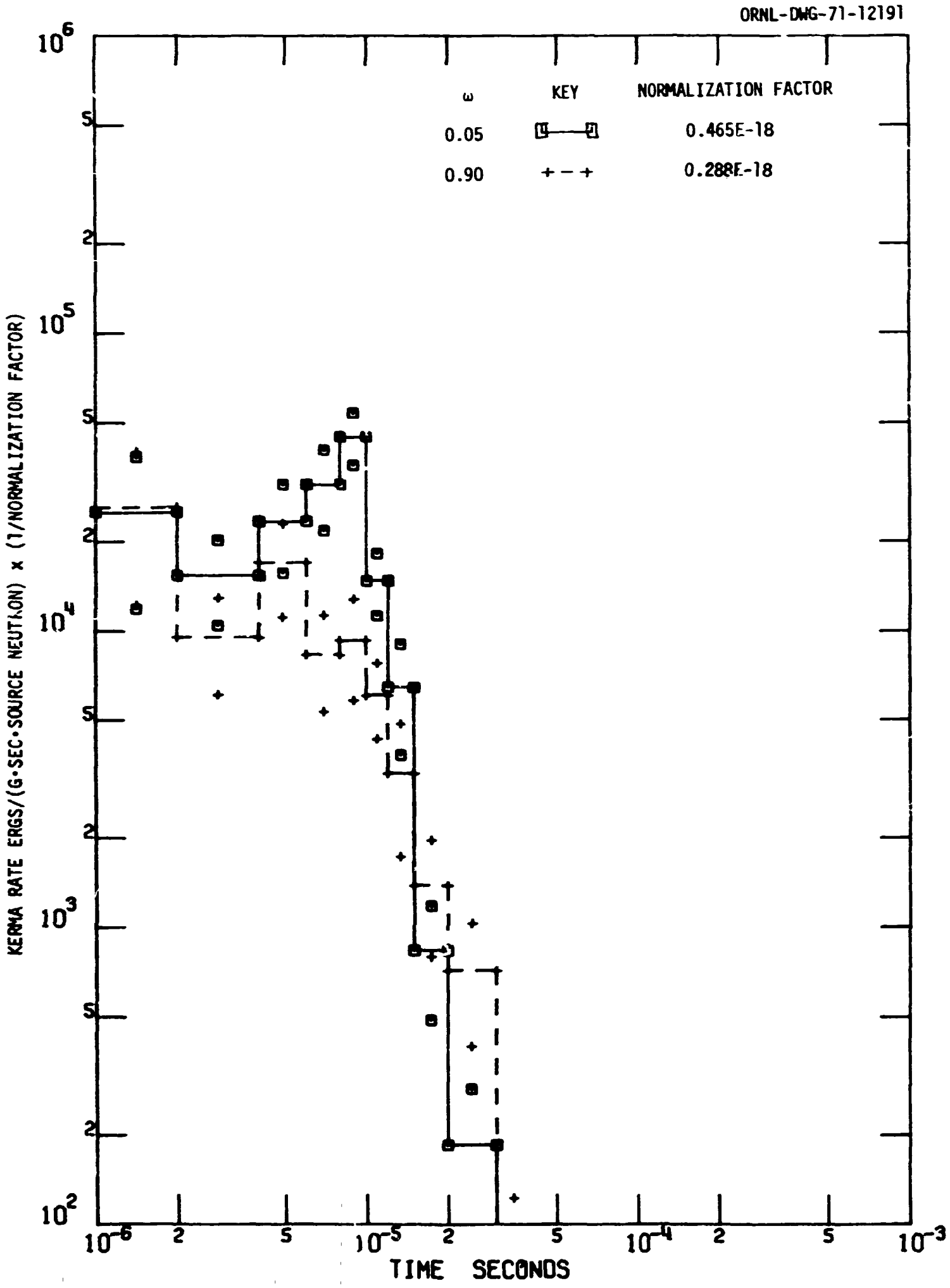

Fig. 115. Time-Dependent Gamma-Ray Air Kerma at a Radius of 300 M Both in the Source Plane and at 70 deg from the Source Plane for a Fission Pancake Source.

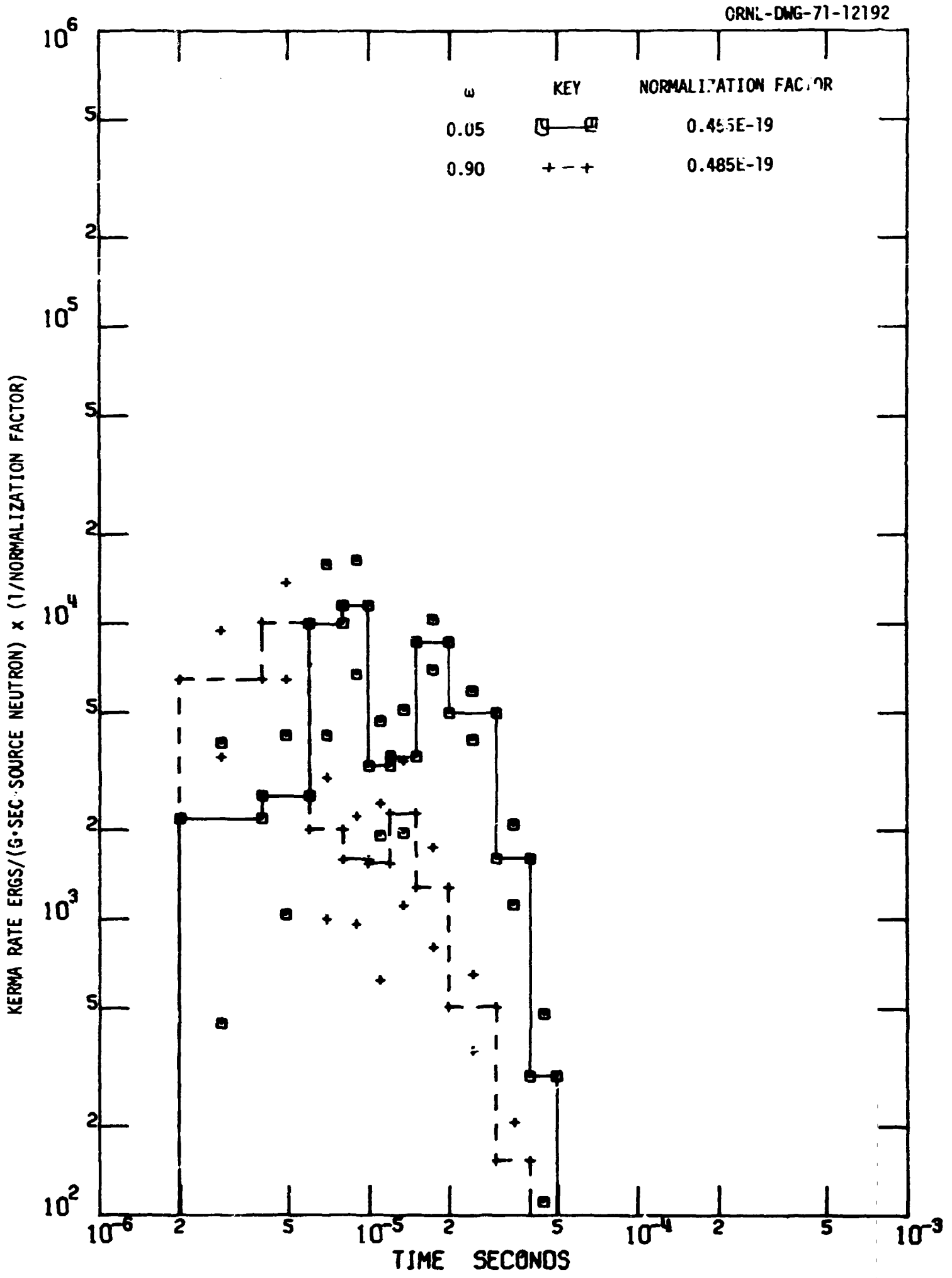

Fig. 116. Time-Dependent Gamma-Ray Air Kerma at a Radius of 800 M Both in the Source Plane and at 70 deg from the Source Plane for a Fission Pancake Source.

References

1. E. A. Straker, P. N. Stevens, D. C. Irving, and V. R. Cain, "The MORSE Code - A Multigroup Neutron and Gamma-Ray Monte Carlo Transport Code," ORNL-4585 (1970).

2. W. W. Engle, Jr., "A User's Manual for ANISN - A One-Dimensional Discrete Ordinates Transport Code with Anisotropic Scattering," K-1693 (1967).

3. E. A. Straker and M. L. Gritzner, "Neutron and Secondary Gamma-Ray Transport in Infinite Homogeneous Air," ORNL-4464 (1969).